UNIVERSITY OF LEEDS

In-situ control of magnetic multilayers studied with polarised neutron reflectometry

Daniel Louis Roe
University of Leeds
School of Physics and Astronomy

Submitted in accordance with the requirements for the degree of
Doctor of Philosophy

March, 2025

Intellectual Property Statement

The candidate confirms that the work submitted is his own and that appropriate credit has been given where reference has been made to the work of others.

Acknowledgements

First of all, I would like to thank my supervisors Prof. Oscar Cespedes, Prof. Sean Langridge and Dr. Andrew Caruana for all the guidance and support throughout. Without their knowledge, insight and expertise, this work would not have been possible. A special thanks must go to Oscar who it has been a pleasure to work with over the course of this PhD and my MPhys and who pointed me in the direction of this PhD. I would also like to thank all the other academics in the Condensed Matter group at Leeds who have helped with useful discussions in group meetings and around the office. I am also grateful for everyone who has helped me over the years. At Leeds, especially Dr. Matt Rogers for training me on almost all pieces of equipment and Dr. Mannan Ali for being the source of all knowledge and keeping everything in the group ticking over. Form ISIS, I would like to thank Dr. Gavin Stenning for helping with all things FMR and use of the measurement lab. The PNR measurements are a major part of this work so I want to give a big thanks to Dr. Christy Kinane and my supervisor Andrew for helping me to use POLREF and with all the various fitting. With that, I must also thank ISIS Neutron and Muon source for the allocation of beamtime and the ISIS Facility PhD studentship programme for co-funding this position. Thanks to everyone who has been a part of the Condensed Matter group at Leeds over the years and have made it such a good place to work. To bad influences, Jack and Katie, the old lunch club, Chris, Robbie and Jintao and to Callum for always keeping me entertained. And to everyone else in the group who has helped me out with things, big or small, I will always be grateful. Outside of science, I would like thank everyone who has put up with living with me throughout, Connor, Emilio, George and, of course, my mum and dad. Also, to Jen and Serena for many lovely meals and drinks in Leeds together. Without all of these people, the last 4 years in Leeds wouldn't have been the same. And last but by no means least, a very special thanks to my parents and Niamh for all their love and support over the years and for always believing in me. Thank you all!

Abstract

Polarised Neutron Reflectometry (PNR) is a powerful measurement technique used for studying structural and magnetic profiles. Here, we develop the ability to perform PNR measurements with external stimuli applied in situ. These in situ measurement techniques provide new avenues of research for functional spintronic devices.

The work of this thesis is split into two main studies. In the first, PNR measurements with in situ annealing are performed on C_{60}/CoB/C_{60} trilayers to monitor the migration of B ions from the CoB magnetic alloy into C_{60} molecular layers. This allows for control of magnetism by changing the B composition of CoB. Initial SQUID magnetometry measurements allowed for a comparison of the magnetisation before and after annealing as well as the monitoring of the magnetic moment during annealing. The C_{60}/CoB/C_{60} sample magnetisation increased by approximately 50% due to annealing. Structural information was gathered using PNR measurements with in situ annealing. The results show a significant injection of B into the C_{60} layers due to annealing. For a 10 hour anneal at 300°C the atomic percentage of the CoB layer reduces by $(7 \pm 4)\%$ resulting in an increase in the magnetic moment of $(80 \pm 30)\%$. Nuclear Reaction Analysis (NRA) measurements show a broadening of the B profile as further evidence of diffusion.

In the second main study of this thesis, an in situ FMR-PNR measurement technique is developed. This technique aims to combine the depth dependent magnetisation measurement of PNR with the measurement of magnetisation dynamics from FMR to unlock the ability to study the depth profile of the cone angle and damping. This measurement was performed in two geometries, one where the sample magnetisation and neutron polarisation are aligned and the other where there is an angle between the magnetisation and neutron polarisation. The second of these allows for a measurement of the magnetisation angle as well as the magnetisation. PNR measurements were performed with the sample on and off resonance to attempt to observe the changes in magnetisation due to the FMR precession. It was found that the measurement sensitivity is much greater for the magnetisation angle than the magnetisation magnitude so the angular

sensitivity is vital for this measurement. Simulations were used to determine the relationship between the measured angle between the magnetisation and neutron polarisation and the FMR cone angle. These demonstrated that the change in the measured magnetisation angle from PNR is proportional to the square of the FMR cone angle, $\Delta\theta_M \propto \phi_C^2$. The experimental measurements in this geometry show a small change in magnetisation angle of $(0.2 \pm 0.3)^\circ$ corresponding to a cone angle of $(3 \pm 2)^\circ$.

CONTENTS

List of Figures

List of Tables

Abbreviations

AC	Alternating Current
AFM	Antiferromagnetic
DC	Direct Current
DFT	Density Functional Theory
ERDA	Elastic Recoil Detection Analysis
FCC	Face Centred Cubic
FM	Ferromagnetic
FMR	Ferromagnetic Resonance
GMR	Giant Magnetoresistance
ImSLD	Imaginary Scattering Length Density
LLG	Landau Lifshitz Gilbert
MFM	Magnetic Force Microscopy
MRAM	Magnetoresistive Random Access Memory
mSLD	Magnetic Scattering Length Density
NEXAFS	Near Edge X-ray Absorption Fine Structures
NRA	Nuclear Resonance Analysis
NSLD	Nuclear Scattering Length Density
PA	Polarisation Analysis
PNR	Polarised Neutron Reflectometry
RKKY	Ruderman Kittel Kasuya Yosida
SA	Spin Asymmetry
SLD	Scattering Length Density
STT	Spin Transfer Torque
TMR	Tunneling Magnetoresistance
TOF	Time-of-Flight
VNA	Vector Network Analyser
XMCD	X-Ray Magnetic Circular Dichroism
XRR	X-ray Reflectivity
YIG	Yttrium Iron Garnet

CHAPTER 1

Introduction

1.1 Introduction

As the global demand for data computation and storage increases, the need to develop low power alternatives to current electronic devices becomes increasingly important. One group of devices that have gathered interest over the last few decades as a promising alternative path for electronics are spintronic devices. In conventional electronics, information is carried by electric charges. Spintronic devices utilise the electron spin as an additional degree of freedom in which more information can be carried and stored [1]. Spintronics devices already have practical applications in the form of hard disk drive read heads, as first developed by IBM [2], which utilised giant magnetoresistance (GMR) spin valve sensors and now use tunnelling magnetoresistance (TMR) sensors. The GMR spin valves consist of two ferromagnetic layers separated by a non-magnetic metal. One of the magnetic layers has a fixed magnetisation direction, whilst the other is free to switch. The resistance of the device is dependent on the relative orientation of the magnetisation in the two magnetic layers, meaning that the ones and zeros of digital data can be stored in the magnetisation direction of the free layer and then read out by measuring the resistance of the device. Larger magnetoresistance effects have been achieved using magnetic tunnel junctions (MTJ) which make use of TMR. The structure of an MTJ is similar to the traditional spin valves except the non-magnetic layer is replaced by an insulator [3, 4]. MTJs have also been used to develop magnetic random access memory [5–8] to provide fast, non-volatile data storage.

Manipulating magnetic moments in spintronics devices is imperative for their ability to read, write and store data. Switching magnetisation using a magnetic field requires large amounts of energy and is difficult to contain to localised areas on ever smaller devices. So, in the pursuit of low power electronics, research has turned to alternative methods such as all-optical switching [9–12], electric field gating [13–17], thermoelectricity [18, 19] and electrical currents [20, 21]. Therefore, experimental techniques in which the magnetic properties and structure can be measured whilst these external stimuli are applied in-situ are extremely useful for investigating the performance of these types of systems. This thesis presents the results of the development of new measurement capabilities for PNR measurements with in-situ control of magnetic multilayers.

PNR is a reflectometry technique that provides magnetic and nuclear structural depth profiles with nanometer resolution. In PNR, the reflection of neutrons occurs when there is a change in structure or magnetisation. This makes it especially useful for studying magnetic multilayers and interfacial effects. Spintronic devices used in practical technology typically consist of magnetic heterostructures made of different types of materials such as ferromagnets, antiferromagnets, insulators, normal metals and metal oxides. The devices utilise the interactions between the different types of materials to manipulate the magnetic behaviour. Therefore, it is crucial to understand how the materials interact and the fundamental explanations for the interactions. The measurement capabilities of PNR mean that it has proven to be a powerful technique for studying spin-valve structures like those used in spintronics devices [22–24] as well as the underlying interactions in magnetic heterostructures and multilayers such as exchange bias [25, 26] and interfacial magnetisation effects [27–30]. By combining the magnetic and structural measurement capabilities of PNR with in-situ annealing and microwave excitation, the results presented in this thesis demonstrate the development of measurement techniques that will aid in optimising and understanding functional spintronic devices with unconventional magnetic control.

The results in this thesis are split into two chapters, corresponding to two device operation methods. The first presents the data for an experiment that utilises PNR measurements with in-situ annealing and electrical gating to monitor the diffusion of B ions in C_{60} from the magnetic alloy CoB. In the second results chapter, results are presented for the FMR-PNR experiment. The aim of this experiment is to observe the precession of a sample magnetisation in FMR resonance using PNR. Both of these measurements provide the first demonstration of such in-situ device control with PNR experiments.

1.1.1 Ionic diffusion in C_{60}

Ionic liquids have been used to control the magnetic and transport properties of various materials via a gate voltage. The ionic liquids contain highly mobile ions. When placed on top of a device and a voltage is applied, the ions diffuse to the oppositely charged electrode and accumulate at the interface. The electric field produced by the ions can electrostatically induce negative charges to accumulate at the opposite side of the interface. Together, the positive and negative charges on either side of the interface form an electric double layer which acts like a nanoscale capacitor [31, 32]. Because of the short range, the electric fields produced by the electric double layers are very strong which gives them the ability to control the magnetic and transport properties of the device. In other cases, the effects are electrochemical and the gating of ionic liquids can cause the ions to migrate into the interfaced material and change its properties via doping or oxidation [31].

In previous research, ionic liquid gating has been used to manipulate magnetisation, anisotropy and exchange coupling in Co-based devices [33–37]. In most of these systems, the changes are electrochemical and the gate voltage is used to move oxygen ions in and out of the Co layer which controls the amount of CoO in the Co and therefore changes the magnetisation and anisotropy [33, 38, 39]. Ionic liquids have also been used to induce superconductivity in metal oxides [40, 41] and transition metal dichalcogenides [42, 43].

However, the nature of ionic liquids limits the functionalities and practicalities of their use in devices. As the ionic liquid needs to be in its liquid state for the ions to be mobile, it means that there is a limited operational temperature range. When they are used for low temperature applications, such as superconductivity, the gate voltage has to be applied at higher temperatures above 200 K before the device can be cooled to operating temperatures [43, 44]. This limits the device functionalities of, for example, switching the superconducting state on and off using the gate voltage whilst the device remains at low temperatures, reducing the practical applications. Also, the ionic liquids are often much bigger than the devices themselves which is a large drawback for use in transistor technology where reducing the size of devices is a substantial focus of modern research and development. Furthermore, ionic liquids prevent the ability to measure the gating effects in-situ using for example PNR, NEXAFS or XMCD.

In the work presented in this thesis, ionic diffusion in C_{60} is investigated with the aim of providing a solid state alternative to ionic liquids. C_{60} is solid at and below room temperature and stable up to 700 K at atmospheric pressure [45, 46]. This means that C_{60} offers a much wider range of operating temperatures to ionic liquids. C_{60} can be deposited by evaporation in ultra-high vacuum conditions. This allows for the deposition of the molecular material in the same conditions and vacuum cycle as the materials used in electronic and spintronic devices and ensures a clean interface between the device and molecules. In comparison, ionic liquids have to be deposited onto the device after sample fabrication, which brings about the possibility of oxidation or contamination of the device surface when it is taken out of vacuum. Also, evaporated C_{60} can be grown as thin films of the order of nm, which means that they can be used in integrated circuits where ionic liquids are too large.

Molecular materials, such as C_{60}, have already been an area of interest in spintronics research as a sustainable alternative to rare earth and precious metals. In what was dubbed as spinterface science by Sanvito [47], molecular materials are interfaced with ferromagnetic metals and the hybridisation at the interface leads to a modification of the magnetic properties of the ferromagnet [48–50]. The use of C_{60} in metal molecular devices at the University of Leeds has revealed many interesting effects such as emergent magnetism in non-magnetic metals [51, 52], enhanced anisotropy in ferromagnetic metals [53] and enhanced spin-orbit coupling in heavy metals [54]. This shows the experience of growing and studying high quality C_{60} films at Leeds. This, along with the large size of the C_{60} cages of 0.7 nm [55] and low density of 1.65 g/cc means that it is a strong candidate material to act as a host for ionic diffusion. The diffusion of Li ions in C_{60} has been observed experimentally with a diffusivity of 3.84 3.84×10^{-10} cm^2s^{-1} at room temperature [56] and an activation energy estimated by density functional theory calculations to be 0.34 eV. These values are comparable to the diffusion of Li in Li_xCoO_2 electrodes, which have activation energies from 0.2 - 0.3 eV and diffusivity between 10^{-10} - 10^{-12} cm^2s^{-1} [57–59], and solid state electrolytes such as Li_2SO_4, $LiNaSO_4$ and $LiAgSO_4$ with diffusivities ranging from 10^{-9} - 10^{-12} cm^2s^{-1} at room temperature [60]. There is also evidence of electrodiffusion of larger metal atoms, such as Au, Ag and In, from contacts into C_{60} films from at temperatures above 100°C [61–63].

1.1.2 FMR-PNR

FMR and PNR are both powerful techniques used to investigate magnetic materials. FMR provides information about the magnetisation and anisotropy of a sample as well as the Gilbert damping. The damping determines the speed and energy cost of switching magnetic moments and is, therefore, an important consideration for STT-MRAM type devices [64, 65]. A limitation of the FMR measurement technique is that there is no spatial resolution and the quantities extracted are an average over the whole sample measured. As previously mentioned, PNR is a reflectometry technique that provides a structural and magnetic depth profile through a sample by utilising the spin of the neutron probe. Therefore, by combining the two techniques, we aim to take advantage of the strengths of each to provide a depth dependant measurement of the magnetisation dynamics and the FMR cone angle.

This new measurement technique should unlock new possibilities in measuring the impact of different interfaces on the magnetisation precession as well as measuring induced moments in adjacent non-magnetic layers due to spin pumping. These capabilities would aid in studying magnetic multilayer structures used in spintronics devices that rely on interface effects, such as exchange bias and perpendicular magnetic anisotropy, for their functionality.

FMR has already been combined with x-ray scattering techniques in XFMR experiments in which the measurements are element specific and therefore provide depth resolution that is not possible with conventional FMR measurements [66–69]. These measurement techniques utilise the XMCD effect to obtain magnetic sensitivity. In XMCD measurements, a singular x-ray energy is used which is tuned to an absorption edge of a specific element to measure its magnetic response. This allows for layer specific FMR measurements when all of a particular element is contained to one layer in the sample. PNR utilises the neutron spin to measure magnetic contrast and therefore the incident neutron energy does not need to be tuned to a specific element absorption edge. This means that in each PNR measurement, all magnetisation in the sample is measured. Therefore, FMR-PNR can provide a complete measurement of the sample's structure, static magnetisation and magnetisation dynamics that is not possible with x-ray based techniques.

In-situ FMR-PNR measurement capabilities have been developed and used for experimental work by Kostylev, Causer et al. [30, 70]. In this experimental configuration, the FMR and PNR measurements are measured on the same sample in the same sample environment, however, there is no interaction between the two techniques. This is shown to be especially useful for sample systems that experience irreversible changes due to external stimuli, in their case due to hydrogen absorption in a Co/Pd system. The novelty of the work presented in this thesis, in comparison, is that we are directly measuring the change in magnetisation due to FMR precession using PNR to provide measurements of the depth dependence magnetisation dynamics and damping.

1.2 Structure of the thesis

Chapter 2 presents an overview of the theory of ferromagnetism and diffusion, covering the relevant theory required to understand the results presented in this thesis. This chapter also introduces the theory of RKKY coupling and exchange bias which are utilised in the samples for the FMR-PNR experiment.

Chapter 3 consists of a theoretical explanation of the concepts of reflectivity. An understanding of the fundamental theory of reflectometry is needed to be able to interpret the features of the data and how the structural information can be extracted from it. This chapter first covers the scattering of x-rays and reflectivity of simple samples, building up to multilayer samples. Neutron scattering mechanisms are then covered and applied to the reflectometry theory. Magnetic neutron scattering is very important to PNR so this is also explained, including how this results in different spin channels in PNR measurements and how the magnetic information of the sample can be extracted from them. The chapter finishes with a comparison of the advantages and disadvantages of PNR and XRR in relation to the two studies of this thesis.

Chapter 4 covers the experimental methods used. The beginning of this chapter describes the growth chamber used to fabricate all the samples used in this work. The vacuum chamber allows for DC magnetron sputtering of metal layers and thermal evaporation of C_{60} molecules meaning metallo-molecule heterostructures can be grown in one vacuum cycle. The operational theories of the sample characterisation techniques are described as well as the layout of the POLREF beamline at ISIS neutron source used for PNR measurements.

In Chapter 5, the results of the temperature driven ionic diffusion experiment are presented. Studies are performed on C_{60}/CoB/C_{60} samples where we aimed to observe the migration of B from the magnetic alloy into the molecular layers. SQUID magnetometry is used to measure the changes in magnetisation during the annealing process. PNR of trilayer C_{60}/CoB/C_{60} samples are measured before, during and after annealing to monitor the structural changes in the sample due the B injection and migration of B ions from the magnetic alloy into the molecular layers.

The development and results of the FMR-PNR measurement technique are given in Chapter 6. In this chapter, two approaches to the FMR-PNR technique are shown. In the first, a 2 spin channel PNR measurement is used, meaning that the measurements are only sensitive to the magnitude of the sample magnetisation. Therefore, the attempted observation of the magnetisation precession is via a reduction in the measured magnetisation. In the second attempt, an exchange bias sample is used, which means the magnetisation is pinned and can be placed at an angle to the neutron polarisation to give a measurable amount of spin-flip scattering. This allows for the magnetisation angle, as well as its magnitude, to be resolved and compared between the PNR measurements taken when the sample is on and off resonance. Simulations are used to determine how the PNR data is expected to change due to a small change in magnetisation angle. The measurement sensitivities of the two methods are compared and used to calculate the cone angle required to observe a difference between PNR data measured on and off resonance.

Finally, in Chapter 7, the results of the whole thesis are summarised. Potential improvements and next steps in the development of the in-situ measurement techniques are discussed, as well as the future work in utilising ionic diffusion in molecular thin films.

Chapter 2

Theoretical Background

2.1 Magnetism Theory

2.1.1 Exchange Interaction

The alignment of spins in ferromagnets is governed by the exchange interaction. This can be understood by considering the interaction of two electrons with wavefunctions of ψ_1 and ψ_2. These wavefunctions consist of a spatial function $\phi(\boldsymbol{r})$ and a spin function $\chi(\boldsymbol{s})$ such that

$$\psi(\boldsymbol{r}, \boldsymbol{s}) = \phi(\boldsymbol{r})\chi(\boldsymbol{s}). \tag{2.1}$$

The total wavefunction of the two electron system is given by

$$\Psi_{1,2} = \psi_{\mathrm{a}}(\boldsymbol{r}_1)\psi_{\mathrm{b}}(\boldsymbol{r}_2) \tag{2.2}$$

where the subscripts a and b correspond to the wavefunctions of the two electrons and $\boldsymbol{r}_1$ and $\boldsymbol{r}_2$ are their spatial positions. Electrons are fermions, so, due to the Pauli exclusion principle, the total wavefunction must be antisymmetric under exchange of the two electrons such that [45, 71, 72]

$$\psi_{\mathrm{a}}(\boldsymbol{r}_1)\psi_{\mathrm{b}}(\boldsymbol{r}_2) = -\psi_{\mathrm{a}}(\boldsymbol{r}_2)\psi_{\mathrm{b}}(\boldsymbol{r}_1). \tag{2.3}$$

Since the total wavefunction consists of the spatial and spin functions, it can be antisymmetric by either a symmetric spatial function and antisymmetric spin function or an antisymmetric spatial function and a symmetric spin function. As the electron has a spin of 1/2, the total spin of the symmetric and antisymmetric spin states must be $S = 1$ and $S = 0$ respectively. This results in one antisymmetric spin function called the singlet state, given by [73, 74]

$$\chi_S = \chi_{\mathrm{asym}} = \frac{1}{\sqrt{2}}(|\uparrow\downarrow\rangle - |\downarrow\uparrow\rangle), \tag{2.4}$$

and three symmetric spin functions called the triplet state given by [73, 74]

$$\chi_T = \chi_{\mathrm{sym}} = \begin{cases} |\uparrow\uparrow\rangle \\ \frac{1}{\sqrt{2}}(|\uparrow\downarrow\rangle + |\downarrow\uparrow\rangle) \\ |\downarrow\downarrow\rangle \end{cases} . \tag{2.5}$$

The singlet and triplet spin states can be combined with the symmetric and antisymmetric spatial functions to give two different versions of the total wavefunction that are both antisymmetric, given by [71]

$$\Psi_S = \frac{1}{\sqrt{2}}[\psi_1(\boldsymbol{r}_1)\psi_2(\boldsymbol{r}_2) + \psi_1(\boldsymbol{r}_2)\psi_2(\boldsymbol{r}_1)]\chi_S, \tag{2.6}$$

$$\Psi_T = \frac{1}{\sqrt{2}}[\psi_1(\boldsymbol{r}_1)\psi_2(\boldsymbol{r}_2) - \psi_1(\boldsymbol{r}_2)\psi_2(\boldsymbol{r}_1)]\chi_T. \tag{2.7}$$

With this, there are two possible configurations of the two electrons, one where the spins are parallel and one where they are antiparallel. In the case where the spins are parallel, the spatial function is antisymmetric so the electrons cannot occupy the same space and are further apart than in the case where the spins are antiparallel. This means that there is a difference in the Coulomb repulsion between the two electrons in each of the configurations. The energies of the singlet and triplet states are given by [71]

$$E_S = \int \Psi_S^* \hat{\mathcal{H}} \Psi_S \; d\boldsymbol{r}_1 d\boldsymbol{r}_2, \tag{2.8}$$

$$E_T = \int \Psi_T^* \hat{\mathcal{H}} \Psi_T \; d\boldsymbol{r}_1 d\boldsymbol{r}_2. \tag{2.9}$$

We can now introduce the exchange integral, $\mathcal{J}$, which is related to the difference in energies of the singlet and triplet states by [71, 73]

$$\mathcal{J} = \frac{E_S - E_T}{2} = \int \psi_1^*(\boldsymbol{r}_1)\psi_2^*(\boldsymbol{r}_2)\hat{\mathcal{H}}\psi_1(\boldsymbol{r}_2)\psi_2(\boldsymbol{r}_1) \; d\boldsymbol{r}_1 d\boldsymbol{r}_2. \tag{2.10}$$

The Heisenberg Hamiltonian generalises the exchange interaction for a many-body system consisting of more than two electrons. It is the sum over all pairs of adjacent spins in the system on sites i and j in the lattice such that

$$\hat{\mathcal{H}} = -2\sum_{i>j}^{N} \mathcal{J}_{ij} \boldsymbol{s}_i \cdot \boldsymbol{s}_j. \tag{2.11}$$

The exchange integral informs us about which orientation of electron spins is energetically favourable in a certain system. If $\mathcal{J}$ is positive, then the triplet state is favourable, so the spins will be aligned, resulting in ferromagnetic coupling. If $\mathcal{J}$ is negative, the singlet state is preferred with adjacent spins antiparallel, resulting in antiferromagnetic coupling.

2.1.2 Band Model of Magnetism in Metals

To understand how spontaneous ferromagnetism can occur in some metals, it is helpful to start with an understanding of Pauli paramagnetism. Consider a normal metal in no external magnetic field. Its valence band consists of two equal sub-bands corresponding to the spin up and spin down states. Both of the spin states will be filled up to the Fermi energy, meaning that there is no net magnetisation as there are an equal number of electrons of either spin. The potential energy of a magnetic dipole in a magnetic field is $\mathcal{E}_m = -m \cdot \boldsymbol{B}$ [74]. For electrons, this energy is given by $E = g\mu_B m_s B$ where g is the Landé g-factor and for electrons $g \approx 2$. Therefore, in an applied magnetic field, electron energy is slit by $g\mu_B B = 2\mu_B B$. This is the Zeeman splitting [71]. This means that, in an applied magnetic field, the energy of the sub-bands will be shifted by $\pm\mu_B B$ (+ for the antiparallel spins and - for the parallel spins). As the electrons can only occupy states up to the Fermi energy, this results in a difference in the number of occupied states of each spin and, therefore, a net moment in the same direction as the applied field. The magnetisation in this case is given by

$$M = (n^{\uparrow} - n^{\downarrow})\mu_B \tag{2.12}$$

where $n^{\uparrow}$ is the number of electrons added to the parallel spin state and $n^{\downarrow}$ is the number of electrons removed from the antiparallel state [71]. These can be expressed as

$$n^{\uparrow} = \frac{1}{2}\mu_B B\, g(E_F) \qquad\qquad n^{\downarrow} = -\frac{1}{2}\mu_B B\, g(E_F). \tag{2.13}$$

It then follows that the induced magnetisation becomes

$$M = \mu_B^2 B\, g(E_F). \tag{2.14}$$

The susceptibility of a paramagnetic metal is given by the Pauli susceptibility

$$\chi_P = \frac{\mu_0 M}{B} = \mu_0\, \mu_B^2\, g(E_F). \tag{2.15}$$

Stoner applied the idea of an internal molecular field present in ferromagnets proposed by Weiss to the understanding of Pauli paramagnetism to develop a prediction for the conditions in which spontaneous ferromagnetism will occur [73]. The molecular field is caused by exchange interactions between the electrons in the metal. The Weiss molecular field is given by $H_{MF} = \lambda M$, where λ is the molecular field constant that quantifies the strength of the molecular field inside a certain material. In this case, the total magnetisation under an applied field of H is given by

$$M = \chi_P(H + H_{MF}). \tag{2.16}$$

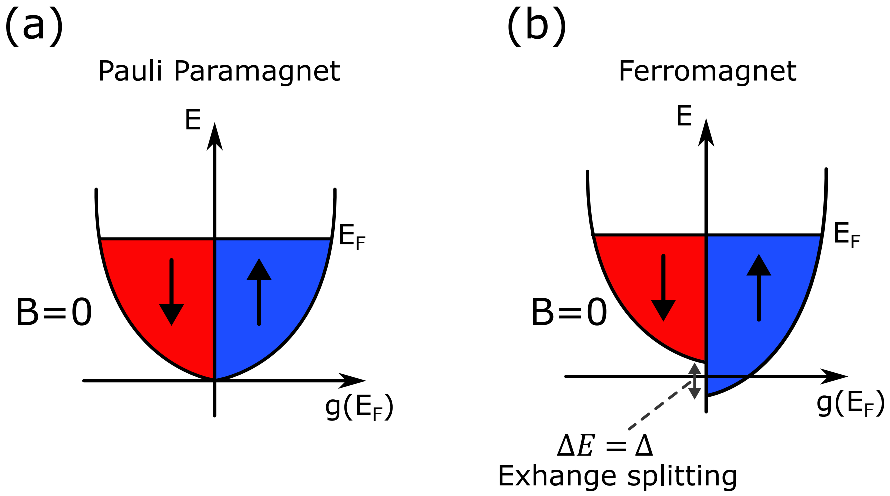

Figure 2.1: (a) Cartoon diagram of the band model of a Pauli paramagnet with an even number of spins in each spin band. (b) In a ferromagnet, no external field is required to split the energy of the two spin bands. The molecular field, due to exchange interactions, is strong enough to cause a splitting of the spin bands and therefore a surplus of electrons of a specific spin state. Figure designed after [73, 75].

The total susceptibility is now

$$\chi = \frac{M}{H} = \chi_P \left(\frac{1}{1 - \lambda \chi_P} \right). \tag{2.17}$$

Here we see that the susceptibility is enhanced when $\lambda\chi_P < 1$ and goes to infinity when $\lambda\chi_P = 1$ [73]. This denotes the point at which spontaneous ferromagnetism occurs. The condition for ferromagnetism is called the Stoner criterion, which is given by

$$\lambda\chi_P > 1 \qquad\qquad \lambda\mu_0\,\mu_B^2\,g(E_F) > 1. \tag{2.18}$$

When the Stoner criterion is met, it is energetically favourable in zero field for the spins to be aligned, resulting in a non-zero magnetisation. For a material to be ferromagnetic, it requires a strong exchange interaction and a large density of states at the Fermi energy. In a ferromagnet in zero applied field, the two spin bands will be split by the exchange splitting Δ as shown in figure 2.1 [71, 74].

2.1.3 Magnetisation Temperature Dependence

The first steps towards describing the temperature dependence of the magnetisation of ferromagnetic metals were made by Weiss in 1906 when he set out his mean field theory of ferromagnetism, which was mentioned in the previous section. This theory states that there is an internal molecular field that acts to align the spins within the ferromagnet and overcome thermal fluctuations [73, 74]. We know now that this molecular field that acts to align the spins is the effect of the exchange interactions. The molecular field is proportional to the magnetisation such that $H_{MF} = \lambda M$. Using this model, the temperature dependence of a ferromagnetic can be calculated by considering a paramagnet that experiences a field of H_{MF}. The magnetisation for a ferromagnet is given by the Brillouin function, $\mathcal{B}_J(x)$, such that [71, 74]

$$\frac{M(T)}{M_s} = \mathcal{B}_J(x) \tag{2.19}$$

where

$$\frac{M(T)}{M_s} = x = \frac{g_J \mu_B J(H + \lambda M(T))}{k_B T}. \tag{2.20}$$

These equations would describe a paramagnet if we set $\lambda = 0$, so the λM term is removed. To find $M(T)$, the simultaneous solutions of equations 2.19 and 2.20 are found. This can either be done graphically, by plotting the two functions and finding the points of intersection, or numerically [71, 73, 74]. The solutions for different values of J are shown in figure 2.2. The Weiss model for $J = s = 1/2$ gives reasonable agreement with experimental data for Ni, Fe and Co, however, there are discrepancies for T near 0 and T_C [74].

The temperature dependence of the magnetisation of a ferromagnet near the Curie temperature can be predicted using another mean field theory developed by Landau [71, 73]. To begin, we write the free energy of the ferromagnet as a power series in M. In this power series, only even powers of M are included as we know that the energy of up and down magnetisation states are equal. The free energy of a ferromagnet can then be written as

$$F(M) = F_0 + a(T)M^2 + bM^4 \tag{2.21}$$

where F_0 is a constant and b is a positive constant [71]. We know that there is a phase transition for all ferromagnets at T_C, above which $M = 0$. For this to be true of equation 2.21, $a(T)$ must change sign at T_C. This can be achieved by defining

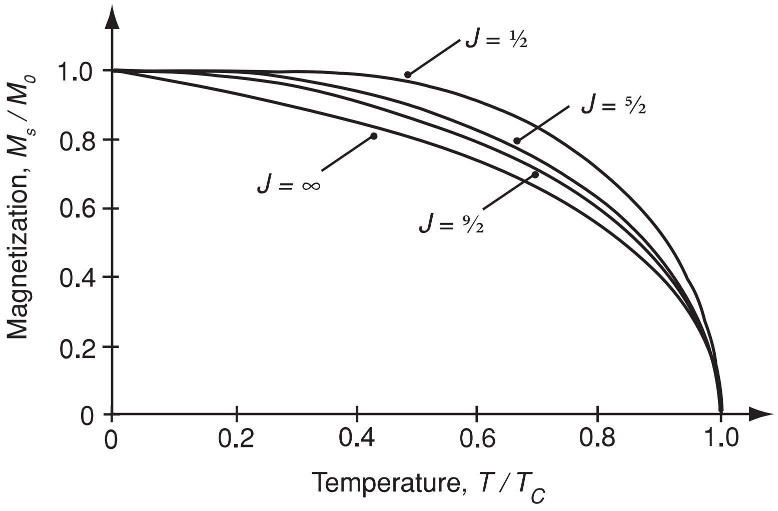

Figure 2.2: Magnetisation temperature dependence calculated from the Weiss mean field model for different values of J. Taken from [73].

$a(T) = a_0[T - T_C]$ near the transition [71, 73]. The energy minima of this system are solutions to $\partial F/\partial M = 0$. The resulting expressions for M are

$$M = 0 \qquad \text{or} \qquad M = \pm\left(\frac{a_0[T_C - T]^{1/2}}{2b}\right). \tag{2.22}$$

The second result in 2.22 is not valid for $T > T_C$, as it would require a square root of a negative number, meaning that we simply have $M = 0$. It can be proven that for $T < T_C$, the $M = 0$ solution is a higher energy than the second result by taking the second derivative of $F(M)$ [71]. Therefore, below T_C, we have a temperature dependence of the magnetisation of $M \propto (T_C - T)^{1/2}$.

The low temperature ($T << T_C$) behaviour of ferromagnets is governed by spin waves. Spin waves are formed from the coherent precession of spins in a lattice, all of which precess around the magnetisation direction of $\boldsymbol{M}$ [74]. The phase of the precession of each spin is shifted slightly from its nearest neighbours. At low temperatures, the energy required to flip one spin in a chain is much greater than the thermal energy. Therefore, the spin reversal is split across all the spins in the lattice by means of a periodic oscillation [73]. The energy of a spin wave of wave vector q is given by

$$E_{\mathrm{SW}} = \hbar\omega = 2\mathcal{J}Sa^2q^2 = Dq^2 \tag{2.23}$$

where $\mathcal{J}$ is the nearest neighbour exchange interaction, a is the interatomic spacing and $D = 2\mathcal{J}Sa^2$ is the spin wave stiffness [71, 73, 74]. The energy cost of producing a long wavelength spin wave is extremely small [71, 73]. Spin-waves are quantised as magnons, which are bosons and are the magnetic analogues of vibrations and phonons in solids [76]. The low energy cost of spin waves is the reason why they govern the low temperature magnetisation. Due to spin waves, the temperature dependence of the magnetisation at low T follows the Bloch $T^{3/2}$ power law

$$M(T) = M(0)[1 - kT^{3/2}] \tag{2.24}$$

where k is a constant containing the spin wave stiffness and parameters relating to the lattice structure of the material. For a full derivation of the Bloch $T^{3/2}$ power law the reader is directed to the book “Magnetism and Magnetic Materials” by J.Coey [73].

2.1.4 Spin-Orbit Coupling

Spin-orbit coupling (also known as the spin-orbit interaction) links the magnetic moment and the orbital momentum of a particle. The concept can be understood by considering the case of an electron orbiting a nucleus. In the rest frame of the electron, it is still, and the nucleus orbits around it. The orbit of the nucleus can be considered as a circular current that then produces a magnetic field at the origin that acts on the electron. The magnetic field produced by the orbit of the nucleus is given by [71]

$$\boldsymbol{B}_{\mathrm{SO}} = \frac{\boldsymbol{\varepsilon} \times \boldsymbol{v}}{c^2} \tag{2.25}$$

where $\boldsymbol{\varepsilon}$ is the electric field acting on the electron. The interaction energy due to the spin orbit coupling field for an outer electron is

$$\mathcal{E}_{\mathrm{SO}} \approx -\frac{\mu_0 \mu_B^2 Z^4}{4\pi a_o^3} \tag{2.26}$$

using the fact that $r \approx a_0/Z$ and $mvr \approx \hbar$ [73]. This electric field can be expressed in terms of the potential energy $V(\boldsymbol{r})$ as [71]

$$\boldsymbol{\varepsilon} = -\nabla V(\boldsymbol{r}) = -\frac{\boldsymbol{r}}{r}\frac{\mathrm{d}\,V(r)}{\mathrm{d}r}. \tag{2.27}$$

In the simple case of a single nucleus orbiting a single electron, the electric field experienced by the electron is

$$\boldsymbol{\varepsilon} = \frac{Ze}{4\pi\epsilon_0 r^2} \tag{2.28}$$

which results in a magnetic field of

$$\boldsymbol{B}_{\mathrm{SO}} = \frac{Zev}{4\pi c^2 \epsilon_0 r^2} \tag{2.29}$$

acting on the electron. The magnetic field interacts with the spin moment of the electron, $\boldsymbol{m}$, giving the Hamiltonian for the spin-orbit coupling [71]

$$\mathcal{H}_{\mathrm{SO}} = -\frac{1}{2}\boldsymbol{m} \cdot \boldsymbol{B}_{\mathrm{SO}} \tag{2.30}$$

By substituting in the forms of $\boldsymbol{B}_{\mathrm{SO}}$ and $\boldsymbol{\varepsilon}$ given in equations 2.27 and 2.28, this can be written as

$$\mathcal{H}_{\mathrm{SO}} = \frac{1}{2c^2 r}\frac{\mathrm{d}\,V(r)}{\mathrm{d}r}\boldsymbol{m} \cdot (\boldsymbol{r} \times \boldsymbol{v}). \tag{2.31}$$

Using the form of the angular momentum of $\hbar\boldsymbol{L} = m(\boldsymbol{r} \times \boldsymbol{v})$ and the expression for the magnetic moment of $\boldsymbol{m} = (ge\hbar/2m_e)\boldsymbol{S}$, the Hamiltonian can be expressed in terms of $\boldsymbol{L}$ and $\boldsymbol{S}$ as

$$\mathcal{H}_{\mathrm{SO}} = \frac{e\hbar^2}{2m_e^2 c^2 r}\frac{\mathrm{d}\,V(r)}{\mathrm{d}r}\boldsymbol{S} \cdot \boldsymbol{L} \tag{2.32}$$

$$\mathcal{H}_{\mathrm{SO}} = \xi(r)\boldsymbol{S} \cdot \boldsymbol{L} \tag{2.33}$$

where $\xi(r)$ is the spin-orbit coupling constant [71, 74]. From this Hamiltonian, we see that the energy shift due to spin-orbit coupling for a particular orbital depends on the electron's spin state, which leads to the splitting of the energy levels. This is the basis of Hund's rules, as for each orbital, there will be an energy preference for the electron to be in a particular spin state.

2.1.5 Domains and the Demagnetising Field

The stray field is the magnetic field outside of a sample produced by its magnetisation. The production of these stray fields comes at an energy cost. At the edges of the sample, the magnetisation must suddenly stop, causing it to diverge. When there are no external fields applied, we can say that $\boldsymbol{B} = \mu_0(\boldsymbol{H} + \boldsymbol{M})$ and $\nabla \cdot \boldsymbol{B} = 0$. From this, we obtain the expression

$$\nabla \cdot \boldsymbol{H} = -\nabla \cdot \boldsymbol{M} \tag{2.34}$$

This expression demonstrates that when there is this divergence of $\boldsymbol{M}$, there is an opposite divergence in $\boldsymbol{H}$ [71]. The H field that is produced is called the demagnetising field as it acts against the magnetisation of the sample and is often denoted by $\boldsymbol{H}_d$. The demagnetising field has an energy cost of

$$E_d = -\frac{\mu_0}{2}\int_V \boldsymbol{M}\cdot\boldsymbol{H}_d \,\mathrm{d}V, \tag{2.35}$$

where V is the volume of the sample. The formation of domains in a magnetic material reduces stray field and therefore reduces the demagnetising energy. Domains are regions within the magnetic sample where the magnetisation points in different directions. Adjacent domains are separated by domain walls which contain a spiral magnetisation pattern to join the different magnetisation directions of the domains. The width of the domain wall is given by

$$d = \pi\sqrt{\frac{A}{K}} \tag{2.36}$$

where A is the exchange stiffness and K is the anisotropy constant [73, 74]. The magnetic sample will split into domains if the energy cost of the domain walls is less than that of the stray field [71].

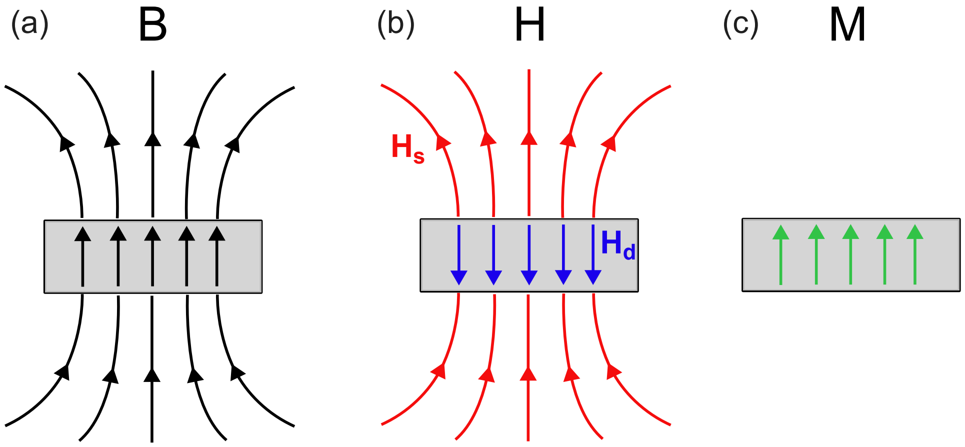

Figure 2.3: Schematic of $\boldsymbol{B}$, $\boldsymbol{H}$ and $\boldsymbol{M}$ for a thin film, uniformly magnetised out of the sample plane. The magnetic field inside the sample $\boldsymbol{H}_d$ is the demagnetising field and opposes the magnetisation $\boldsymbol{M}$. The magnetic field outside of the sample is in the stray field $\boldsymbol{H}_s$. Figure designed after [74].

2.1.6 Magnetic Anisotropy

Most magnetic materials will have an energy preference to align their magnetic moment along a certain axis. This phenomenon is known as magnetic anisotropy. The axis along which the magnetisation prefers to lie is called the easy axis and the hard axis refers to the most energetically unfavourable axis for the magnetisation to lie along. In samples with magnetic anisotropy, the magnetisation will lie along the easy axis when there is no field applied. Rotating the magnetisation away from the easy axis and towards the hard axis requires an additional energy input. The anisotropy energy, to second order, is given by

$$E_a = K_1 \sin^2(\theta) + K_2 \sin^4(\theta) \tag{2.37}$$

where θ is the angle between the magnetisation and the easy axis and K_1, K_2 are the anisotropy constants [73, 74]. The first order anisotropy constant is typically much larger than the higher order constants and so the equation can be simplified to the first term. The anisotropy constant consists of different components related to the different types of anisotropy. These include magnetocrystalline, shape and interfacial anisotropy. The anisotropy constant can then be expressed as

$$K_1 = K_{MCA} + K_S + K_I. \tag{2.38}$$

Shape Anisotropy

The shape anisotropy sets a preference for the magnetisation to lie in certain planes in order to minimise the demagnetising field. We first consider the case where there is no shape anisotropy, a sphere. The stray field is the same in all directions so there is no energy saving if the magnetisation lies in any direction. However, for thin films, the stray field caused by the magnetisation pointing out of the plane of the sample is much larger than the magnetisation pointing in the sample plane. The shape anisotropy for a thin film is given by

$$K_S = \frac{1}{2}\mu_0 M^2 \cos^2(\theta) \tag{2.39}$$

where θ is the angle between the magnetisation axis and the sample normal [71]. The shape anisotropy in thin films, therefore, heavily favours an in-plane magnetisation direction. In our FMR experiments, this means that the precession of the magnetisation will not be circular and instead be elliptical with an in-plane cone angle larger than the out of plane cone angle.

Magnetocrystalline Anisotropy

Magnetocrystalline anisotropy arises from the interactions of the electron spin moments with the crystal lattice. The spin moments are coupled to the electronic orbitals in the crystal lattice via spin-orbit coupling. The arrangement of atoms in a crystal produces a potential called a crystal field [73]. The crystal field means that the potential experienced at a certain atomic site will cause the electronic orbitals to align along a specific plane in the lattice. Therefore, when the spin moments couple to these orbitals via the spin-orbit interaction, they will preferentially align along a specific crystallographic direction. This anisotropy is shown by the different magnetisation curves observed for the different crystal directions for single-crystal ferromagnets [73].

Interfacial Anisotropy

Interfacial anisotropy is the anisotropy that occurs in thin film magnetic materials when they are interfaced with other materials. Two main examples of interfacial anisotropy are exchange bias, which will be discussed later in this chapter, and perpendicular magnetic anisotropy (PMA). PMA is most common in multilayer samples in which a ferromagnet, such as Co, is interfaced with a heavy metal with large spin orbit coupling such as Pt or Pd [77, 78]. PMA occurs due to the orbital hybridisation of the Co 3d electrons and the heavy metal 5d electrons at the interface [79–82]. This hybridisation causes an enhancement of perpendicular orbital moments in Co, producing PMA at the interface [83].

The anisotropy of a material can be split into surface and volume components, given by K_S and K_V respectively,

$$K = K_\mathrm{V} + \frac{2K_\mathrm{S}}{t} \tag{2.40}$$

where t is the thickness of the magnetic material. Here, the volume anisotropy includes the shape anisotropy and magnetocrystalline anisotropy components. Typically, the volume anisotropy term is in-plane, meaning that the overall anisotropy thick films, in which the volume term dominates, is in-plane [71, 75, 84]. In ultra-thin films of the order of 1 nm and below, the interfacial term can dominate and cause an overall anisotropy that lies perpendicular to the film surface if the surface anisotropy lies out of the plane.

2.1.7 Magnetisation Dynamics

A magnetic moment in the presence of an external magnetic field will experience a torque of

$$\boldsymbol{T} = \boldsymbol{m} \times \boldsymbol{B}. \tag{2.41}$$

If the magnetic moment is independent of the angular momentum, this torque would force the moment to align with the magnetic field. However, as the magnetic moment is related to the angular momentum by $\boldsymbol{m} = \gamma \boldsymbol{L}$, the torque causes a change in angular momentum and forces the magnetic moment to precess about the applied field in what is known as a Larmor precession [71, 73]. The frequency of this precession is the Larmor frequency and is given by $f_L = \omega_L / 2\pi$ with $\omega_L = \gamma B$ where γ is the gyromagnetic ratio [74]. Considering only the Larmor precession, the equation of motion for a magnetic moment in an external field is given by

$$\frac{\mathrm{d}\boldsymbol{m}}{\mathrm{d}t} = \gamma(\boldsymbol{m} \times \boldsymbol{B}) = \gamma \boldsymbol{T}. \tag{2.42}$$

This equation of motion results in a continuous precession around the applied field with no change in the angle between the magnetic moment and the applied field. This will continue forever if there is no change in the angular momentum. However, in most cases, there are dissipative forces that cause the moment to eventually align with the static applied field [85]. Therefore, there must be an additional term in this equation of motion to fully describe the precession of the moment. This additional term is the damping torque. Adding this into the equation of motion we obtain the Landau-Lifshitz-Gilbert (LLG) equation,

$$\frac{\mathrm{d}\boldsymbol{m}}{\mathrm{d}t} = \gamma(\boldsymbol{m} \times \boldsymbol{B}) + \frac{\alpha}{m}(\boldsymbol{m} \times \frac{\mathrm{d}\boldsymbol{m}}{\mathrm{d}t}), \tag{2.43}$$

which describes the dynamics of magnetic moments [74]. α is the Gilbert damping parameter which quantifies the amount of damping in a system. A large Gilbert damping means that, after being forced into precession, the moments will quickly align with the applied field. The LLG equation can be applied to a larger system of many magnetic moments where the magnetisation, $\boldsymbol{M} = \boldsymbol{m}/V$, is assumed to remain constant in magnitude [74]. The precession of a magnetic moment can be enhanced by applying a weak time dependent oscillating field perpendicular to the strong static applied field. When the frequency of the time dependent field is equal to the Larmor frequency there is a resonance condition and there is a maximum in the absorption of the time dependent magnetic field by the sample. The Zeeman splitting of the energy levels due to the static applied field is $\Delta E = g\mu_B B$. At the FMR resonance condition, the time dependent oscillating field causes transitions between the two states because the frequency satisfies the condition $\hbar\omega = g\mu_B B$ [86].

2.1.8 Ruderman-Kittel-Kasuya-Yosida Interaction

In metals, magnetic ions can couple indirectly via the conduction electrons. The magnetic moment induces a spin polarisation in the surrounding conduction electrons, which then couples to another magnetic moment in the system some distance r away [71, 74]. This interaction was first theorised by Ruderman and Kittel [87], Kasuya [88] and Yosida [89] in relation to the interaction between magnetic atoms in a host non-magnetic metal. The sign of the exchange coupling oscillates with the distance between the magnetic atoms. In the case of a point magnet in a sea of electrons, the RKKY exchange coefficient is given by

$$J_{\mathrm{RKKY}}(r) \propto \frac{\cos(2k_F r)}{r^3} \tag{2.44}$$

where k_F is the Fermi wave vector and r is the distance from the point magnet [71, 74]. This gives an oscillating exchange energy which is damped as you move away from the point magnet. This interaction is responsible for emergent ferromagnetism in rare-earth elements where the localised moments of the 4f electrons are indirectly coupled via the 5d/6s electrons [73, 74].

RKKY interactions can also occur in ferromagnetic layers separated by a non-magnetic spacer [90]. In this case, the form of the exchange coupling is slightly different as it is no longer radial. Considering the spacer layer to have a thickness d, the interlayer exchange coupling at distance z in the spacer layer away from the magnetic interface is given by [74, 75]

$$J(z) = J_0 \frac{d^2}{z^2} \sin 2k_F z. \tag{2.45}$$

In this scenario, the RKKY interaction induces a spin density wave in the spacer layer which indirectly couples the two magnetic layers. Therefore, ferromagnetic and antiferromagnetic coupling between the magnetic layers can be achieved by adjusting the spacer thickness. This has been seen experimentally using spacer layers such as Ru and Cr [91–93].

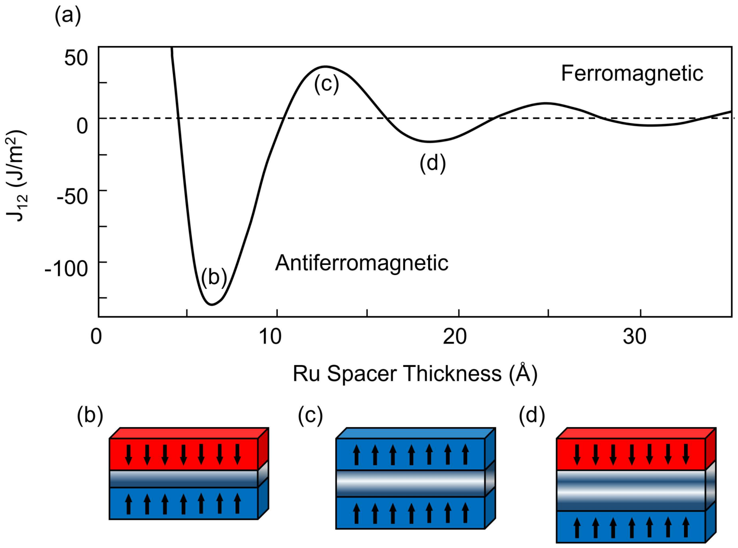

Figure 2.4: (a) RKKY coupling strength for thin film multilayer structure as a function of the Ru spacer thickness that separates $Ni_{80}Co_{20}$ layers. (b)-(d) Schematics of the exchange coupling between adjacent ferromagnetic layers as the spacer thickness increases, corresponding to the labelled points in (a). Figure taken from [75] where the data in (a) is adapted from [92].

2.1.9 Exchange Bias

Exchange bias is a unidirectional magnetic anisotropy which is typically induced in a ferromagnet (FM) when it is interfaced with an antiferromagnet (AFM) [94]. However, the effect has also been observed in systems with ferromagnets interfaced with other types of materials such as a spin glass [95]. Meiklejohn and Bean first discovered this anisotropy in particles Co surrounded by antiferromagnetic CoO [96]. This effect arises when the sample is cooled through the Néel temperature, T_N, of the antiferromagnet in an applied magnetic field (assuming the Curie temperature, T_C, of the ferromagnet is greater than T_N). It can also occur in as-grown samples if they are grown below both T_N and T_C [97]. In these cases, the exchange bias can be increased by applying a magnetic field to the sample during the growth process [98, 99]. The typical observation of exchange bias is a field shift in the hysteresis loop by H_{ex} and an enhanced coercive field H_c [96, 100–103].

The exact mechanism by which the FM/AFM interface causes a unidirectional

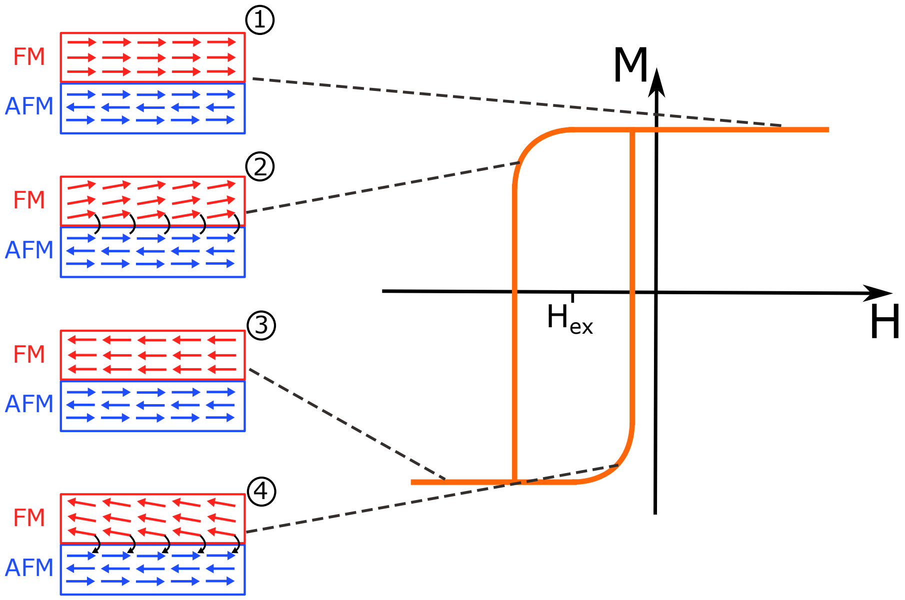

Figure 2.5: Diagram showing the spin orientations at different points in the shifted hysteresis loop of an exchange bias system. At saturation (1) the FM are all aligned and are pointing in the same direction as the uncompensated AFM spins at the interface. As the field is swept to negative fields (2), the FM spins are still exchanged coupled to the AFM spins meaning that a larger negative field is needed to switch the spin orientation in the FM, hence the shifting of the loop. (3) Once a sufficiently large field is applied to overcome the additional exchange coupling at the FM/AFM interface, the FM spins are saturated in the opposite direction to the uncompensated AFM spins. As the field is swept in the opposite direction, the interface exchange coupling means that a smaller field is required to reverse the FM spins. Figure designed after [94].

anisotropy can depend on the exact structure of the sample, but the basic concepts are intuitive. The exchange bias arises from the alignment of the spins at the interface between the FM and AFM. The exchange between the interface FM and uncompensated AFM spins adds an extra energy term that the external field has to overcome. When a field is applied in the opposite direction to the FM spins, the spins will start to rotate. Due to the strong anisotropy of the AFM, the AFM spins remain in the original direction. Therefore, for the applied field to rotate the FM spins, it has to provide extra energy to them to overcome the coupling with the AFM spins. When the applied field direction is reversed, the coupling between the FM and AFM interface spins will act with the applied field, meaning a smaller magnitude applied field is required to switch the FM spins [104]. Figure 2.5 shows a graphical representation of these concepts of exchange bias. In this idealistic scenario of a perfectly smooth FM/AFM interface, the additional field exerted on the FM spins is given by

$$H_{\mathrm{ex}} = \frac{\Delta\sigma}{M_{\mathrm{FM}} t_{\mathrm{FM}}} = J \frac{\boldsymbol{s}_{\mathrm{AFM}} \boldsymbol{s}_{\mathrm{FM}}}{a_{\mathrm{AFM}}^{2} M_{\mathrm{FM}} t_{\mathrm{FM}}} \tag{2.46}$$

where $\Delta\sigma$ is the interfacial exchange energy density, M_{FM} and t_{FM} are the magnetisation and thickness of the FM layer, a_{AFM} is the interatomic spacing of the AFM and $\boldsymbol{s}_{\mathrm{AFM}}$ and $\boldsymbol{s}_{\mathrm{FM}}$ are the atomic magnetic moments of the AFM and FM respectively [101, 105]. However, in experimental measurements of exchange bias, the resulting exchange bias fields are orders of magnitude lower than those calculated using equation 2.46 [97, 104]. Therefore, this idealistic model is clearly not sufficient to fully explain the origin of exchange bias at these interfaces. Measurements where the individual spins at the interface can be probed, such as XMCD (X-Ray Magnetic Circular Dichroism) [105, 106] and MFM (Magnetic Force Microscopy) [107], have demonstrated that in real systems, only 5-7 % of the AFM interface spins are uncompensated. Scaling the exchange coupling energy, and therefore the exchange bias field, by a factor of 0.05-0.07 results in values much closer to those that have been observed experimentally [74].

Although the expression in equation 2.46 predicts exchange bias fields that are orders of magnitude larger than experimentally observed, the important thing to take away is the dependence of the exchange bias on the FM thickness as this influences sample design. The exchange bias field is related to the ferromagnetic thickness by $H_{ex} \propto 1/t_{FM}$, as has been confirmed experimentally [100, 108–111]. This dependence arises because the exchange bias effect is interfacial and therefore the influence of the exchange bias decreases as the thickness of the ferromagnet is increased. Similarly, it has been shown that the AFM thickness also influences the strength of the exchange bias field. The antiferromagnet thickness does not have the same relationship with the exchange bias field as the ferromagnetic thickness. Instead, for extremely thin antiferromagnetic layers no exchange bias effect is observed. As the antiferromagnet thickness is increased above this, there is a rapid increase in the exchange bias field which then saturates above a certain threshold thickness [103, 109, 112]. In FeMn systems, like the sample used in the measurements in Chapter 6, at room temperature, the onset of exchange bias occurs at a FeMn thickness of 30 - 40 Å and the exchange bias strength saturates at a thickness of around 80 - 90 Å [103, 113]. The exchange bias structure used for our sample closely follows the sample structure used in reference [99] which had an exchange bias of 130 Oe at room temperature in its as-grown state.

Adjusting the thickness of the FM and AF layers allows for tuning of the strength of the exchange bias field. In the case of the exchange bias samples used in this thesis for the FMR-PNR experiment, the sample was required to have a strong anisotropy and a large magnetic moment. Therefore, the sample optimisation focused on adjusting the ferromagnet thickness to find the largest thickness that would provide a sufficiently strong exchange bias field while keeping the antiferromagnet thickness above the threshold thickness.

2.2 Diffusion

2.2.1 Driving Forces of Diffusion

The most basic driving force of diffusion is the thermodynamic force. This occurs when there is a difference in the composition of specific components throughout a system. The difference in composition means that there is a difference in the chemical potential energy. The thermodynamic driving force acts to minimize the Gibbs free energy of a system [114]. This driving force means that components diffuse down chemical gradients, moving from areas of high to low concentration. The flux due to the thermodynamic driving force of a specific species is given by [115, 116]

$$J = -Mc\nabla\mu \tag{2.47}$$

where c is the number of particles per unit volume, M is the mobility of the species and μ is it's chemical potential. In an ideal system with no external driving forces, the mobility can be related to the diffusion coefficient D by [115, 116]

$$MRT = D \tag{2.48}$$

where T is the temperature and R is the gas constant. External electric fields can also be a driving force of diffusion. The electric field causes an additional force to the charged particles in a system given by $q\nabla\phi$, where q is the charge of the particle and $\nabla\phi$ is the electric field. The total flux is then given by

$$J = -Mc\left(\frac{\partial\mu}{\partial x} + q\frac{\partial\phi}{\partial x}\right), \tag{2.49}$$

assuming that μ and ϕ only vary along one given axis, here it is the x axis [116]. The flux of ions due to an electric field produces an electrical current. The conductivity can be related to the diffusivity by first expressing the current I in terms of the flux J, conductivity σ and electric field $\nabla\phi$

$$I = Jq = -\sigma\nabla\phi \tag{2.50}$$

Assuming that $\partial\mu/\partial x = 0$ and using the expression for the mobility from equation 2.48, the conductivity, for a specific species i, can then be written as

$$\sigma_i = \frac{c_i q_i^2}{RT} D_i \tag{2.51}$$

This is the Nernst-Einstein equation [116, 117].

2.2.2 Fick's Laws of Diffusion

The most fundamental expressions used to describe diffusive processes were first proposed by Adolf Fick [114, 118]. Fick's first law states that, in a one-dimensional system, the flux of a certain component is proportional to the concentration gradient of that component in the system. This is expressed by the equation

$$J = -D\left[\frac{\partial c}{\partial x}\right] \tag{2.52}$$

where J is the flux, D is the diffusion coefficient and c is the concentration [114, 116, 119]. It follows from Fick's first law that in a homogeneous system there is no flux. The negative sign in this expression means that diffusion occurs from high to low concentrations. This expression can be used to calculate the diffusion coefficient of a system which is a measure of the mobility of the component species.

Fick's First law is used to describe a concentration profile that is constant in time. This is rarely the case in physical systems as the flux will cause the concentration profile to change. To derive an expression to describe a non-steady state system, one in which the concentration profile changes with time, we consider a slab of material A with some concentration of material B. A small length in the slab $\Delta x = x_2 - x_1$ has a flux of component B of J_2 at x_2 and J_1 at x_1. If Δx is very small, then the difference between the fluxes can be expressed as [114, 116]

$$J_1 - J_2 = -\Delta x\left(\frac{\partial J}{\partial x}\right) \tag{2.53}$$

In the time, δt, the amount of B entering the area Δx is $J_1\delta t$ and the amount leaving the area is $J_2\delta t$. Therefore, the total change in concentration is

$$\delta c = \frac{(J_1 - J_2)\delta t}{\Delta x} \tag{2.54}$$

Equations 2.53 and 2.54 can then be combined to give

$$\frac{\partial c}{\partial t} = -\frac{\partial J}{\partial x} \tag{2.55}$$

Substituting in Fick's first law, this can then be written as

$$\frac{\partial c}{\partial t} = \frac{\partial}{\partial x}\left(D\frac{\partial c}{\partial x}\right) \tag{2.56}$$

This is Fick's second law of diffusion [114, 116, 119].

Thin Film Solution

Here, the derivation of the thin film solution to Fick's second law will be laid out. This would represent our C_{60}/CoB/C_{60} under the assumption that the CoB film is sufficiently thin relative to the overall system. Consider a thin film of material B of thickness b and concentration c_0 within a much larger block of material A. In the analogy to our sample system, here A would represent the C_{60} layers and B would represent the boron. The concentration profile of material B is given by [114, 116, 119]

$$c_B(x,t) = \frac{bc_0}{2\sqrt{\pi D t}} \exp\left(\frac{-x^2}{4Dt}\right) \tag{2.57}$$

where x is the distance along the block of A normal to the thin film of B, with $x = 0$ at the centre of the film of material B and t is the time. To show that this is a valid solution for this scenario, it must satisfy Fick's second law as well as the boundary conditions of the system. Fick's second law is satisfied because we have

$$\frac{\partial c}{\partial t} = \frac{1}{2t}\frac{bc_0}{2\sqrt{\pi D t}} \exp\left(\frac{-x^2}{4Dt}\right)\left(\frac{x^2}{2Dt} - 1\right) = \frac{\partial}{\partial x}\left(D\frac{\partial c}{\partial x}\right) \tag{2.58}$$

The boundary conditions of the system mean that the total amount of B must remain the same for any time, t. This can be expressed as [114, 116]

$$\int_{-\infty}^{\infty} c(x,t)\mathrm{d}x = bc_0$$

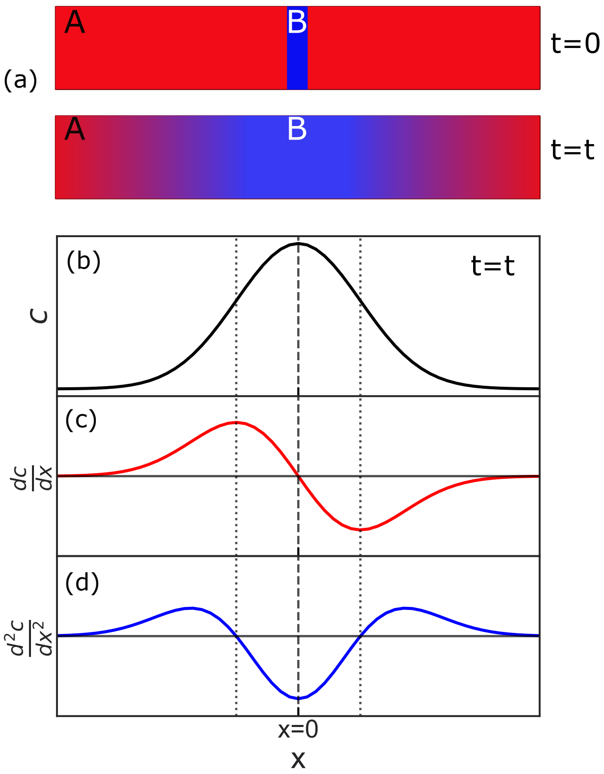

Figure 2.6: (a) Schematic showing the system consisting of a thin film of material B inside a slab of material A in its initial state, t=0, and after some time, t=t. (b),(c) and (d) show the concentration profile, $c(x)$, its derivative with respect to x, dc/dx, and its second derivative, d^2c/dx^2, respectively using arbitrary units. The dotted lines show the border between the regions in which the concentration is increasing or decreasing with increasing time. Between the dotted lines, the concentration is decreasing with time, outside of the lines, the concentration is increasing with time. Figure designed after [114, 116].

By substituting $\lambda = x/(2\sqrt{Dt})$ and using the fact that $\int_{-\infty}^{\infty} \exp(-\lambda^2)\mathrm{d}\lambda = \sqrt{\pi}$, we can see that the equation given in 2.58 satisfies this condition as [114]

$$\int_{-\infty}^{\infty} c(x,t)\mathrm{d}x = \frac{bc_0}{2\sqrt{\pi Dt}} 2\sqrt{Dt} \int_{-\infty}^{\infty} \exp\left(-\lambda^2\right)\mathrm{d}\lambda = bc_0 \tag{2.59}$$

Also, as all of the concentration of B is initially at $x = 0$, we have that

$$c \to 0 \text{ as } |x| \to \infty$$

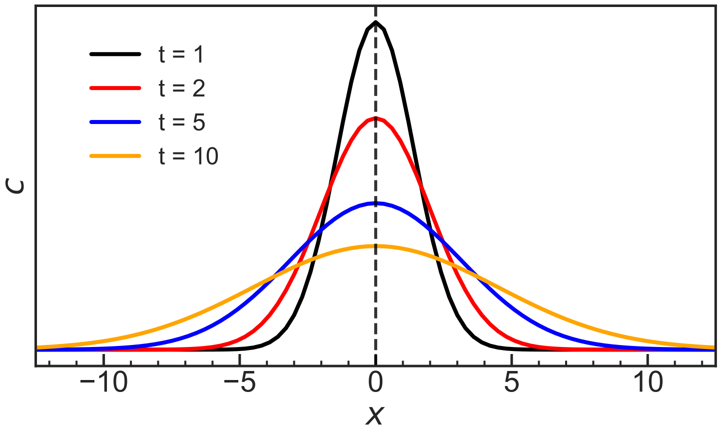

Figure 2.7: The time evolution of the concentration profile c(x,t) for the thin film solution, as given in equation 2.57, using $bc_0 = D = 1$.

The graphical form of the concentration profile and its derivatives are shown in figure 2.6. From Fick's second law, we know that the second differential of $c_B(x,t)$ with respect to x is proportional to the rate of change in concentration. So where this is positive it means that the concentration of B is increasing, and where it is negative the concentration of B is decreasing. The concentration takes the form of a Gaussian function with a standard deviation $\sigma = \sqrt{2Dt}$.

From the expression for the concentration profile of B, we can see that the concentration at $x = 0$ is proportional to $1/\sqrt{t}$ while the width of the function is proportional to $\sqrt{t}$ [116, 117]. The profile of the concentration at different times can be seen in figure 2.7.

Two semi-infinite slabs

In our C_{60}/CoB/C_{60} system, the source of the B, the CoB layer, is not infinitesimally thin so the thin film solution may not be the most accurate representation. If there is a sufficient amount of B in the CoB layer for it to act like an infinite source in the time frames of our experiment then the solution of two semi-infinite slabs would be a more appropriate theoretical model. Here, we consider the interface between two semi-infinite slabs that are purely composed of materials A and B respectively. This would represent one of the C_{60}/CoB interfaces in our samples. The x axis is the axis normal

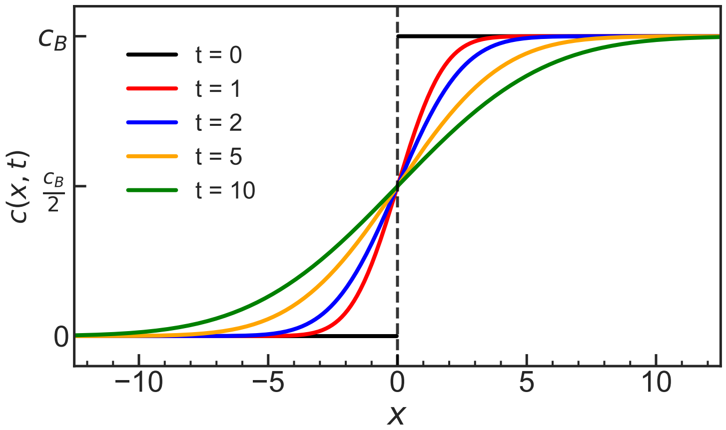

Figure 2.8: Graphical representation of the concentration profile for a semi-infinite diffusion pair, as given in equation 2.63, at different times using $D = 1$.

to the interface, with the interface located at $x = 0$ such that the concentration of B is $c = c_B$ for $x > 0$ and $c = 0$ for $x < 0$. We can treat the $x < 0$ region as being made up of n thin slices of thickness $\Delta\alpha$. In each slice, the total concentration is $c_B\Delta\alpha$. The total concentration profile $c(x,t)$ is a superposition of the thin film solution for all n slices. If the distance between $x = 0$ and the i^{th} slice is α_i, then the total concentration profile can be written as [114, 116]

$$c(x,t) = \frac{c_B}{2\sqrt{\pi D t}} \sum_{i=1}^{n} \Delta\alpha \exp\left(\frac{-(x-\alpha_i)^2}{4Dt}\right) \tag{2.60}$$

If we take the limit that n goes to infinity and $\Delta\alpha$ goes to zero, then this summation becomes an integral

$$c(x,t) = \frac{c_B}{2\sqrt{\pi D t}} \int_0^\infty \exp\left(\frac{-(x-\alpha_i)^2}{4Dt}\right) \mathrm{d}\alpha \tag{2.61}$$

By substituting $u = (x-\alpha)/2\sqrt{Dt}$, and using the definition of the error function,

$$\operatorname{erf}(z) = \frac{2}{\sqrt{\pi}} \int_0^z \exp\left(-u^2\right) \mathrm{d}u, \tag{2.62}$$

the concentration can be written as [114, 116]

$$c(x,t) = \frac{c_B}{2}\left(1 + \operatorname{erf}\left(\frac{x}{2\sqrt{Dt}}\right)\right) \tag{2.63}$$

We can see from the expression that for $t > 0$, the concentration at $x = 0$ is always half of the original concentration in B. Figure 2.8, shows the evolution of the concentration profile for this solution over time.

2.2.3 Diffusion Theory Summary

Here, the solutions for the time evolution of the concentration profile due to diffusion in model systems have been covered. These can be used to give the basis of how the B profile is expected to evolve during our annealing experiments. In our experiments, the concentration profile $c_B(x,t)$ would represent the profile of B within our system which we measure directly using reflectivity and ion beam analysis and indirectly using magnetometry. However, these models oversimplify the energy landscape in our sample systems. There are energy barriers that the B must overcome before the diffusion can occur, first to escape CoB and then to inject into the C_{60} layers. Therefore, these solutions for the concentration profile do not fully describe the experimentally observed profiles but they still provide a starting point for analysis.

2.2.4 Ionic Diffusion In C_{60}

Research surrounding ionic diffusion in C_{60} is mainly focused on applications in molecular alkali ion batteries as an alternative to the current lithium ion batteries [120, 121]. In this context, the crystal structure of C_{60} allows for high diffusivities and low activation energies. C_{60} molecules form a FCC structure with interstitial voids that are much larger than covalent, metallic or ionic solids [121, 122]. These large voids provide diffusion paths for ions and cause a large diffusivity. Research by Ricco et al. [123] suggested Li_4C_{60} demonstrated high Li ion mobility at room temperature and conductivity of the order of 10^{-2} S cm^{-1}, comparable to the highest conductivity traditional liquid ionic conductors [124, 125]. However, some work suggests that there is a mixed ion-electron conductivity contribution in these systems [121, 126, 127]. Although the high conductivity in Li_4C_{60} may be partially due to electron transport, there is still evidence of ionic mobility in C_{60} systems using Li [120, 124] and other ions, for example Mg [128] and Na [129].

Alkali Ion diffusion in C_{60} occurs via intravoid motion and intervoid jumps between tetrahedral and octahedral sites [120, 121, 124]. The intervoid jumps have the largest activation energy and are, therefore, the limiting factor of the diffusion path. DFT calculations show the activation energies of Li and Na in C_{60} to be 0.34 eV and 0.27 eV respectively [121]. These values are comparable to the lowest measured activation energies for Li diffusion in solid state electrolytes [130] and are slightly larger than the activation energies of Li in Li_xCoO_2 electrodes which range from 0.2 - 0.3 eV [57, 58].

Diffusivities for Li ions in C_{60} have been estimated by Tachikawa using a direct molecular orbital-molecular dynamics (MO-MD) study to be 1.67×10^{-6} cm^2s^{-1} at room temperature [131] and also by a combined DFT and MO-MD study to be 5×10^{-3} cm^2s^{-1} at 250 K [132]. Experimental measurements of Li ion diffusion in C_{60} nanoparticles give a much smaller diffusivity of 3.84×10^{-10} cm^2s^{-1} [56]. In comparison to other layer types, these values are relatively large. Values for Li diffusivity in Li_xCoO_2 electrodes have been observed between 10^{-10} - 10^{-12} cm^2s^{-1} [57–59]. Solid state electrolytes Li_2SO_4, $LiNaSO_4$ and $LiAgSO_4$ demonstrate Li ion diffusivity of $10-5$ cm^2s^{-1} at 550°C [60]. Using the Arrhenius law of the diffusivity and the activation energies of Li in these materials, the room temperature diffusivities can be calculated. This results in approximate values of 4×10^{-9} cm^2s^{-1}, 2×10^{-12} cm^2s^{-1} and 2×10^{-10} cm^2s^{-1} for Li_2SO_4, $LiNaSO_4$ and $LiAgSO_4$ respectively. Larger values of diffusivity have been observed in β-Li_3PS_4 of the order of 10^{-8} cm^2s^{-1} at 100°C [133]. These values of diffusivity in solid state electrolytes are comparable to the observed values in C_{60} nanoparticles and much smaller than the theoretically predicted values given by Tachikawa. The measured values of Li diffusivity in C_{60} nanoparticles are also larger than observed values for Li diffusivity in Si films, which are around 10^{-11} cm^2s^{-1} [134, 135]. The research on diffusivity in Si films also demonstrates an increase in the diffusivity to 10^{-9} cm^2s^{-1} when the Si is coated in C_{60} or boron doped C_{60}. This comparison of Li diffusivity of C_{60} with different electrode and electrolyte materials demonstrates the high potential for C_{60} to be used as a host material for diffusion. The diffusivity of Li in C_{60} is comparable or greater than Li_xCoO_2 and Si electrodes and solid state electrolyte materials.

Oxygen diffusion from air into C_{60} films and single crystals has also been of interest in past research as exposure of C_{60} to air and UV light causes C-O reactions that irreversibly damage the C_{60} molecules and consequently any device functionality [136]. The decay in C_{60} conductivity over time when exposed to air has been used to determine the diffusivity of O_2 in C_{60}. These measurements, performed on single crystal C_{60}, have resulted in large measured diffusivities of 10^{-7} cm^2s^{-1} at 294 K [137]. Pevzner et al. [138] studied O diffusion into C_{60} thin films by dielectric measurements. Charge transfer between O_2 and C_{60} forms electric dipoles which flip as the O_2 molecule diffuses through the film. The rate of the flipping of the dipoles is related to the diffusivity of the O_2 molecules in the C_{60} film and, therefore, peaks in the dielectric measurements can be used to determine the diffusivity. This resulted in a measured diffusivity of $D \approx 10^{-13}$ $\mathrm{cm^2s^{-1}}$ at room temperature. The authors also propose that the diffusion of O_2 into C_{60} occurs by two processes. The first is a fast process where O diffuses in quickly through grain boundaries. The second process is the diffusion of O into interstitial sites which occurs on much longer timescales. The idea of two diffusion processes for O_2 in C_{60} has been supported by electron paramagnetic resonance measurements presented by Katz et al. [139]. Here, the diffusion into a polycrystalline thin film and a highly crystalline $\langle 111 \rangle$ thin film were compared. The results showed a much faster initial diffusive process in the polycrystalline film where the grains are smaller so there are more grain boundaries. Molecular-dynamics calculations for oxygen diffusion in C_{60} result in a lower diffusion coefficient of the order of 10^{-15} $\mathrm{cm^2s^{-1}}$ at 300 K [140]. All of these diffusion coefficients are over 10 orders of magnitude larger than simulated values in fcc C_{70} of 10^{-31} $\mathrm{cm^2s^{-1}}$ at 298 K [141]. The diffusion coefficient of O in C_{60} measured by Pevzner et al. is orders of magnitude larger than the those for O diffusion in metals such as Zr, which has a diffusivity of 10^{-15} $\mathrm{cm^2s^{-1}}$ at 300°C [142], and Hf, with a diffusivity of 10^{-16} $\mathrm{cm^2s^{-1}}$ at 500°C [143, 144].

Similar effects to those observed in the diffusion of O in C_{60} were seen when comparing the electrodiffusion of Au from contacts in C_{60} films [61]. Evidence of Au diffusion into a series of C_{60} films of different crystallinities was observed after applying electric fields of 500 $\mathrm{Vcm^{-1}}$ at a temperature of 150°C. The maximum effect on the conductivity was observed for the polycrystalline sample with the most grain boundaries, demonstrating Au diffusion from the electrode occurs predominantly along grain boundaries. There is also evidence of metal ions diffusing into C_{60} from Ag and In contacts at temperatures above 100°C and voltages above 20 V [62, 63].

It seems reasonable to expect the diffusion coefficient for B in C_{60} to be similar to those observed for Li due to the similar atomic weight. The atomic radius of B is smaller than that of Li which could suggest a greater diffusivity for B, however, some research has suggested that the diffusivity does not scale consistently with the atomic radius of the diffusing ion and in some systems there is an optimum size of ion for the greatest diffusivity [130, 145]. By using the reported diffusivities for O and Li in C_{60} we can estimate that the diffusion coefficient for B will be approximately 10^{-8} - 10^{-12} $\mathrm{cm^2s^{-1}}$ at room temperature. These diffusivities would result in diffusion lengths of $\approx 10^{-3} - 10^{-6}$ m over 1 hour which are larger than the total sample thickness meaning the diffusion of B in C_{60} should not be a limiting factor of our experiments.

2.2.5 Boron Diffusion

Boron diffusion in amorphous ferromagnets is of great importance in CoFeB/MgO based magnetic tunnel junction (MTJ) structures that are used in MRAM and STT-RAM devices. Extremely large TMR ratios of over 600% have been reported in Ta/CoFeB/MgO/CoFeB/Ta MTJs [146]. Achieving large TMR ratios in these structures requires annealing at temperatures of at least 300°C to crystallise CoFe and expel B from the CoFeB layer. The B is observed to diffuse away from the MgO layer and is absorbed by the Ta, or other B getter underlayer/cap material such as W [147–151]. This leaves a sharp CoFe/MgO interface with the CoFe crystallising into a bcc structure due to the template MgO (001) crystal structure [152]. The TMR and PMA in the system results from CoFe - O bonds, so the diffusion of B away from the MgO interface and the formation of a sharp CoFe/MgO interface enhances the TMR [153–155]. Some groups observe B diffusion into the MgO layer, forming Mg-B-O compounds [156, 157]. This has been attributed to oxygen vacancies in the MgO layer that result in B diffusion into the MgO layer due to the strong affinity of B and O [148, 158]. The research conducted into annealing of these MTJ structures demonstrates that B in amorphous ferromagnets, similar to the CoB used in our experiments, is activated at moderate annealing temperatures of around 300°C.

Experimental results by Sinha et al. [159] suggest that, for Ta/CoFeB/MgO structures annealed at 300°C for 1 hour, there is a critical CoFeB thickness of 2 nm, above which the B cannot diffuse across the CoFeB layer into the Ta, meaning there is still B at the CoFeB/MgO interface. This result indicates that the diffusion length for B in CoFeB at 300°C for 1 hour is approximately 2 nm. In our experiments, we anneal at 300°C for 1 and 10 hours. Using the fact that the diffusion length, x_d, is related to the annealing time, t, by $x_d \propto \sqrt{t}$, this result would suggest a diffusion length of 6.3 nm for a 10 hour anneal.

Most studies conducted into diffusion of B in Co are performed at high temperatures of around 950°C, so it is difficult to make direct comparisons to our experimental conditions where we anneal at temperatures up to 300°C. Table 2.1 shows the diffusion parameters for B in Co and Fe based systems gathered from the literature. Using the D_0 value and activation energy, E_A, given in the references, the diffusivity at 573 K (300°C) can be calculated using the equation

$$D(T) = D_0 \exp\left(-\frac{E_A}{k_B T}\right), \tag{2.64}$$

where T is the temperature and k_B is the Boltzmann constant. This diffusivity can be used to calculate a diffusion length using the expression $x_d = \sqrt{2Dt}$. The values obtained for amorphous FeB and the ASTM F-75 Co based alloy, between 8-16 nm, are the most comparable to the estimated diffusion length for 10 hours at 300°C in Ta/CoFeB/MgO of 6.3 nm. A diffusion length of the order of 10 nm in the experimental conditions is sufficient to observe diffusion to the edges of the CoB layer for thicknesses around 20 nm or less, as the CoB in our samples is sandwiched between two C_{60} layers. The table also shows the range of values obtained in the literature for the activation energy for B diffusion. The average activation energy for the Co based materials is approximately 1.9 eV. The activation energy of B in C_{60} can be estimated by assuming it is similar to the activation energies of Na and Li in C_{60} due to the similar atomic radii. The activation energies of Li and Na in C_{60} are calculated to be 0.34 eV and 0.27 eV respectively [121], giving an approximate B activation energy of 0.3 eV. This demonstrates the large difference in the diffusion barriers for B in CoB and in C_{60} and highlights that the CoB diffusivity will limit the diffusion in our system. Values for ion diffusivity in C_{60} are typically in the range of 10^{-8} cm^{2}s^{-1} to 10^{-13} cm^{2}s^{-1} at room temperature [56, 138]. Using these diffusivities and an approximate activation energy of 0.3 eV we obtain diffusivities at 300°C (573 K) of 10^{-6} - 10^{-11} cm^{2}s^{-1}. These values are approximately 10 orders of magnitude larger than the calculated diffusivities for B in CoB, further demonstrating that the diffusion in CoB is the limiting factor for our experiment. The estimated diffusivities in C_{60} result in diffusion lengths of greater than 10^{-4} m for the 10 hour anneal, which is orders of magnitude greater than the sample thickness.

X-ray diffraction measurements suggest that adding B to Co causes the formation of 2 phases, CoB and Co_2B [160–162]. Despite the different phases, the mass density in CoB alloys does scale linearly with the B composition [163]. A magnetic study of CoB samples showed evidence for the existence of Co_3B phases as well as Co_2B [163].

The Co_1B_1 phase is diamagnetic, so any contributions to the magnetisation in our CoB samples must come from the Co_3B and Co_2B phases which have saturation magnetic moments of 1.12 μ_B per atom and 0.76 μ_B per atom respectively [164].

Material	E_A (eV)	D_0 (cm^2s^{-1})	Temperature Range (K)	D(573K) (cm^2s^{-1})	x_d(573 K, 10 h) (nm)
Co Sinters [161]	1.64	4.36×10^{-3}	> 690	1×10^{-15}	86
Pure Co [160]	2.4	9.15×10^{1}	1173 - 1273	7×10^{-20}	0.7
ASTM F-75 (Co_2B) [162]	1.72	4.73×10^{-2}	1223 - 1273	3.6×10^{-17}	16
ASTM F-75 (CoB) [162]	1.94	1.01	1223 - 1273	8.7×10^{-18}	8
Amorphous $Fe_{83.5}B_{16.5}$ [165]	1.5	3.0×10^{-4}	533 - 653	1.6×10^{-17}	11
Pure Iron [166]	1.63	8.43×10^{-1}	1223 - 1323	4.1×10^{-15}	172

Table 2.1: Diffusion parameters of B in Co Fe based alloys. Diffusivities at 573 K are calculated from the parameters found in the references. x_d is the calculated diffusion length at a temperature of 573 K and a time of 10 hours.

Adding B into Co reduces the saturation magnetic moment per Co atom as the B donates electrons to the Co d-band, meaning there are fewer unpaired d-band electrons [163]. The Curie temperature of Co-B amorphous alloys, T_C is related to the B composition, x, by the expression

$$T_C^2(x) = C^2 \left[1 - \frac{x}{x_c}\right] \tag{2.65}$$

where $C = T_C(0)$ is the Curie temperature of pure Co and x_c is the critical B concentration for spontaneous magnetism [167]. With x greater than x_c, the alloy is no longer ferromagnetic. The temperature dependence of the magnetisation at high temperature is given by $M(T) \propto (T_C - T)^{\beta}$ where we can approximate that $\beta = 1/2$. Using this and the expression in equation 2.65, we obtain the following expression for the B composition dependence of the magnetisation

$$M(T, x) \propto \left(C \left[1 - \frac{x}{x_c}\right]^{\frac{1}{2}} - T \right)^{\beta}. \tag{2.66}$$

This suggests that the B composition can be estimated through measurements of the magnetisation. However, there are other structural factors, such as the crystallinity, that also influence the magnetisation and result in differences between the extrapolations of measurements of CoB alloys to the magnetisation at $x = 0$ and that of pure Co [163].

CHAPTER 3

Reflectometry

3.1 Reflectometry

Reflectometry measurements are a major part to the investigations presented in this thesis. In the ionic diffusion experiment, we utilise the structural and magnetic profiling provided by reflectometry measurements to observe the migration of B in C_{60} molecular thin films. The unique properties of neutrons mean that it is possible to distinguish light elements and also measure the changes in magnetism of our samples due to the migration of B ions. In the FMR-PNR experiment, the measurement of both the magnitude and angle of magnetisation allows us to monitor the precession of magnetisation under FMR precession. As these measurements have such significance in our investigations, it is important to understand the basics of scattering interactions and reflectometry. This chapter will give an overview of the background theory of reflectometry and x-ray and neutron scattering which is needed to understand and interpret the data in this thesis.

3.2 Elastic Scattering

Incident electromagnetic waves scatter when they interact with the electrons of the material. In reflectometry experiments, we are only measuring elastic scattering events. In this scenario, the scattering vector is defined as the difference in the incident and scattered wavevectors $\vec{Q} = \vec{k_i} - \vec{k_f}$. The geometry of an elastic scattering event is shown in figure 3.1a. The photon energies for X-ray and neutrons are $E_x = \hbar c|k|$ and $E_n = \frac{|\hbar k|^2}{2m_n}$ respectively, so in elastic scattering $|k_i| = |k_f| = \frac{2\pi}{\lambda}$. From this and the scattering geometry in figure 3.1 it is possible to express $\vec{Q}$ in terms of θ and λ,

$$Q = \frac{4\pi}{\lambda}\sin\theta \tag{3.1}$$

In most x-ray reflectivity measurements a monochromated beam is used, therefore Q and θ are interchangeable when presenting or analysing data. However, the PNR measurements presented in this thesis were performed using a time-of-flight neutron probe. This means that the incident neutron beam contains many different wavelengths of neutrons. In this case, we must use Q to fully encompass all of the information about the scattered neutron as a single θ sample angle will result in some finite range of Q.

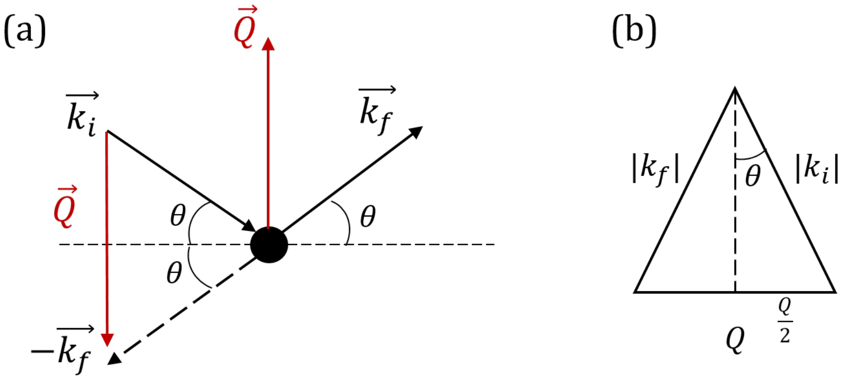

Figure 3.1: (a) Schematic of the geometry of an elastic scattering event. (b) Geometric representation of the relation between Q and the magnitudes of the incident and final wavevectors that is used to produce the expression that links Q and θ given in equation 3.1.

3.3 X-Ray Refraction and Reflectivity

When an electromagnetic wave is incident on the interface between two mediums at an angle larger than the critical angle, it is partially reflected and partially refracted. The refracted light will change its angle of travel as it passes into the new medium. The change in angle is determined by the difference in the refractive index between the two mediums. The x-ray refractive index for any given material is defined by

$$n = 1 - \delta - i\beta. \tag{3.2}$$

Here, δ and β are the real and imaginary components of the refractive index and they represent the scattering and absorption of the material respectively [168, 169]. δ and β can be given by

$$\delta = \frac{r_e}{2\pi}\lambda^2\rho_e \tag{3.3}$$

$$\beta = \frac{\lambda}{4\pi}\mu \tag{3.4}$$

where r_e is the Thomson scattering length, which describes the radius of an electron [170], λ is the x-ray wavelength, ρ_e is the electron density of the material and μ is the linear absorption coefficient [168]. For air, we can approximate $n = 1$ as it would be for a vacuum. In most materials, the absorption component is negligible, in which case,

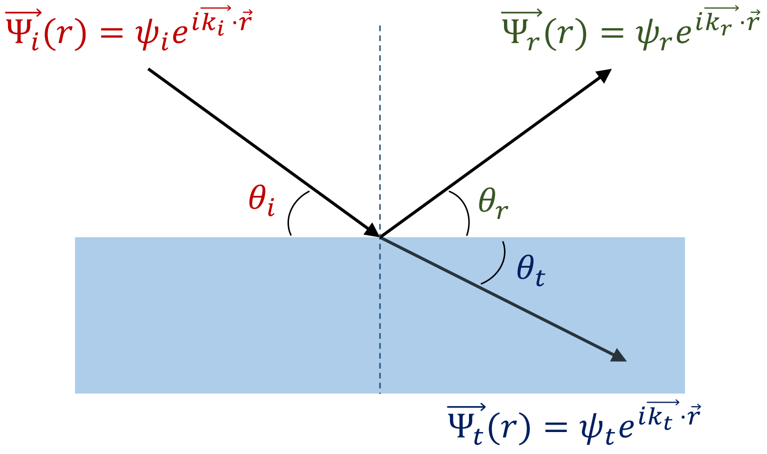

Figure 3.2: Schematic of the reflection and refraction of a planar wave as it is incident on a perfectly flat homogeneous medium. Labels show the wavefunctions of the incident, reflected and transmitted wave.

the expression can be simplified to $n = 1 - \delta$. Typically, the values of δ and β are of the order of $10^{-5} - 10^{-8}$ [170, 171].

Snell's law and the Fresnel equations can be derived by considering x-rays incident on an ideal surface as shown in figure 3.2. The following derivation was understood by studying the books of D.S.Sivia [172], C.MacDonald [173] and J.Als-Nielsen and D.McMorrow [174] as well as the thesis of C.Kinane [175]. In this scenario, there is an incident wave, Ψ_i, which splits into two waves upon interacting with the surface. One is refracted into the material, Ψ_t and the other is reflected away from the surface, Ψ_r. The waves amplitudes, ψ, and derivatives, $\frac{\mathrm{d}\Psi}{\mathrm{d}r}$, must be continuous at the interface. This gives the following relationships between the wave amplitudes,

$$\psi_i + \psi_r = \psi_t \tag{3.5}$$

$$\psi_i \vec{k_i} + \psi_r \vec{k_r} = \psi_t \vec{k_t} \tag{3.6}$$

Snell's law follows from taking equation 3.6 and considering the parallel, $\hat{x}$, components of $\vec{k}$. From this, we arrive at the expression,

$$\psi_i k_i \cos\theta_i + \psi_r k_r \cos\theta_r = \psi_t k_t \cos\theta_t \tag{3.7}$$

The magnitude of the wavenumbers are given by $k_i = k_r = n_i k$ and $k_t = n_t k$. n_i is the refractive index of air so it can be set to 1, and n_t denotes the refractive index of the material. Also, considering specular reflection gives $\theta_i = \theta_r$. Using this to simplify equation 3.7, we can obtain Snell's law

$$\cos\theta_i = n_t \cos\theta_t \tag{3.8}$$

The Fresnel equations can be derived by taking the perpendicular components of the wavevectors and applying them to equation 3.6. From this, we obtain

$$\psi_i k_i \sin\theta_i - \psi_r k_r \sin\theta_r = \psi_t k_t \sin\theta_t \tag{3.9}$$

As we are in a specular reflection geometry, it is known that $\theta_i = \theta_r = \theta$ and $|k_i| = |k_r| = k$. Therefore we can simply the expression to

$$k(\psi_i - \psi_r)\sin\theta = \psi_t k_t \sin\theta_t \tag{3.10}$$

The magnitude of the wavevectors can be written in terms of the wavelength and refractive index as $|k_x| = \frac{2\pi}{\lambda} n_x$ [172, 173]. As the initial and reflected waves travel through air, the refractive index for both is the same and thus the expression can be written as

$$\frac{\psi_i - \psi_r}{\psi_i + \psi_r} = \frac{n_t \sin\theta_t}{n \sin\theta} \tag{3.11}$$

The reflectivity, r, and transmissivity, t, are defined by the ratio of the reflected amplitude over the initial amplitude and the transmitted amplitude over the initial amplitude respectively.

$$r = \frac{\psi_r}{\psi_i} \qquad\qquad t = \frac{\psi_t}{\psi_i} \tag{3.12}$$

Equation 3.11 can be rearranged into the form of r to give

$$r = \frac{\psi_r}{\psi_i} = \frac{n\sin\theta - n_t \sin\theta_t}{n\sin\theta + n_t \sin\theta_t} \tag{3.13}$$

Using equation 3.5, t can be rearranged to the form $t = 1 + r$. Then it follows that t can be written in the form

$$t = \frac{2n\sin\theta}{n\sin\theta + n_t\sin\theta_t} \tag{3.14}$$

The equations 3.13 and 3.14 are the Fresnel equations. The Fresnel reflectivity is defined as $R_F = |r|^2$ and this determines the intensity of the reflected wave.

3.3.1 Critical Angle

Below a certain incident angle, all of the incident wave is reflected. This angle is called the critical angle, θ_c. Using this in Snell's law (equation 3.8) we obtain

$$n = 1 - \delta - i\beta = \cos\theta_c \tag{3.15}$$

as $\theta_t = 0$. The absorption component is typically negligible compared to the scattering component so by performing a Taylor expansion of $\cos\theta_c$, the critical angle can be approximated by [168, 170]

$$\theta_c \approx \sqrt{2\delta} = \sqrt{\frac{r_e\lambda^2\rho_e}{\pi}} \tag{3.16}$$

We can see from this expression that the only material parameter which determines the critical angle of a layer is its electron density.

3.3.2 Small Angle Regime

To better understand the behaviour of the reflectivity at low angles, it is helpful to rewrite equation 3.13 in a different form. First, Snell's law can be used to describe the perpendicular transmitted wavevector $k_{t,z}$ in terms of the incident angle θ [170]

$$\begin{aligned} k_{t,z} &= n_t k \sin\theta_t \\ k_{t,z}^2 &= k^2(n_t^2 - n_t^2\cos^2\theta_t) \\ k_{t,z}^2 &= k(n_t^2 - \cos^2\theta) \end{aligned} \tag{3.17}$$

In the small angle regime, a Taylor expansion can be used to approximate $\cos^2\theta$. Also, we know that the transmitted refractive index can be expressed as $1 - \delta_t + i\beta_t$. When expanding the equation, the 2nd order powers of δ_t and β_t can be neglected because they are both of the order of 10^{-5} to 10^{-8}. This means that $k_{t,z}$ can be approximately written as [171]

$$k_{t,z} \simeq k(\theta^2 - 2\delta_t + 2i\beta_t)^{1/2} \tag{3.18}$$

Now, we can define $f_t = k_{t,z}/k$ and therefore

$$f_t = (\theta^2 - 2\delta_t + 2i\beta_t)^{1/2} \tag{3.19}$$

In the small angle approximation, $\sin\theta \simeq \theta$ and consequently equation 3.13 can be rewritten as

$$r = \frac{\theta - f_t}{\theta + f_t} \tag{3.20}$$

To then express R_F in a form that it is possible to compute, A and B are defined such that [170, 171, 173]

$$f_t = A - iB \tag{3.21}$$

where

$$\begin{aligned} A &= \frac{1}{\sqrt{2}}\left([(\theta^2 - \theta_{ct}^2)^2 + 4\beta_t^2]^{1/2} + (\theta^2 - \theta_{ct}^2)\right)^{1/2} \\ B &= \frac{1}{\sqrt{2}}\left([(\theta^2 - \theta_{ct}^2)^2 + 4\beta_t^2]^{1/2} - (\theta^2 - \theta_{ct}^2)\right)^{1/2} \end{aligned}$$

recalling that $\theta_{ct} = \sqrt{2\delta_t}$. Using this substitution of f_t, the Fresnel Reflectivity is given by

$$R_F = |rr^*| = \frac{(\theta - A)^2 + B^2}{(\theta + A)^2 + B^2} \tag{3.22}$$

Figure 3.3 shows the Fresnel reflectivity plotted as a function of the incident angle normalised by the critical angle for different ratios between the absorption and scattering components of the refractive index $\frac{\beta}{\delta}$. This is obtained by rearranging into the form

$$R_F = \frac{(x - f(x))^2 + (\frac{B}{\theta_C})^2}{(x + f(x))^2 + (\frac{B}{\theta_C})^2} \tag{3.23}$$

where

$$\begin{aligned} x &= \frac{\theta}{\theta_C} \\ f(x) &= \frac{1}{\sqrt{2}}\left(\sqrt{x^4 - 2x^2 + 1 + \frac{\beta^2}{\delta^2}} + (x^2 - 1)\right)^{1/2} \\ B^2 &= \frac{\theta_C^2}{2}\left(\sqrt{x^4 - 2x^2 + 1 + \frac{\beta^2}{\delta^2}} - (x^2 - 1)\right) \end{aligned}$$

The comparison in figure 3.3a shows that the absorption component has the most significant impact below the critical edge, where it acts to round off the critical edge. With no absorption, the reflectivity is unity until the critical angle where it begins to drop off rapidly. The plot in figure 3.3b shows the Fresnel Reflectivity on a log scale, which is often how x-ray and neutron reflectivity data is presented due to the rapid

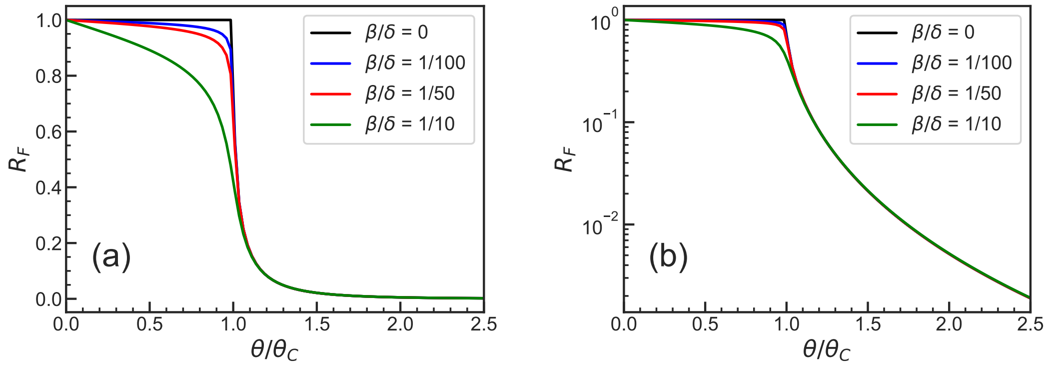

Figure 3.3: Fresnel Reflectivity for a single layer/air interface for different ratios between the absorption and scattering components of the refractive index $\frac{\beta}{\delta}$ plotted on a linear (a) and log (b) y scale. The incident angle is normalised by the critical angle θ_C.

decrease in intensity after the critical edge. Table 3.1 contains values for the ratio between the absorption and scattering components of the refractive index for some example elements.

Element	β/δ
B	0.0008
C	0.0016
Si	0.023
Co	0.15
Pt	0.099
Au	0.10

Table 3.1: Example values for the ratio of the x-ray absorption/scattering intensity for different elements. The values are calculated using the NIST activation SLD calculator [176]

3.3.3 Multiple Interfaces

To extrapolate the Fresnel reflectivity, previously derived, onto a system with multiple different layers with different refractive indices, the recursive formulism first developed by Parratt [171] will be followed. Here, Parratt considers a structure with N layers in which all of the interfaces are perfectly smooth. Each of the individual layers n has a thickness denoted by d_n. The continuity of the electric vectors E at the boundary between the $n-1$ and n layers is used to ultimately result in the recursive formula

$$R_{n-1,n} = a_{n-1}^4 \left(\frac{R_{n,n+1} + F_{n-1,n}}{R_{n,n+1}F_{n-1,n} + 1} \right) \tag{3.24}$$

with R and F defined by

$$R_{n,n+1} = a_n^2 \left(\frac{E_n^R}{E_n} \right) \qquad\qquad F_{n-1,n} = \frac{f_{n-1} - f_n}{f_{n-1} + f_n}$$

and

$$a_n = exp\left(-ik_1 f_n \frac{d_n}{2} \right)$$

where E_n and E_n^R are the transmitted and reflected electric vectors at the n^{th} interface respectively and f_n is a generalised version of equation 3.19. The reflectivity of the structure is found by starting from the bottom (N^{th}) layer and moving up through the layers. For the bottom layer, $R_{n,n+1} = 0$ as it is assumed to be an infinitely thick slab. Also, as the top layer (1) is air, it follows that $a_1 = 1$ and $f_1 = \theta$.

3.3.4 Roughness and Intermixing

In real-life systems, the surfaces and interfaces between layers will very rarely be perfectly flat and smooth, and the boundaries between different layers will not be perfectly sharp. This causes a faster decrease in reflectivity with increased Q. There are two forms of interfaces to consider: graded interfaces and roughness in the form of a random height profile along the interface between two layers.

A graded interface, often called intermixing, is the case where, instead of a perfectly sharp interface between two layers, there is a gradual change in the SLD as a function of the depth z, as demonstrated by figure 3.4. This results in a reflectivity from a graded surface of [174]

$$R(Q) = \left| \int_0^\infty \left(\frac{df}{dz} \right) \exp(iQz) dz \right|^2 R_F(Q) \tag{3.25}$$

where $f(z)$ is the function of the graded interface. A common function used to describe intermixing is an error function of the form

$$f(z) = \operatorname{erf}\left(\frac{z}{\sqrt{2}\sigma_g} \right) \tag{3.26}$$

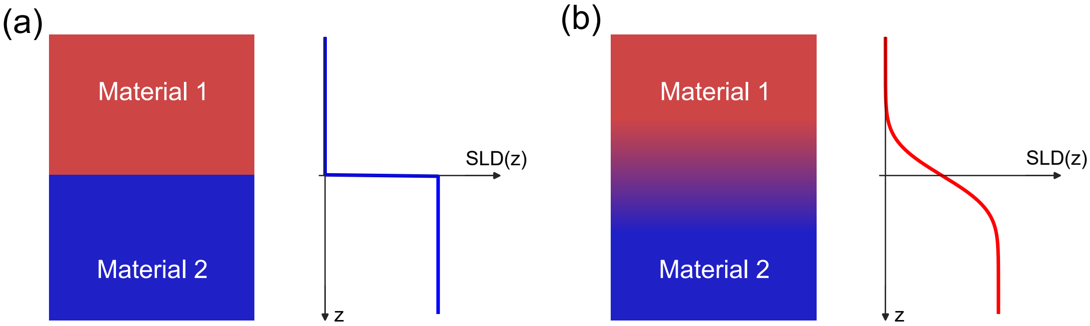

Figure 3.4: (a) Perfectly sharp interface between two layers. The SLD profile changes as a step function at the interface. (b) Graded interface between two layers. The interface is modelled by an error function as shown in the SLD profile.

where σ_g is the width of the error function [175]. Substituting this function into 3.25 gives a final form of the reflectivity of

$$R(Q) = R_F(Q)\exp\left(-Q^2\sigma_g^2\right) \tag{3.27}$$

In the case of an uncorrelated rough interface, the specular reflectivity is reduced because the surface profile will cause some of the beam to be reflected at a different angle, resulting in diffuse scatter (also known as off-specular scatter) [175]. Here, uncorrelated means the variations in height along the surface vary randomly with the x, y positions [174]. The reflection from this surface is found by averaging the reflection across all of the area within the beam footprint [168, 173]. To simplify the problem, we consider the deviations in height from the average height to be Gaussian in nature with a standard deviation of σ_r. In this scenario, the specular reflectivity can be written as

$$R_S(Q) = R_F(Q)\exp\left(-Q^2\sigma_r^2\right) \tag{3.28}$$

which is the same form as that of the graded interface.

Both forms of interfaces cause an increase in the decay of the reflectivity with increasing Q by the same factor. This means that, when analysing specular reflectivity data, it is impossible to differentiate between intermixing or interface roughness. By fitting x-ray data, a σ value is obtained which quantifies the combined roughness and intermixing at the interface between layers. Here, σ is the RMS (root mean square)

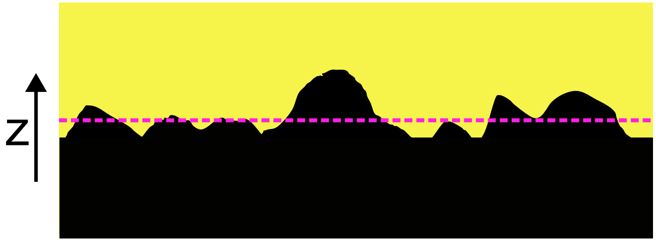

Figure 3.5: Schematic of a rough interface between two distinct layers. The pink dashed line shows the mean height of the interface.

roughness, which is the square root of the sum of the squares of the distances from the mean to the edge of the interface. Figure 3.6 shows simulated data for a Si substrate with varying roughness, demonstrating how the reflectivity decreases faster with larger roughness.

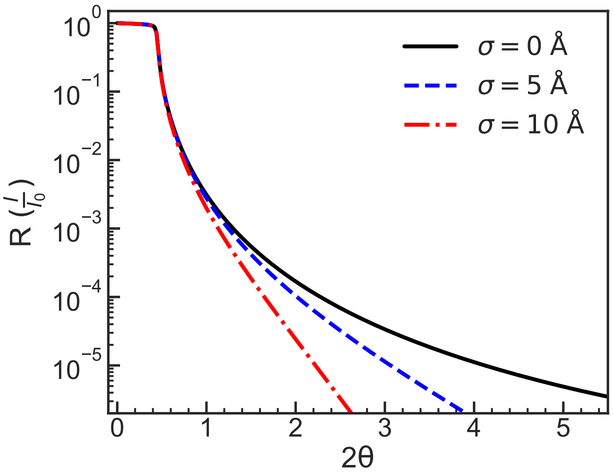

Figure 3.6: Comparison of the x-ray reflectivity of a Si substrate with different surface roughness (σ) values. The data was simulated using Refl1D software [177] with an x-ray wavelength of 1.54 Å.

3.3.5 Single Layer on a Substrate

In the case of a single layer of finite thickness on an infinitely thick substrate, the transmitted wave will reflect off of the substrate interface and travel towards the detector along with the wave reflected from the top interface. The interference that occurs

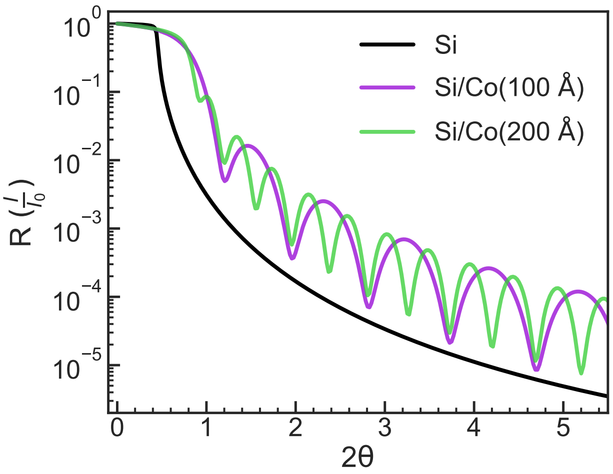

Figure 3.7: Simulated X-Ray reflectivity data of a plain Si substrate topped with single Co layers of 100 Å and 200 Å. All the layers are perfectly smooth ($\sigma = 0$). The data was simulated using Refl1D software [177] with an x-ray wavelength of 1.54 Å.

between these two waves is analogous to Bragg's law for x-ray diffraction, but the much larger length scales of a thin film compared to the atomic spacing of a crystal lattice mean the interference pattern appears at much smaller angles [178, 179]. The phase difference between the two waves is given by [180]

$$\Delta = 2t \sin \theta_t \tag{3.29}$$

where t is the layer thickness and θ_t is the angle of the transmitted wave. From Snell's law, we know that θ_t is related to the incident angle and the refractive index by

$$n_t \cos \theta_t = \cos \theta_i$$

By using the form of the refractive index of $n = 1 - \delta$, taking the square of both sides and then performing a Taylor expansion, only keeping first-order terms of δ as $\delta << 1$, θ_t can be written as

$$\theta_t^2 = \theta_i^2 - 2\delta \tag{3.30}$$

Therefore, by using the small angle approximation and the fact that $\theta_c \approx \sqrt{2\delta}$, the phase difference is given by

$$\Delta = 2t(\theta_i^2 - \theta_c^2)^{1/2} \tag{3.31}$$

The interference will be constructive and result in a maximum in the reflectivity when the phase difference is equal to an integer number of the probe wavelength. The angular position of the n^{th} maxima, θ_n, is then given by

$$\theta_n^2 = \theta_c^2 + \frac{\lambda^2 n^2}{4t^2} \tag{3.32}$$

The interference fringes are called Kiessig fringes [181]. The spacing of the fringes can be used to calculate the thickness of the film, see figure 3.7. With an increase in film thickness, the fringes become closer together.

3.4 Scattering Cross-Section

The differential scattering cross-section is the quantity that we measure in scattering experiments. It is a measure of the number of x-rays or neutrons scattered per second per unit solid angle $d\Omega$ [182]. It is denoted by

$$\frac{\mathrm{d}\sigma}{\mathrm{d}\Omega} = \frac{\text{Number scattered per second into } \Delta\Omega}{\Phi\Delta\Omega} \tag{3.33}$$

where Φ is the flux of the incident x-ray or neutron beam. The solid angle Ω refers to a small area on the sphere of radius r around the sample and has units of steradians [172]. This can be expressed more algebraically in the form

$$\frac{\mathrm{d}\sigma}{\mathrm{d}\Omega} = \frac{C}{\eta\Phi N\Delta\Omega} \tag{3.34}$$

where C is the count rate, η is the efficiency of the detector and N is the number of identical atoms in the beam [183]. If the energy is also analysed by the detector, then we must instead consider the double differential scattering cross-section which is defined by

$$\frac{\mathrm{d}^2\sigma}{\mathrm{d}\Omega\mathrm{d}E} = \frac{C}{\eta\Phi N\Delta\Omega\Delta E}. \tag{3.35}$$

The total scattering cross-section is defined as

$$\sigma_{tot} = \frac{\text{total number of neutrons scattered per second}}{\Phi} \tag{3.36}$$

The total, differential and double differential cross-sections are linked by the following expressions [182, 183]

$$\frac{\mathrm{d}\sigma}{\mathrm{d}\Omega} = \int_0^\infty \left(\frac{\mathrm{d}^2\sigma}{\mathrm{d}\Omega\mathrm{d}E'}\right)\mathrm{d}E', \tag{3.37}$$

$$\sigma_{tot} = \int_{\text{all directions}} \left(\frac{\mathrm{d}\sigma}{\mathrm{d}\Omega} \right) \mathrm{d}\Omega \tag{3.38}$$

The expression for the total scattering cross-section can be simplified if it only depends on one angle θ and re-written as

$$\sigma_{tot} = \int_0^{\pi} \frac{\mathrm{d}\sigma}{\mathrm{d}\Omega} 2\pi \sin\theta \ \mathrm{d}\theta \tag{3.39}$$

3.5 Neutron Scattering

3.5.1 Neutron Properties

A summary of the basic properties of neutrons can be seen in table 3.2. Neutrons are uncharged, meaning they do not interact with the electrons in the medium and therefore penetrate deeper into a sample than x-rays. Also, the magnetic moment of neutrons allows for magnetic scattering experiments, such as PNR, where both the nuclear and magnetic structure of a sample can be investigated.

Property	Value
Mass	1.675×10^{-27} kg
Charge	0
Spin	1/2
Magnetic Dipole Moment	$-1.913\ \mu_{\mathrm{N}}$ $-1.041\ \mu_{\mathrm{B}}$
Nuclear Magneton (μ_{N})	$5.051\ \times 10^{-27}\ \mathrm{JT}^{-1}$

Table 3.2: Key properties of a neutron.

Neutrons used in reflectometry experiments are cold neutrons. These neutrons have a typical wavelength of 2.6-26 Å and energies ranging from 0.12 meV to 12 meV [184]. The wavelengths of neutrons are determined by their kinetic energy. As the velocity of thermal neutrons is of the order of km/s, the kinetic energy can be given by the non-relativistic kinetic energy expression

$$E = \frac{1}{2} m v^2 \tag{3.40}$$

where m is the neutron mass and v is its velocity. The wavelength of this neutron is given by the de Broglie expression

$$\lambda = \frac{h}{mv} \tag{3.41}$$

The energy, temperature, velocity, wavelength and wavevector, $\boldsymbol{k}$, of a thermal neutron are related by [175]

$$E = k_B T = \frac{1}{2} m v^2 = \frac{h^2}{2m\lambda^2} = \frac{\hbar^2 k^2}{2m}. \tag{3.42}$$

3.5.2 Neutron Scattering

To understand neutron scattering, we must first consider the scattering from a single nucleus. The neutron interacts with the nucleus via the strong nuclear force. The range of these forces is of the order of $10^{-14} - 10^{-15}$ m and the cold neutrons have wavelengths of $10^{-9} - 10^{-10}$ m so we can treat the nucleus as a point scatterer [182, 185]. Because of this, the scattered wave is spherically symmetric. We can then say that the incident and scattered waves are of the form

$$\psi_i = \exp(ikz) \qquad\qquad \psi_s = -\frac{b}{r}\exp(ikr) \tag{3.43}$$

where k is the wavevector of the neutrons, z is the axis along which the incident wave travels and r is the radial distance away from the nucleus. The b parameter here is the scattering length, a single nucleus version of the scattering length density. b contains real and imaginary components corresponding to the scattering and absorption of neutrons respectively. For the majority of materials, the imaginary component is very small and b is independent of the neutron energy. There are, however, some materials, such as Gd and B, in which the neutron can be absorbed by the nucleus and in these cases the imaginary component is significant and is wavelength dependent [172].

3.5.3 Neutron Scattering Cross-Section

The differential scattering cross-section for a condensed matter system which changes from a state λ to λ' after a scattering event where the scattered neutron changes state from $\boldsymbol{k}$ to $\boldsymbol{k}'$ can be evaluated by using Fermi's golden rule [182, 183]. Fermi's golden rule is an expression that describes the rate of transition from a quantum state to a continuum of states due to some interaction [175]. Using this, we can write the differential scattering cross-section in this case as [182]

$$\left(\frac{\mathrm{d}\sigma}{\mathrm{d}\Omega}\right)_{\lambda\to\lambda'} = \frac{k'}{k}\left(\frac{m}{2\pi\hbar^2}\right)^2 |\langle \boldsymbol{k}'\lambda'|\boldsymbol{V}|\boldsymbol{k}\lambda\rangle|^2 \tag{3.44}$$

In this expression, V is the scattering potential between the neutron and the scattering system. To write the double differential scattering cross-section in the same form we must introduce the energies E and E' of the initial and final states of the scattered neutron and E_λ and $E_{\lambda'}$ of the initial and final states of the scattering system. The expression for the double differential scattering cross-section becomes

$$\left(\frac{\mathrm{d}^2\sigma}{\mathrm{d}\Omega\mathrm{d}E'}\right)_{\lambda\to\lambda'} = \frac{k'}{k}\left(\frac{m}{2\pi\hbar^2}\right)^2 |\langle \boldsymbol{k}'\lambda'|\boldsymbol{V}|\boldsymbol{k}\lambda\rangle|^2\delta(E_\lambda - E_{\lambda'} + E - E') \tag{3.45}$$

where $\delta(E_\lambda - E_{\lambda'} + E - E')$ is a Dirac delta function [182].

We can use the expressions given previously in equation 3.43 for the scattering of a neutron from a single nucleus to obtain the scattering cross-section for a single nucleus. The number of neutrons, travelling at a velocity v, that pass through the area dA per second is given by [182, 183]

$$v\,\mathrm{d}A\,|\psi_s|^2 = v\,\mathrm{d}A\,\frac{b^2}{r^2} = vb^2\mathrm{d}\Omega \tag{3.46}$$

where we have used the definition of the solid angle that $\mathrm{d}\Omega = \mathrm{d}A/r^2$ [172]. The total flux of the incident neutrons is

$$\Phi = v\,|\psi_i|^2 = v, \tag{3.47}$$

which means that the differential cross-section is given by

$$\frac{\mathrm{d}\sigma}{\mathrm{d}\Omega} = \frac{v\,b^2\mathrm{d}\Omega}{\Phi\mathrm{d}\Omega} = b^2 \tag{3.48}$$

Using equation 3.39, the total scattering cross-section can then be expressed as

$$\sigma_{tot} = 4\pi b^2 \tag{3.49}$$

3.5.4 Fermi Pseudopotential

As neutrons interact with the nucleus of an atom, we know that the scattering potential must be very short range. Therefore, the scattering potential can be approximated to

$$V(\boldsymbol{r}) = a\,\delta(\boldsymbol{r}) \tag{3.50}$$

where a is a constant and $\delta(\boldsymbol{r})$ is a three dimensional Dirac-delta function [182]. Using this as the scattering potential in equation 3.44 along with $\lambda = \lambda'$ and $\boldsymbol{k} = \boldsymbol{k}'$ results in

$$\frac{\mathrm{d}\sigma}{\mathrm{d}\Omega} = \left(\frac{m}{2\pi\hbar^2}\right)^2 a^2 \tag{3.51}$$

Comparing this result to equation 3.48, we see that the scattering potential can be written in the form

$$V(\boldsymbol{r}) = \frac{2\pi\hbar^2}{m}\, b\, \delta(\boldsymbol{r}) \tag{3.52}$$

This is known as the Fermi pseudopotential and is commonly used to describe the scattering potential between a neutron and a nucleus [182]. This expression can be written in a more general form for a system containing many nuclei. If we say that the scattering length of the j^{th} nucleus is b_j and its position is $\boldsymbol{r}_j$ then the Fermi pseudopotential for the full system of the assembly of nuclei is [185]

$$V(\boldsymbol{r}) = \frac{2\pi\hbar^2}{m} \sum_j b_j\, \delta(\boldsymbol{r} - \boldsymbol{r}_j) \tag{3.53}$$

For a continuous medium with a number density of N atoms per unit volume, the potential energy can be simplified to

$$V = \frac{2\pi\hbar^2}{m} N b = \frac{2\pi\hbar^2}{m}\rho \tag{3.54}$$

where all atoms have the same scattering length b and ρ is the scattering length density (SLD) [186].

3.5.5 Neutron Refractive Index and Critical Wave Vector

The same concepts of refraction and reflectivity apply to neutrons as described in section 3.3 for x-rays. The difference between the two probes and the corresponding reflectivity data and expressions comes from the different interactions with matter. An incident neutron, before it interacts with the sample medium, has an energy of

$$E_0 = \frac{\hbar^2 k_0^2}{2m} \tag{3.55}$$

as the total energy is equal to the kinetic energy [186]. When the neutron interacts with a sample medium, the total energy of the neutron becomes the kinetic energy plus the interaction potential between the neutron and the medium, as given in equation 3.54. We can then write the energy of the neutron inside the medium as

$$E = \frac{\hbar^2 k^2}{2m} + \frac{2\pi\hbar^2}{m}\rho \tag{3.56}$$

By equating the energy of the neutron before it enters the medium with the energy inside the medium, we can obtain the following relationship between the neutron wavevector inside and outside the medium,

$$k^2 = k_0^2 - 4\pi\rho \tag{3.57}$$

From this, we can define the neutron refractive index as

$$n(k_0) = \sqrt{1 - \frac{4\pi\rho}{k_0^2}}, \tag{3.58}$$

by using the fact that $n(k_0) = k/k_0$ [186]. Using this form of the neutron refractive index, we can produce an expression for the critical wavevector transfer, Q_c. We can see from the refractive index that the expression is not valid for $k_{0z}^2 < 4\pi\rho$. When the wavevector of the incident neutron is less than $4\pi\rho$, there is total external reflection and there is no transmitted wave. The wavevector transfer is defined as $Q = k_z - k_{0z}$, so when the incident wave is totally reflected, meaning $k_0 = -k_{0z}$, it can be written as $Q = 2k_{0z}$. The critical condition for Q is then [187]

$$k_{0z}^2 = 4\pi\rho$$

$$Q_c = \sqrt{16\pi\rho} \tag{3.59}$$

3.5.6 Born Approximation

The reflectivity can be estimated using the Born approximation, also known as the kinematic approximation. This approximation is valid when the interactions are weak and multiple scattering events can be neglected [170, 175]. For an in-depth derivation of the Born approximation and the distorted wave approximation, the reader is directed to the journal article of Sinha et al [188]. Here, we take the key points to obtain some expressions to help understand neutron reflectivity. The scattering cross-section in the Born approximation is given by [188]

$$\frac{\mathrm{d}\sigma}{\mathrm{d}\Omega} = N^2 b^2 \int_V \mathrm{d}\boldsymbol{r} \int_V \mathrm{d}\boldsymbol{r}' e^{-i\boldsymbol{q}\cdot(\boldsymbol{r}-\boldsymbol{r}')} \tag{3.60}$$

It is worth noting that this expression is valid for both neutron and x-ray reflectivity. For x-ray reflectivity, $b = r_e$ is the Thomson scattering length of an electron, $r_e = (e^2/mc^2)$ and in the case of neutrons, b is the scattering length used in the previous sections. The Born approximation can be used to produce an expression for the specular reflection amplitude by replacing the neutron wave function in the medium with that for a vacuum. The result of this is [186]

$$r_{BA}(Q) = \frac{4\pi}{iQ} \int_{-\infty}^{+\infty} \rho(z) e^{-iQz} \mathrm{d}z \tag{3.61}$$

This expression links the SLD and specular reflection amplitude by a Fourier transform. The Fresnel reflectivity is then [175, 188]

$$R_F = |(r_{BA}(Q)|^2 \approx \frac{16\pi^2}{Q^4} (Nb)^2 \tag{3.62}$$

where we have used $\rho(z) = Nb$.

3.6 Magnetic Neutron Scattering

As neutrons have a magnetic moment, they also interact with the internal magnetic field of the scattering medium. This means that the scattering potential for neutrons has an additional term relating to the magnetic field of the medium and the spin angular momentum of the incident neutron. The additional potential is given by

$$V_{\mathrm{mag}\,\pm} = \mp \boldsymbol{\mu} \cdot \boldsymbol{B}, \tag{3.63}$$

where $\boldsymbol{\mu}$ is the neutron moment and $\boldsymbol{B} = \boldsymbol{B}_0 + \mu_0 \boldsymbol{M}$ [175, 186]. B_0 is the applied magnetic field and is the same inside and outside of the medium meaning that it does not contribute to the scattering. Magnetic fields are applied at the sample point to retain the neutron polarisation and set the magnetic state of the sample. This additional potential results in an additional SLD component which follows from the relationship between the SLD and potential seen in equation 3.54,

$$\rho_{\mathrm{mag}\pm} = \mp \frac{m}{2\pi\hbar^2} \boldsymbol{\mu} \cdot \boldsymbol{B} \tag{3.64}$$

Therefore, for a magnetic medium, the total SLD is the sum of the nuclear and magnetic components

$$\rho_{tot} = \rho_N + \rho_M = \frac{m}{2\pi\hbar^2} (V_N \mp \boldsymbol{\mu} \cdot \boldsymbol{B}) \tag{3.65}$$

The additional term in the total SLD means that the critical angle of a magnetic sample depends on the spin state of the incident neutron. Following from equations 3.59 and 3.65, the critical angle of a magnetic material is given by

$$Q_C^{\pm} = \sqrt{\frac{8m}{\hbar^2} (V_n \mp \boldsymbol{\mu} \cdot \boldsymbol{B})} \tag{3.66}$$

For a particular sample, the critical angle will take two discrete values that depend on the magnitude of the magnetisation and are independent of the angle between the neutron polarisation and sample magnetisation, as has been shown experimentally and theoretically by Radu et al [189].

We have seen that the scattering potential of neutrons is dependent on the neutron spin. As the neutron spin can take two values, $+$ or $-$, the scattering potential must account for a total of 4 processes because we must now also consider the case in which the neutron spin is flipped by the scattering process. In the case that the neutron spin is not flipped by the scattering event, the two possibilities are $++$ and $--$ and when the neutron spin is flipped we have, $+-$ and $-+$. In each expression, the first and second $\pm$ correspond to the spin of the neutron before and after the scattering event respectively. This means that the scattering potentials can be expressed in matrix notation, with each element corresponding to one of the neutron spin configurations. The nuclear scattering potential operator is scalar, so only has non-zero diagonal terms, and is given by [186]

$$\hat{V}_N = \frac{2\pi\hbar^2}{m}\begin{pmatrix} Nb & 0 \\ 0 & Nb \end{pmatrix}. \tag{3.67}$$

The matrix operator for the magnetic scattering potential can be given in terms of the Pauli matrices, but here we will present the form where we write it in terms of the magnetic scattering length $p(x, y, z)$ and the number density of magnetic atoms N_M as a better comparison to the nuclear scattering potential [186]. The magnetic scattering potential, in this form, is given by

$$\hat{V}_M = \frac{2\pi\hbar^2}{m}\begin{pmatrix} N_M p_z & N_M p_x - iN_M p_y \\ N_M p_x + iN p_y & -N_M p_z \end{pmatrix}. \tag{3.68}$$

For magnetic scattering, we must consider not only the magnitude but also the direction of the sample magnetisation, which is why we consider the (x, y, z) components separately. The total scattering potential, $\hat{V}$ is simply given by the sum of the nuclear and magnetic components, and is therefore expressed as [186]

$$\hat{V} = \frac{2\pi\hbar^2}{m}\begin{pmatrix} Nb + N_M p_z & N_M p_x - iN_M p_y \\ N_M p_x + iN p_y & Nb - N_M p_z \end{pmatrix} = \frac{2\pi\hbar^2}{m}\begin{pmatrix} \rho_{++} & \rho_{+-} \\ \rho_{-+} & \rho_{--} \end{pmatrix} \tag{3.69}$$

This scattering potential shows that the spin-flip components ($+-$ and $-+$) are only influenced by magnetic scattering, meaning that in a non-magnetic sample, there would be no spin-flip scattering. Also, we can see from the scattering potential that the two non-spin-flip components ($++$ and $--$) are split by $2N_M p_z$.

3.6.1 Neutron Reflectometry Spin Channels

The neutron scattering potential is dependent on the initial and final spin state of the incident neutron. This means that there are 4 different reflectometry channels, corresponding to the 4 possible scattering processes. The 4 spin channels are denoted by R^{++}, R^{--}, R^{+-} and R^{-+} where the notation of the spin states is the same as for the SLD and scattering potentials. Consider the case where the neutron polarisation is parallel to the applied field and lies in the plane of the sample, perpendicular to the wave vector transfer, Q, and the sample magnetisation lies in some direction in the plane of the sample. The Born approximation for the non-spin-flip case for a magnetic sample of thickness L is proportional to [186]

$$r_{BA}^{\pm\pm} \propto \int_0^L (\rho_N(z) \pm \rho_M(z)\cos(\phi(z)))e^{iQz}\, dz, \tag{3.70}$$

where $\phi(z)$ is the angle between the sample magnetisation and the neutron polarisation axis. The non-spin-flip reflectivity is dependent on the structural and magnetic SLDs of the sample. The $++$ and $--$ spin channels are split by the magnetic scattering of the sample, which is maximum when the sample magnetisation is parallel to the neutron polarisation ($\phi = 0°$) and the splitting disappears when they are perpendicular ($\phi = 90°$). In the case of $\phi = 0°$, the difference between the $++$ and $--$ spin channels will give information about the magnetic SLD profile. This is typically presented in the form of the spin asymmetry which is defined as

$$SA = \frac{R^{++} - R^{--}}{R^{++} + R^{--}} \tag{3.71}$$

Assuming a sample magnetised to saturation parallel to the neutron polarisation, the Fourier transform of the spin asymmetry will result in the magnetic SLD profile ($\rho_M(z)$) parallel to the neutron polarisation axis [24]. As the magnitude of the sample magnetisation tends to zero, the splitting between the R^{++} and R^{--} spin channels reduces until, at $\rho_M = 0$, they are identical.

For the spin-flip components, the Born approximation is proportional to [186]

$$r_{BA}^{\pm\mp} \propto \int_0^L \rho_M(z)\sin(\phi(z))e^{iQz}\, dz, \tag{3.72}$$

where L and $\phi(z)$ are defined the same as before. This shows us that the spin-flip reflectivities are, not only purely magnetic, but also dependant on the magnetisation components perpendicular to the neutron polarisation. The R^{+-} and R^{-+} spin channels are zero when either the magnitude of the sample magnetisation goes to zero ($\rho_M = 0$) or if all of the magnetisation components are parallel to the neutron polarisation axis ($\phi = 0$).

Because the non-spin flip channels are dependent on the parallel magnetisation components and the spin-flip channels are dependent on the perpendicular magnetisation components, the combination of spin-flip and the non-spin-flip allows for the extraction of the depth profile of both the magnitude and angle of the magnetisation through a sample.

3.7 Neutron Absorption

As for x-rays, the neutron SLD has an imaginary component relating to the absorption cross section. For the majority of elements, this absorption term is very small so it can be ignored. There are some elements, such as Cd, B and Gd, in which the absorption cross-section is significant and must be considered [172]. Neutrons are absorbed by the nuclei as part of a nuclear reaction so it specifically occurs in isotopes of these elements which are strongly absorbing. In the case of the elements listed here, the specific isotopes that are strongly absorbing are ^{113}Cd, ^{10}B and ^{157}Gd [186, 190]. The element of note for this thesis, and it is used in some of the samples, is B. The strongly absorbing ^{10}B isotope makes up approximately 20% of naturally occurring B [190–192]. For some of the absorbing elements, such as Gd, the absorption cross-section is heavily dependent on the neutron wavelength, with peaks at certain resonant energies [193]. However, the absorption of B scales linearly with the neutron wavelength which makes analysing PNR data of samples containing B simpler. A summary of neutron scattering and absorption cross-sections for different elements can be found in table 3.3.

3.8 XRR vs PNR

XRR and PNR are both useful techniques for investigating the structure of thin film samples. Although the concepts of refraction and reflection are consistent between the two techniques, the different interactions with matter of the two probes mean that

Element	σ_{scat} (barn)	σ_{abs} (barn)	NSLD ($\times 10^{-6}$Å^{-6})	ImSLD ($\times 10^{-6}$Å^{-6})
B	5.24	767	6.908	-0.278
C	5.551	0.0035	7.534	-0.000
O	4.232	0.00019	3.122	-0.000
Al	1.503	0.231	2.078	-0.000
Mn	2.15	13.3	-2.960	-0.003
Co	5.6	37.18	2.265	-0.009
Nb	6.255	1.15	3.919	-0.000
Ru	6.6	2.56	5.174	-0.001
Gd	180	49700	1.658	-4.152

Table 3.3: Nuclear scattering σ_{scat} and absorption cross sections σ_{abs} for selected elements. NSLD and ImSLD refer to real and imaginary components of the nuclear scattering length density respectively. The scattering cross section data is taken from [194]. SLD values are calculated using the NIST SLD calculator with standard densities [176].

certain experiments will be better suited to one or the other.

Neutrons interact with the atomic nuclei whereas x-rays interact with the electrons within a sample medium. This means that neutrons have much larger penetration depths than x-rays as the scattering potentials are much shorter range. Therefore, neutrons are more suitable for measuring thicker samples of the order of μm, where an x-ray technique would not be able to probe the entire sample.

The nature of the x-ray interactions means that the SLD scales linearly with the atomic number of the element in the sample. As the reflectivity is dependent on the change in SLD at an interface, this means that elements of similar atomic numbers are very difficult to distinguish when using XRR. This also means that the scattering of samples consisting of only light elements such as C, Al, and B is very weak, making extracting structural information difficult. In chapter 5, we investigate the diffusion of B ions in C_{60} thin films. This is extremely difficult to investigate using only XRR as the x-ray SLDs of B and C are almost identical so it is very difficult to distinguish between the two elements. In contrast, the neutron SLD changes sporadically in relation to the element's atomic number and, also, the SLD can be large for some light elements, as can be seen in figure 3.8. This makes neutrons useful when investigating either light

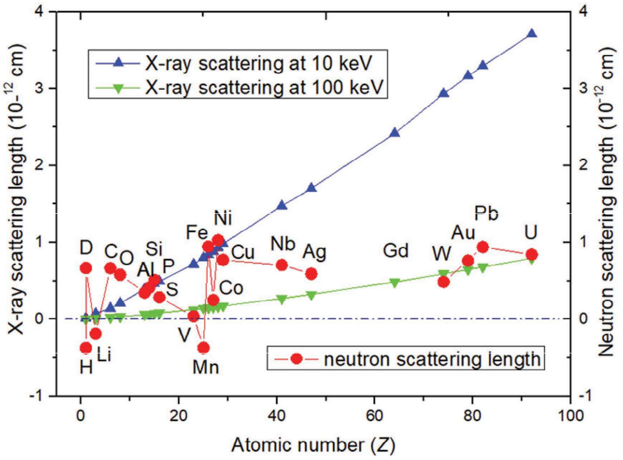

Figure 3.8: Comparison of neutron and x-ray nuclear SLD as a function of atomic number. The x-ray SLD scales linearly with the atomic number whereas for neutrons the SLD changes more randomly. Figure taken from [195].

elements or samples consisting of elements with similar atomic numbers, in our case B and C, as SLD contrast can be achieved where it would not be possible using x-rays.

PNR also has the advantage of magnetic contrast. As we have seen in this chapter, the neutron spin allows for measurements of the magnetic depth profile as well as the structural profile. This makes PNR a powerful technique for investigating magnetic dead layers [196] and proximity induced magnetisation effects [197, 198]. Standard XRR measurements do not provide magnetic sensitivity, although it is possible to use x-rays for probing magnetisation in techniques such as XMCD (X-ray magnetic circular dichroism) and PEEM (Photo-emission electron microscopy) [199]. However, in these types of x-ray techniques, x-ray energies have to be tuned to specific absorption edges which means that the magnetic characteristics of only one element can be measured in each measurement. The magnetic contrast of PNR is what allows for the investigations into magnetisation dynamics that we have performed in the FMR-PNR experiment. The magnetic sensitivity allows us to measure the profile of magnetisation and magnetic angle with nm resolution. This is also utilised in the ionic diffusion experiment as the source of the B ions is a magnetic CoB alloy, so, using PNR, we can monitor the change in magnetisation of the sample which indicates the migration of B.

X-ray sources can produce a much higher flux than neutron sources. This means that XRR measurements are much faster, of the order of 30-60 minutes as opposed to hours or days PNR measurements, and allow for measurement up to a higher range of Q where reflectivity is small. This means that XRR provides more information about the thinner elements of the sample as the higher order Fourier components correspond to thinner regions in the sample. The reduced flux of neutrons means that often larger surface area samples, up to 20 mm x 20 mm, are used to maximise the measured intensity. This has the disadvantage of requiring samples with extremely uniform layer thicknesses throughout the whole area.

Because of the different advantages and disadvantages of XRR and PNR, it is useful to use both techniques on samples to perform a comprehensive study of a sample structure.

CHAPTER 4

Methods

4.1 Sample Fabrication

4.1.1 Growth Chamber Details

Samples are grown using a combination of DC magnetron sputtering for metallic layers and thermal evaporation for C_{60}. The deposition chamber has 7 sputter guns and 1 C_{60} evaporation source. Substrates are taped onto plates using Kapton tape and attached to a wheel which rotates to move between the guns in the chamber. A roughing pump is used to reduce the pressure to around 20 mbar, then a cryopump is used for 12-14 hours to reduce the pressure down to the order of 10^{-7} mbar, with typical partial pressures of: H_2O=8×10^{-8} mbar, N_2=1×10^{-8} mbar and O_2= 1×10^{-9} mbar. A Meissner cold trap filled with liquid nitrogen further reduces the base pressure to the order of 10^{-8} mbar. The liquid nitrogen in the Meissner cold trap reduces the temperature of the inner casing of the chamber. This causes heavier molecules, such as water, to condense onto the inner chamber walls, taking them out of the atmosphere in the chamber and reducing the water partial pressure to below 1×10^{-8} mbar. Samples were grown on thermally oxidised silicon substrates with a 100 nm thick layer of SiO_x. The substrates are cleaned by sonicating in acetone to remove any organic residue and then sonicating in isopropyl alcohol to remove any acetone left on the substrates. If any acetone were put into the system it would damage the rubber seals in the system and therefore destroy the vacuum.

4.1.2 Magnetron Sputtering

DC Magnetron sputtering is a thin film growth technique whereby a target material is bombarded with ions, causing atoms of the target material to be ejected and then diffuse onto the substrate. Ar is used as the atmosphere gas as it is inert and sufficiently heavy to impart enough momentum into the target material atoms so that they have enough energy to leave the target. For growth, the chamber is filled with Ar gas which is pumped into the chamber with a flow of 24 sccm - 38 sccm, leading to a chamber pressure of between 2.5 - 3.4 mTorr, depending on the material and target. This pressure is optimised for the system to minimise strain in the deposited thin films [45]. Once the chamber is at the desired Ar pressure, a strong electric field is applied across the cathode and anode of the sputter gun [72, 201]. This electric field acts to ionise the Ar gas, forming a plasma [84]. The Ar ions in the plasma are then accelerated towards

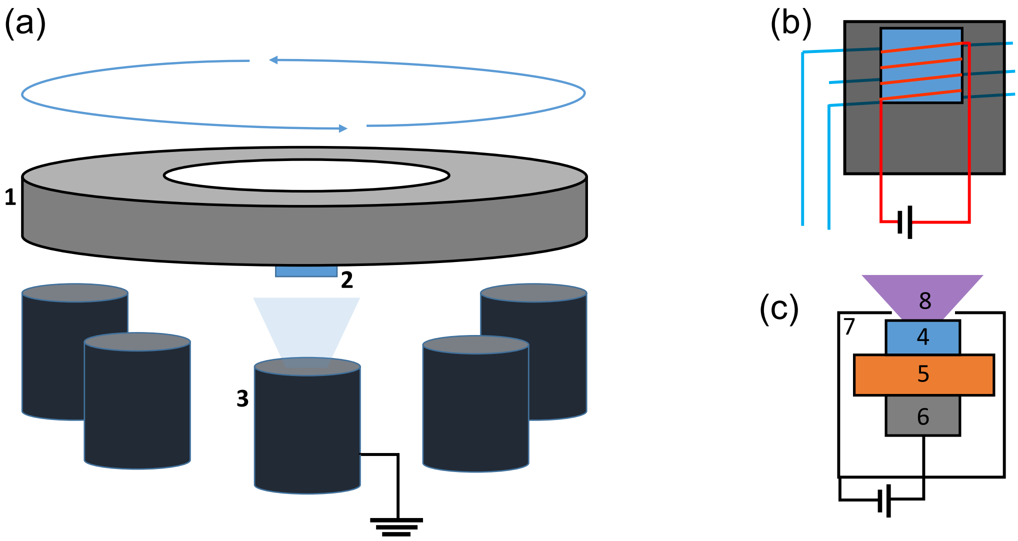

Figure 4.1: Schematic of the components inside the growth chamber (a) and cross sections of the C_{60} evaporation source (b) and DC magnetron sputtering guns (c). In the growth chamber, the substrates (2) are situated on a wheel (1) which can rotate to hold the substrate over the required gun (3) in the chamber. The chamber consists of 7 DC magnetron sputter guns and 1 C_{60} evaporation source. For the C_{60} evaporation source, C_{60} sits in an alumina crucible that is heated by a tungsten coil wrapped around it. A current of 22-23.5 A is passed through the coil to heat the crucible and evaporate the C_{60}. Water cooling surrounds the casing to prevent excessive heating. In the sputter gun, the target (4) sits on a copper block (5) which separates the target from a permanent magnet (6). The target and metal casing (7) act as the cathode and anode respectively. When the gun is ignited in an argon atmosphere a plasma is produced above the gun (8). Adapted from the author's previous work [200].

the cathode target. The bombardment of Ar ions onto the target surface causes the ejection of the metal target atoms which then diffuse through the plasma towards the substrate. The collisions with the target also cause the release of secondary electrons. These secondary electrons cause further ionisation of the Ar gas atmosphere [202]. To improve the efficiency of the ionisation and sputtering process, a magnetic field is used

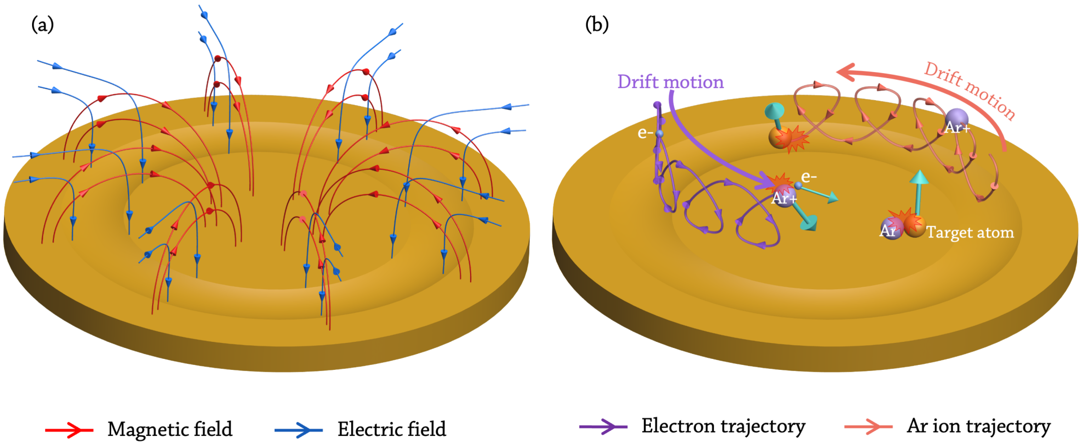

Figure 4.2: (a) Schematic of the electric and magnetic fields at the target in DC magnetron sputtering. (b) The drift motion of Ar ions and electrons due to the electric and magnetic fields at the target surface. The drift motion traps the electrons at the surface of the target to increase the rate of Ar ionisation and target deposition. Figure taken from [201].

to contain the secondary electrons and the plasma close to the surface of the target [203]. The magnetic field exerts a Lorentz force onto the electrons to confine them to a circular path above the surface of the target [204]. The shape of the magnetic field influences the rate of ionisation and therefore deposition rate resulting in the characteristic racetrack pattern seen on sputter targets [205, 206]. The magnetic field is produced by a set of permanent magnets housed within the sputter gun. When using ferromagnetic targets, a stronger permanent magnet is required so that the stray field penetrates through the magnetic target material.

4.1.3 C_{60} Evaporation

The evaporation cell consists of an alumina crucible that sits inside of a Tungsten filament. This is encased by a water cooled copper casing to prevent contamination or excessive heating of the sputter guns within the vacuum chamber. The crucible is filled with sublimation grade (99.9% purity) C_{60} molecules. Before any evaporation of the molecules, any atmospheric Ar gas is pumped out of the chamber to return to a base pressure of around 10^{-7} mbar. A current of 22-23.5 A is passed through the filament which heats the C_{60} to approximately 500-600 K and causes evaporation of the molecules. This produces a C_{60} evaporation rate of $\approx 0.2\text{Å}s^{-1}$. The temperature of sublimation T is influenced by the vapour pressure P by

$$\log(P) = A - \frac{B}{T} \tag{4.1}$$

where A and B are positive constants [46, 207]. Because of this, the rate is monitored in-situ rather than using the current as a reference as the growth rate at a certain current can vary depending on the vapour pressure. The rate of C_{60} growth is monitored using a quartz crystal microbalance which is located within the copper housing, above the crucible. Some of the evaporated C_{60} molecules are deposited onto the quartz crystal which then changes its resonant frequency [72, 208]. Measurement of the change in resonant frequency allows for monitoring the rate of deposition onto the quartz crystal. This is calibrated to correspond to a growth thickness using a tooling factor which is calculated by growing calibration samples.

4.2 SQUID Magnetometry

For the characterisation of magnetic properties, a Superconducting Quantum Interference Device Vibrating Sample Magnetometer (SQUID VSM) is used. This uses the same concepts as a standard VSM, where a sample is placed in a uniform magnetic field and oscillated, parallel to the magnetic field, between two pick-up coils. The motion of the sample induces an electromotive force (EMF) in the pick-up coils due to Faraday's law of induction which is proportional to the moment of the sample [209]. In a SQUID-VSM, the detection coils are coupled to the SQUID via a flux transformer [210]. A SQUID comprises two parallel Josephson junctions, which are superconducting rings that contain two tunnel junctions [211, 212]. When a constant bias current is passed through the Josephson junction, any change in magnetic flux causes a phase shift in the current [72, 211, 213]

$$I_m = 2I_c|\cos(\frac{\pi\phi}{\phi_0})| \tag{4.2}$$

Here, I_c is the critical current of the two Josephson junctions, I_m is the current flowing through the SQUID, ϕ is the external flux and ϕ_0 is the flux quantum ($\phi = h/2e$). The advantage of using a SQUID over a standard VSM is the much greater sensitivity of the SQUID as compared to standard pick-up coils, with a sensitivity down to 10^{-8} emu

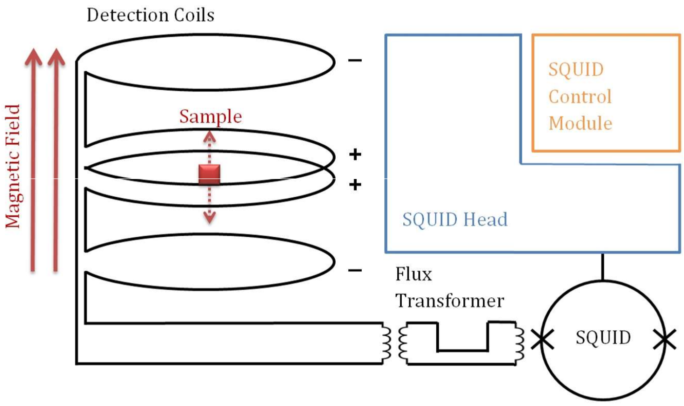

Figure 4.3: Schematic of the operation of the Quantum Design MPMS 3. The sample is vibrated within a set of pick-up coils, inducing an EMF which is then measured. The SQUID allows for the detection of much smaller signals and therefore provides greater sensitivity. Figure taken from [72].

[214]. In standard operation, samples are stuck to a quartz paddle using GE varnish. Samples can be up to 4 mm × 4 mm in size therefore sister samples to the much larger PNR samples are used for these measurements.

The SQUID-VSM used at Leeds is a Quantum Design MPMS 3. In its standard operating mode, temperatures in the range of 1.8K - 400 K are accessible. For high-temperature measurements, the oven operating mode must be used. Here, the sample space is pumped down to a vacuum of around 70 mTorr, compared to around 4 Torr in normal operation, to decouple the stick from the dewar that hosts the superconducting magnet. This is done with a turbo pump in addition to the standard oil pump. A ceramic sample stick containing a Pt resistance heater and temperature sensor is used which allows the sample to be heated up to 1000 K [215]. Samples are attached to the oven stick using an alumina based cement. The sample and stick are wrapped in a thin copper foil which reduces the radiation of heat into the chamber and maintains a uniform temperature over the sample. The copper foil also thermally connects the surface of the sample to the thermocouple on the back of the stick so that the read-back temperature is the same as that at the sample surface. Because of the flow of current and the different stick used for oven mode measurements, the measurement sensitivity drops from 10^{-8} emu to 10^{-6} emu.

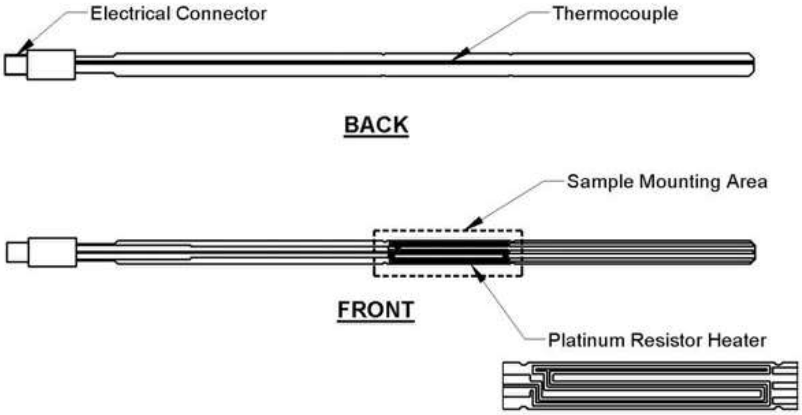

Figure 4.4: Diagram of the Quantum Design SQUID oven mode sample stick which allows for sample annealing up to 1000 K. The sample is placed on the front of the stick on the Pt resistor heater and the stick and sample are wrapped with a thin sheet of Cu. Figure taken from [215].

4.3 X-Ray Reflectometry

X-Ray Reflectometry (XRR) is a measurement technique to characterise the thickness, roughness and density of thin films. XRR measurements were done using two different systems. A Bruker Discover D8 was used at the University of Leeds and a Rigaku SmartLab at ISIS Neutron and Muon Source. Both systems supply Cu Kα x-ray radiation at a wavelength of 1.54 Å. X-rays are produced by accelerating electrons across a potential of 40 kV which then strike a Cu target. The radiation caused by the rapid deceleration of electrons is known as Bremsstrahlung. Some incident x-rays cause Cu electrons to be ejected from the core shell (n = 1). Outer shell electrons recombine with the core holes and cause the emission of the characteristic radiation energies. In the case of Cu Kα, the outer shell electrons from the n = 2 L shell recombine with the core electron holes in the n = 1 K shell causing the emission of the 1.54 Å (8.04 keV) characteristic radiation [72, 175]. In a standard XRR scan the sample and detector arm are moved such that the angle between the detector arm and the incident x-ray beam is 2 times the angle between the incident beam and the sample surface θ. The intensity of the reflected x-ray is measured as the angle is increased, resulting in a specular scan, such as the one shown in figure 4.5. The sample is aligned such that the x-ray beam is incident on its surface. This is done by aligning the angle of the sample stage and the x, y and z coordinates of the sample.

A detailed overview of x-ray scattering and reflectometry was given in chapter 3, here is a brief summary in relation to XRR. X-rays are reflected when there is a change in refractive index, defined by $n = 1 - \delta - i\beta$. Here δ and β are the real and imaginary components of the refractive index respectively [168, 169]. These quantities depend on the electron density and therefore the x-ray scattering length density (SLD) increases with atomic number. As x-rays are reflected when there is a change in refractive index, the contrast is larger between materials where the atomic numbers vary greatly. Below a certain incident angle, all of the x-ray beam is reflected. As shown in section 3.3, this angle is the critical angle θ_C and its value is related to the electron density of the material ρ_e by equation 3.16, which results in a critical angle of

$$\theta_c \approx \sqrt{\frac{r_e \lambda^2 \rho_e}{\pi}} \tag{4.3}$$

where r_e is the Thomson scattering length and λ is the x-ray wavelength. For example, a low-density material such as Si has a lower critical angle than a high-density material like Pt.

In the case of a single thin film on a substrate, there will be two contributions: one from the atmosphere/film interface and one from the film/substrate interface. The interference between these two contributions causes oscillations in the reflectivity curves known as Kiessig fringes [181, 216]. The distance between the fringes is related to the thickness of the layer. Interface roughness results in a decrease in intensity with the scattering angle. The thickness of the layer can be calculated from the difference in angle between the fringes using the equation

$$t^2 = \frac{\lambda^2(2n+1)}{4(\theta_{n+1}^2 - \theta_n^2)} \tag{4.4}$$

where t is the layer thickness, λ is the x-ray wavelength, θ is the angle of the fringe and n is the fringe number. Therefore, by finding the difference between the angles of all fringes and plotting $\lambda^2(2n+1)/4$ against $\theta_{n+1}^2 - \theta_n^2$, as shown in figure 4.5b, the layer thickness can be calculated from the gradient.

In a multilayer sample, each layer's thickness, roughness and density will contribute to the overall reflectivity, creating a more complex curve. In these cases, fitting software

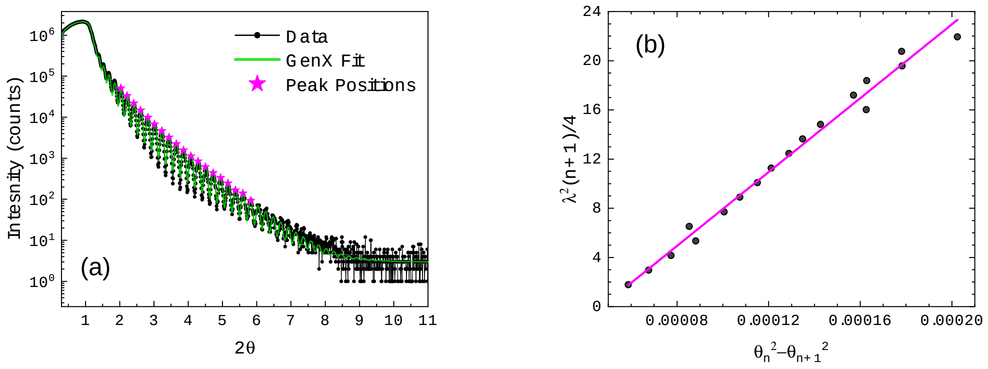

Figure 4.5: (a) Example XRR data of a sample with nominal thicknesses of Si/SiOx(1000 Å)/Pt(400 Å). The red line shows a fit to the data using GenX fitting software resulting in a Pt thickness of 394.5 ± 0.7 Å and a Pt roughness of 3.4 ± 0.1 Å. (b) Kiessig plot for the same reflectometry data as seen in (a) used to calculate the thickness of the film based on the separation of the Kiessig fringes as described by equation 4.4. This results in a film thickness of 388 ± 5 Å. The pink stars in (a) show the peak positions used to perform the Kiessig thickness calculation shown in (b).

such as Refl1D [177] or GenX [217] are used to fit a model structure to the curves. The majority of the functionality of Refl1D and GenX are identical. However, Refl1D software is used for the PNR and XRR fitting results presented in the results of this thesis as it allows for more complex model structures that are required for modelling the inter-diffusion observed in chapter 5. Figure 4.5 shows the comparison of using the Kiessig fringes analysis and GenX fitting to find the thickness of a film of Pt(400 Å) on Si/SiOx substrate. The resulting thicknesses found using both methods are very similar, differing by only 6.5 Å for a 400 Å thick film. However, the Kiessig fringes analysis only informs us about the thickness of the film, whereas the software modelling also gives values for the roughness and density/SLD, meaning that it is only used for thickness calibration samples.

4.4 Ferromagnetic Resonance

FMR is a measurement technique used to obtain a sample's static and dynamic magnetic parameters. The underlying physics of magnetisation dynamics utilised in FMR measurements is explained in section 2.1.7. When a ferromagnetic material is placed in a static external magnetic field (H_0), its magnetic moment will begin to precess about H_0. This precession will be quickly damped until the moment aligns with the static field if no other fields are applied. In FMR, an RF field is applied perpendicular to H_0. When the frequency of RF field is the same as that of the magnetisation precession the resonance condition is met and there is a maximum in the absorbance [218, 219]. By measuring the resonance condition at many different fields and frequencies, quantities such as Gilbert damping, saturation magnetisation and magnetic anisotropy can all be obtained from FMR measurements.

When measuring FMR data, either the frequency or applied field is swept to find the resonance condition which can be seen as a Lorentz peak [220] or a differential Lorentz peak [221–223] depending on the experimental set up. A differential lorentz peak is measured when a lock-in detection technique is used. Here, the DC field is modulated by a weak AC field that oscillates at a known fixed frequency. This means that the transmitted signal varies with time at the frequency of the lock-in. The measured signal is referenced against the lock-in modulation signal to extract the FMR signal [224]. As the time dependant change in the FMR signal is due to the oscillating AC field, the measured signal is in fact dP/dH, resulting in a differential Lorentzian at the resonance condition [85, 225, 226]. The FMR measurement set-ups used for characterisation measurements at Leeds and ISIS both utilise a co-planar waveguide to produce the RF magnetic field. The schematics in figure 4.6 show the configurations of both set ups. The difference is in the equipment used to generate and measure the microwave radiation.

In the set up used at ISIS, as described by figure 4.6a, a vector network analyser (VNA) is used to produce the microwave input and measure the returning signal after it has passed through the waveguide. This results in data resembling a Lorentz peak at the resonance condition.

In the Leeds set up, as described by figure 4.6b, a separate RF generator and detector are used instead of a VNA. A lock in detection technique is used to improve the signal to noise ratio as described earlier. The small alternating modulating field denoted by H_{AC} is produced by Helmholtz coils and is generated by a lock-in amplifier. The signal measured by the RF detector is multiplied by the lock-in reference signal to amplify the variations in absorption with respect to field caused by FMR excitations.

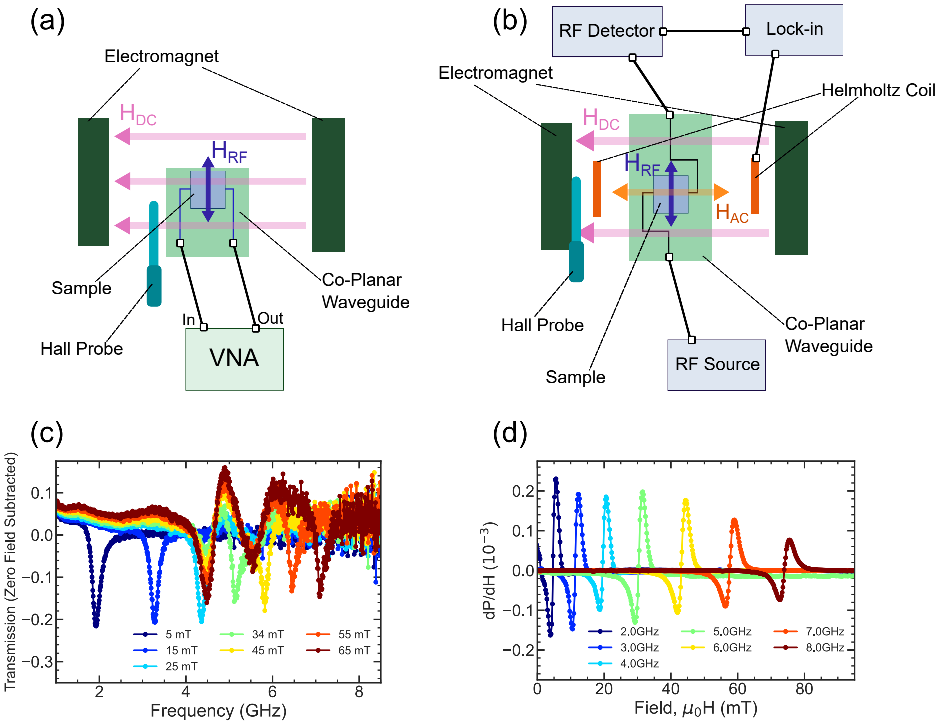

Figure 4.6: Schematics of the co-planar waveguide (CPW) FMR measurement setups used at ISIS (a) and the University of Leeds (b). The sample sits face down on a CPW in between an electromagnet. A microwave signal passes through the waveguide to produce an RF magnetic field perpendicular to the DC field produced by the electromagnet. The DC field is measured using a Hall probe. In the Leeds setup, a lock-in technique is used where the Helmholtz coils produce a small modulating AC magnetic field to improve the signal to noise ratio. (c) and (d) show example data obtained using the ISIS and Leeds setups respectively. The data in (c) is for a 30 nm thick film grown using the deposition chamber described in section 4.1. Data in (d) is from a 30 nm Py film grown by sputtering in the Royce deposition system at the University of Leeds by M.Rogers and P.Shepley.

The resulting measurement is of dP/dH meaning that FMR absorption peaks arise as differential Lorentz peaks in the data, see figure 4.6d.

From the Lorentzian or differential Lorentzian peaks, one can extract the peak position (H_0) and the linewidth (ΔH) which when plotted against the frequency allow us to extract values for the Gilbert damping parameter, effective magnetisation and anisotropy field. The frequency is related to the peak position by the Kittel equation [64]

$$f(H) = \frac{\mu_0 \gamma}{2\pi}\sqrt{((H + H_k)(H + H_k + M_{eff}))} \tag{4.5}$$

So by fitting this equation to the peak position data values for γ and M_s can be extracted. The peak widths are then related to the damping parameter by the equation [65]

$$\Delta H = \frac{4\pi}{\mu_0 \gamma}\alpha f + \Delta H_0 \tag{4.6}$$

Typical FMR data for a 30 nm thick Permalloy film measured using the Leeds set up with fits to equations 4.5 and 4.6 can be seen in figure 4.7. The fits to equations 4.5 and 4.6 can be seen in figures 4.7a and b respectively. First, the Kittel equation was used to extract values of γ, H_K and M_{eff}. Then, using γ, equation 4.6 can be used to extract a value of the Gilbert damping parameter. Performing these fits on the data shown in figure 4.7, gives values of $\mu_0 M_{eff} = 966 \pm 6$ mT and $\alpha = (4.94 \pm 0.02) \times 10^{-3}$. These are both in good agreement with the literature values [227–229].

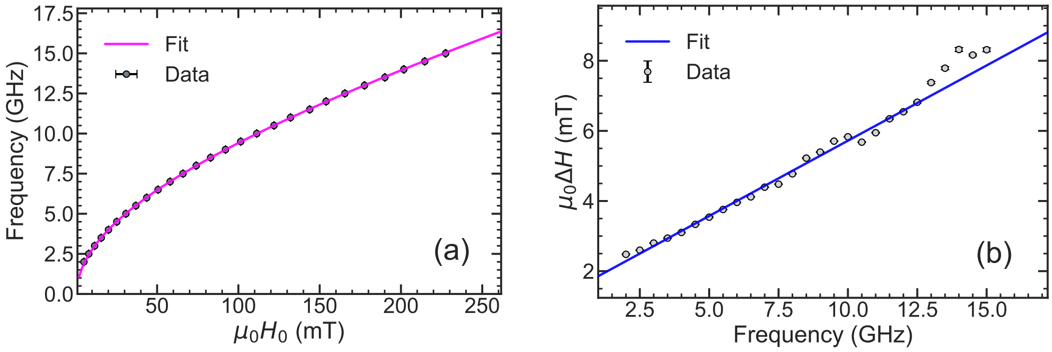

Figure 4.7: Example FMR results for a 30 nm thick permalloy film. (a) The peak position versus the frequency and the orange line shows fit with the Kittel equation 4.5 (b) The peak line width against frequency with the red line showing the fit of equation 4.6. These fits result in extracted values of $\mu_0 M_{eff} = 966 \pm 6$ mT and $\alpha = (4.94 \pm 0.02) \times 10^{-3}$. Example raw data for this sample can be seen in figure 4.6d.

4.5 POLREF Beamline

The PNR data presented in this thesis was collected using the POLREF beamline at ISIS neutron and muon source. POLREF is a time-of-flight polarised neutron reflectometer. The levels of polarisation analysis can be changed between measurements to measure standard neutron reflectometry (NR), half-polarised neutron reflectometry (PNR) (2-spin state) or fully polarised neutron reflectometry, also known as polarisation analysis (PA) (4-spin state). In a standard NR measurement, only the total reflected intensity of neutrons is measured, with no measurement of the neutron spin. In a half-polarised PNR experiment, the measured reflectivity has 2 channels, R^{+} and R^{-}. The + and - refers to the neutrons spin before it reaches the sample. In total, there are 4 different spin channels: R^{++}, R^{--}, R^{+-} and R^{-+}. The first + or - is the spin before the sample and the second is the spin after scattering from the sample. In the case of a half polarised measurement, the neutron spin after the sample is not measured so $R^{+} = R^{++} + R^{+-}$ and $R^{-} = R^{--} + R^{-+}$. For a PA measurement, the spin state is measured before and after the sample, giving data for all 4 spin channels. This is achieved using a series of flippers, analysers and polarising supermirrors along the beamline, as seen in figure 4.8, which can be added or removed to change between NR, PNR or PA measurements.

A magnetic field is applied across the sample point to ensure the polarisation of the neutron beam. This is done using an electromagnet which can apply fields up to 700 mT. The minimum field that can reliably retain polarisation of the neutron beam is 5 mT. This magnetic field can also be used to control the magnetic state of the sample. Typically, in 2-spin state measurements the full field strength is used so that the sample is saturated and to ensure the sample magnetisation is aligned with the neutron polarisation and therefore the spin splitting is maximised. Different guide fields may be used in experiment specific conditions e.g investigating domain states, or in our case, accessing a specific FMR resonance condition. In 4-spin state measurements, where the perpendicular magnetisation components are also measured, full sample saturation is not desired so weaker guide fields are used. In the case of the fully polarised PNR measurements presented in this thesis, the weakest field of 5 mT was used to limit the effect that the guide field had on the sample magnetisation direction.

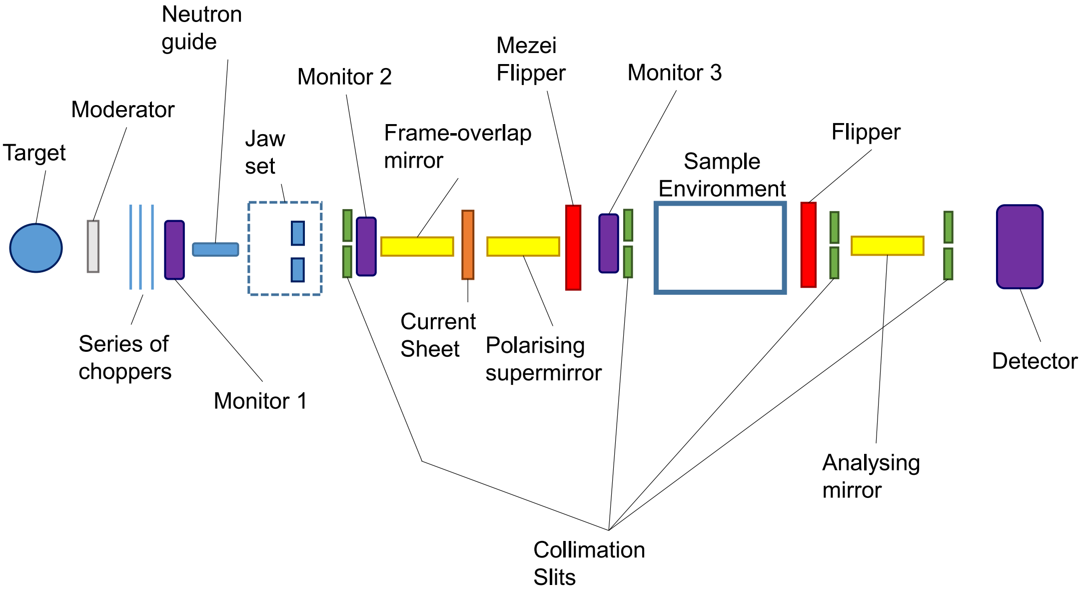

Figure 4.8: Schematic of the POLREF beamline at ISIS Neutron and Muon Source.

Supermirrors

Neutron Supermirrors are made of extremely smooth multilayer structures using materials with large neutron SLD contrasts such as Ni/Ti and Fe/Si. In a high repeat number, uniform multilayer made of such bilayer repeat structures with consistent bilayer thickness, the resultant reflectivity would contain a large Bragg peak at some Q value with a reflectivity intensity of the same order as that of the critical edge. The position of this Bragg peak decreases in Q as the thickness of the bilayer increases. Therefore, by manufacturing a multilayer structure whereby the bilayer thickness increases throughout the stack, the Bragg peaks overlap to form a large Q region where the reflectivity is close to 1 [230]. This concept was first proposed by Mezei in 1976/77 [231, 232]. Ni/Ti multilayers are typically used in the case of non-polarising supermirrors due to the high positive SLD of Ni and the negative SLD of Ti giving an extremely large contrast between the layers in the superlattice [233–236]. The large scattering contrast is the reason for the Bragg peak intensity being similar to that of total external reflection. Supermirrors are quantified by an m-value which relates its critical angle to that of a single film of Ni, with $m = 1$ meaning the critical angle is the same as natural

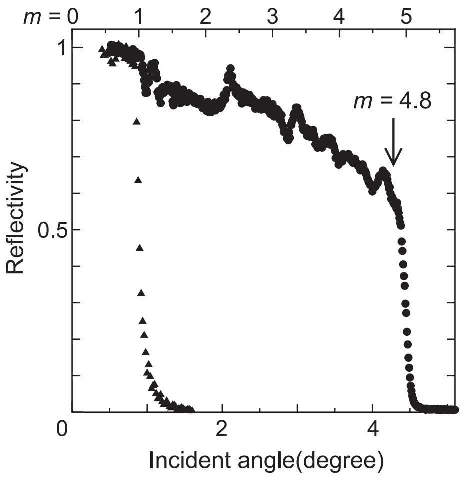

Figure 4.9: Example of the reflectivity of a Ni/Ti supermirror. The triangles show the reflectivity for a 200 nm film of Ni and the circles correspond to the supermirror. The supermirror has high, almost unity, reflectivity at angles almost 5 times greater than that of a simple Ni film. Figure taken from [235].

Ni [234, 235]. Example reflectivity data for an $m = 4.8$ supermirror can be seen in figure 4.9 (figure originally from [235]). High reflectivity supermirrors such as these are used to direct and focus the neutron beam and ensure the maximum possible neutron flux reaches the sample.

Supermirrors can also be used to polarise the neutron beam. Polarising supermirrors utilise the same concepts as previously mentioned with a large multilayer structure. However, by using a bilayer consisting of a high magnetisation ferromagnet (FM) such as Fe and a non-magnetic (NM) layer, the magnetic scattering contrast between the layers is such that the neutrons with spin parallel to the supermirror magnetisation are totally reflected ($R^{+} \approx 1$) and the antiparallel spins are transmitted ($R^{-} \approx 0$) [237–241]. Polarising supermirrors utilise the fact that the total SLD in an FM is a sum of the nuclear and magnetic SLD components. This means that, for certain combinations of FM and NM materials, the total SLD of the antiparallel state in the FM is approximately equal to the SLD of the NM [242]. Therefore, there is no reflection at the interface as there is no SLD contrast and subsequently, the anti-parallel state is fully transmitted.

Flippers

The Mezei flipper, as first described by F. Mezei [243], consists of a crossed coil. The coils produce a crossed magnetic field which causes the neutrons to precess as they pass through. With the correct magnitude of magnetic field, this causes the neutrons to complete a full π rotation and flip between up and down states [244]. The frequency of the precession is determined by the wavelength of the neutron and the magnetic field in the flipper. POLREF is a time-of-flight neutron probe so the neutron beam contains a range of neutron wavelengths. The speed of the neutrons is also dependent on their wavelength meaning that the different wavelengths of neutrons arrive at the flipper at different times. Therefore, by sweeping the current through the Mezei flipper, it is possible to adjust the field strength over time so that all wavelengths of neutrons are flipped.

4.5.1 Neutron Production

At ISIS, neutrons are produced from a spallation source. An 800 MeV beam of protons is fired at a heavy metal target of tungsten, coated with tantalum. This knocks out protons, neutrons and other clusters of particles from the nucleus. These ejected neutrons are of too high energy to use. Neutrons with energy up to the energy of the proton beam are emitted from the de-excitation of the nuclei fragments. The ejected high-energy protons go on to cause further spallation reactions within the target [245, 246]. Neutrons used in scattering experiments are cold neutrons with energies ranging from 0.12 meV to 12 meV [184]. The MeV energy neutrons are slowed by a series of moderators in which the neutrons scatter from light nuclei. The moderators are made of substances containing H such as water, liquid hydrogen and methane, to utilise the large incoherent scattering cross section of H [245]. The resulting pulse of neutrons, used for experiments, consists of a range of energies and therefore wavelengths.

4.6 Refl1D: XRR and PNR fitting

Fitting is required to extract nuclear and magnetic structural information from XRR and PNR data. The fitting presented in the results of this thesis was performed using Refl1D software [177]. Refl1D is a Python-based reflectometry fitting software which uses Bumps [247] as the underlying fitting algorithm.

Reflectometry fitting is performed by, first, producing a model sample structure. This consists of slabs of material with a set thickness, roughness and SLD. The SLD consists of nuclear, imaginary and, in the case of a PNR, magnetic components. The structural components are determined by the material density and elemental composition.

In Refl1D, materials can be defined in two ways. The first is to input the elemental composition and then either input the density or, if no density is specified, Refl1D will use the bulk density. In this scenario, the density is the fitting parameter that determines the magnitude of the nuclear and imaginary SLD values for that material. The second way to define a material in Refl1D is to manually define the nuclear and imaginary SLD. Here, the nuclear and imaginary SLD become direct independent fitting parameters. Mixture materials can also be set up whereby two or more defined materials are combined to make an alloy or other compound. The fitting parameter then becomes the composition of each of the materials. This feature is utilised in both of the experiments in this thesis. In the case of the FMR-PNR experiment, the FeMn alloy must be fit as a mixture to get agreement between XRR and PNR data sets. This is because the neutron SLDs of Mn and Fe are very different as the SLD of Mn is negative, whereas the x-ray SLD for the two materials are very similar due to the similar electron number. The negative neutron SLD of Mn means that the FeMn alloy's total SLD does not change with the composition in the same way as the total density of the alloy. In the ionic diffusion experiment in chapter 5, the mixture material allows us to sensibly link the changes in absorption and nuclear SLD of B injection into C_{60} to more accurately map its migration through the sample.

In all material slabs in the sample models, the interface roughness is described by an error function which links the SLDs of the two adjacent layers. The interface roughness value is related to the width of the error function such that an interface with 0 roughness would be modelled as a step function.

In the case of PNR, magnetic materials have an additional magnetic SLD component. This is defined by a magnitude, ρ_M, that is proportional to the magnetisation and dead layers and interfaces at the top and bottom of the magnetic layer. The initial ρ_M value is calculated from expected magnetisation values from literature and squid measurements, then the value is fit independently of other parameters. The magnetic dead layers and interfaces allow for additional freedom of the thickness and roughness of the magnetic profile outside of that defined by the physical structural parameters. There is also a θ_M fitting parameter which determines the angle of the magnetisation with respect to the neutron polarisation. It is only possible to extract this parameter when the PNR data consists of all 4 spin states.

The model is made up of slabs representing the layers of the physical sample using approximate values for thickness, roughness and density often found from previous calibration measurements or previous samples of a similar structure. This model is then used to produce an SLD profile. Reflectometry data is simulated for this profile. The goodness of the fit is determined using a reduced χ^2 which quantifies how close the simulation curve is to the data relative to the uncertainty in the data. The χ^2 value is calculated using the equation

$$\chi^2 = \frac{1}{D} \sum_{i=1}^{n} \frac{S_i^2 - f(Q)^2}{\Delta S_i^2} \tag{4.7}$$

where S_i is the individual data point, ΔS_i is its uncertainty, $f(Q)$ is the model line, D is the degrees of freedom of the model and n is the total number of data points. The fitting algorithm then gradually adjusts the fitted parameters so that the model SLD corresponds to a reflectometry curve that better represents the data. This process is repeated many times until, eventually, the global minimum of the parameter space is found, corresponding to the best fit of the data. In some cases, this simple slab model is not sufficient to accurately fit the measured data and so more complex modelling is required. This can involve, for example, adding in extra layers, changing the composition of the layers or representing a layer with a functional profile. Multilayer systems are initially modelled by the parameters of the repeat stack being copied exactly throughout the sample. For these types of samples, an additional complexity to the model could be a scaling on the e.g roughness as you move through the layers.

The uncertainty analysis on Refl1D fits is performed using DREAM [248] which is a Markov chain Monte Carlo method with a differential evolution step generator. These fits return parameter uncertainties as well as their correlations. This allows for a comprehensive analysis of parameters and a comparison of fitting models to determine the best model to describe the data. Unlike many other fitting algorithms, DREAM can accept steps that make the fit worse, depending on the scenario, which means that is less likely to be trapped in local minima.

4.7 Ion Beam Analysis Techniques

During the investigation on ionic diffusion of B in C_{60} thin films we use ion beam analysis measurements to investigate the B profile in the sample. These techniques are specifically useful for investigating light elements such as the B and C in our samples. All of the TOF-ERDA and NRA measurements presented in this thesis were performed by Eduardo Pitthan and Daniel Primetzhofer at the Tandem Laboratory at Uppsala University.

4.7.1 Time-of-Flight Elastic Recoil Detection analysis

TOF-ERDA is a technique used to measure element specific depth profiles of a sample. An incident heavy ion beam, in our case $^{127}\mathrm{I}^{8+}$, recoils particles out of the target sample which are then detected and analysed [249]. In TOF-ERDA, the energy, E, and time-of-flight, t, of the recoiled particle are used to calculate its mass m using

$$m = 2E\left(\frac{t}{l}\right)^2 \tag{4.8}$$

where l is the flight path distance [250, 251]. An example of the measured TOF vs energy spectrum can be seen in figure 4.10a. The calculation of the mass allows for ions to be separated and therefore element specific depth profiles can be determined [252, 253].

The incident ions and recoiled species lose energy as they travel through the sample. The measurement of the recoiled particle energy therefore allows for the calculation of its depth within the sample. The measured energy of the recoiled particle is related to the depth x by [250, 251]

$$E_2 = k_r E_0 - x\left(k_r \frac{S_i}{\sin\alpha} + \frac{S_r}{\sin\beta}\right) \tag{4.9}$$

where E_0 is the incident energy, S_i and S_r are the stopping powers of the incident and recoiled particles respectively and α and β are the angles of the incident and recoiled particles respectively. k_r is the called k-factor and is defined by

$$k_r = \frac{4M_iM_r}{(M_i + M_r)}\cos^2\phi \tag{4.10}$$

where M_i and M_r are the masses of the incident and recoiled particles and ϕ is the recoil angle ($\phi = \alpha + \beta$).

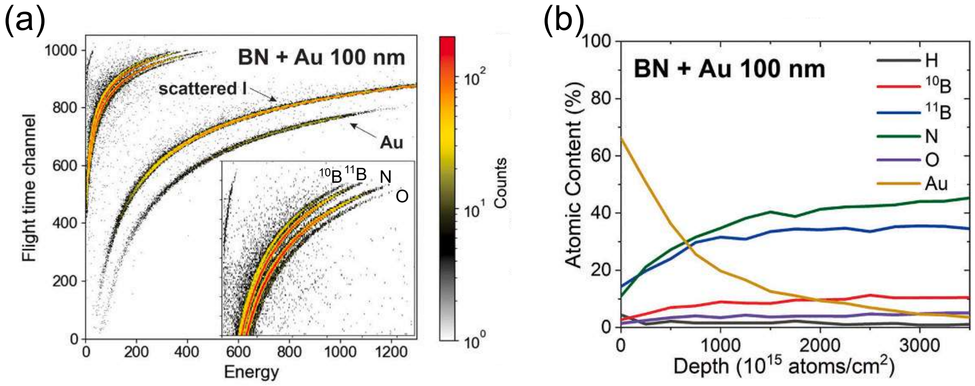

Figure 4.10: Example TOF-ERDA data for a sample of BN/Au(100nm) measured using a $^{127}\mathrm{I}^{8+}$ 36 MeV beam. (a) Shows the TOF-Energy spectra. From this spectra, the ions are separated and the energy is used to calculate the depth profile. (b) Elemental depth profile extracted from the TOF-Energy spectra displayed in (a). Figure adapted from [249].

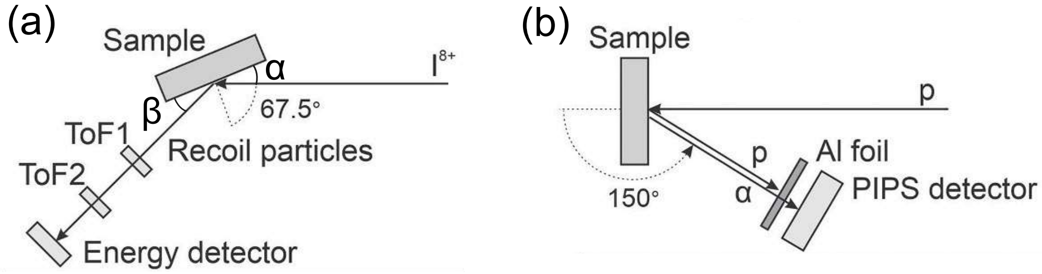

Figure 4.11: (a) Simple schematic of the TOF-ERDA measurement geometry. α and β are the angles of the incident and recoiled particles respectively. (b) Schematic of the NRA measurement geometry. The Al foil prevents backscattered protons from reaching the detector. Figure adapted from [249].

This analysis of the measured particle's original depth within the sample allows for the production of element specific depth profiles as seen in figure 4.10b.

The depth resolution of ERDA measurements is dependent on the composition of the measured sample, the incident angle and the incident beam energy. For a ^{127}I beam, depth resolutions of <6 nm can be achieved at the surface using a beam energy of 4

MeV [254]. However, at these low beam energies, the resolution increases drastically with increasing depth and for thicker films, higher energy beams are more suitable [254, 255]. For the $^{127}\mathrm{I}^{8+}$ beam at 36 MeV used in the measurements presented in this thesis, the depth resolution at the interface is approximately 30 nm [256]. The element sensitivity for this beam and energy of between 0.1 - 0.5 % atomic composition for C and O in Cu have been demonstrated [257]. For B in Si, detection of 0.2 - 1 % atomic percent has been achieved [249].

4.7.2 Nuclear Reaction Analysis

NRA is a technique that can be used for isotope-specific depth profiling [258]. Many different reactions can be used for profiling different isotopes, but in the measurements presented in this thesis, NRA is used to measure the ^{11}B profile. This is done with the $^{11}\mathrm{B}(\mathrm{p},\alpha)^{8}\mathrm{Be}$ reaction at the 163 keV resonance energy. The sample is irradiated with a proton beam causing the ^{11}B to experience a nuclear reaction which results in the ejection of alpha particles. The reaction is [259]

$$
\begin{aligned}
{}^{11}\mathrm{B} + p &\rightarrow {}^{8}\,\mathrm{Be} + \alpha_0 \\
{}^{11}\mathrm{B} + p &\rightarrow {}^{8}\,\mathrm{Be}^{*} + \alpha_1 \rightarrow \alpha_{11} + \alpha_{12} + \alpha_1
\end{aligned}
$$

The different characteristic energies of the emitted alpha particles appear as features on the measured spectra. The number of emitted alpha particles, typically at one specific characteristic energy, is measured for a range of incident proton energies to form the excitation curve [249]. The energy at which the ^{11}B peak appears in the excitation curve is dependent on it depth in the sample. The deeper the ^{11}B is in the sample, the higher the energy of the peak in the excitation curve. This energy curve can then be converted into a depth profile using knowledge of the stopping power for the material [249].

The depth resolution of this technique depends on both the composition of the sample and the incident angle used. In a Si matrix, the surface depth resolution for the $^{11}\mathrm{B}(\mathrm{p},\alpha)^{8}\mathrm{Be}$ nuclear reaction at 163 keV ranges from $\approx$ 30 - 65 nm for incident angles ranging from 60° - 0° [249, 258]. In terms of the sensitivity of the technique, benchmark experiments undertaken at Uppsala have demonstrated that the NRA measurements can detect B atomic concentrations as low as 0.02 % in a Si matrix [249].

Chapter 5

Monitoring Ionic Diffusion in C_{60}

5.1 Introduction

Molecular thin films have been used in spintronic research to control and manipulate the magnetic properties of metallic thin films. C_{60} in particular has been used to enhance the anisotropy of ferromagnetic metals [53], increase spin-orbit coupling in heavy metals [54] and induce ferromagnetism in non-magnetic metals [51, 52]. Molecular thin films offer a low-cost and sustainable alternative to rare-earth and heavy metals that are currently used in magnetic devices.

Here, we explore the possibility of using molecular thin films as a host for ionic diffusion and consequently as a way to control the magnetic properties of a ferromagnetic alloy such as the magnetisation and anisotropy. In this context, molecular materials offer an alternative to ionic liquids as a way to electrically control magnetism. Ionic liquid gating has been used to control the magnetic and electrical properties of many different materials such as metals, organic semiconductors, complex oxides and superconductors [31, 260]. These systems work in one of two ways. In electrostatic systems, the gate voltages cause a build up of charge at the interface between the ionic liquids and metals, forming electric double layers, producing strong, short range electric fields. The other category is electrochemical systems, where the gate voltage forces ions into the interfaced material, altering its properties via doping or oxidation [31].

However, the applications of ionic liquids in devices is limited by their size and operational temperature range. The ionic liquids themselves are larger than modern integrated circuits and the deposition cannot be controlled on the nanometer scale required for electronic or spintronic device applications. Also, the ionic liquids need to remain in the liquid state for the ions to be mobile meaning their functionality is limited in low temperature devices. Molecular thin films would allow for ultra-thin layers (nm scale), ultra high vacuum deposition meaning clean interfaces with the functional material, the possibility for nano-scale device fabrication and device functionality from low temperatures ($<$10K) to hundreds of degrees above room temperature [53].

CoFeB and CoB are magnetic alloys that are commonly used in spintronics research due to their relatively low damping and low pinning [261–265]. Often, they are used as part of perpendicular magnetic anisotropy multilayers where the magnetic alloy is interfaced with heavy metals such as Pt or Ta. When these types of structures are annealed, the B diffuses away from the magnetic alloy. However, as the adjacent layers are heavy metals, the B is absorbed and accumulates at the heavy metal interface

[159, 266, 267]. By replacing the heavy metal layers with low-density molecular thin films we expect the B ions to migrate into the molecule layers and act as free ions. This would provide the ability to reversibly control devices using gate voltages to move the ions within the molecular layers and also open research avenues into thin film molecular batteries and capacitors.

To investigate this, trilayers of C_{60}/CoB/C_{60} were grown and annealed, in which we anticipate boron ions to diffuse from within the CoB alloy into the C_{60} molecular layer. Using a magnetic alloy as the source of ions has the additional effect of the diffusion causing a change in the magnetic properties, such as saturation magnetisation and anisotropy, in addition to structural changes.

For the thin film multilayers used in this experiment, which contain low density materials such as C and B, Polarised Neutron Reflectometry (PNR) provides benefits compared to measurements such as x-ray reflectivity or Transmission Electron Microscopy. First of all, x-ray scattering length densities scale linearly with the atomic number, meaning that when using light elements such as C and B, there is limited scattering and also little contrast between them. This makes it very difficult to differentiate between C and B in the structure. In the case of PNR where the probe is neutrons, the SLD, as explained in chapter 3, for elements with similar atomic numbers can vary significantly. This means that it is possible to get significant SLD contrast between elements with similar atomic numbers. Using PNR, we can observe not only the changes in the nuclear structure but also the magnetic structure, as is explained fully in chapter 3. The magnetic scattering component of the neutron refractive index provides sensitivity to the in-plane magnetisation as a function of depth. PNR is also specifically sensitive to B due to its large neutron absorption cross-section. One of the profiles extracted from the PNR data is the imaginary component of the SLD profile which is a depth profile of the neutron absorption. The absorption cross-section of B comes from the ^{10}B isotope which makes up approximately 20% of naturally occurring boron [190, 191]. A comparison of the neutron absorption cross-section for B compared to other elements can be found in table 3.3. In the C_{60}/CoB sample structure boron has a significantly larger ImSLD than any other element [194], and therefore, the imaginary SLD profile will map out the location of B within the sample.

5.2 Sample Growth

All samples presented in this section were grown using a combination of DC magnetron sputtering for the metallic layers and in-situ thermal evaporation for C_{60}. The final sample structure is Si/SiO$_x$/C_{60}/CoB/C_{60}/Al. The CoB layers are grown using a $Co_{68}B_{32}$ alloy target. The CoB composition in the structures is not given because the sputtering growth rate of the B and the Co in the target is not the same meaning that the composition of the target changes over time and therefore the composition in the film can vary. Al is used as a cap because it oxidises when exposed to air, and when this happens, the layer expands, meaning that it forms a capping layer that reliably covers the whole sample area [45].

5.3 Effects of Annealing

5.3.1 SQUID Magnetometry

To investigate the influence of annealing on the magnetic response of the trilayer C_{60}/CoB/C_{60}, we used SQUID magnetometry measurements. The sample used had a nominal structure of Si/SiO$_x$(1000) /C_{60}(200)/CoB(150)/C_{60}(200)/Al(50) (thickness in Å). The magnetisation of Co is much greater than that of CoB [163]. Therefore, measuring the magnetisation and hysteretic response of the samples can be used to inform us of the change in the composition of the CoB during and after the annealing process. Using the SQUID oven mode, as described in chapter 5, it is possible to anneal the sample inside the VSM whilst simultaneously measuring the magnetic moment. This also allowed us to measure magnetic hysteresis loops before and after annealing on the same sample, providing more accurate comparisons.

A hysteresis loop was measured at room temperature and then the sample was heated to 300°C, at a heating rate of 5°C/min, to begin the annealing process, during which, the magnetic moment was continuously measured. An applied field of 700 mT was applied throughout heating, annealing and cooling as this is the maximum field that can be applied on the PNR beamline. These measurements were also performed on a C_{60}/Co/C_{60} sample (Si/SiO$_x$(1000)/C_{60}(200)/Co(320)/C_{60}(200)/Al(50) (thickness in Å)) which allows us to differentiate between B diffusion effects and Co crystallisation effects.

Hysteresis loops measured before and after annealing for both the CoB and Co

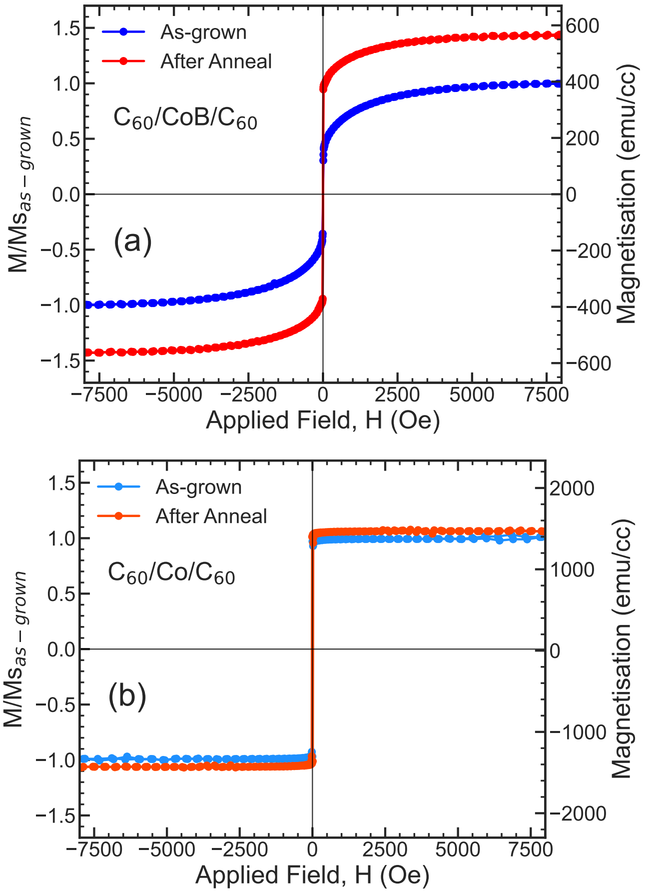

Figure 5.1: Room temperature magnetic hysteresis loops of samples of Si/SiO$_x$(1000)/C$_{60}$(200)/CoB(150)/C$_{60}$(200)/Al(50) (a) and Si/SiO$_x$(1000) /C$_{60}$(200)/Co(320)/C$_{60}$(200)/Al(50) (b) as grown and after annealing at 300°C for 10 hours. All thicknesses in sample structures are in Å.

samples are shown in figure 5.1. In the case of the CoB sample, the total magnetisation of the sample increases by approximately 50% due to the annealing process. This increase in M_s is evidence of B migrating from the CoB layer and leaving Co rich regions that have a much larger magnetic moment, therefore increasing the overall moment of the sample. For the Co sample, the moment increases by only ≈10% in agreement with the effects seen in other work [268]. This shows that there is some increase in magnetisation when the Co layer is annealed and cooled all in an applied field, which can be accounted to improved crystallinity in the Co film. However, as the relative increase in magnetisation for the CoB sample is significantly larger than 10%, this shows that the improved crystallinity after annealing cannot fully account for the increase in magnetisation that is observed for the CoB sample. Therefore, it is reasonable to explain this by the migration of B and the changing composition of the CoB, as the only change between the two samples is the addition of B. The as-grown M_s of the CoB sample is approximately 30% of the M_s of the Co M_s. The literature values show that for Co_2B, the moment is around 45% of the moment for Co, so this suggests that the B atomic % of the samples is significantly more than the 32% expected from the target [163, 164].

The heating curves in figure 5.2 show that the moment drops much more dramatically with temperature for the CoB sample than the Co sample. This is expected because the Curie temperature of CoB decreases with increasing B content [163]. However, the Curie temperature for Co_2B is 429 K [164], meaning the Curie temperature for our samples is significantly greater than expected considering the M_s suggests a B composition of greater than 33 %. A noticeable feature in the heating curves is the upturn at around 460 K for the CoB sample, which is not present for the Co sample. The upturn in moment is interesting because it is not expected in common $M(T)$ measurements and suggests that there is some form of phase transition. Considering the migration of B we expect in these samples and that is suggested by the increase in moment after anneal, it is reasonable to conclude that this transition could be the onset of B migration into the C_{60} layers.

The different effects of the annealing process on the C_{60}/CoB/C_{60} and C_{60}/Co/C_{60} samples can be seen by comparing the heating and cooling curves for each sample. In the case of the Co sample, the cooling curve traces back parallel to the heating curve. This shows that the gradients of the curves are very similar and therefore suggests that the composition of the magnetic layer in the sample has little change due to annealing. This follows the results seen in the before and after anneal hysteresis loops where there is only a small 10% increase in magnetic moment. In contrast, the heating and cooling curves for the CoB sample show very different behaviours. Notably, there is a significant separation between the two curves, showing that the magnetic behaviour of the sample has changed considerably due to annealing. The upturn in the heating curve at around 460 K is not seen during cooling. Also, the gradient of the heating curve around 300 K is much steeper than that of the cooling curve, suggesting that after annealing the

Curie temperature of the sample has increased.

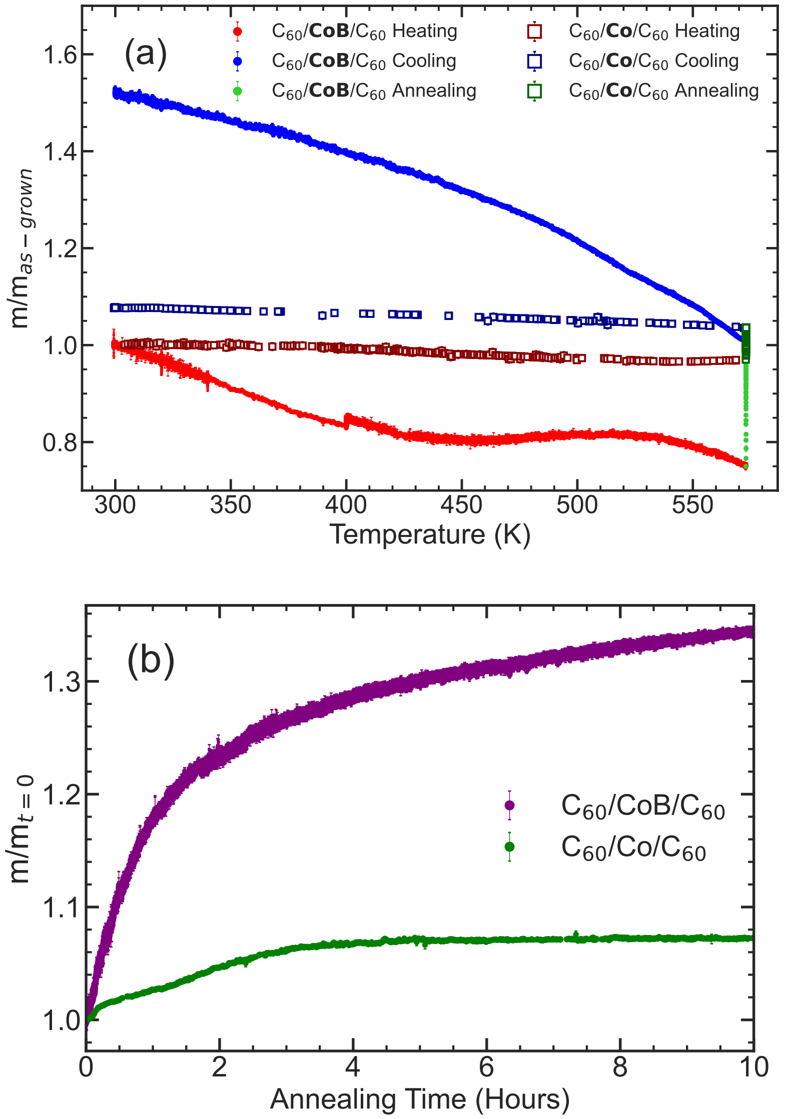

Figure 5.2: (a) Magnetic moment vs temperature during heating, cooling and annealing. Closed circles show data for the C_{60}/CoB/C_{60} sample and the open squares show data for the C_{60}/Co/C_{60}. The data for each sample is normalised to its moment at 300 K. (b) Magnetic moment time evolution during annealing at 573 K. Purple data is for the CoB sample and green data is for the Co sample. During all of these measurements the applied field was 700 mT.

During annealing, there are also significant differences between the CoB and Co samples. In both, we observe an increasing moment for the first three hours. In the Co sample, the increase in moment then flattens out whereas, for the CoB sample, the moment is continuously increasing throughout the ten hour annealing process. This provides evidence of a diffusive process causing a consistent decrease in the B content of the CoB layer, and therefore increasing the moment, throughout the annealing process. Notably, the relative change in moment is significantly greater for the CoB sample which further suggests an influence from the migration of B.

The contrast between the curves for the CoB sample and the Co sample shows that there is a definite influence of B in the annealing process in these metal molecular trilayer samples which we attribute to the migration of B from the CoB alloy into the adjacent C_{60} layers.

5.3.2 Polarised Neutron Reflectometry: Introduction

To investigate the structural and magnetic changes that occur in these structures due to annealing, Polarised Neutron Reflectivity (PNR) measurements were performed at ISIS Neutron and Muon source using the POLREF beamline. On POLREF, there is the capability to measure PNR and vacuum anneal the sample in-situ [269]. In this first section, data will be displayed for a series of 3 samples where the influence of annealing the samples at 300°C was investigated. Samples 1 and 3 share nominally the same sample structure with a slightly different CoB layer thickness and Sample 2 shares the same structure as samples 1 and 3 except that its CoB layer was grown from a different target and has a larger thickness. The estimated sample structures of the 3 samples can be seen in table 5.1.

Sample	Layer Thickness (Å)				
	SiO_2	C_{60}	CoB*	C_{60}	Al
Sample 1	1000	200	150	200	50
Sample 2	1000	200	300	200	50
Sample 3	1000	200	140	200	50

Table 5.1: Table of the structural parameters of the 3 samples used in this part of the experiment. *The CoB target used to grow Sample 2 is different than the one used for Samples 1 and 3 although they have nominally the same composition.

In all cases, PNR was first measured at room temperature before the sample was heated to the annealing temperature. In the case of Sample 1, PNR was measured before and after a 1 hour anneal at 300°C. For samples 2 and 3, PNR was measured before, during and after a 10 hour anneal at 300°C. During the annealing process, PNR is measured continuously. This can then be split into 1 hour time slices of data which can be analysed to observe the time-dependent structural changes during annealing. This is possible because the POLREF beamline is a time-of-flight neutron probe which means that a range of Q can be measured for one sample angle. For our measurements, the sample angle was 0.7° which gave a Q range of 0.012 Å^{-1} to 0.070 Å^{-1}. This is vital for doing time-dependent measurements because, in a monochromated beam, the sample angle would have to be swept during the measurement meaning that there is a time delay between measurements at different Q values.

5.3.3 Reflectometry Comparison

To demonstrate further why this investigation was performed using PNR as opposed to XRR, here the reflectometry results of one of the samples used in the PNR experiment are compared.

PNR and XRR fits for Sample 3 can be seen in figure 5.3. The XRR fit is good below $Q = 0.1$ Å^{-1} but misses key features in the data at higher Q values. The PNR fit is good throughout however, the Q range is much smaller, meaning it is less sensitive to thin layers in the sample. The XRR fit is further hindered by the Al cap. To achieve a reasonable fit of the data, an additional layer had to be added to the cap which results in the seemingly unphysical SLD profile seen in figure 5.3 where the SLD drops to almost 0. This is not the case for the PNR data where a good fit of the data and the cap structure is achieved with one layer each of Al and AlO_x. This could be due to the different scattering interactions of the two probes with the sample. The XRR SLD profile highlights how weak the x-ray scattering is for elements in the multilayer structure. For reference, the SLD for Pt is over 130 $\times 10^{-6}\text{Å}^{-2}$, over 3 times greater than that of the CoB layer. The weak scattering and small changes in x-ray SLD throughout the sample make it difficult to differentiate the different layers in the structure and therefore make modelling more difficult. In contrast, the neutron scattering length of C is large and there is good contrast throughout the sample, making the transitions in SLD between the layers more prominent and easier to model.

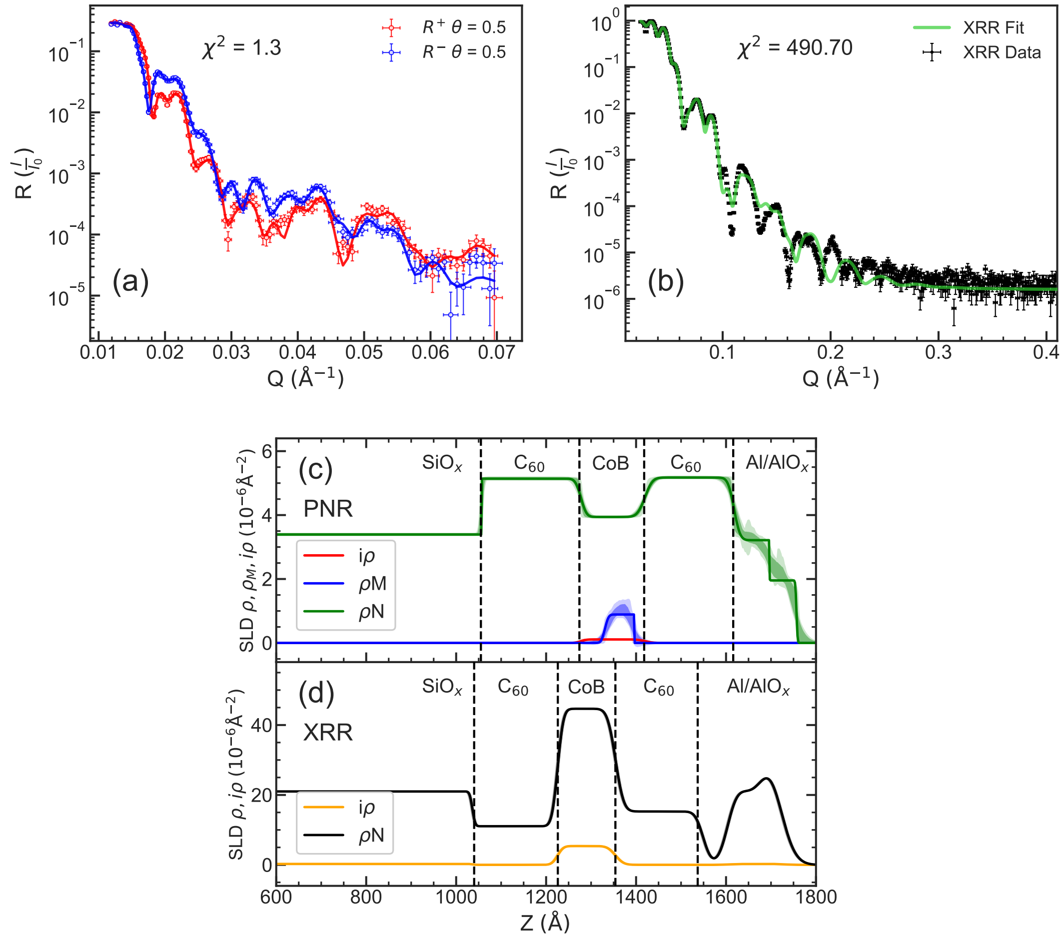

Figure 5.3: PNR (a) and XRR (b) data for Sample 3 with a nominal structure of Si/SiO$_x$(1000)/C$_{60}$(200)/CoB(140)/C$_{60}$(200)/Al(50) (thicknesses in Å). (c) and (d) are the SLD profiles extracted from the fits in (a) and (b) respectively. In (c), the blue, green and red lines represent the best fits of the magnetic, nuclear and absorption profiles respectively. In (d), the black line shows the nuclear SLD and the yellow shows the absorption SLD. The shaded bands represent the σ and 2σ ranges for each profile.

The structures obtained from both fits are somewhat similar with the XRR and PNR values for the top C$_{60}$ thickness within 5 Å and the CoB within 15 Å. However, there are clear differences in the C$_{60}$ densities obtained from the XRR and PNR fits. In the XRR fit, the density obtained for the two C$_{60}$ layers varies by 0.5 g/cc which is surprising as the two layers are deposited in the same growth conditions so should have very similar densities. The two C_{60} densities obtained from the PNR fit are different only by 0.01 g/cc and are within 7% of the bulk density of 1.65 g/cc. This, again, shows that PNR is much more suitable for studying these structures and results in more sensible structural parameters.

The vast differences in the goodness of fit between PNR and XRR data for the same sample highlight that, as a technique, PNR is much more suited to studying these structures than XRR. This is why the following studies on the structural changes and the movement of B within the sample due to annealing are performed using PNR measurements. If the reduced χ^2 for the PNR and XRR data were of the same order of magnitude, then a co-fit of both would be a good method to determine the structure, utilising the strengths and sensitivities of both measurement techniques. However, the vast difference in the reduced χ^2 in our case make such a co-fit less useful. As the fitting algorithm acts to try and reduce the overall χ^2, a co-fit here would be dominated only by the XRR fit as the χ^2 is orders of magnitude greater than the PNR χ^2 and therefore dominates the χ^2 of a combined fit. For the co-fit to work effectively, the two data sets would have to be weighted accordingly so that the model takes into account changes for both data sets. An arbitrary scaling like this would not appropriately represent the measured uncertainty of each data set, and as a result, the data sets were fitted independently.

Layer	Thickness (Å)		Roughness(Å)		Density (g/cc)*	
	PNR	XRR	PNR	XRR	PNR	XRR
SiO_x	1056(2)	1035(4)	2(1)	4.89(6)	2.15(1)	2.45
C_{60} Bot	221(1)	189.43(5)	9(4)	10.28(2)	1.543(6)	1.2996(4)
CoB	143(2)	128.82(3)	14(3)	14.33(3)	13.0(2) %B	15.52(2) %B
C_{60} Top	197(3)	194.64(8)	9(5)	13.97(6)	1.552(5)	1.796(2)

Table 5.2: Comparison of the structural parameters obtained from the XRR and PNR on the $Si/SiO_x(1000)$ /$C_{60}(200)$ /CoB(140) /$C_{60}(200)$ /Al(50) (thickness in brackets in Å) sample used for the gated PNR measurements. The fits are shown in figure 5.3. The numbers in brackets are the uncertainties in the last digit of the value e.g. $2.15(1) = 2.15 \pm 0.01$. *For the density column of CoB, the value gives the mass composition percentage of B.

5.3.4 PNR Results and Discussion

Model development

To extract quantitative information about the structural and magnetic changes that occur during the annealing process, we must fit model structures to the data, starting with the simplest description of the sample and gradually getting more complex. PNR fitting gives us information about the nuclear and magnetic profile of the sample as well as a nuclear absorption component, represented by iρ on the scattering length density (SLD) profiles. In the trilayer, the only element that has a non-negligible neutron absorption is B. This means that it is possible to determine the location of the B explicitly via the absorption profile, iρ. This section will outline the development of the fitting models that took place to find a model that accurately fits the data and describes the sample structure after the annealing process. The results for three models of increasing complexity are displayed. They will be labelled as Model A, Model B and Model C. The models will be described in more detail in this section, but a summary is as follows:

- Model A - Simple slab model
- Model B - Simple slab model with B added to the C_{60} layers
- Model C - C_{60} layers split into two sections with varying B composition

The model development was performed on the before and after anneal data sets for Sample 3. This is because it experienced the longest anneal meaning any changes in structure will be greatest and, unlike Sample 2, has a significant splitting of the spin states which makes fitting more accurate as there is more information to fit to. A comparison of the results of applying all 3 fitting models to the as-grown data set can be seen in figure 5.4 and the same for the after anneal data can be found in figure 5.5. Here, the data is plotted as the Fresnel reflectivity which is the total reflectivity divided by the substrate reflectivity. This makes the features on the data more pronounced and makes it easier to compare the fits of each model.

First, we fit a simple slab model (Model A) to the data. Here, all of the layers are modelled as a single slab with some thickness, interfaces described by error functions and magnetism in the CoB layer. For the as-grown data, shown in figure 5.4, we see that the model describes the data well, achieving a χ^2 of 1.3 ± 0.2. The χ^2 informs us about

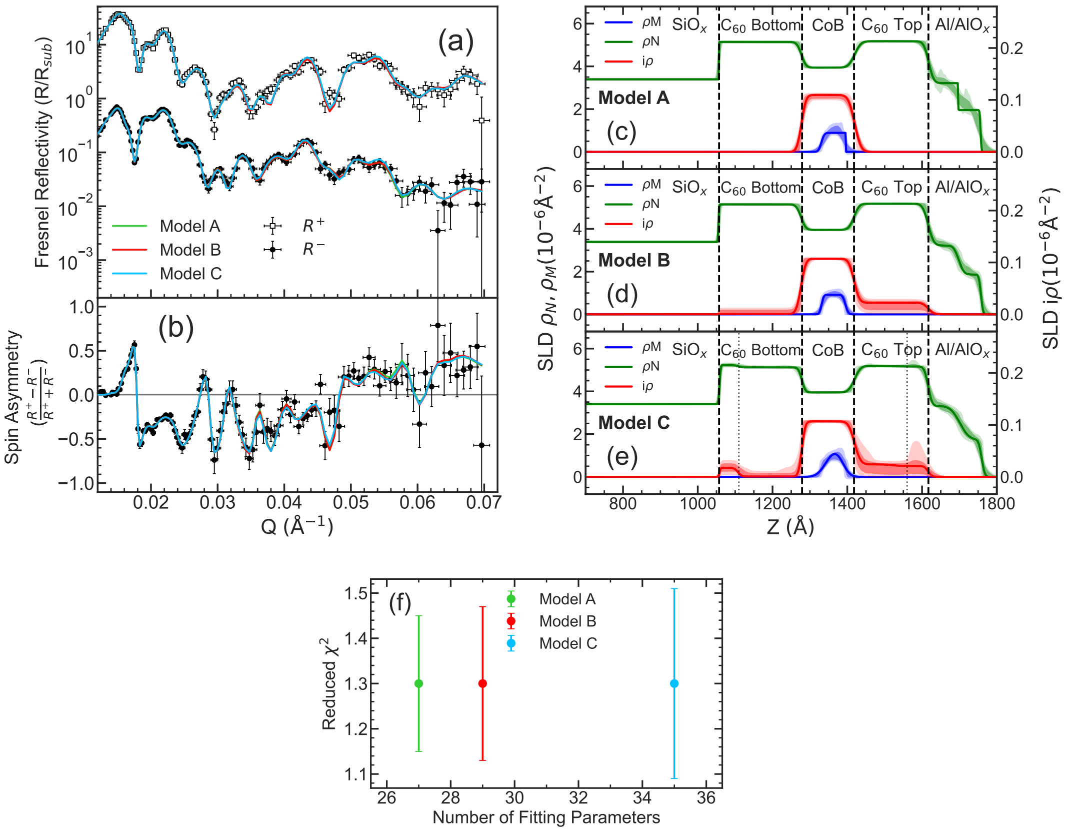

Figure 5.4: Comparison of fitting results for models A, B and C when used to fit the as-grown Sample 3 data set. The as-grown structure of Sample 3 was Si/SiO$_x$(1000) /C$_{60}$(200)/CoB(140)/C$_{60}$(200)/Al(50) (thickness in Å). The Fresnel reflectivity data and spin asymmetry are shown in (a) and (b) with the green, red and blue solid lines showing the fits to models A, B and C. The R^- reflectivity is shifted downwards by a factor of 50 for clarity. (c), (d) and (e) show the extracted SLD profiles from the fits with models A, B and C respectively. The blue, green and red lines represent the best fits of the magnetic, nuclear and absorption profiles respectively. The shaded bands represent the σ and 2σ ranges for each profile. (f) Comparison of the reduced χ^2 value and number of fitting parameters for each model. The χ^2 is a measure of the goodness of the fit. The smaller the χ^2, the better the fit describes the data.

the goodness of the fit and how close the model curve is to the data points, relative to the uncertainty of the data. A χ^2 of close to 1 indicates a very good agreement between the model curve and the experimental data. The SLD profiles show that, before annealing, the layers in our sample have clean interfaces between the C_{60} layers and the CoB. This indicates that there is little inter-diffusion between the layers when the sample is as-grown. There is a magnetic dead layer at the top and bottom of the CoB layer. However, when applying this model to the after anneal data set, see figure 5.5, the fit is predictably much worse as this simple model does not fully capture the post anneal sample structure and gives a χ^2 of 4.3 ± 0.2. One change this model does show is that the B composition of the CoB layer reduces due to annealing. In the CoB layer, we observe a reduction in B composition from $(13.0 \pm 0.2)\%$ to $(9.8 \pm 0.3)\%$ which would indicate that the B has migrated into the adjacent C_{60} layers. This idea is also supported by the fact that there is an increase in magnetisation within the CoB layer which we can attribute to the layer becoming more Co rich. The magnetisation also becomes more spread out, indicating that the Co may also diffuse into the C_{60}.

Fitting Parameter	As-grown Sample 3		
	Model A	Model B	Model C
C_{60} Bottom Thickness (Å)	221 ± 1	221 ± 1	220 ± 2
C_{60} Bottom Density (g/cc)	1.543 ± 0.006	1.537 ± 0.007	1.534 ± 0.005
CoB Thickness (Å)	143 ± 1	142 ± 2	142 ± 3
B% Mass in CoB (%)	13.0 ± 0.2	13.1 ± 0.1	13.0 ± 0.2
Mean Integrated ρ_M Area ($\times 10^{-6}$Å^{-1}) ($\propto$ Magnetic Moment)	60 ± 10	60 ± 10	60 ± 10
C_{60} Top Thickness (Å)	197 ± 3	197 ± 3	197 ± 5
C_{60} Top Density (g/cc)	1.552 ± 0.005	1.52 ± 0.02	1.52 ± 0.02

Table 5.3: Comparison of selected fitting parameters from the results of applying Model A, B and C to the as-grown data set for samples 3. Sample 3 has a nominal structure of $Si/SiO_x(1000)/C_{60}(200)/CoB(140)/C_{60}(200)/Al(50)$ (thickness in Å)

As the result of Model A indicates that B migrates out of the CoB layer, in Model B, the C_{60} layers were modelled as as $C_{60}B$ mixtures, whereby the B composition is introduced as an additional fitting parameter. Adding B to the C_{60} will increase the nuclear SLD and add an absorption component, which is shown by $i\rho$ (red lines) in the SLD profiles. Although Model A accurately describes the as-grown data, it is still important to apply Models B and C to the as-grown data to make sure that they converge on the same or a very similar structure to that of Model A. Also, this ensures that any features seen on the post anneal data are not just an artefact of the model.

For the as-grown data, the χ^2 value for the fit using Model B is the same as that for Model A and the SLD profiles are extremely similar with a small B composition in the C_{60} layers. When we use this model on the after anneal data set, there is a slight improvement in the fit when compared to Model 1 with the χ^2 reducing to 3.8 ± 0.2. The only difference in the SLD profiles for these two models is that in Model B there is a large absorption component in the C_{60} layers which comes from the introduction of B. This further supports the idea that B is migrating from the CoB layer into the C_{60} during the annealing process.

In Model C, the C_{60}B mixture layers are split into two regions which share the same C_{60} density but have independent B composition parameters. The thickness fitting parameters then become the overall thickness of the C_{60} layer and a thickness fraction parameter, β. So the thickness of the two sections within the C_{60} layer, $s1$ and $s2$, are given by

$$t_{s1} = t_{\text{total}} \times \beta \qquad\qquad t_{s1} = t_{\text{total}} \times (1 - \beta) \tag{5.1}$$

Due to the limit of the Q range, there is little information in the measured data about any very thin layers within the system. Thin layers appear in the data as long-range oscillations as the difference in the square of the angular position of neighbouring Kiessig fringes is inversely proportional to the square of the thickness as shown in chapter 3. As the maximum Q measured is 0.07 Å^{-1}, very thin layers are not captured in our data. Therefore, β is limited to vary between 0.2 to 0.8 in the fitting to ensure that the sections within the C_{60} are larger than around 40 Å. Using this model to fit the as-grown data results in a χ^2 of 1.3 ± 0.2, the same value as Models A and B. The SLD profile, as shown in figure 5.4, is again very similar to that of Models A and B.

Using Model C the fit for the after anneal data is much improved from the previous models, with a reduced χ^2 of 2.7 ± 0.2 compared to 4.3 ± 0.2 and 3.8 ± 0.2 for Models A and B respectively, demonstrating this to be a more accurate description of the sample after annealing. The improvement in the fit is also clear when looking at the fit lines on the raw data. The comparison of all the different models with the raw data, as seen in figure 5.5, shows clearly that Model C better follows the data points. Features in the spin-asymmetry at 0.025 Å^{-1} and 0.034 Å^{-1}, highlighted by the pink circles, are

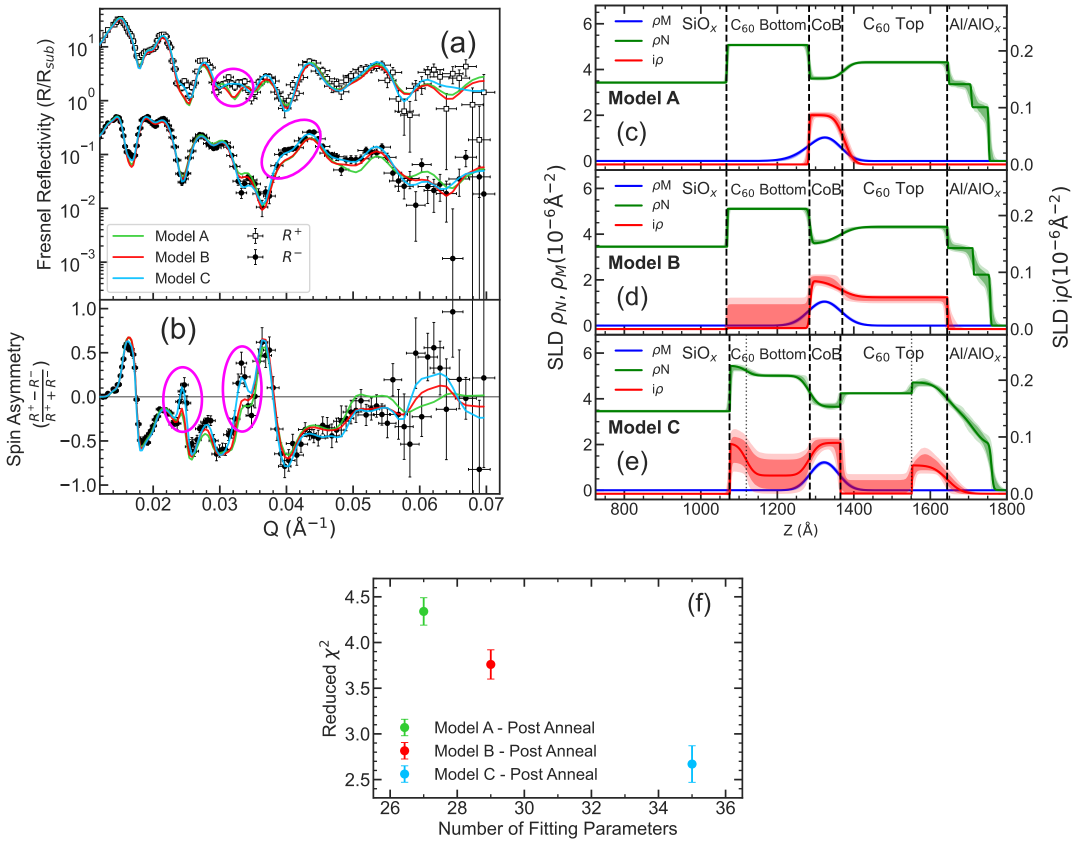

Figure 5.5: Comparison of fitting results for models A, B and C when used to fit the post anneal Sample 3 data set. The as-grown structure of Sample 3 was Si/SiO$_x$(1000)/C$_{60}$(200)/CoB(140)/C$_{60}$(200)/Al(50) (thickness in Å). The reflectivity data and spin asymmetry are shown in (a) and (b) respectively with the green, red and blue solid lines showing the fits to models A, B and C. The R^- reflectivity is shifted downwards by a factor of 50 for clarity. The pink circles highlight regions in the data where Model C captures the data features much better than A and B. (c), (d) and (e) show the extracted SLD profiles from the fits with models A, B and C. The blue, green and red lines represent the best fits of the magnetic, nuclear and absorption profiles respectively. The shaded bands represent the σ and 2σ ranges for each profile. (f) Comparison of the reduced χ^2 value and number of fitting parameters for each model. The χ^2 is a measure of the goodness of the fit. The smaller the χ^2, the better the fit describes the data.

Fitting Parameter	After Anneal Sample 3		
	Model A	Model B	Model C
C_{60} Bottom Thickness (Å)	214 ± 1	216 ± 1	207 ± 3
C_{60} Bottom Density (g/cc)	1.523 ± 0.004	1.50 ± 0.04	1.42 ± 0.05
CoB Thickness (Å)	93 ± 5	79 ± 4	82 ± 7
B% Mass in CoB (%)	9.8 ± 0.3	10.6 ± 0.5	10.3 ± 0.7
Mean Integrated ρ_M Area ($\times 10^{-6}$Å^{-1}) ($\propto$ Magnetic Moment)	110 ± 7	109 ± 7	108 ± 7
C_{60} Top Thickness (Å)	273 ± 6	283 ± 6	280 ± 10
C_{60} Top Density (g/cc)	1.293 ± 0.007	1.01 ± 0.01	1.24 ± 0.03

Table 5.4: Comparison of selected fitting parameters from the results of applying Model A, B and C to the after anneal data set for samples 3. Sample 3 has a nominal as-grown sample structure of Si/SiO$_x$(1000)/C$_{60}$(200)/CoB(140)/C$_{60}$(200)/Al(50) (thickness in Å

not captured by Models A and B but are included in the Model C fit. This shows that Model C is a much more accurate representation of the sample structure and justifies the increased number of parameters in the fit.

PNR Fitting Results

The results of fitting for Sample 3 using Model C on the as-grown and post anneal data along with the corresponding SLD profiles are presented together in fig 5.6. Although the as-grown data does fit well to a simple slab model (Model A), here we show the results of fitting with Model C to confirm that the differences we see after annealing are not due to anomalies from the model. We see that, even with this more complex model with more degrees of freedom, the fit to the as-grown data results in an SLD profile that is very close to a simple slab model. This confirms that the sample originally had well defined layers with little inter-diffusion and that there are no issues with the model. After annealing we see many changes in the sample structure. The CoB layer thickness reduces drastically from (142 ± 3)Å to (82 ± 7)Å and the B mass composition of this layer also reduces from $(13.0 \pm 0.2)\%$ to $(10.3 \pm 0.7)\%$. Converting this mass percentage into an atomic percentage, we get that the as-grown atomic percentage of B

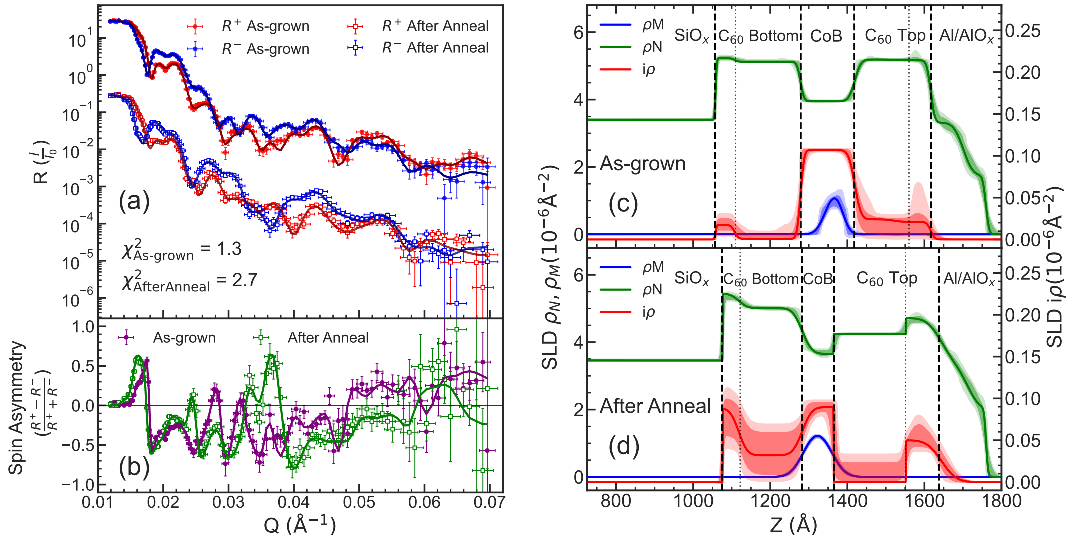

Figure 5.6: (a) PNR data for the C_{60}/CoB/C_{60} sample (Sample 3) before a 10 hour anneal at 300°C. The full structure of the sample was Si/SiO$_x$(1000)/C_{60}(200)/CoB(140) /C_{60}(200)/Al(50) (thickness in Å). R^+ and R^- represent the spin up and spin down reflectivities respectively. Solid lines are fits to the data using Model C. The after anneal data has been shifted downwards for clarity. (b) Spin asymmetry for the as-grown (purple) and after anneal (green) data sets, which is calculated as the difference in the two spin channels divided by their sum. (c) and (d) SLD profiles obtained from the fits using Model C for the as-grown and after anneal data respectively. The blue, green and red lines represent the best fits of the magnetic, nuclear and absorption profiles respectively. The shaded bands represent the σ and 2σ ranges for each profile.

was $(44.9 \pm 0.8)\%$ and after annealing, this reduced to $(38 \pm 3)\%$. These values do agree with the SQUID magnetometry results where the M_s suggested that in the as-grown samples the B atomic percentage was significantly larger than 32%. The reduction in B composition and the CoB thickness indicates that the overall B content of the CoB layer decreases dramatically due to annealing and migrates into the adjacent C_{60} layers.

The magnetic depth profile, shown by the blue lines on the SLD profiles, changes significantly due to annealing. There is a slight increase in the magnitude of ρ_M after annealing but more noticeably, there is a large broadening of the magnetic moment. We propose that the increase in magnitude can be explained by the formation of a

Co rich region within the CoB which will have a greater magnetic moment than that of CoB. The broadening in the magnetic depth profile suggests that Co also begins to intermix with the adjacent C_{60} layers. The total magnetic moment of the sample is proportional to the integrated area underneath the magnetic depth profile. This is calculated to be $(60 \pm 10) \times 10^{-6}\text{Å}^{-1}$ for the as-grown sample and $(108 \pm 7) \times 10^{-6}\text{Å}^{-1}$ after annealing. Therefore, we see that the sample moment increases by $(80 \pm 30)\%$ due to B migration caused by annealing. This change is noticeably larger than the changes seen in the SQUID measurements, where the increase in moment was under 50%. The magnetisation of the CoB in the sample is relatively low, $\approx$ 400 emu/cc, hence the uncertainty in the magnetisation extracted from the PNR data is relatively large, with a 17% uncertainty in the as-grown magnetisation. This could explain the discrepancy between the changes in magnetization measured in PNR and using SQUID magnetometry.

The SLD profiles show that the B, displayed by the absorption profile, aggregates at the interfaces furthest from the CoB. In the bottom C_{60} layer, the B migrates from the CoB until it encounters the SiO_x substrate where there is a further energy barrier which it cannot overcome and so congregates at this interface. At the interface between the top C_{60} layer and the Al/AlO_x cap, the absorption profile is much more dispersed, suggesting a large amount of mixing and inter-diffusion as the B migrates through the C_{60}. As can be seen clearly in the SLD profiles in fig 5.6, B addition into the C_{60} acts to increase the nuclear SLD and so this cannot explain the reduction in nuclear SLD that occurs in the top C_{60} layer after annealing. The diffuse top interface demonstrates the possibility that this reduction in nuclear SLD is caused by Al diffusing into the top C_{60} layer. This would also explain why this change in nuclear SLD is not seen in the bottom C_{60} layer. All of this shows that C_{60} is a good host matrix for ionic diffusion as we see that the B ions liberated from the CoB alloy layer migrate through the full 200 Å C_{60} layers until they are eventually stopped at the Al and SiO_x interfaces.

The total amount of B in the system can be estimated by integrating the area under the iρ profile. This quantity should be conserved during the annealing process. However, it is not possible to feed this information back into the PNR fitting algorithm to ensure B conservation. Calculating the integrated iρ area for results of Sample 3 we obtain values of $(20 \pm 4) \times 10^{-6}\text{Å}^{-1}$ before annealing and $(24 \pm 9) \times 10^{-6}\text{Å}^{-1}$ after annealing. Even though the total B is not constrained by the model, the results show

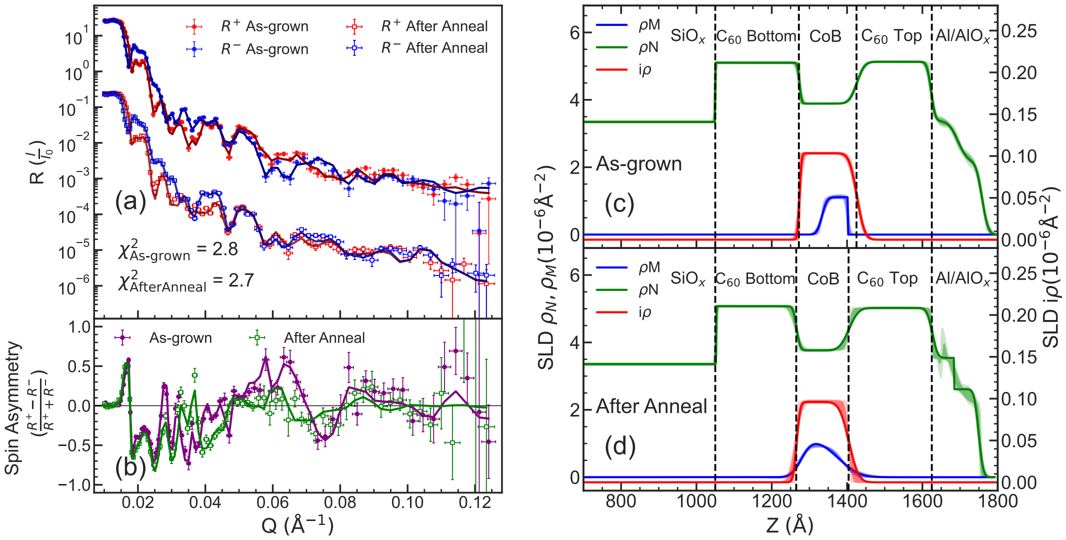

Figure 5.7: (a) PNR data for the C_{60}/CoB/C_{60} sample (Sample 1) before a 10 hour anneal at 300°C. The full structure of the sample was Si/SiO$_x$(1000)/C_{60}(200)/CoB(150) /C_{60}(200)/Al(50) (thickness in Å). R^+ and R^- represent the spin up and spin down reflectivities respectively. Solid lines are fits to the data using Model A. The after anneal data has been shifted downwards for clarity. (b) Spin asymmetry for the as-grown (purple) and after anneal (green) data sets, which is calculated as the difference in the two spin channels divided by their sum. (c) and (d) SLD profiles obtained from the fits using Model A for the as-grown and after anneal data respectively. The blue, green and red lines represent the best fits of the magnetic, nuclear and absorption profiles respectively. The shaded bands represent the σ and 2σ ranges for each profile.

that the total amount of B within the as-grown and after-anneal sample are within the uncertainty range. This further supports the PNR profiles being accurate descriptions of the sample before and after annealing.

Sample 1 experienced a shorter anneal at the same temperature as Sample 3, so we would expect to see similar changes but with a smaller magnitude. Comparing the results for both samples and confirming this is the case can help to verify the observations seen for Sample 3. When fitting Sample 1, it is found that, using Model A, the χ^2 values for the as-grown and post-anneal data are 2.8 ± 0.2 and 2.7 ± 0.2 respectively. Fitting the same data using Model C, we obtain χ^2 values for the as-grown and post-anneal data of 2.7 ± 0.3 and 2.5 ± 0.3 respectively. Because the difference in χ^2 is so small, it is correct to use the model with the least degrees of freedom, and so here the results of Model A are used for analysing the changes before and after annealing. The fits and SLD profiles for this sample are shown in figure 5.7. From only the χ^2 results of the fits, it is clear that the changes in the sample structure are less pronounced than for Sample 3 as the simple slab model fits the pre and post anneal data equally well. This shows that with the reduced annealing time we no longer observe the congregation of B ions in the C_{60} layers which requires more degrees of freedom in the model to be accurately described.

A comparison of some of the key parameter changes observed before and after annealing for Samples 1 and 3 can be seen in table 5.5. As expected, in both samples, the same changes occur but with different amplitudes. In both cases, after annealing, the CoB thickness decreases, and the layer's B composition decreases as well as there being an increase in magnetisation per unit area. For Sample 1, the B% mass compositions before and after annealing correspond to atomic percentages of $(43.6 \pm 0.4)\%$ to $(40.7 \pm 0.9)\%$ respectively. The slightly reduced B composition in this sample and greater CoB thickness compared to Sample 3 explains why the as-grown magnetisation for this sample is greater. It is not possible to obtain a time dependence of the annealing effects from just these two samples, however, the data from Sample 1 supports the conclusion that we are observing the migration of B ions in the sample due to annealing. The B composition of the CoB layer decreasing as well as the magnetisation of this layer increasing both implies that there is some migration of B into the adjacent C_{60} layers. Also, the fact that the changes are smaller with a shorter the annealing time further supports the idea of the B migrating in a slow-moving diffusion process.

The same analysis was performed on the data for Sample 2 to verify that the same or similar changes were observed due to the same annealing process. This sample had a thicker CoB layer of 300 Å compared to 140 Å for Sample 3 and the CoB target was different meaning the composition of the CoB layer was slightly different. The PNR data and corresponding SLD profiles for this sample from fitting using Model C can be seen in figure 5.8. From the SLD profile after anneal, we see the same aggregation of B at the top and bottom interfaces as was seen in Sample 3. The shapes of the absorption SLD profiles inside the C_{60}, which map out the B, for samples 2 and 3 after annealing are extremely similar, demonstrating that the movement of B once in the C_{60}

Fitting Parameter	Sample 1 (1 hour anneal) Si/SiO$_x$/C$_{60}$/CoB(150 Å)/C$_{60}$/Al	
	As-Grown	After Anneal
CoB Thickness (Å)	152.6 ± 0.9	140 ± 1
B% Mass in CoB (%)	12.4 ± 0.1	11.2 ± 0.2
Mean Integrated ρ_M Area ($\times 10^{-6}\text{Å}^{-1}$) ($\propto$ Magnetic Moment)	76 ± 7	109 ± 9
Fitting Parameter	Sample 2 (10 hour anneal) Si/SiO$_x$/C$_{60}$/CoB*(300 Å)/C$_{60}$/Al	
	As-Grown	After Anneal
CoB Thickness (Å)	307 ± 4	312 ± 5
B% Mass in CoB (%)	14.45 ± 0.06	14.2 ± 0.1
Mean Integrated ρ_M Area ($\times 10^{-6}\text{Å}^{-1}$) ($\propto$ Magnetic Moment)	15 ± 5	9 ± 5
Fitting Parameter	Sample 3 (10 hour anneal) Si/SiO$_x$/C$_{60}$/CoB(140 Å)/C$_{60}$/Al	
	As-Grown	After Anneal
CoB Thickness (Å)	142 ± 3	82 ± 7
B% Mass in CoB (%)	13.0 ± 0.2	10.3 ± 0.7
Mean Integrated ρ_M Area ($\times 10^{-6}\text{Å}^{-1}$) ($\propto$ Magnetic Moment)	60 ± 10	108 ± 7

Table 5.5: Comparison of some PNR fitting parameters for samples 1,2 and 3 before and after annealing. In each sample the SiO$_x$, C$_{60}$ and Al thicknesses are 1000 Å, 200 Å and 50 Å respectively. The mean integrated ρ_M area is calculated by taking the average of the integrated area under the ρ_M curve for the 68% upper and lower bounds and the uncertainty is half of the difference between the upper and lower bounds. Sample 1 is fit using Model A and Samples 2 and 3 are fit using Model C. *The CoB target used in Sample 2 is different to the one used for samples 1 and 3.

is consistent for both samples. The magnetisation of this sample measured from SQUID magnetometry was extremely low (< 100 emu/cc) and we see from the SLD profile that this is because of magnetic dead layers that cover almost all of the CoB layer with only the top ≈ 50 Å that has a non-zero ρ_M. The extremely low M_s is also explained by the B

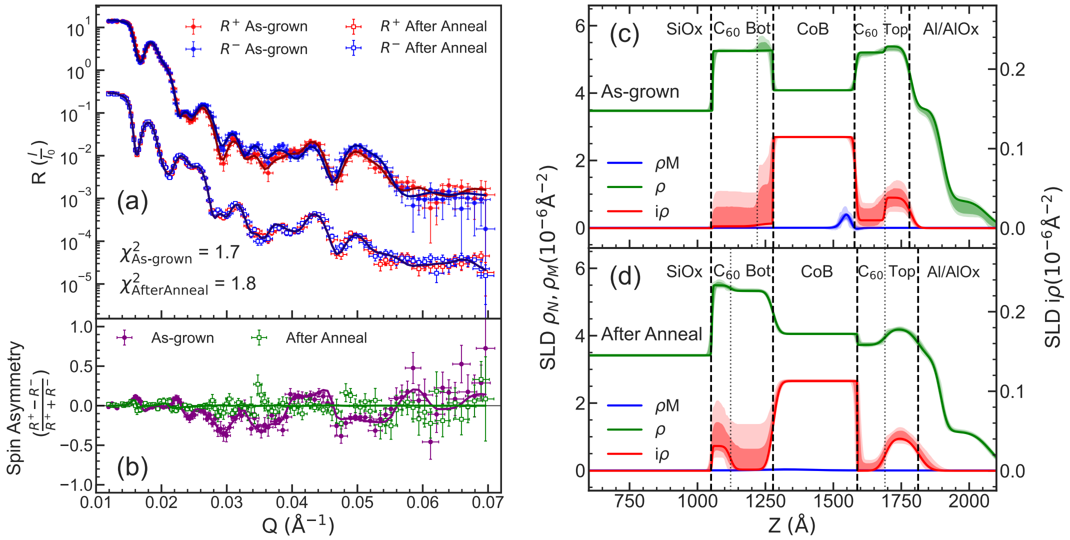

Figure 5.8: PNR data for the C_{60}/CoB/C_{60} sample (Sample 2) before (a) and after (b) a 10 hour anneal at 300°C. The full structure of Sample 2 was Si/SiO$_x$(100)/C_{60}(200) /CoB(300)/C_{60}(200)/Al(50) (thickness in Å). R^+ and R^- represent the spin up and spin down reflectivities respectively. Solid lines are fits to the data using Model C. (b) Spin asymmetry for the as-grown (purple) and after anneal (green) data sets, which is calculated as the difference in the two spin channels divided by their sum. (c) and (d) SLD profiles obtained from the fits using Model C for the as-grown and after anneal data respectively. The blue, green and red lines represent the best fits of the magnetic, nuclear and absorption profiles respectively. The shaded bands represent the σ and 2σ ranges for each profile.

composition. In the as-grown sample, the B mass percentage composition corresponds to an atomic percentage of $(47.9 \pm 0.2)\%$ and Co_1B_1 is nonmagnetic [164, 270]. The dead layers seen in the magnetic SLD profile, highlighted by figure 5.9, could suggest a variable B distribution throughout the layer, meaning that the dead layer area has a higher B concentration, making it no longer ferromagnetic.

Quantitatively, we can compare some important parameters from the fitting models as shown in table 5.5. For Sample 2, we see that, unlike Sample 1 and 3, there is no reduction in the CoB thickness after annealing. There is still a slight decrease in the CoB B% composition after annealing from 14.45 ± 0.06 % to 14.2 ± 0.1 %, however,

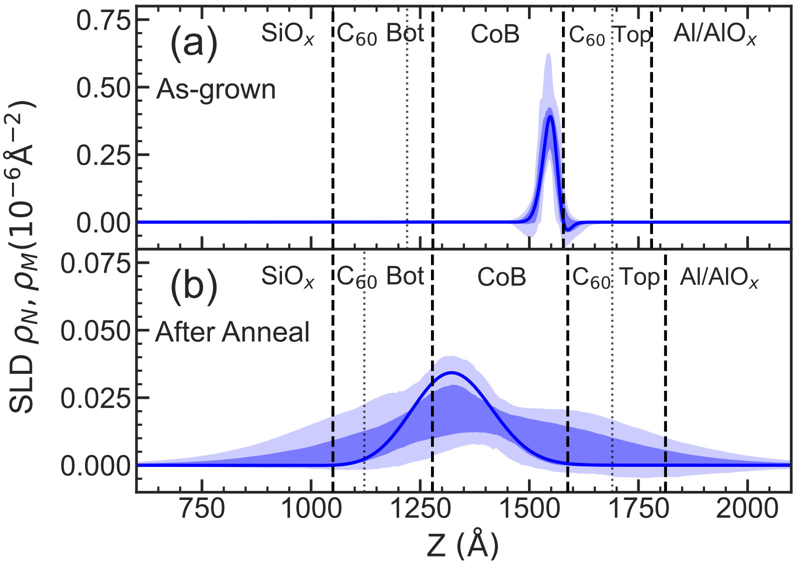

Figure 5.9: Enlarged plots of the magnetic SLD profiles for Sample 2 before and after annealing as originally shown in figure 5.8.

this is much smaller than the reductions observed in samples 1 and 3. The thickness of the CoB layer in Sample 2 is over twice that of Sample 3 so this small reduction in B composition still accounts for a significant injection of B, assuming the lost B migrates into the C$_{60}$ layers. Also, this larger CoB thickness limits the proportion of B that is able to diffuse to the C$_{60}$ layers. As seen in chapter 2, we estimate the diffusion length of B in CoB to be approximately 80 - 100 Å for a 10 hour anneal at 300°C. This means that, for samples 1 and 3 with thinner CoB layers, all of the B is within 1 diffusion length of the C$_{60}$ layers. However, for sample 2, the B in the middle 100 - 140 Å of the layer is further from the C$_{60}$ layers than the diffusion length. This limits the decrease we observe in the B composition of the CoB layer as the B originating in the centre of the layer cannot reach the edges of the CoB layer within the annealing time. Additionally, the changes in magnetisation for Sample 2, given by the integrated ρ_M area, do not follow the same trends as for samples 1 and 3. Here, we see a slight reduction in magnetisation after annealing. Looking closer into the magnetic SLD profile in figure 5.9, we see that the magnetic region is spread out to cover all of the CoB layer after annealing which is an effect also observed in Sample 3, see figure

5.6. This suggests that there are similar changes in magnetic profile between the two samples however, because the initial magnetic moment is so small and the magnetic layer is much thicker in this case, once spread out, the individual moments are below the noise floor and are too small to observe using PNR.

The PNR results of the 3 different samples show that annealing causes the migration of B from CoB into C_{60} films. However, the amount of B migration does vary from sample to sample. In Sample 2, where a different CoB target was used for the growth and the CoB thickness was approximately twice that of samples 1 and 3, the reduction in B composition in the CoB layer is significantly less than for the other samples. In sample 2, the sample thickness is approximately 3 times the estimated diffusion length of B in CoB in our experimental conditions meaning that a smaller proportion of the B can diffuse into the C_{60} layers. In all of the samples, we observe a broadening of the magnetic profile and in samples 1 and 3 there is an increase in the overall magnetisation which is accounted to the reduction in B content of CoB. Also, the SLD profiles for Samples 2 and 3 indicate that, once in the C_{60} layer, the B ions are very mobile and diffuse all the way through the 200 Å C_{60} layers until they reach the substrate or cap interfaces where they congregate. The results also show the suitability and strength of PNR in investigating diffusion structures involving light elements. The final structures are complex but are able to be carefully and reproducibly determined using PNR measurements and sophisticated fitting models.

Comparing the B profiles we observe here with PNR with the theoretical model systems presented in section 2.2, we see significant differences. The theoretical models predict that the B concentration would be larger near the CoB source and decrease further away from the CoB layer. However, in our fitting, we see consistently that the injected B aggregates at the farthest interfaces with the substrate (SiO_x) and cap (AlO_x). This therefore suggests that there are additional forces acting on the B once it is in the C_{60}. This addition force could be due to dipole formation in C_{60}. Negatively charged dipoles have been observed in Co/C_{60} interfaces [53] and in C_{60}-O bonds at a C_{60}/MnOx interfaces [271]. The forces acting on the B ions due to these dipoles would be competing with the Co/C_{60} dipole forcing the B towards the CoB layer, and the dipole due to C_{60}-O bonds forcing the B toward the substrate and cap interfaces. As the sample is only heated from the back of the substrate using the copper heater puck, there is also the possibility of a temperature gradient forming across the sample. This would act as an additional driving force of diffusion, however, this driving force would act in the same direction throughout the depth of the sample so it cannot fully explain the movement of B to both the cap and substrate.

PNR Measurements during Annealing

Using the same 0.7° sample angle and 0.012 Å^{-1} to 0.070 Å^{-1} Q range, PNR is measured throughout the annealing process and is time sliced into data for each hour of the 10-hour anneal. We can use these PNR measurements for Sample 3 to monitor the changes in the sample throughout the annealing process. Because of the time slicing, there are fewer statistics for each data set, meaning there is more uncertainty in the obtained structural parameters. Also, there is added uncertainty as the sample structure is changing consistently during the annealing process. Furthermore, with the sample being at 300°C, the magnetic moment drops below the magnetic sensitivity of PNR, meaning that the R^- and R^+ reflectivities are almost identical. In PNR, the splitting of R^- and R^+ adds extra data which helps to fix certain parameters within the fitting,

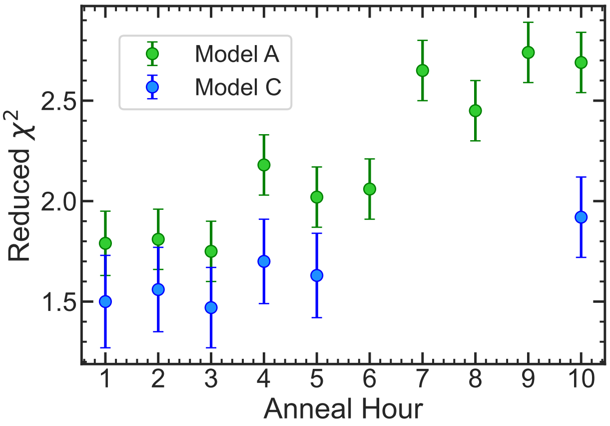

Figure 5.10: Comparison of the χ^2 values for fits on the time sliced during annealing PNR data using Model A and Model C. The χ^2 quantifies the goodness of the PNR fit. Here we see that, for the first 3 hours, the χ^2 values for the two models are within the uncertainty range and as the annealing time increases the fit using Model A gets gradually worse. However, the difference in χ^2 is not large enough to justify the 8 extra fitting parameters that are included in Model C.

such as the magnetic layer thickness and the position of the magnetism within the sample that aids with fitting. Due to all of these reasons, the difference in the χ^2 for the simple slab model (Model A) and the more complex model (Model C) is small, see figure 5.10. The increased uncertainty in the data means that there is not enough information to resolve all the parameters within Model C with any certainty. As the extra fitting parameters don't provide a substantial improvement in the fit, Model A was used for the analysis of these data sets.

Figure 5.11 shows the extracted nuclear and absorption SLD profiles from the fits for each hour of annealing (5.11a) as well as how some specific parameters change over the process (5.11c-d). The density of the top C_{60} layer significantly reduces throughout annealing, following an exponential decay with time. However, as is seen in the fitting results for Sample 3 shown in figure 5.6, B injection into the C_{60} layer increases the nuclear SLD and therefore would act to increase the C_{60} density obtained from fitting. Instead, we account the apparent reduction in C_{60} density over time to metallic Al from the cap intermixing with the top C_{60} layer. This would also explain why the change in density of the two C_{60} layers is asymmetric. In the top C_{60}, the fitted density reduces by ≈ 0.1 g/cc whereas, for the bottom C_{60} layer, the reduction is only ≈ 0.04 g/cc.

As the bottom C_{60} layer is not in contact with the Al cap, there will be no effect due to Al diffusion. There is still some reduction in density over time in the bottom C_{60} layer which also follows an exponential decay. This therefore suggests that in both C_{60} layers there is some contribution to the reduction in density because of a change in ordering or crystallinity. However, the much larger density reduction in the top layer supports the suggestion that there is Al diffusion into the top C_{60} layer.

In the CoB layer, the thickness and B composition decreases linearly with annealing time. As B composition here is a function of the depth (z), the actual total amount of B still with the CoB layer is given by the thickness × B composition. This can be estimated by integrating the area beneath the absorption SLD profile (iρ) which is shown in 5.11. As the CoB thickness and B composition change linearly with time, it follows that the integrated iρ area should show a quadratic time dependence, however, the uncertainties in these values are too large to accurately determine the functional shape.

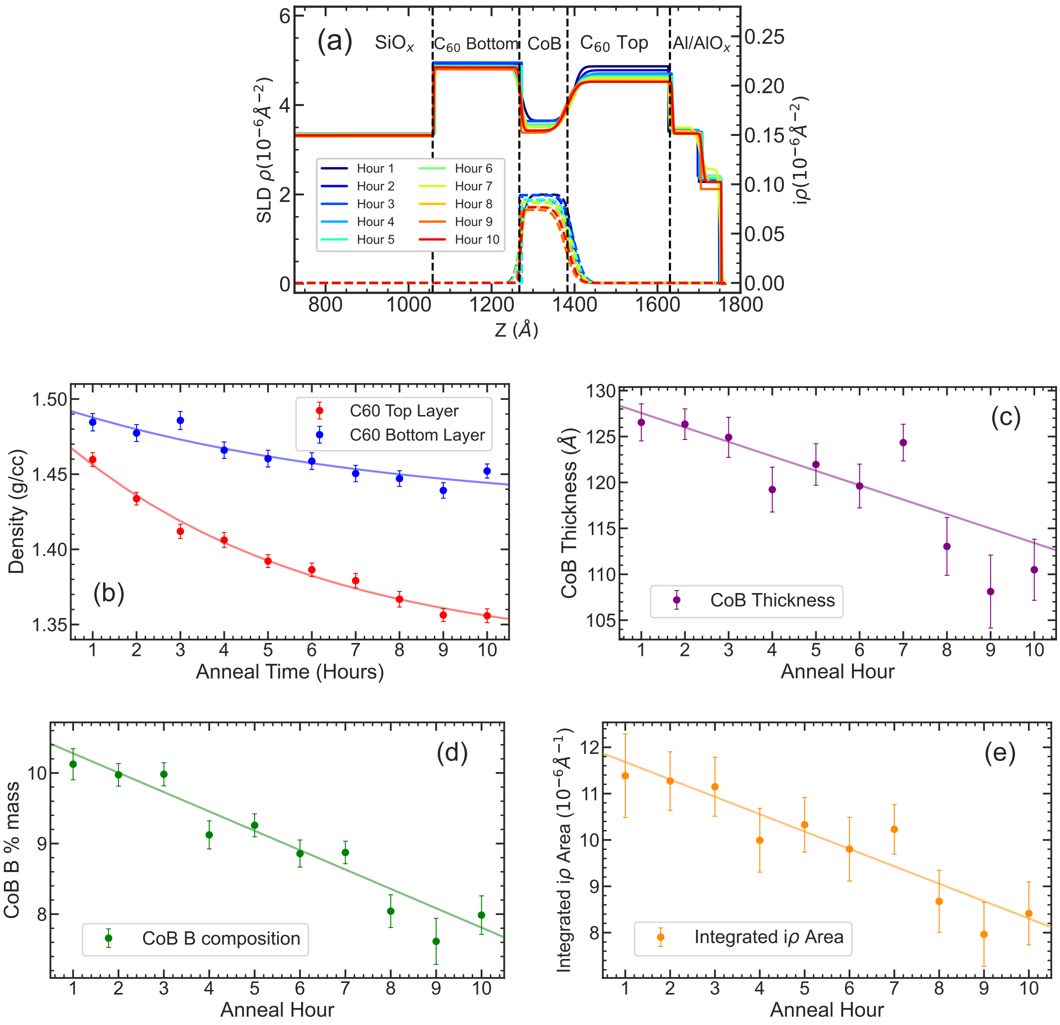

Figure 5.11: Fitting results from the time sliced PNR measured during the annealing process of the C_{60}/CoB/C_{60} sample at 300°C. All fitting was done using a simple slab model. (a) Extracted nuclear SLD (solid lines) and absorption (dashed lines) profiles. (b) Density of the top and bottom C_{60} layers obtained from the fit as a function of annealing time with solid lines showing an exponential fit as a guide to the eye. (c) and (d) show the CoB thickness and CoB B mass composition versus time respectively. (e) integrated iρ area which is proportional to the total amount of B within the CoB layer. Here the solid lines show a linear fit as a guide to the eye.

5.3.5 Ion Beam Analysis

To further study the structural changes due to annealing that occur in our trilayer samples, Time of flight Elastic Recoil Detection Analysis (TOF-ERDA) and Nuclear Reaction Analysis (NRA) measurements were used. These measurements were performed by Eduardo Pitthan and Daniel Primetzhofer at the Tandem Laboratory at Uppsala University. TOF-ERDA was used as it is profiling technique that is specifically sensitive to light elements [250, 253]. The measurements were performed on the samples used in the PNR experiments after they had been measured and annealed. As-grown samples of nominally the same structure, grown around the same time as the PNR samples, were used to compare the before and after annealed structures. The TOF-ERDA data for these samples is shown in figure 5.12. In the data for Sample 3 and the as-grown reference, see (a) and (b), there is little change between the as-grown and annealed profiles outside of slight changes in thickness due to sample-to-sample variation. Notably, the C profile, which corresponds to the two C_{60} layers above and below the CoB layer, appears as one broad peak. This shows that the depth resolution of the TOF-ERDA measurement is a limiting factor as the two C_{60} layers cannot be distinguished when they are separated by around 150 Å. We see that in the data for Sample 2 and its as-grown reference shown in (c) and (d), there are two separate peaks in the C profile as the CoB layer is thicker so the separation distance of the two C_{60} layers is larger.

In the PNR results, we observed a significant increase in the absorption SLD profile in the C_{60} layers after annealing, which is attributed to B migration due to its large neutron absorption cross section. Therefore, in the TOF-ERDA data, we would expect to see a broadening of the B profile after annealing. The comparison between the boron profiles for the two samples before and after annealing can be seen in 5.12e and f. This shows no significant change in the width of the B distribution for either sample after annealing. The lack of observed changes here is rationalised by considering the measurement depth resolution. In the case of the as-grown samples, where we expect all of the B in the sample to be in the CoB layers, the B peak is very broad and, as is shown in figures 5.12a and c, crosses over well into the C_{60} layers. This shows that the layers in our samples are too thin, and the structural changes occur on a scale that is too small to be observable in TOF-ERDA measurements.

NRA measurements were also performed on the same samples as used in the ERDA

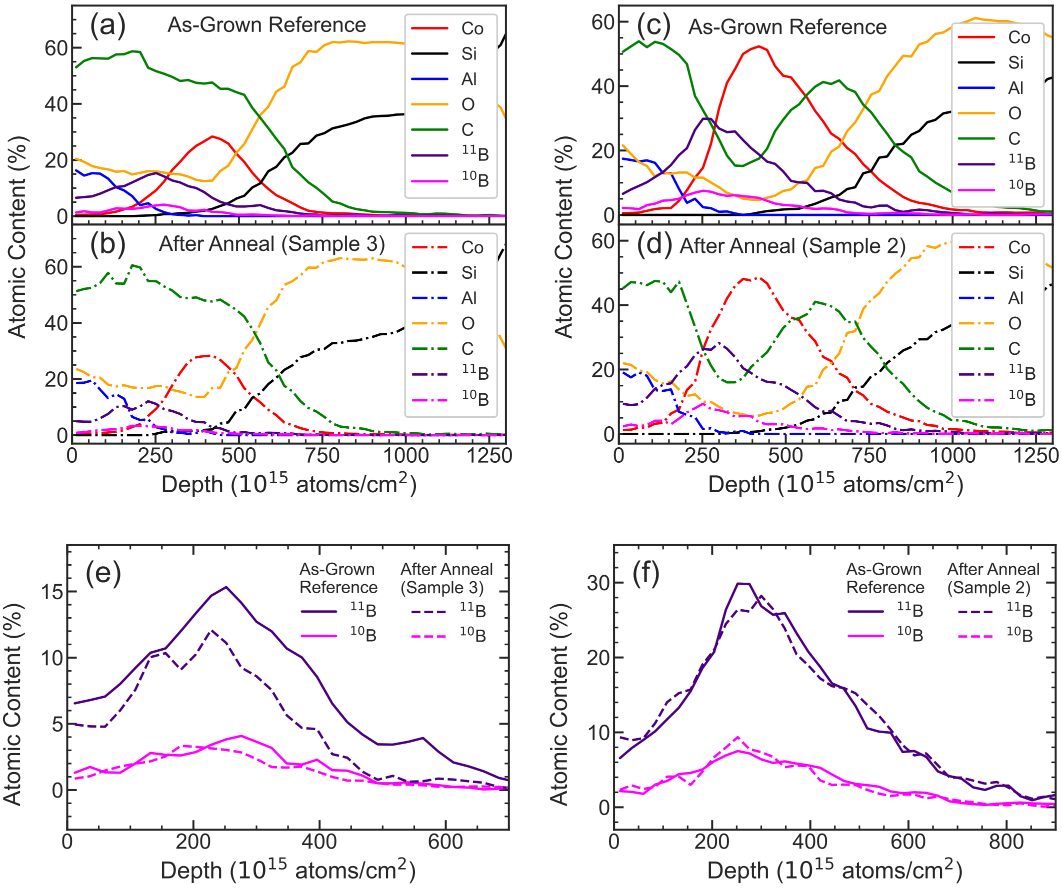

Figure 5.12: TOF-ERDA data measured on Samples 2 and 3 from the PNR experiment after annealing compared against as-grown samples of nominally the same structure. The structure of Sample 3 is Si/SiO$_x$(1000)/C$_{60}$(200)/CoB(140)/C$_{60}$(200)/Al(50) (thickness in Å) and the structure of Sample 2 is Si/SiO$_x$(1000)/C$_{60}$(200)/CoB(300)/C$_{60}$(200)/Al(50) (thickness in Å). The ERDA profiles in (a)-(d) show the elemental specific depth profile for each sample. (e) and (f) are zoomed in to show the comparison of the ^{11}B and ^{10}B profile before and after annealing. The data was collected using a ^{127}I^{8+} 36 MeV ion beam. The measurements and data processing were performed and by Eduardo Pitthan and Daniel Primetzhofer at the Tandem Laboratory at Uppsala University. The figure plotting and subsequent discussion was by the author.

measurements. This measurement is specifically measuring the depth and quantity of ^{11}B in the sample. The NRA data collected for Sample 3 can be seen in figure 5.13. The black data is from a B thin film on a C substrate which is used to show the energy at which the peak would appear if the B is on the surface of the sample. The higher the energy, the deeper into the sample the B is located. In figure 5.13b, the two data sets have been normalised by the integrated area under the curve between 155 and 185 keV under the assumption that the total amount of boron in the sample is equal. This comparison shows a broadening of the peak and a reduction in the central intensity after annealing. The centre of the peak corresponds to the CoB layer so this data suggests a reduction in the B content of the CoB layer, as is also shown repeatedly in the PNR data. The broadening can be quantified by fitting a Gaussian function to the peaks. The FWHM of the as-grown and after anneal peaks are found to be 7.7 ± 0.2 keV and 8.5 ± 0.2 keV respectively. The broadening of 0.8 keV indicates that the B has spread out within the sample, supporting the evidence of it diffusing into adjacent

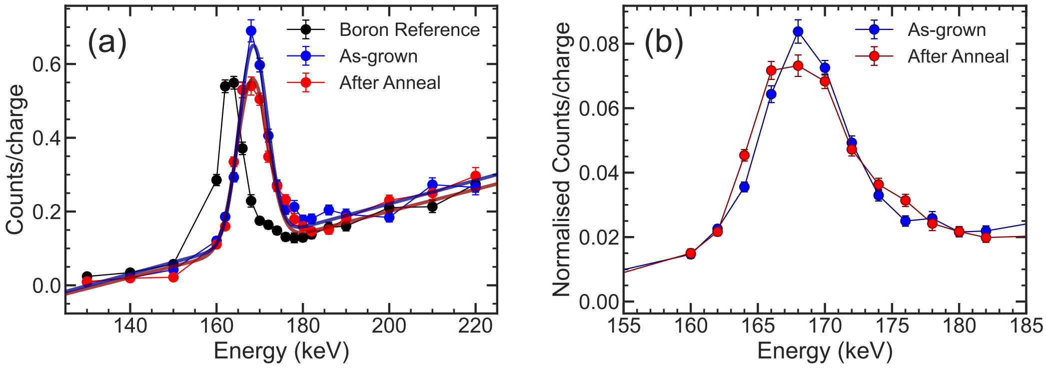

Figure 5.13: NRA (Nuclear Reaction Analysis) data measured on Sample 3 after annealing (structure of Si/SiO$_x$(1000)/C$_{60}$(200)/CoB(140)/C$_{60}$(200)/Al(50) (thickness in Å)) and an as-grown sample of nominally the same structure. (a) Full range of the ^{11}B(p,α)^{8}Be excitation curves. The black data is for a reference sample of a thin B film (<100 Å) on C substrate to show the excitation energy of B on the surface of the sample. (b) Data is normalised to the integrated area under the curve between 155 and 185 keV under the assumption that the total B content in each sample is the same. Measurements were performed by Eduardo Pitthan and Daniel Primetzhofer at the Tandem Laboratory at Uppsala University.

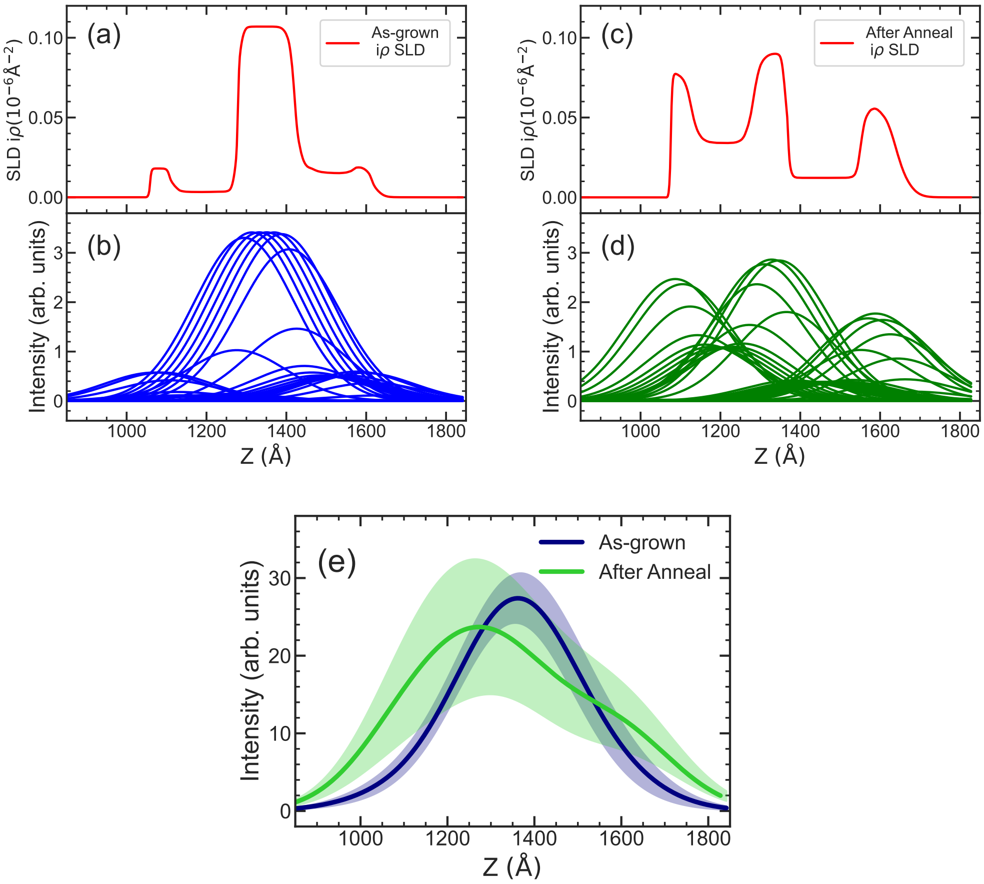

Figure 5.14: Demonstration of how a 250 Å broadening is applied to the PNR absorption curves to compare to the NRA data. (a) and (c) show the as-grown and post annealed absorption SLD profiles respectively. (b) and (d) show Gaussian curves calculated every 20 Å through the profile with a peak width of 250 Å and an intensity proportional to the magnitude of the absorption SLD. (e) Results of summing all of the Gaussian curves for the as-grown (blue) and after anneal (green) data. The error bands are calculated by performing the same analysis on the σ upper and lower bounds from the SLD profiles. This plot shows the as-grown and after annealed absorption SLD profiles with a 250 Å broadening applied.

layers. In terms of thickness, the resolution of this measurement is around 250 Å which explains why the changes between the as-grown and annealed samples are small.

To compare the NRA data to the PNR SLD profiles, we apply a 250 Å broadening to the absorption SLD profile. This is done by calculating a Gaussian curve with a 250 Å peak width and an area proportional to the magnitude of the nuclear absorption SLD for many points along the SLD profile. These curves are then summed to form the superposition representing how we expect to observe the B profiles with a 250 Å resolution. This analysis is shown in figure 5.14. The uncertainty bands are calculated by performing the same analysis on the 1σ upper and lower bounds from the SLD profiles, shown by the dark red shaded region in figure 5.6d. The comparison of the broadened as-grown and after anneal $i\rho$ SLD profiles in 5.14e shows a similar relationship to that observed in the NRA data. In both, the after anneal peak has a larger width and a reduced peak height. However, the size of the changes seen in the NRA data are much smaller. In the broadened PNR SLD profiles, the FWHM increases from 380 ± 40 Å before annealing to 560 ± 10 Å after annealing, meaning the peak width increases by 47% compared to the 10% increase observed in the NRA measurements.

The same analysis and comparison between the NRA data and the PNR SLD profiles was done for Sample 2, see figure 5.15. For this sample, the NRA peaks for the as-grown and annealed samples are almost identical. Between the as-grown and annealed samples, there is a slight reduction in peak amplitude and an increase in FWHM from 8.6 ± 0.1 keV to 8.9 ± 0.2 keV. The corresponding broadened PNR SLD profiles show a similar change with an increase in FWHM from 460 ± 2 Å to 487 ± 1 Å. However, these changes are noticeably smaller than those seen in Sample 3. Sample 2 contains a thicker CoB layer of 300 Å, compared to the 140 Å layer in Sample 2, so this will dominate the NRA data. Also, from the PNR fitting, we see that there is a smaller reduction in B composition in the CoB layer of this sample which we account to the layer thickness being over 3 times larger than the estimated diffusion length of B in CoB to be 80-100 Å for our annealing conditions. This means that we expect the effects of B diffusion to be harder to observe in this sample. The same trends are seen in the broadened SLD profile where there is a peak broadening and reduction in amplitude after annealing, but the changes are much smaller compared to Sample 3. The similarities in the NRA data and the broadened SLD profiles suggest that the small changes in the B profile observed in the NRA data due to annealing are real. However, again, the depth resolution limits the analysis of the B profile within our samples.

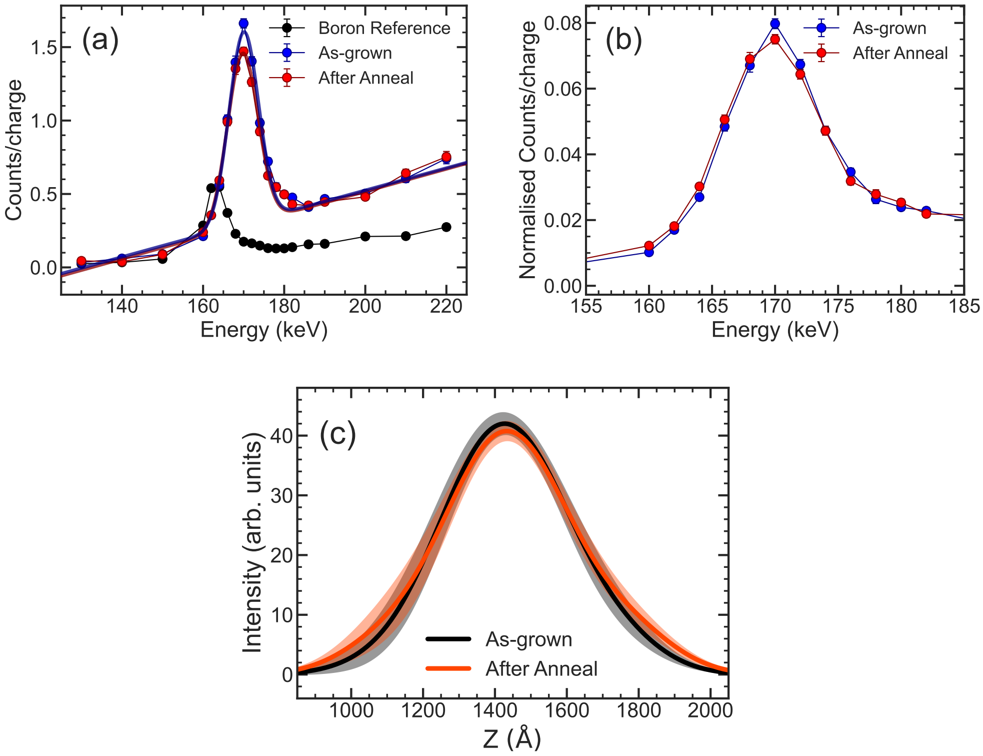

Figure 5.15: (a) and (b) NRA (Nuclear Reaction Analysis) data measured on Sample 2 after annealing (structure of Si/SiO$_x$(1000)/C$_{60}$(200)/CoB(300)/C$_{60}$(200)/Al(50) (thickness in Å)) and an as-grown sample of nominally the same structure. (a) Full range of the ^{11}B(p,α)^{8}Be excitation curves. The black data is for a reference sample of a thin B film (<100 Å) on C substrate to show the excitation energy of B on the surface of the sample. (b) Data is normalised to the integrated area under the curve between 155 and 185 keV under the assumption that the total B content in each sample is the same. Measurements were performed by Eduardo Pitthan and Daniel Primetzhofer at the Tandem Laboratory at Uppsala University. (c) As-grown and after anneal absorption PNR SLD profiles with a 250 Å broadening applied. The methodology for calculating this was the same as shown in figure 5.14.

5.4 Comparing Annealing Temperatures

5.4.1 Introduction and Note on Gated Measurements

The following section presents some of the results of attempted in-situ gated PNR measurements. In the previous sections of this chapter, it has been shown that it is possible to inject B into a C_{60} layer from an adjacent CoB alloy layer by annealing. To move towards device applications, measurements were performed using gate voltages to attempt to manipulate the B ions within C_{60} layers.

For this experiment, the sample structure is changed slightly to add a thick Nb layer underneath a C_{60}/CoB/C_{60} trilayer. This is used as an electrode to apply voltages to. The final sample structure used is Si/SiO$_x$(1000)/Nb(1000)/C_{60}(280)/CoB(170)/C_{60}(280)/Al(30) (thickness in brackets in Å). Nb was chosen as the metal to contact to because of its good SLD contrast with C_{60}. Also, it has no neutron absorption component which is important as the absorption is used to map out the B location in the final SLD profiles. These facts were verified using Refl1D simulations with a layer of Nb added below the trilayer structure. Other metals, such as Pt, Au and Cu, were also simulated in the structure in place of the Nb layer but it was found that either they have a nuclear absorption and or the nuclear SLD was too similar to that of C_{60}.

To avoid metallic Al diffusing into the top C_{60} layer, as was observed in the previous set of samples, the Al cap thickness here was reduced to 30 Å. This change was made to ensure that the vast majority of the cap oxidises when the sample is brought out of vacuum and to reduce the metallic Al content. Furthermore, the C_{60} layers were made thicker, from 200 Å to 280 Å. Thicker layers contribute higher frequency fringes in the reflectivity measurements and therefore produce more fringes at a lower Q value which aids in the fitting. The diffusion length of B in C_{60} is expected to be of the order of 10^{-4} m in our experimental conditions meaning that the B is still able to diffuse through the whole layer. The layer thicknesses were limited to 280 Å due to time constraints with growing samples to ensure all the layers could be deposited on the same growth day.

In these experiments, the same vacuum furnace as for the previous measurements was used. A new sample holder was developed by the sample environment team at ISIS that allowed for electrical contact to be made with the Nb layer and apply voltages, with the furnace itself acting as the ground to form a floating gate. Figure 5.16 shows

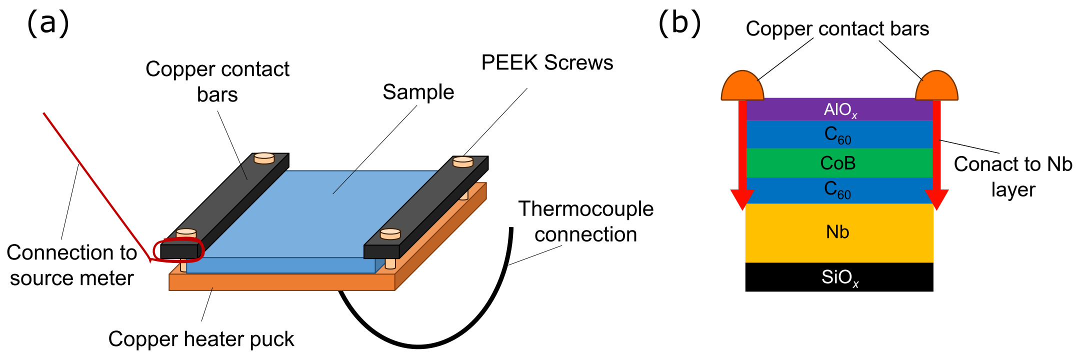

Figure 5.16: (a) Schematic of the sample holder used to allow for heating of the sample as well as applying gate voltages in situ. (b) Sample structure used for the gated measurements. Electrical contact is made to the Nb layer that is below the C$_{60}$/CoB/C$_{60}$ trilayer.

a schematic of the sample holder. Copper contact bars press down on the sample to make electrical contact.

After this experiment was conducted, it became apparent that the gating geometry would not lead to a significant potential difference across the sample as desired. Figure 5.17 demonstrates the geometry of the gating contacts and the sample and where the resultant potentials were. From this figure, we can see that the voltage V output by the source meter results in the Nb and CoB layers being at the potential V. The copper heater puck that sits underneath the Si/SiO$_x$ substrate is grounded. This means that the potential difference in the sample lies across the Si/SiO$_x$ substrate from the Nb layer to the copper heater puck. Any leakage currents that were observed during the measurements, therefore, were due to currents flowing from the Nb layer, through the Si/SiO$_x$ substrate to the heater puck and ground.

This means that the PNR measurements performed using a gate voltage do not allow for the investigation of gate controlled B diffusion in the C$_{60}$ layers and, because of this, the voltage measurements have been omitted from this thesis. However, during this experiment, annealing of the sample was performed at 200°C and 250°C for 10 hours and these different annealing temperatures are still interesting to compare to the measurements presented previously in this chapter where the annealing temperature

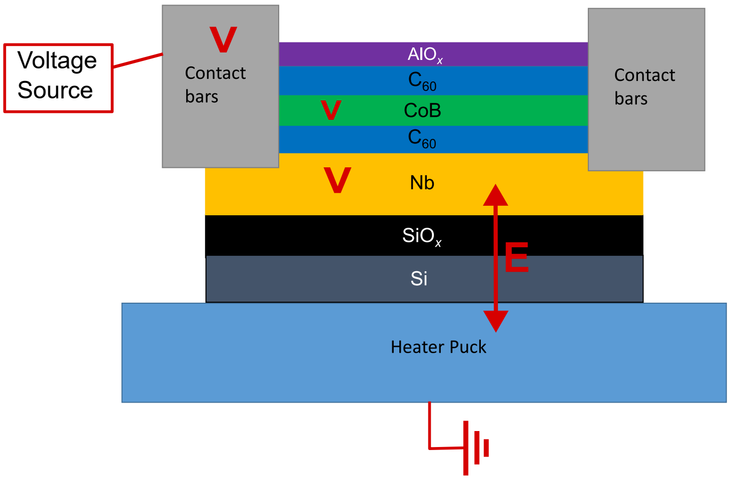

Figure 5.17: Experiment geometry for attempted gated PNR measurements. V represents the parts of the sample that are at the voltage that is output by the voltage source. The heater puck is grounded which means that the potential difference in fact lies over the Si/SiO$_x$ substrate.

was 300°C.

The contact bars are attached to the sample holder using PEEK (Polyetheretherketone) screws which are electrically insulating and ensure that the bars do not short to the copper puck that the sample sits on. The PEEK screws can only operate up to 250°C which did limit the annealing temperatures that were used in this experiment.

5.4.2 Reflectometry Results

Before annealing the sample, a wide Q range PNR measurement of the sample was taken to be used as a baseline to compare future measurements to. This measurement involved two sample θ angles, 0.5° and 1.2°, which resulted in a maximum Q of 0.11 Å^{-1}. In typical PNR measurements that involve multiple sample angles, the data from all the angles is stitched together to produce one complete data set. However, during the data collection, it was noticed that the alignment peaks were very broad, indicating a significant amount of diffuse scattering. The force applied by the contact bars on the sample holder acted to bend the sample slightly, which caused diffuse scattering to occur. Stitching together multiple sample angles when there is a significant amount of diffuse scatter will lead to artefacts in the PNR data. In this case, the data sets for the different angles can be extracted separately and then co-fitted using the same model structure and different instrument parameters. The PNR data and fits for the as-grown sample can be seen in figure 5.18a. These fits were performed using Model A as described in the previous sections, but now with a 1000 Å Nb slab inserted between the SiO_x substrate and the bottom C_{60} layer. XRR measurements of the sample were also taken to verify the sample structure. The fit for this using the same model as for the PNR data is shown in figure 5.18c. The χ^2 for the fit of the XRR data is noticeably much higher than that of the PNR measurement. However, qualitatively, we can see that the fit line closely matches the raw data. Due to the much greater flux in XRR measurements, the overall measured intensity is greater and therefore the relative error in the counts is very small as the uncertainty in counting experiments is calculated by $\sqrt{n}$. This means that the calculated χ^2 value for XRR measurements is larger than that of PNR measurements because there is a smaller tolerance.

The SLD profiles for the PNR and XRR data in figure 5.18 show that there is some good agreement in the structure extracted from the two fits. The parameters with the largest differences are the C_{60} layer thicknesses and the C_{60} densities. The difference in the thickness of the top C_{60} layer could be accounted for by the discrepancy in the AlO_x cap thickness. Figure 5.18 highlights the large difference in the Q range of the two measurement techniques. The much larger flux generated by x-ray sources means that it is possible to get a substantial measured intensity up to high Q in short 30 minutes to 1 hour measurements. This means that XRR measurements are more sensitive to thinner layers in the sample that cause longer wavelength oscillations in the reflectivity data. The comparison of the PNR and XRR SLD profiles in figure 5.18c and d also demonstrates graphically the difference in the scattering strength between the two measurement techniques.

The first anneal of the sample was at 200°C for 10 hours. After the sample had returned to room temperature, PNR was measured with 0 V applied and then with positive and negative gate voltages. To further add B into the C_{60} layers, the sample was annealed again at 250°C for 10 hours after which measurements were taken with no gate voltage and with positive and negative gate voltages. In the case of the 200°C anneal, PNR data was only measured for 2 hours for each of the gate voltages whereas for the measurements taken after the 250°C anneal, data was measured for 10 hours

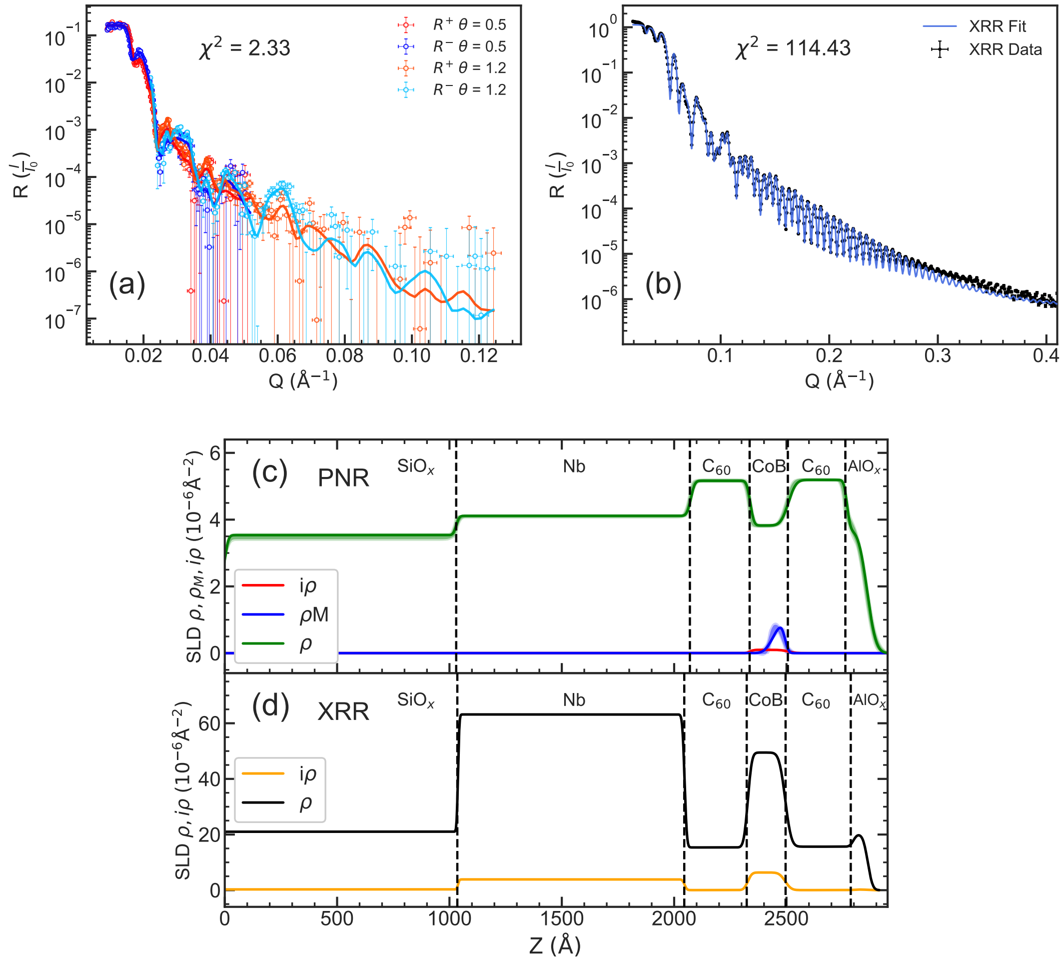

Figure 5.18: (a) PNR data for the as-grown gating sample (Si/SiO$_x$(1000) /Nb(1000) /C$_{60}$(280) /CoB(170) /C$_{60}$(280) /Al(30) (thickness in brackets in Å)). The data is split into individual sample angles that are cofit with all the same structural parameters but different beam parameters. (b) XRR data for the same sample. The solid lines show fits to the data. (c) and (d) are the SLD profiles extracted from the fits in (a) and (b) respectively. In (c), the blue, green and red lines represent the best fits of the magnetic, nuclear and absorption profiles respectively. In (d), the black line shows the nuclear SLD and the yellow shows the absorption SLD. The shaded bands represent the σ and 2σ ranges for each profile.

Layer	Thickness (Å)		Roughness(Å)		Density (g/cc)*	
	PNR	XRR	PNR	XRR	PNR	XRR
SiO_x	1028(5)	1038.12(9)	11(5)	4.851(5)	2.21(3)	2.44997(3)
Nb	1043(4)	1008.52(1)	14(3)	8.090(5)	8.96(3)	8.4544(9)
C_{60} Bot	264(1)	281.37(2)	12(3)	14.249(8)	1.550(7)	1.807(2)
CoB	168(2)	166.40(3)	25(3)	21.28(1)	11.6(2) %B	10.34(2) %B
C_{60} Top	260(5)	303.22(6)	11(5)	12.93(7)	1.559(5)	1.838(2)
AlO_x	91(2)	64.21(6)	34(5)	16.94(2)	2.7(2)	2.381(6)

Table 5.6: Comparison of the structural parameters obtained from the XRR and PNR on the Si/SiO_x(1000)/Nb(1000)/C_{60}(280)/CoB(170)/C_{60}(280)/Al(30) (thickness in brackets in Å) sample used for the gated PNR measurements. In the table, the numbers in brackets are the uncertainties in the last digit of the value. The fits are shown in figure 5.18. *For the density column of CoB, the value gives the mass composition percentage of B.

with no gate voltage and 8 hours with positive and negative voltages. Therefore, for the analysis, the focus will be on the data after the 250°C anneal, using the 200°C to support and verify the observations.

PNR Anneal Temperature Comparison

To compare the annealing temperature dependence on the injection of B into C_{60} we can use the 0 V measurements after the 200°C and 250°C annealing processes. The PNR data and fits, along with the extracted SLD profiles for the data of the as-grown sample and after both annealing processes can be seen in figure 5.19. For these fits, an updated version of Model C was used with a Nb layer inserted in between the SiO_x and bottom C_{60} layer. Unlike the results presented in the previous chapter, there is no significant decrease in the density and SLD of the top C_{60} layer after the sample is annealed. In the samples used for the measurements presented in figure 5.19, the cap thickness was reduced to ensure that the whole cap would oxidise. This supports the idea that the apparent decrease in density observed in figure 5.6 was due to Al diffusion from the cap. Not only does this help in understanding the changes after annealing seen in the previous results, but this confirmation of the diffusion of Al into C_{60} is important for optimising future device structures and furthers the understanding of metal diffusion

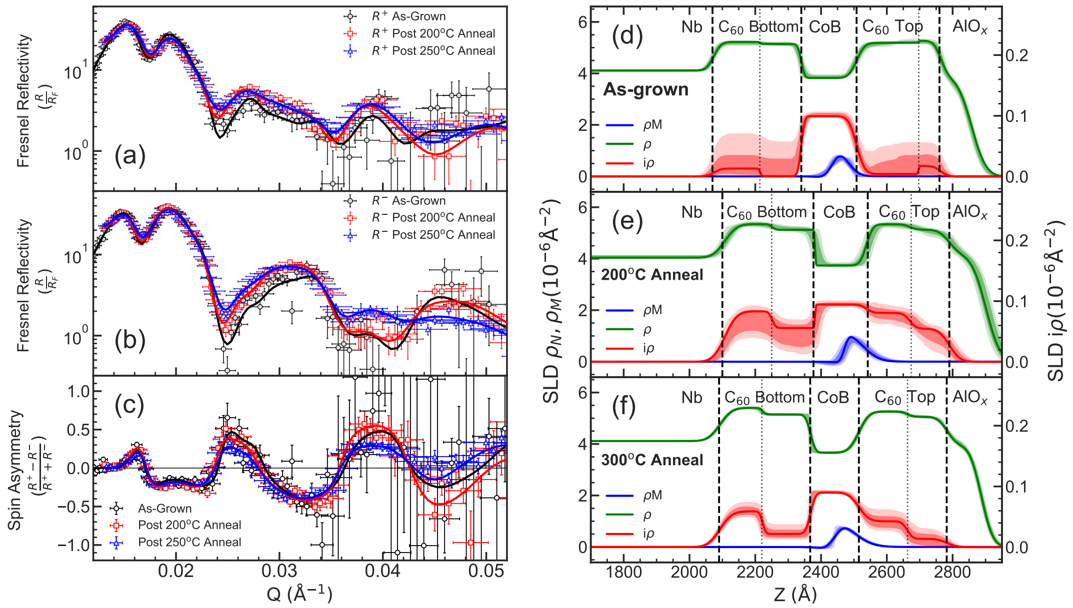

Figure 5.19: PNR data for a Nb/C_{60}/CoB/C_{60} sample after a 10 hour anneal at different temperatures. (a), (b) and (c) show comparisons of R^+, R^+ and spin asymmetry data respectively for the as-grown sample and after annealing at 200°C and 250°C respectively. Solid lines are fits to the data. Extracted SLD profiles for the sample under 0 V, -22 V and 100 V can be seen in (d), (e) and (f). The blue, green and red lines represent the best fits of the magnetic, nuclear and absorption profiles respectively. The shaded bands represent the σ and 2σ ranges for each profile.

in C_{60}. In the R^+ and R^- PNR data we can see that there is a substantial change from the as-grown sample to the post 200°C anneal data with a more subtle change between the post 200°C and 250°C curves. This gradual change between the post 200°C and 250°C anneal data sets is apparent in the SLD profiles. The SLD profiles show that before any annealing there was limited B in the C_{60} layers, but after both annealing processes, a significant amount of B has migrated from the CoB layer as was expected following our previous measurements. However, an interesting result here is that, for both annealing steps, the B in the top C_{60} layer is concentrated at the CoB interface. This is different to the observations seen in section 5.3.4 where the B in the top C_{60} layer was concentrated at the cap interface. As the cap was changed for this sample and we have seen that there is significantly less Al diffusion in this sample, this could suggest that the diffusive driving force that acted to force the B to the top interfaces seen in the results in section 5.3.4 was in fact due to the cap. The B profiles seen in the bottom C_{60} layer in figure 5.19 are much more similar to those seen in section 5.3.4. This consistency in the B profiles provides more evidence that there is an additional driving force that is acting on the B, producing B profiles that are significantly different from the theoretical model systems derived in section 2.2.

Figure 5.20 shows a comparison of some of the important parameters from the fits for the as-grown and two post anneal data sets. The CoB thickness and B composition fall

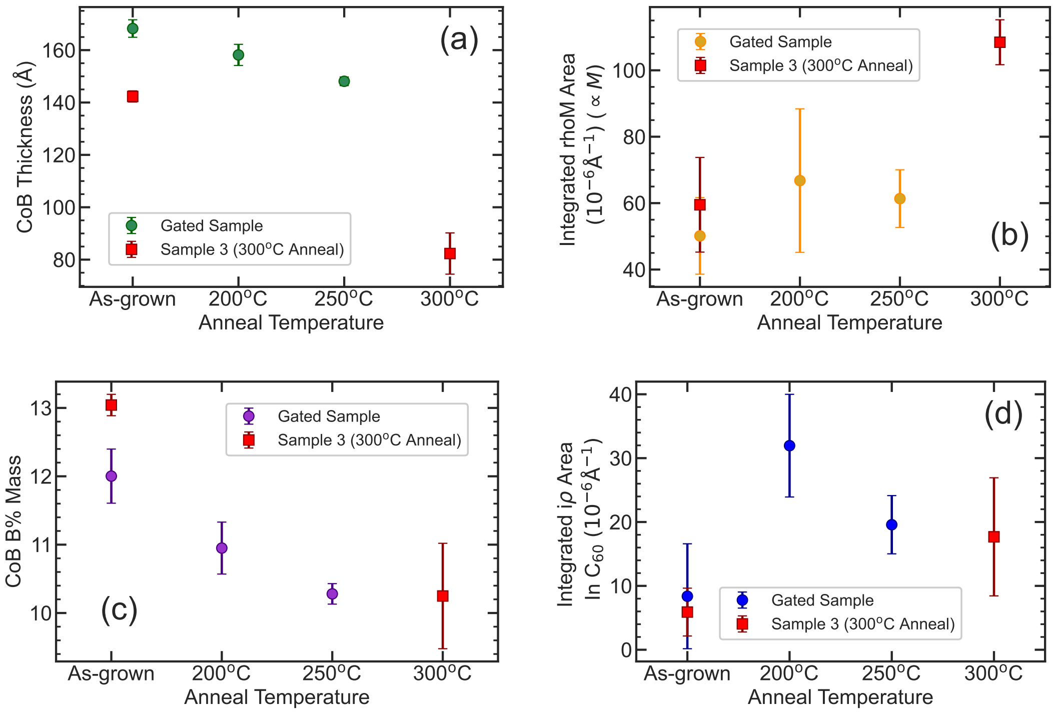

Figure 5.20: Annealing temperature dependence of chosen PNR fitting parameters. (a) and (c) show the CoB layer thickness and B% mass respectively. (b) The integrated ρ_M area after the different anneal steps. This is found by integrating the area under the blue curves in figures 5.19d-f, with the error given by the upper and lower limits of the 1σ range. This gives a measure of the magnetic moment per unit area of the sample. (d) is the integrated $i\rho$ area in the C_{60} layers, which represents the amount of injected B. The red squares show data from Sample 3 from the 300°C anneal measurements as originally shown in figure 5.6.

with the annealing temperature, suggesting that the amount of B injected into the C_{60} layers increases as the annealing temperature increases. This is to be expected as with a greater annealing temperature the B ions will have more kinetic energy and therefore more of the ions can overcome the energy barrier to migrate into the C_{60} layers. Still, the decrease in CoB thickness for the 200°C and 250°C annealing processes was much less than the decrease observed after the 300°C anneal.

There is a slight increase in the magnetisation of the sample as the annealing temperature is increased, however, the change is within the uncertainty range. This is noticeably different from the results of the 300°C anneal where the increase in magnetisation was 80%. The integrated iρ area in the C_{60} (d) quantifies the amount of B that is injected into the C_{60} layers. This was calculated by integrating the area under the iρ SLD profile for the whole sample and subtracting the integrated area under the CoB layer. As mentioned earlier, it was not possible to feed this information back into the fitting algorithm so the total amount of B in the sample before and after annealing is not conserved in the fitting models. This is why the large value of the injected B after the 200°C anneal is possible. Also, although the amount of injected B is slightly lower for the 300°C anneal than the 250°C anneal, the amount of B in the as-grown sample was larger in the gated sample than in Sample 3 due to the CoB thicknesses. The total integrated iρ area, which quantifies the total amount of B, was $(26 \pm 8) \times 10^{-6}\text{Å}^{-1}$ for the as-grown gated sample and $(20 \pm 4) \times 10^{-6}\text{Å}^{-1}$ for the as-grown Sample 3 measurement. This could explain why there is a greater amount of B injected into the C_{60} after the 250°C anneal when the other parameters suggest that the injected should be greater after the 300°C anneal.

The comparison between the results of the 200°C, 250°C and 300°C anneal shows that, although the same changes in the sample structure and magnetism are observed for all temperatures, the magnitude of these changes is substantially greater for the 300°C anneal.

5.4.3 Improvements Required for Gated Measurement

The issue with our measurement geometry for the gated PNR measurements was that the potential difference produced was not across the C_{60}/CoB/C_{60} trilayer and instead was across the Si/SiO_x substrate. This issue would be solved by adjusting the sample structure such that the contact was made to the top of the trilayer. The reason that no contact was made to the top of the sample in our experiments was that this is difficult to do when using molecular layers. Due to the low density of the molecular layers, any bonds or contacts made on top will punch through the molecular layers. Typically, to solve this issue, a metal layer would be grown on top of the low-density material that is sufficiently thick, around 1000 Å, so that the bond or contact would not pierce through. However, due to the large cages of carbon in the C_{60} matrix, metals grown on top are strained. The effects of strain increase as the thickness of the metal layer increases. This means that if a thick layer of metal is grown on top of the C_{60} layer the metal will become extremely rough and flakey. Also, adding more layers to the structure adds more parameters to the PNR fitting and, consequently, more uncertainty to the fitted structure and B distribution within the CoB and C_{60} layers. Future work should start by optimising a method to contact to the top of the sample such that the electric field acts across the C_{60}/CoB/C_{60} trilayer.

5.5 Chapter Summary

In conclusion, the ionic diffusion of B in molecular thin film C_{60} has been investigated using in-situ annealing PNR measurements, SQUID magnetometry, and ERDA and NRA ion beam analysis techniques. The motivation for this is to analyse the potential of using C_{60} instead of ionic liquids as a host for ionic diffusion in gate-controlled devices. In this context, using molecular thin films offers a range of advantages such as in-situ ultra-high vacuum deposition, wider temperature range of operation and nanofabrication capabilities.

It was seen that annealing trilayer C_{60}/CoB/C_{60} samples at 300°C caused B to migrate from the CoB alloy into the C_{60} layers and diffuse through them until the substrate and cap interfaces were reached. This was observed in PNR fitting, see figure 5.6, in which the B profile can be mapped out using the absorption SLD due to the unique neutron absorption cross-section of B. The aggregation at the substrate and cap interfaces demonstrates that there are additional driving forces acting on the B once in the C_{60}, which could be explained by dipole formation in C_{60} interfaces. The migration of B also resulted in a large increase in magnetisation for this sample which was confirmed again using SQUID magnetometry. Using the in-situ vacuum furnace on the POLREF beamline, we were able to observe the changes in the sample during the annealing process which showed the B composition of the CoB reducing over time. In these measurements, the density of the top C_{60} layer decreases over time, and significantly more than the bottom C_{60} layer, which indicated that metallic Al from the cap was diffusing into the top layer.

In SQUID magnetometry measurements, the CoB sample showed a significant increase in moment during annealing at 300°C which is further evidence of the B migration. Comparing the heating and cooling curves for both the CoB and Co samples we see a change in the temperature dependence of the moment for the CoB sample after annealing which is not seen in the Co sample. This demonstrates that the changes in the sample before and after annealing are due to the B addition to Co and therefore corroborate the B migration observed in the PNR measurements.

To move towards device applications, future work should focus on controlling the diffusion of ions within C_{60} using gate voltages. Our experiments demonstrate the ability to measure PNR within a sample holder that allows for gate voltages to be applied. Although our sample geometry did not allow for such an investigation, the sample environment can be used successfully without negatively impacting the measured PNR data and could therefore be used for future experiments.

CHAPTER 6

In-situ FMR-PNR Measurement Technique

6.1 Introduction

In this part of the project, we attempt to measure the induced precession of the magnetisation of a sample due to ferromagnetic resonance (FMR) using polarised neutron reflectometry (PNR). FMR is a technique that can give information about a sample or material's magnetisation dynamic properties e.g. Gilbert damping, and static magnetic properties such as the magnetisation and anisotropy. However, conventional FMR measurements can only inform us of the bulk properties of the sample - there is no spatial resolution. PNR is a measurement technique that is used to measure the in-plane magnetisation profile through the depth of a sample and is specifically sensitive to interfacial magnetism. By performing these two techniques in tandem, we aim to combine the benefits of both to determine depth-dependent magnetisation dynamics.

6.2 Aligned Magnetisation and Neutron Polarisation Geometry

6.2.1 Introduction to the Method

In this section, the methods and results of the experiment in which we aim to measure a change in magnetisation due to FMR precession in a half-polarised PNR measurement geometry will be described. A half-polarised PNR geometry means that only two spin states are measured + and -. In this geometry, the PNR measurement is only sensitive to the in-plane magnetisation components of the measured sample that are parallel to the neutron polarisation; hence, there is no sensitivity to the magnetisation angle. Therefore, the resonant precession of magnetic moments under FMR must be measured as a reduction in the projected magnetisation component parallel to the neutron polarization as shown in figure 6.1.

6.2.2 Sample Development/Characterisation

For this experiment, a sample structure of Si/SiOx/Ru(38)/Co(48)/[Ru(12)/Co(48)]x9 /Ru(38) (thicknesses in Å) was used. A multilayer structure provides some advantages for this experiment compared to a single thick film of magnetic material. By using this structure, we can introduce many interfaces into the sample whilst still ensuring that there is a large amount of magnetic material to aid in FMR measurements. The more

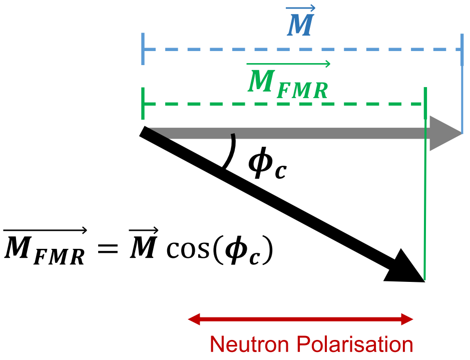

Figure 6.1: Cartoon demonstrating how the FMR precession can be observed when measuring only the sample in-plane magnetisation component parallel to the neutron guide field. In resonance, the cone angle means that the projection of the magnetisation along the neutron polarisation axis is reduced to Mcos(ϕ_c).

magnetic material there is in the sample, the larger the microwave absorption and therefore, the FMR absorption peaks are easier to observe with lower measurement sensitivity. As PNR is sensitive to changes in magnetic and nuclear structure, introducing more interfaces means that there are more features of interest in the PNR data which helps to accurately model the sample structure and magnetism when performing the fitting. Also, repeated interfaces mean that any interfacial effects will be amplified as the effect is repeated at each interface through the multilayer. This can be shown using Refl1D simulations comparing the differences in spin asymmetry between on and off states for a Co/Ru multilayer and a single Co layer of the same total thickness, as shown in figure 6.2. For each sample structure, the difference in on and off resonance spin asymmetry is calculated by simulating PNR data using magnetisation values of 1400 emu/cc for the off state and $1400\cos(5^{\circ}) = 1395$ emu/cc for the on resonance state, where 5° is the cone angle that was used. Each structure contains the same total amount of Co with the same magnetisation. Yet, it is clear from the simulation results that the differences between the on and off states for the same cone angle are much more significant in the multilayer sample. Ru is used as the non-magnetic spacer layer between the Co layers to utilise the ferromagnetic RKKY coupling and make the independent Co layers act as 1 bulk magnetic layer. The RKKY coupling of Ru can be either antiferromagnetic or ferromagnetic, depending on the layer thickness. Initially

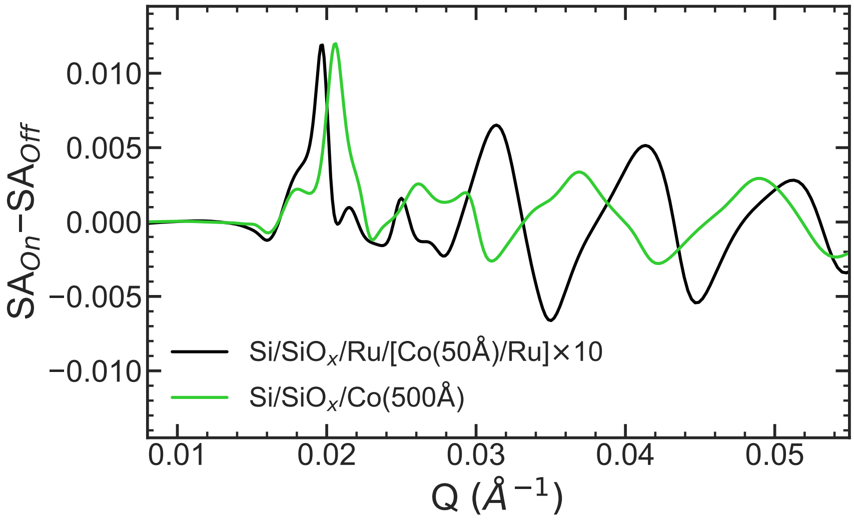

Figure 6.2: Refl1D Simulation results of the difference in spin asymmetry between on and off resonance states for a single layer sample and a multilayer sample structure. The full sample structures are Si/SiOx/Ru(30)/Co(50)/[Ru(10)/Co(50)]x9 /Ru(30) (thicknesses in Å) (black line) and Si/SiOx/Co(500Å) (green line). For each sample structure, the off state has Co magnetisation of 1400 emu/cc and the on state is modelled by a reduction in the projected magnetisation to $1400\cos(5^\circ) = 1395$ emu/cc.

using a value from the literature [91, 92, 272], the Ru thickness in the structure was optimised to obtain a sample with a high remanent magnetisation, indicating that the Co layers are ferromagnetically coupled. The magnetic hysteresis loop for the sample structure used in the PNR experiment is shown in figure 6.3b. This sample has a magnetic remanence of $M_r/M_s = 0.94$ signifying ferromagnetic coupling of the Co layers. This is very important for this experiment because if the Co layers are not coupled to each other, the anisotropy and magnetisation dynamics could vary from layer to layer. This would result in different cone angles or resonant field and frequency conditions for the various layers and therefore, the contribution to the change in magnetisation at resonance in the PNR experiment would differ from layer to layer.

Before the PNR measurements, the structure and quality of the sample were confirmed using XRR measurements. The XRR data and fit, along with the extracted SLD profile of the sample, are shown in figure 6.4. The XRR data contains Bragg peaks up to a large Q wavevector of 0.7 Å^{-1}, showing that the sample quality is good and with

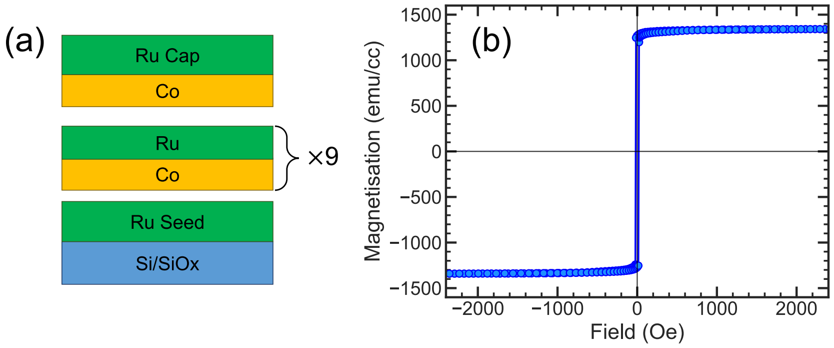

Figure 6.3: (a) Schematic of the structure of the Si/SiOx/Ru/[Co/Ru]x10 sample used for this experiment. (b) SQUID-VSM magnetic hysteresis loop of the sister sample of the one used in the PNR experiment.

smooth interfaces between layers. The Ru/Co repeat structure is modelled such that all of the Co layers are identical and all of the Ru layers are identical, sharing density, thickness and interface roughness. The fact that this model fits the data well shows that there is little variation in the growth of each layer in the multilayer. This is very important for this experiment as the Co layers need to behave as one uniform magnet to ensure coherent precession when at the FMR resonance condition. If the structural parameters changed significantly between the layers, the changing magnetic properties and magnetisation dynamics throughout the sample could have caused incoherent FMR precession. As mentioned previously, the RKKY coupling strength and sign (ferromagnetic or anti-ferromagnetic) are dependent on the Ru thickness. Therefore, it was also vital that the Ru thickness is consistent throughout the structure which was confirmed by the XRR modelling and SQUID hysteresis loop of the sample.

FMR characterisation measurements of the sister sample, which was grown on the same plate as the PNR sample, are shown in figure 6.5. Field sweep measurements are taken at microwave frequencies varying from 2.5 GHz to 14 GHz, an example of which can be seen in figure 6.5c. A differential Lorentzian function is fit to all field sweeps sets to extract values for the peak width and peak position. This equation is given by [85]

$$\frac{dP}{dH_{DC}} = K1\frac{4\Delta H(H-H_0)}{(4(H-H_0)^2+(\Delta H)^2)^2} - K2\frac{(\Delta H)^2-4(H-H_0)^2}{(4(H-H_0)^2+(\Delta H)^2)^2} + mH + c \quad (6.1)$$

Here, ΔH is the peak width, H_0 is the resonant peak position, $K1$ and $K2$ are asym-

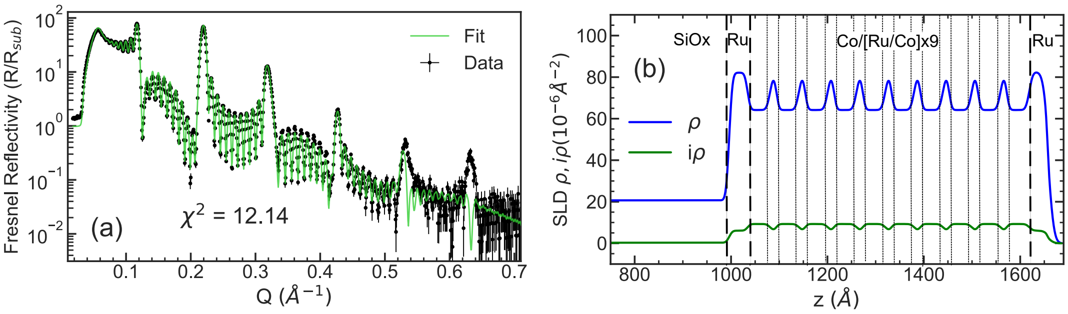

Figure 6.4: (a) XRR data for the Si/SiOx/Ru/[Co/Ru]x10 sample used for the PNR experiment. The solid green line shows the fit to the data. (b) X-ray SLD profile extracted from the fit to the XRR data shown in (a). The blue and green lines correspond to the scattering and absorption SLD profiles respectively.

Layer	Thickness (Å)	Roughness(Å)	Density (g/cc)
SiOx	995.9 ± 0.5	5.38 ± 0.02	2.409 ± 0.002
Ru Seed	37.95 ± 0.04	4.86 ± 0.03	11.105 ± 0.005
Co	46.96 ± 0.2	5.85 ± 0.02	9.057 ± 0.006
Ru	12.79 ± 0.03	4.56 ± 0.01	11.1003 ± 0.0003
Ru Cap	37.51 ± 0.04	2.51 ± 0.02	11.15 ± 0.01
RuOx	2.52 ± 0.06	8.9992 ± 0.0008	9.30 ± 0.2

Table 6.1: Structural parameters extracted from the XRR fit of the Si/SiOx/Ru/[Co/Ru]x10 sample shown in figure 6.4.

metry scaling factors, m and c are a dP/dH vs H background slope and dP/dH offset, respectively. The relationship between the microwave frequency and the resonance field H_0 is described by the in-plane Kittel equation (equation 4.5). Then, the Gilbert damping parameter can be obtained by analysing the relationship between the microwave frequency and the resonant peak width which is described by equation 4.6. Co was used as the ferromagnetic layer instead of Py in the measurements presented in this chapter. This decision was made under the assumption that the greater magnetisation of Co would mean that small changes in magnetisation angle would lead to greater changes in net magnetisation along the neutron polarisation axis, despite the fact that the lower Gilbert damping of Py means that the cone angle is larger in Py. However, as is demonstrated in the following sections of this chapter, the results of our experiments suggest that the measurement is more sensitive to changes in cone angle rather than magnetisation. Therefore, using Co instead of Py in our experiments may have reduced the observed differences between on and off resonance states in our PNR experiments. In future work, magnetic materials with low Gilbert damping, such as Py, should be used.

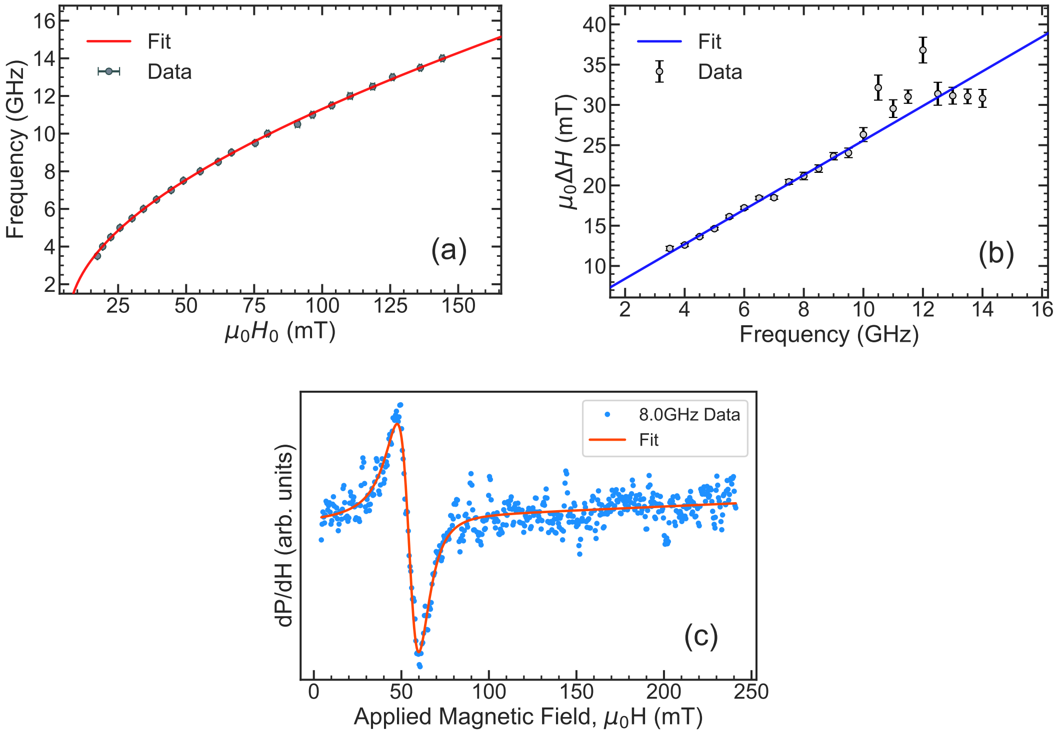

Figure 6.5: FMR characterisation data for a sample of structure Si/SiOx/Ru(38)/Co(45)/[Ru(10)/Co(45)]x9/Ru(38) (a) Kittel plot of the FMR resonance peak centre field against the microwave frequency. The solid line shows the fit to the Kittel equation (equation 4.5). From this, values of the saturation magnetisation and anisotropy field obtained are $\mu_0 M_s = 1170 \pm 70$ mT and $\mu_0 H_k = -6.74 \pm 0.09$ mT. (b) FMR linewidths (ΔH) plotted as a function of the microwave frequency. The solid line shows a fit to equation 4.6 from which the Gilbert damping parameter is calculated to be $\alpha = (2.81 \pm 0.09) \times 10^{-2}$. (c) Example FMR field sweep data at a microwave frequency of 8 GHz. The solid line is a fit to a differential Lorentzian function given in equation 6.1 from which the peak centre and peak width are extracted.

6.2.3 PNR Results

Experiment Set Up

To perform the PNR measurements, the sample is first loaded into the microwave cavity and the cavity is then mounted into the beamline between the poles of the magnet which is used to generate the neutron guide field. A vector network analyser (VNA) was used as the microwave source and to measure the returning signal. The working frequency range in the microwave cavity used is approximately 5.4 to 8.2 GHz. In this experiment, the influence of FMR on the sample was investigated by comparing PNR measurements with the microwave output being switched on or off. Before PNR data was measured, a microwave frequency and magnetic field combination that resulted in an FMR resonance mode within the optimal frequency range of the cavity was found. The resonance condition was initially estimated using hysteresis loops and FMR characterisation previously measured for the sister sample. By performing a field sweep on the sample in the cavity in the beamline using the neutron guide field electromagnet, the resonance condition was verified. From these measurements, a microwave frequency of 8 GHz and an applied field of approximately 50 mT were used for the PNR experiment.

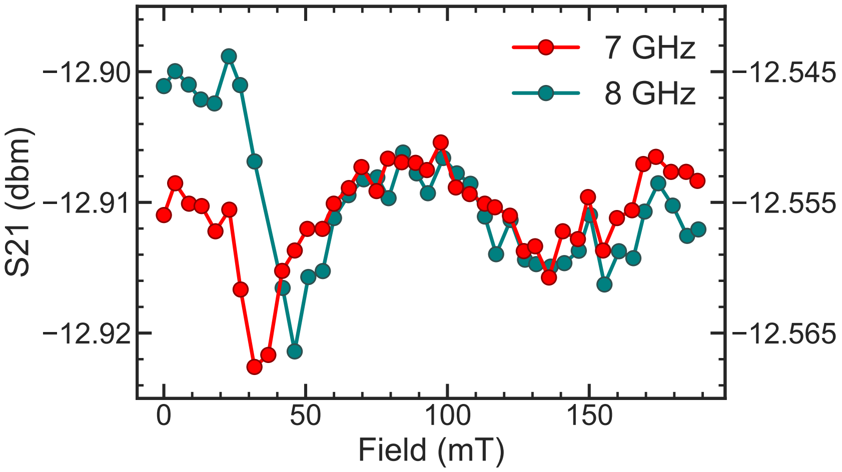

Figure 6.6: FMR field sweeps measured on the Si/SiOx/Ru/[Co/Ru]x10 sample in the cavity in the beamline at frequencies of 7 and 8 GHz. The data shows a resonance peak at around 50 mT.

As the POLREF beamline is a time-of-flight probe, there is a finite Q range that can be measured for each sample angle. Once the resonance condition was found, the field and frequency were set to the resonant condition found previously and PNR is continuously measured. During the measurement, the on and off FMR resonance states were achieved by alternating between the microwave output being switched on or off every hour. The data for each state can then be averaged across all of the individual hours of counting to give two final data sets: one of all PNR measured with the microwave output switched on and the other of PNR whilst the microwave output is off. The states were measured alternately in this fashion to reduce the effects of sample heating or variations in the environment e.g. room temperature and to ensure that there was an equal amount of counting on each state. In total, each state was counted for 32 hours.

PNR Data and Analysis

The final PNR results for the on and off resonance states can be seen in figure 6.7. As the only changes in the sample between the on and off states are its magnetic state, these data sets can be fit simultaneously in a model where all structural parameters are shared. As well as the on and off resonance data, a PNR measurement of a wider Q range is also included in the simultaneous fit to ensure the fitting of the structural parameters is more accurate. The larger Q range means the data includes higher order Fourier components therefore giving information about the thinner layers in the structure. The structural parameters from the PNR fit, along with the XRR parameters for comparison, are presented in table 6.2. The results for both measurement techniques are mostly in good agreement demonstrating the model's suitability in describing the sample structure. Although there are some discrepancies in the results, the Co and Ru multilayer parameters are very consistent. These are the most important parameters as they determine the magnetic behaviour of the sample.

The parameter correlation matrix for the Co and Ru thicknesses as well as the off and on resonance magnetic SLD (ρ_M) is shown in figure 6.8. In the correlation plots, a circular distribution indicates that the parameters are uncorrelated and therefore changing one of the parameters does not affect the other. A correlation plot that is a diagonal line, like that of the Co and Ru thickness, means that the parameters are highly correlated so changing one influences the other. In the case of the Co and Ru

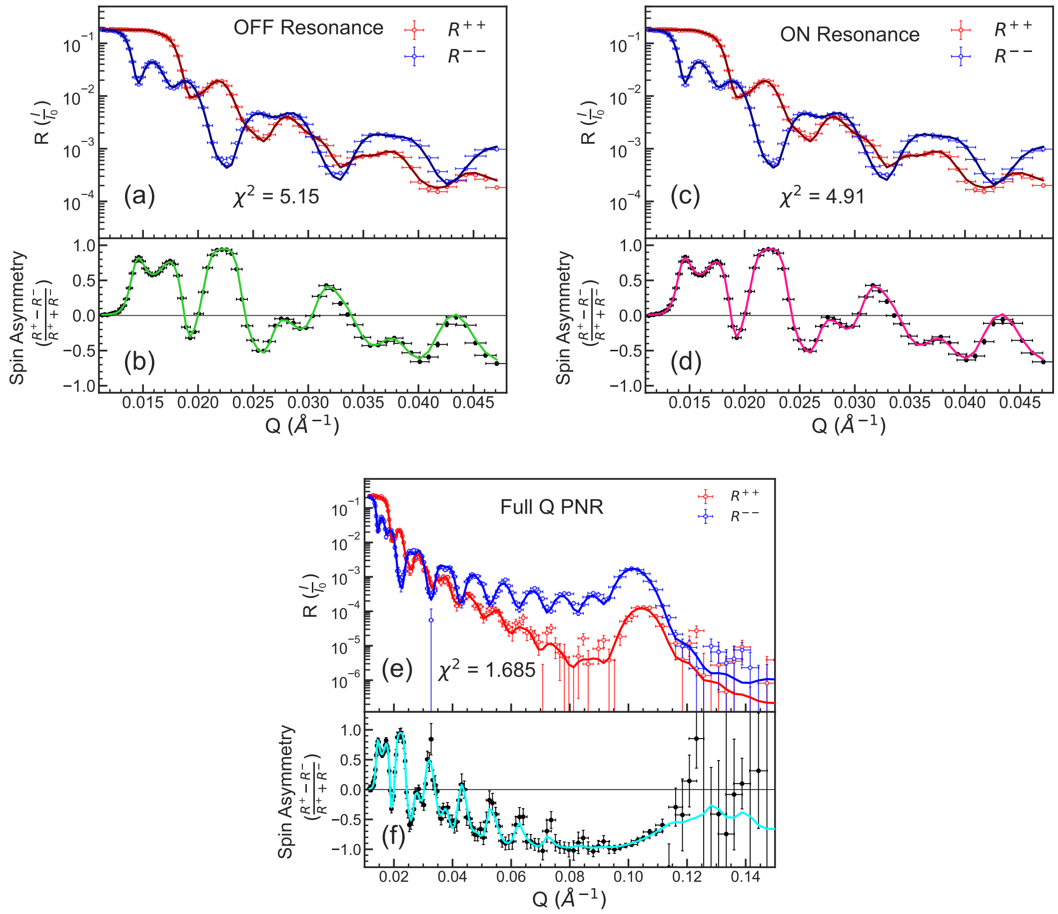

Figure 6.7: PNR data and fits for the three different data sets measured on the Si/SiOx/Ru/[Co/Ru]x10 sample used in the co-fitting. (a) and (b) show the PNR and spin asymmetry for the off resonance state. (c) and (d) show the PNR and spin asymmetry for the on resonance state in which the sample is irradiated with microwaves at 8 GHz. (e) and (f) show the PNR and spin asymmetry for a larger Q range PNR measurement which is used in the trifit to provide information about the thinner layers in the sample. The solid lines show fits to the data.

thicknesses, the plot demonstrates that increasing one parameter leads to the other decreasing. This highlights that in the multilayer structure, the fit is more sensitive to the combined Co/Ru bilayer thickness than it is to the individual thicknesses of the layer. This is because the angle of the Bragg peaks, which have a large reflectivity and therefore are heavily weighted in the fitting, are determined by the combined bilayer thickness. However, we see that the on and off resonance ρ_M values are not correlated to the Co or Ru thickness, so this doesn't affect the magnetisation value obtained from the fitting.

Layer	Thickness (Å)		Roughness(Å)		Density (g/cc)	
	PNR	XRR	PNR	XRR	PNR	XRR
SiOx	1041(2)	995.9(5)	14.3(8)	5.38(2)	2.1730(8)	2.409(2)
Ru Seed	34(2)	37.95(4)	8.8(2)	4.86(3)	12.2(2)	11.105(5)
Co	48.3(6)	46.96(2)	4.2(9)	5.85(2)	8.56(8)	9.057(6)
Ru	12.6(6)	12.79(3)	2(1)	4.56(1)	11.4(3)	11.1003(3)
Ru Cap	35(2)	37.51(4)	16(2)	2.51(2)	12.0(2)	11.15(1)
RuOx	10(1)	2.52(6)	15.8(2)	8.9992(8)	7(1)	9.30(2)

Table 6.2: Comparison of the structural parameters for the Si/SiOx/Ru/[Co/Ru]x10 sample extracted from both XRR fitting (figure 6.4) and PNR fitting (figure 6.7). The numbers in brackets are the uncertainties in the last digit of the value.

Information about the magnetic depth profile within the sample is contained in the spin asymmetry defined as $(R^+ - R^-)/(R^+ + R^-)$. Therefore, any changes in the magnetic profile between the on and off resonance states would result in a difference in the spin asymmetries for the two data sets. The comparison of the spin asymmetries for the two resonance states can be seen in figure 6.9. If there is a substantial change in the magnetic profile between the two states, we would see significant non-zero features in the difference between the two asymmetries. Although the difference between the spin asymmetries for the two states does show some asymmetry about zero, this is not matched by the solid line showing the difference in the fits. The vast majority of the data points in the difference plot, figure 6.9b, are within one error bar of zero, suggesting that the difference in magnetisation between the two data sets is below the sensitivity of the measurement. The difference from zero can be quantified by calculating the reduced χ^2 of the data compared to the line $f(Q) = 0$ using the equation

$$\chi^2 = \frac{1}{D} \sum_{i=1}^{n} \frac{S_i^2 - f(Q)^2}{\Delta S_i^2} \tag{6.2}$$

Where S_i are the data points for the difference in spin asymmetry, ΔS_i is the S_i uncertainty for each data point, $f(Q)$ is the function to compare the data against which in this case is simply 0, n is the total number of data points and D is the degrees

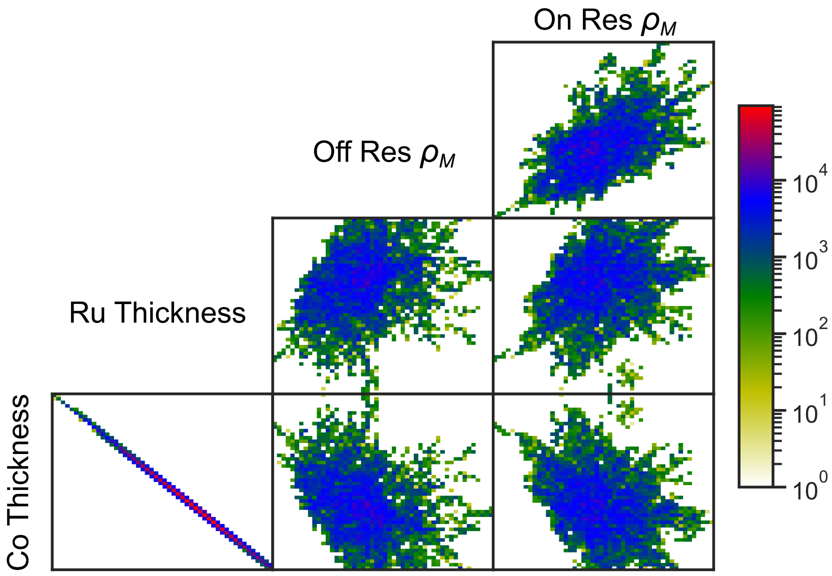

Figure 6.8: Correlation matrix for some selected parameters from the XRR fitting of the Si/SiOx/Ru/[Co/Ru]x10 shown in figure 6.4. This shows the correlation between the parameters. A diagonal plot, such as that for the Co and Ru thicknesses, demonstrates highly correlated parameters. A circular plot demonstrates uncorrelated parameters.

of freedom which here is defined by $n-1$. The value obtained when performing this calculation is $\chi^2 = 0.65$. The chi-squared value is less than 1 indicating that the vast majority of the data points are within 1 error bar of the line $y = 0$ where y represents the difference in spin asymmetry between the on and off states and can be expressed as $y = (\mathrm{SA}_{\mathrm{on}} - \mathrm{SA}_{\mathrm{off}})$. Here, the $y = 0$ line represents the case that there is no change in spin asymmetry and magnetism between the on and off states ($\mathrm{SA}_{\mathrm{on}} = \mathrm{SA}_{\mathrm{off}}$). Therefore, this analysis suggests that there is negligible change in magnetism observed between the on and off states.

To further compare the difference between the extracted magnetisation values for the two data sets, we can analyse the parameter probability histograms as shown in figure 6.10. These histograms show the probability density function of the obtained values for the fitting parameter, in this case ρ_M, for the total number of samples run during the fit. ρ_M denotes the magnetic scattering strength of the layer and is proportional to the layer's magnetisation. These histograms should approximately take

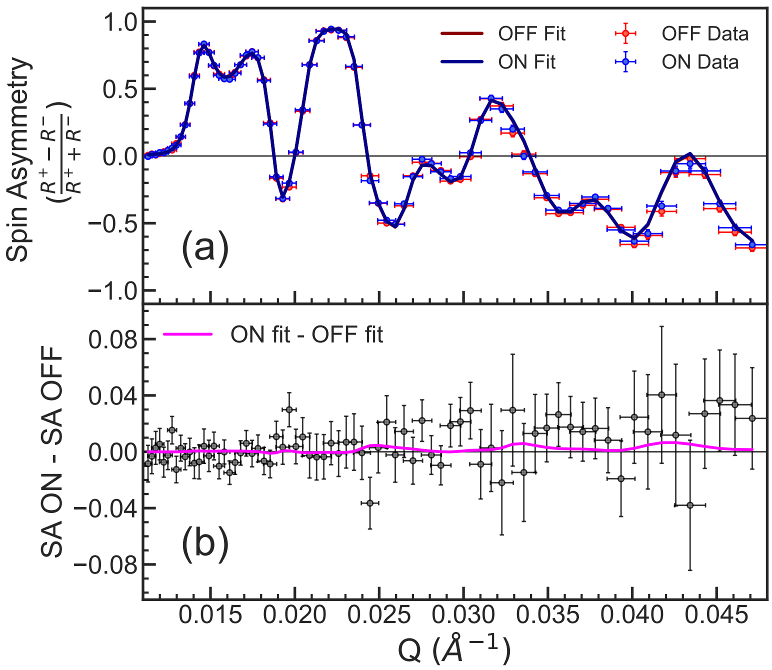

Figure 6.9: Comparison of the spin asymmetries of the on and off resonance states for the Si/SiOx/Ru/[Co/Ru]x10 sample as originally shown in figure 6.7. (a) Spin asymmetry data and corresponding fits for the on and off resonance states. (b) Black dots show the difference in the spin asymmetry data between the on and off resonance states (Spin asymmetry for on resonance minus spin asymmetry for off resonance). The pink line shows the difference between the fits for on and off resonance.

the shape of a Gaussian distribution given that the parameters are totally uncorrelated in the fit. If they are a normal distribution, the uncertainty in the fitting parameter is given by the standard deviation, shown on these histograms as the width of the peak. Otherwise, the 1 and 2 σ ranges correspond to the 68% and 95% Bayesian confidence intervals. To confidently claim from the fitting results that two parameters are significantly different, the obtained values need to be different by more than two standard deviations and the probability histograms should not overlap. Comparing the probability histograms for ρ_M for the on and off resonance states, it is clear to see that the histograms heavily overlap. The numerical data from the fitting shown in table 6.3 further demonstrates the overlapping of the two fitting parameters as both the 68%

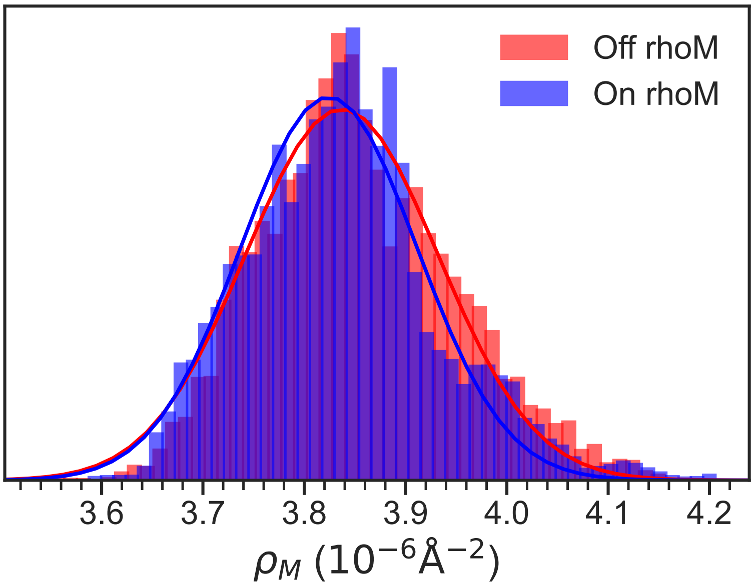

Figure 6.10: Probability histograms for the magnitude of the magnetic moment (ρ_M) for the on and off states of the Co/Ru sample obtained from the fits shown in figure 6.7. The solid lines show a Gaussian fit to the histogram.

and 95% confidence intervals of the parameters are the same within 0.03 $\times 10^{-6}\text{Å}^{-1}$. The mean values do vary slightly and change in the direction that would be expected with the precession of the magnetisation in the on state causing a reduction in ρ_M of $0.01 \times 10^{-6}\text{Å}^{-2}$. However, the uncertainty in the difference in ρ_M is $0.1 \times 10^{-6}\text{Å}^{-2}$, so, quoted with the uncertainty, the difference is $(0.0 \pm 0.1) \times 10^{-6}\text{Å}^{-2}$. If we take the raw number for the difference and consider the case where the reduction ρ_M is due to a change in magnetisation angle of ϕ_c, resulting in a reduction in the projected magnetisation along the original magnetisation axis, then we can calculate the angle required to cause this magnitude change in ρ_M using the equation

$$\phi_c = \arccos\left(\frac{\rho_{Mon}}{\rho_{Moff}}\right) \tag{6.3}$$

Using the values in table 6.3, the estimated cone angle ϕ_c is calculated to be 4°.

Using the uncertainty in the ρ_M values obtained from the fitting, we can calculate a resolution of this measurement configuration which can be used to estimate the change in moment, and therefore cone angle, required to observe a clear difference between the

State	Mean Value	σ range	2σ range
Off ρ_M ($\times 10^{-6}$Å^{-2})	3.85	(3.76, 3.95)	(3.69, 4.06)
On ρ_M ($\times 10^{-6}$Å^{-2})	3.84	(3.74, 3.92)	(3.68, 4.04)

Table 6.3: ρ_M fitting parameter results for the on and off resonance PNR data sets. 1σ and 2σ correspond to the 68% and 95% Bayesian confidence intervals respectively.

on and off states. The on state would need to have a ρ_M value of more than 2σ less than that of the off state. The value for 2σ can be calculated by taking the difference between the higher and lower bounds of the 1σ range. This value is 0.19 which is 4.9% of the mean value. As done previously, this can be estimated in terms of a change in angle of the magnetisation. This angle ϕ_c is the cone angle required to observe a well resolved change in magnetisation between the on and off resonance states using the same experimental set up and counting time as was done for the results presented here. From this calculation, we find that the angle required to observe this change is $\approx 18°$. This is almost 4 times larger than the estimated cone angle calculated from the difference in mean values of ρ_M for the on and off states. Therefore, this demonstrates that the changes in projected magnetism due to FMR precession are too small to measure in the current measurement configuration. The reported values for the precession cone angle which range from $0.5 - 15°$ depending on the material, measurement configuration and microwave power [66, 220, 273–276]. However, of those that are measured on samples of similar size and structure as ours, the cone angle is of the order of 1° [66, 273, 275]. This means that the required cone angle to see a significant difference in the off and on state ρ_M is much larger than the cone angles observed in similar systems. As we are using a microwave cavity for this experiment, the input power and therefore AC magnetic field are relatively small so the maximum cone angle that is achievable will be more of the order of 1° rather than 10°.

6.3 Polarisation Analysis and Angular Sensitivity

Sample Characterisation

The sample used requires a strong anisotropy so that the magnetisation does not align with the guide field. Also, a strong sample anisotropy field is required to act as the DC field for the FMR precession as we can no longer use the neutron guide field for this. A

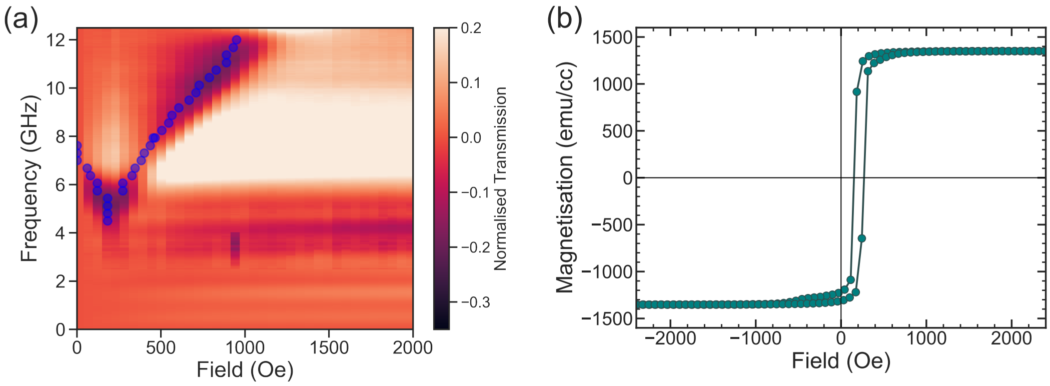

Figure 6.11: (a) Waveguide FMR map of a sample of a Si/SiOx/Ta(60)/[Co(55)/FeMn(120)]x10/Ta(60) sample. The blue dots show the resonance peak positions (b) Easy axis SQUID magnetic hysteresis loop of the same structure.

sample of Si/SiOx/Ta(60)/[Co(50)/FeMn(120)]x10/Ta(60) (thicknesses in Å) was used in which there is a strong exchange bias formed at the FM/AF interface between Co and FeMn which provides the anisotropy. By using a 10 repeat multi-layer, we increased the amount of magnetic material in the sample, which helps with FMR characterisation due to a greater absorption at the resonance condition. Also, the multilayer structure introduces Bragg peaks at low Q which aid with fitting by providing another Q region with high reflectivity, improving the signal to noise ratio.

Figure 6.11 shows the magnetic characterisation of the FM/AF multilayer sample. The sample has an exchange bias of around 210 Oe which can be seen in the offset from zero applied field of both the hysteresis loop and the FMR Kittel curve. The exchange bias in the sample can also be checked in PNR measurements as can be seen in figure 6.12. Here we see that if the sample is first saturated at 2000 Oe and then the applied field is reduced to 50 Oe, the sample magnetisation direction is flipped even though the sign of the applied field remains the same. The switching of the magnetisation direction of the sample is shown by the spin asymmetry swapping sign when the applied field is reduced to 50 Oe.

The XRR characterisation data for the sample can be seen in figure 6.13. Since the total sample thickness is large, with a total metal thickness of over 200 nm, the data has few fringes and features. This is especially noticeable when comparing to the

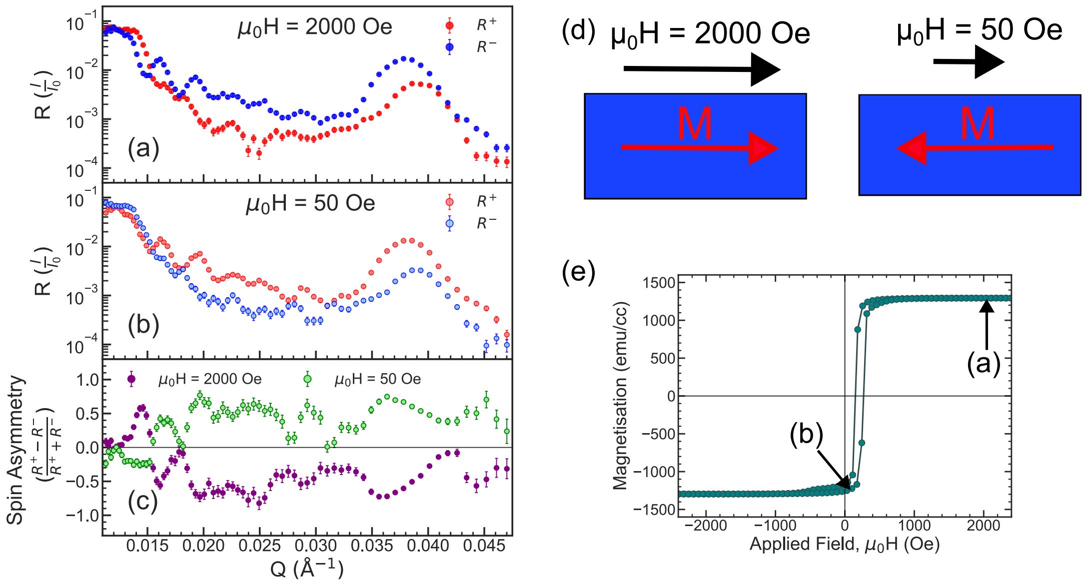

Figure 6.12: PNR measurements of the Si/SiOx/Ta(60)/[Co(55)/FeMn(120)]x10/Ta(60) sample with the applied field at 2000 Oe (a) and 50 Oe (b). (c) The spin asymmetry switches sign for the two fields, showing the exchange bias in the sample. (d) Schematic showing the magnitude and direction of the external field and the sample magnetisation. (e) SQUID magnetic hysteresis loop of a sister sample to the PNR sample, as shown in figure 6.11, with the labels showing the positions in the hysteresis loop of the PNR plots in (a) and (b).

XRR data shown in figure 6.4 for the Co/Ru multilayer sample used in the previous experiment which has total metal thickness of just under 70 nm. Also, as can be seen from the SLD profile, the x-ray SLDs for Co and FeMn are very similar which also contributes to the lack of features in the data due to the limited contrast between the repeat layers. The fitting parameters from the XRR analysis can be seen in table 6.4.

6.3.1 In-situ FMR-PNR Measurements

The PNR measurements for this iteration of the experiment were performed using the same experimental set up as in section 6.2.3. However, for this experiment, the sample was physically rotated so that it was mounted into the cavity such that the physical

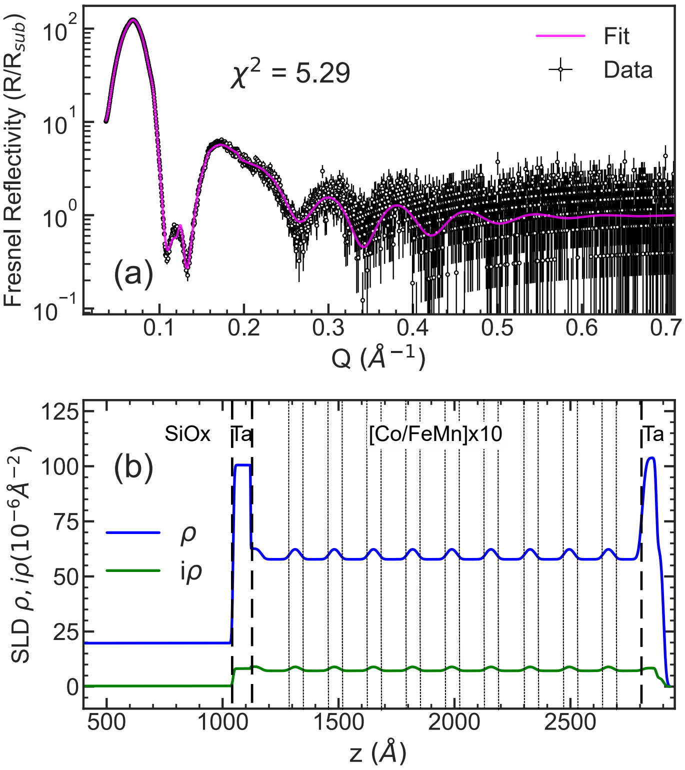

Figure 6.13: (a) XRR data for the Si/SiOx/Ta(60)/[Co(50)/FeMn(120)]x10/Ta(60) sample used for the PNR measurements. The solid line is a fit to the data (b) SLD profile extracted from the fit shown in (a). The blue line is the nuclear SLD and the green line is the imaginary SLD governed by the x-ray absorption.

axis along which the easy axis lay was approximately 45° to the neutron polarisation axis. We then performed FMR field sweep measurements at different frequencies to find a frequency where the resonance peak is at a field of 50 Oe, as this is the minimum field that can be used to keep the neutrons polarised. The FMR field sweep of the resonance condition used for the PNR measurements is shown in figure 6.14. This field sweep shows a clear resonance peak which encompasses 50 Oe when the frequency is 7.3 GHz.

Similarly to the previous measurements (section 6.2.3), once the resonance condition is found, we set the field and frequency to these values and measured full 4 channel PNR measurement (R^{++}, R^{+-}, R^{-+}, R^{--}) continuously and alternate each hour of measurements between the microwave output being on or off. In these measurements,

Layer	Thickness (Å)	Roughness(Å)	Density (g/cc)*
SiOx	1000 ± 60	4.40 ± 0.2	2.23 ± 0.06
Ta Seed	75.6 ± 0.1	1.0 ± 0.1	16.0 ± 0.2
Co	46.2 ± 0.4	12.9 ± 0.3	8.85 ± 0.01
FeMn	122.7 ± 0.3	12.82 ± 0.04	(40.04 ± 0.04) % Mn
Ta Cap	61.04 ± 0.06	5.17 ± 0.06	16.397 ± 0.005
TaOx	31.05 ± 0.02	9.33 ± 0.05	9.31 ± 0.03

Table 6.4: Structural parameters extracted from the XRR fit of the Si/SiOx/Ta/[Co/FeMn]x10/Ta sample shown in figure 6.13. *For the FeMn layer, the density column displays the Mn mass composition percentage.

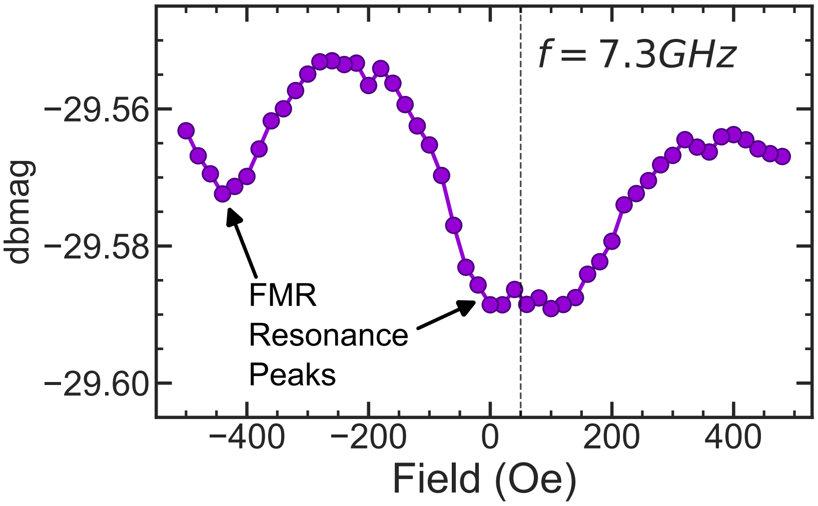

Figure 6.14: FMR field sweep measured in-situ on the PNR beamline at a microwave frequency of 7.3 GHz. The dashed line shows the applied field used for the PNR measurements.

each state was measured for 29 hours of counting time.

The PNR data for the on and off states, as well as a full Q half polarised measurement, can be seen in figure 6.15. The half polarised PNR measurement is used to help fix the structural parameters in the fitting as it is measured over a larger Q range so it provides more sensitivity to thinner layers within the sample. The fitting of the three data sets is done simultaneously, with all of the structural parameters shared and

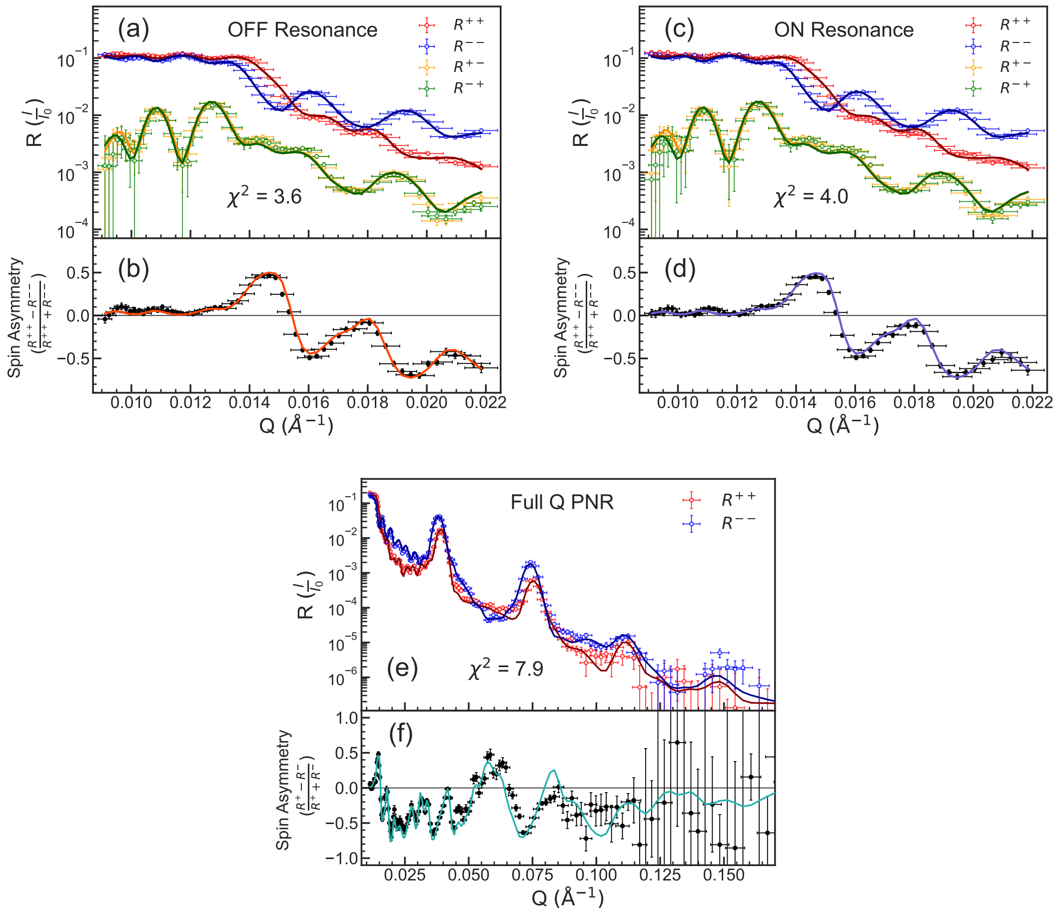

Figure 6.15: PNR data and fits for the three different data sets used in the co-fitting for the Co/FeMn sample. (a) and (b) show the 4 spin state PNR measurement and spin asymmetry for the off resonance state. (c) and (d) show the 4 spin state PNR measurement and spin asymmetry for the on resonance state. The resonance frequency used was 7.3 GHz. (e) and (f) show the 2 spin state (half polarised) PNR measurement and spin asymmetry for a larger Q range PNR measurement. This is used in the trifit to provide information about the thinner layers in the sample. All data sets are co-fit, sharing all structural parameters. The solid lines show fits to the data.

only the magnetic parameters being fitted independently. This ensures that there is no change in the structure between the on and off states and, consequently, that the magnetic parameters are comparable. The only change between the two measurements is the input of microwaves into the cavity which we know will not change the structure

Layer	Thickness (Å)		Roughness(Å)		Density (g/cc)*	
	PNR	XRR	PNR	XRR	PNR	XRR
SiOx	1080(2)	1000(60)	14.3(8)	4.4(2)	2.174(3)	2.23(6)
Ta Seed	52.4(5)	75.6(1)	10(2)	1.0(1)	15.807(7)	16.0(2)
Co	53(1)	46.2(4)	11.6(4)	12.9(3)	8.79(8)	8.85(1)
FeMn	117(1)	122.7(3)	7(2)	12.82(4)	43.69(3) %	40.04(4) %
Ta Cap	70(2)	61.04(6)	14(1)	5.17(6)	15.803(3)	16.397(5)
TaOx	28(3)	31.05(2)	14(1)	9.33(5)	8.6(5)	9.31(3)

Table 6.5: Comparison of the structural parameters extracted from the PNR and XRR fits for the SiOx/Ta/[Co/FeMn]x10/Ta sample. The XRR data and fit is shown in figure 6.13 and the PNR data and fits are shown in figure 6.15. The numbers in brackets are the uncertainties in the last digit of the value. *For the FeMn layer, the density column displays the Mn mass composition percentage.

of the sample in any way.

The structural parameters from the trifit compared to those obtained from the XRR fitting of the same sample can be seen in table 6.5. Across all the layers in the sample, there is good agreement in the parameters for the two measurement techniques. The most important parameters are those for the Co and FeMn layers as these determine the magnetic response of the sample. The data in the table shows that the results for both of the layers in the repeated bilayer structure are consistent across the two measurement techniques. This verifies that the structural parameters of the bilayer used in the final PNR fit, from which we compare the magnetic parameters between the on and off states, are an accurate representation of the sample. The correlations between the PNR fitting parameters, seen in figure 6.16, show that the Co and FeMn thicknesses are highly correlated. Similarly to the Co/Ru sample, this indicates that the fit is more sensitive to the combined Co/FeMn bilayer thickness than it is to the individual thicknesses. Although there is some difference in the Co and FeMn thicknesses between the XRR and PNR fits, the combined bilayer thickness is very similar. For the PNR fit it is 170 Å and for the XRR fit it is 168.9 Å.

The correlation matrix shows that the magnetic scattering, ρ_M, of the Co layers is correlated to the Co thickness. This is because ρ_M is proportional to the moment per unit depth so as the Co thickness increases, ρ_M must decrease to retain the same total

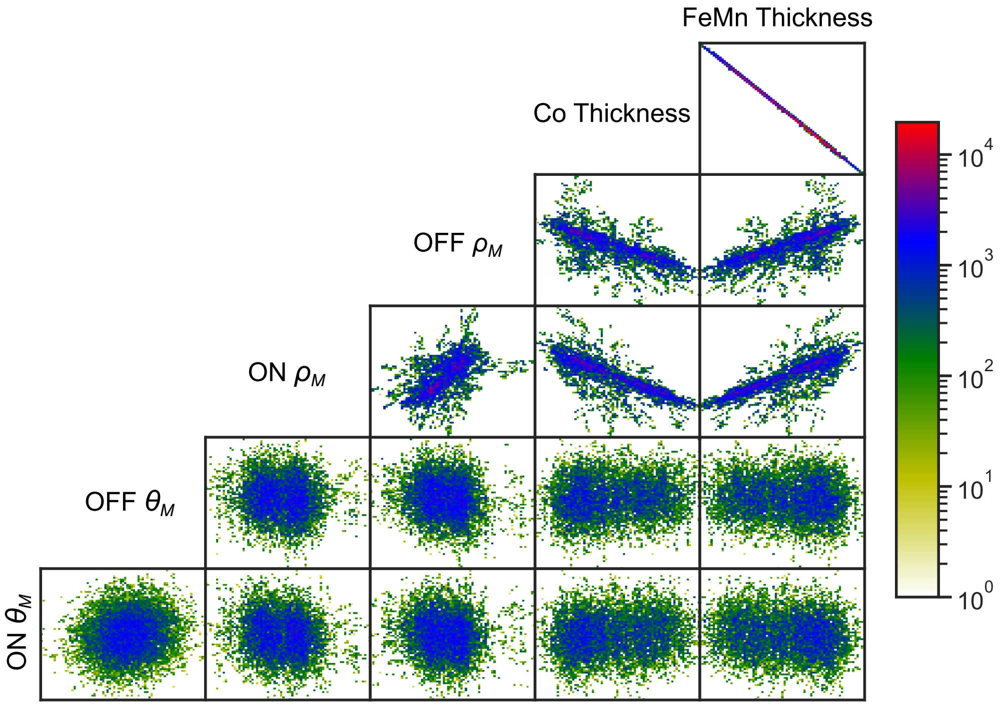

Figure 6.16: Correlation matrix for some selected parameters from the PNR fitting of the Co/FeMn shown in figure 6.15. A diagonal plot, such as that for the Co and FeMn thicknesses, demonstrates highly correlated parameters. A circular plot demonstrates uncorrelated parameters.

moment of the sample. The reverse relationship is true for the correlation between the FeMn thickness and ρ_M due to the correlation between the Co and FeMn thicknesses. Although these correlations may mean that the resultant values of ρ_M are not completely accurate, the fact that the on and off resonance states are cofit using the same structural parameters means that we can still compare ρ_M between the two states. Between the on and off ρ_M fitting parameters, there is a positive correlation, indicating that their values are dependent on each other. The positive correlation means that as one increases, the other also increases. Therefore, this could suggest that it is favourable in the fitting for the two ρ_M values to be equal. The θ_M and ρ_M values for both on and off resonances are all uncorrelated which demonstrates that θ_M and ρ_M can be

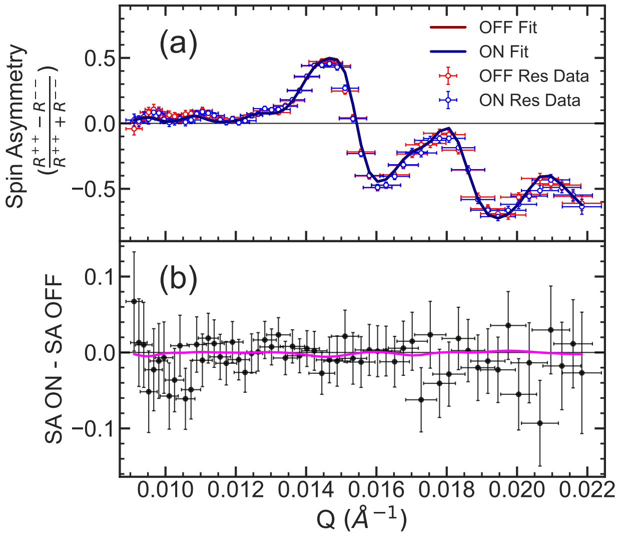

Figure 6.17: (a) Comparison of spin asymmetries between the on (blue) and off (red) resonance states for the Co/FeMn sample as originally shown in figure 6.15. Solid lines show the fitting results for each state. (b) Difference between the on resonance spin asymmetry and the off resonance spin asymmetry. The pink line shows the difference between the spin asymmetry fitting results for the two states.

fully resolved independently from each other and also that there is no link between the on and off resonance magnetisation angles.

As we are now measuring 4 state PA PNR measurements, information about the sample magnetisation in the on and off resonance states is held within the spin-flip reflectivity components as well as the spin asymmetry. The data for these components is shown in figures 6.17 and 6.18. The two spin flip channels will be slightly different near 0 Å^{-1} so we can compare both channels between the on and off states separately. Again, we see only small fluctuations from zero in the difference in spin asymmetry and the two spin-flip channels. By performing the same χ^2 analysis as described in equation 6.2 and comparing the data to the line $f(Q) = 0$, the difference from zero can be quantified. For the difference in spin asymmetry, a value of $\chi^2 = 0.42$ is obtained, which is much smaller than 1, showing that there is no significant difference in the spin asymmetry between the two states within the uncertainty range of the data. For the difference in R^{-+} and R^{+-} the χ^2 values are calculated to be 0.64 and 0.88 respectively.

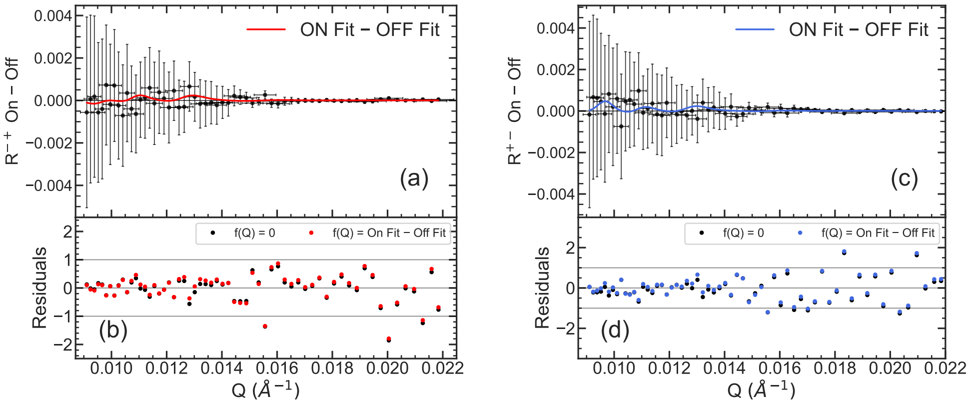

Figure 6.18: Difference between the on and off resonance state in the R^{+-} (a) and R^{-+} (c) spin states for the Co/FeMn sample as originally shown in figure 6.15. Residual plots show two different sets of points. Black points are the residuals calculated against zero (f(Q) = 0) and the red/blue points show the residuals calculated using the difference in on and off fits, shown by the solid lines in (a) and (c).

The residual plots in figure 6.18 help to demonstrate this result as the majority of the points lie within ±1. Similarly to the difference in spin asymmetry, these values are both less than 1 suggesting the line of $f(Q) = 0$ is a good fit to the data. As the $f(Q) = 0$ line here represents there being no change in the spin-flip components of the reflectivity, this analysis suggests that there is no statistically significant difference in the spin-flip channels and therefore, the in-plane perpendicular magnetisation components.

The 4 spin state measurement allows for the magnetisation angle to be determined as well as the magnetisation magnitude, hence the fitting parameters ρ_M and θ_M can be compared between the on and off states as seen in figure 6.19. ρ_M is the magnitude of the magnetic SLD and is proportional to the magnitude of the in-plane magnetization. θ_M is the angle of the magnetisation with respect to the neutron polarisation, for example, when $\theta_M = 0°$ this means that the magnetisation is aligned with the neutron polarisation and $\theta_M = 90°$ would mean they are perpendicular to each other. The numerical results for these parameters can be found in table 6.6. Here, 1σ and 2σ correspond to the 68% and 95% Bayesian confidence intervals respectively. In the case that the probability distributions are Gaussian, σ is the same as the standard deviation. The ρ_M parameter histograms heavily overlap. The mean values for the two states are

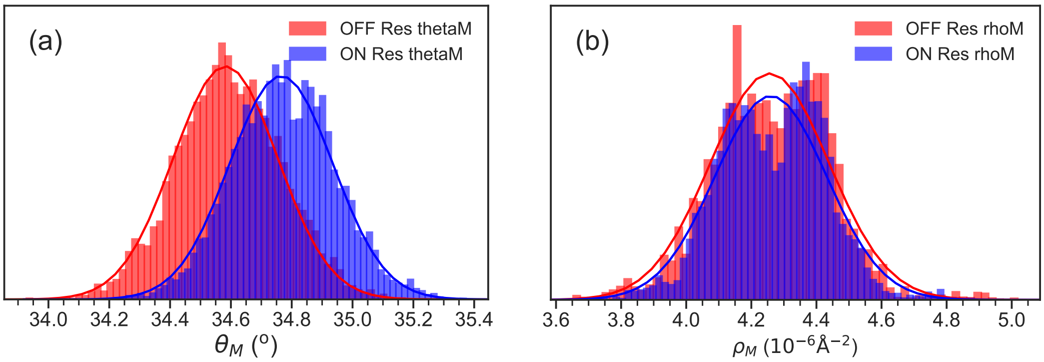

Figure 6.19: Probability histograms for the magnitude of the magnetisation angle (θ_M) (a) and the magnetic moment (ρ_M) (b) for the on and off states obtained from the fits shown in figure 6.15. The solid lines show a Gaussian fit to the histogram.

approximately equal, clearly showing that there is no measurable difference between the effective magnetisation of the sample when it is in an FMR resonance state. However, for the θ_M fitting parameter, there is a small but clear difference in the two histograms. Comparing the histograms in figure 6.19a and b shows a distinct difference between a parameter that has not changed between the two states and one that has. The ρ_M histograms overlap almost identically, whereas that is an obvious shift between the on and off θ_M parameter histograms.

Analysing the numerical data in table 6.6, we see that the mean value for θ_M of each state is outside of the 1σ range of the other. This suggests that there is a change in the magnetisation angle of the sample when it is in an FMR resonance state. Nonetheless, the 1σ uncertainty ranges for on/off θ_M do overlap meaning that we cannot claim here that there is statistical proof of a change between the two states. Still, compared to the indistinguishable ρ_M data and histograms, the differences between the on and off state θ_M histograms and associated values provide strong evidence that we have observed a change in magnetisation with PNR due to the precession of the magnetisation under FMR.

The ρ_M numerical data and histograms strongly suggest that there is no change in the in-plane magnetisation magnitude. This is further evidenced by the additional fitting parameters in the model. As well as ρ_M and θ_M, the magnetic dead layers and interfaces above and below the Co layer are also fitted in the model independently for

Parameter	Mean Value	σ range	2σ range
Off ρ_M ($\times 10^{-6}$Å^{-2})	4.26	(4.09, 4.43)	(3.92, 4.59)
On ρ_M ($\times 10^{-6}$Å^{-2})	4.27	(4.10, 4.42)	(3.96, 4.56)
Off θ_M (°)	34.59	(34.42, 34.77)	(34.26, 34.93)
On θ_M (°)	34.78	(34.61, 34.94)	(34.45, 35.11)

Table 6.6: ρ_M and θ_M fitting parameter results for the on and off resonance PNR data sets. 1σ and 2σ correspond to the 68% and 95% Bayesian confidence intervals respectively. Results of the fitting shown in 6.15

each state. The magnetic dead layers act as additional parameters which allow for the depth and thickness of the magnetic SLD profile of the layer to be shifted relative to the structural profile. The magnetic interface parameters act on the magnetic SLD profiles to determine the transition in ρ_M between adjacent layers in the same way that the structural interfaces act on the nuclear and imaginary SLD profiles. The results of these parameters, see table 6.7, show no change between the on and off states, further demonstrating that there is no change in mSLD across many fitting parameters.

The 1 and 2 σ ranges for ρ_M and θ_M also indicate why it may be easier to observe the FMR resonance as a change in angle rather than a change in effective magnetisation. As discussed in the analysis of the results presented in section 6.2.3, the confidence intervals can be used to generate a measurement resolution for θ_M and ρ_M. By saying that 2σ is equal to the difference in the upper and lower bounds of the 1σ range, we calculate 2σ for the off state ρ_M to be $\approx 0.34 \times 10^{-6}$Å^{-1} which is almost 10% of the mean value. This means that, for an observable change in effective magnetisation, the on state would need to have a mean ρ_M of more than 0.34 less than the mean of the

Magnetic Thickness Parameter	Off Resonance	On Resonance
M dead layer above (Å)	6 ± 1	6.4 ± 0.9
M dead layer below (Å)	0.4 ± 0.7	0.3 ± 0.6
M interface above (Å)	4 ± 2	3 ± 2
M interface below (Å)	6.5 ± 0.7	6.5 ± 0.6

Table 6.7: Magnetic dead layer and interface fitting parameter results for the on and off resonance PNR data sets. Above and below correspond to the top and bottom interface of the Co layer respectively.Results of the fitting shown in 6.15

off ρ_M. If we consider this reduction as a projection along the original axis due to a change in magnetisation angle, this results in a required cone angle of 25°.

Explaining Changes in Magnetisation Angle

Under FMR precession, the magnetisation rotates around the DC magnetic field, which in our case is the exchange bias field of the sample, with a constant cone angle throughout. Therefore, it is not initially obvious why the FMR precession would result in a measured change in the magnetisation angle. To explain the observed change in magnetisation angle, first, data was simulated for the spin-flip reflectivity and spin asymmetry for magnetisation angles between 0-90°. Examples of the simulated data for 3 different magnetisation angles can be seen in figure 6.20. These simulations were performed on Refl1D using the nominal parameters of the SiOx/Ta/[Co/FeMn]x10/Ta sample used in the PNR experiments. Data was simulated only for the Q range of 0.008 - 0.022 Å^{-1} to mirror the range of the experimental data. To investigate the angular dependence of the spin-flip scattering, the maximum magnitude of each curve is taken to turn the curves into single quantities. As can be seen in figure 6.20, changing the magnetisation angle causes a significant change in the magnitude of the spin-flip reflectivity with no change in the fringe separation or position. Therefore, we can simply use the maximum magnitude of the curves to compare the spin-flip reflectivity at different magnetisation angles. In the case of the spin asymmetry, the maximum occurs at 0.022 Å^{-1} where the spin asymmetry is negative. For ease of comparing the spin-flip reflectivity and spin asymmetry, the absolute value of this is taken to quantify the magnitude of the spin asymmetry.

The angular dependence of the spin-flip reflectivity is shown in figure 6.21a. These results show that the spin-flip reflectivity has a sinusoidal relationship with the angle of the magnetisation with respect to the neutron polarization. The significant point here is that the relationship is not linear. Therefore, for some given starting magnetisation angle $\theta_{M,i}$, a shift of 1 degree away from the neutron polarisation and 1 degree towards the neutron polarisation will result in asymmetric changes in the magnitude of the spin-flip reflectivity. In the on state of the FMR-PNR experiment where the magnetisation is continuously precessing, we can consider the PNR data to be the time average of the sample with magnetisation angle of $\theta_{M,i} + \phi_c$ and $\theta_{M,i} - \phi_c$ where ϕ_c is the cone angle of the precession. In this case, the spin-flip scattering of the on state will differ from

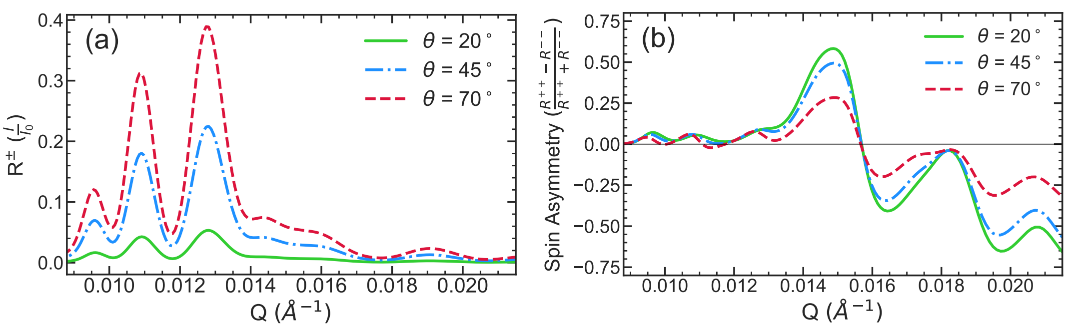

Figure 6.20: (a) Refl1D simulations of the $R^{\pm}$ spin-flip reflectivity of a SiOx/Ta/[Co/FeMn]x10/Ta sample, using structural and magnetic parameters to mirror the sample used in the PNR experiments. (b) Simulated spin-asymmetry for the same sample. Here, θ_M represents the angle between the sample magnetisation and neutron polarisation, with $\theta_M = 0°$ corresponding to the magnetisation and neutron polarisation being parallel.

that of the off state.

$$SF_{\theta_{M,i}} \neq \frac{1}{2}(SF_{\theta_{M,i}+\phi_c} + SF_{\theta_{M,i}-\phi_c}) \tag{6.4}$$

This can be verified with simulations whereby the on state is modelled as the average of the spin-flip reflectivity of $\theta_M + 5$ and $\theta_M - 5$, where 5° is chosen arbitrarily as the cone angle, see figure 6.21. Then, the off state can be subtracted from the on state to find the difference between the two states. The angular dependence of the difference between the on and off states is shown in figure 6.21b. This figure highlights that the magnitude and sign of the difference in spin-flip reflectivity is dependent on the starting magnetisation angle. The shift in spin-flip reflectivity between the on and off resonance states will be interpreted in PNR fitting as a change in magnetisation angle because of the angular dependence of the spin-flip reflectivity. If the difference is positive, and therefore the on state has a larger spin-flip reflectivity than the off state, this will result in an apparent increase in the magnetisation angle because the spin-flip reflectivity increases with magnetisation angle. Consequently, the simulations show that, with initial magnetisation angles of 0-45^{o} the on state will have a larger effective magnetisation angle than the off state, when considering the spin-flip reflectivity.

The same analysis can be performed for the spin asymmetry, again modelling the on state as the average of $\theta_M + 5$ and $\theta_M - 5$. The angular dependence of the spin

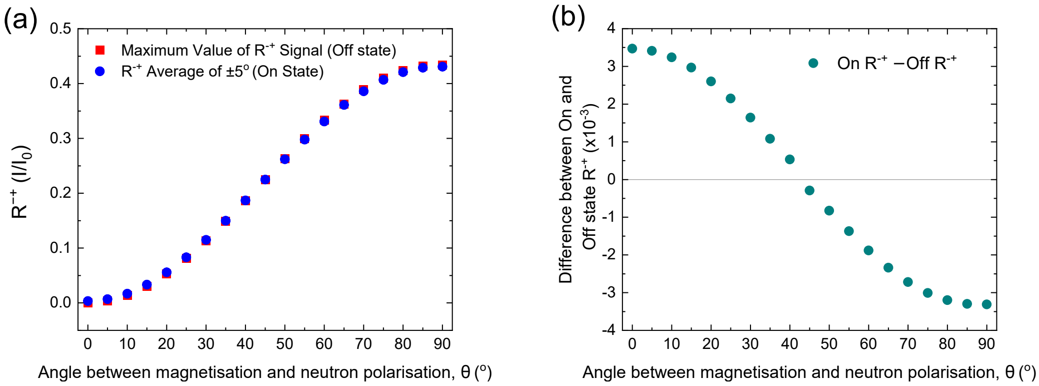

Figure 6.21: (a) Magnetisation angle dependence of the maximum in the R^{-+} channel (red squares) and the average of R^{-+} for $\theta_M \pm 5°$ (blue circles) e.g for 30° this is the average of R^{-+} for 25° and 35°. This is the on resonance state in this scenario. (b) Magnetisation angle dependence of the difference in the on and off states (On - Off) as shown in (a).

asymmetry in the on and off resonance states, as well as the difference between them, can be seen in figure 6.22. Similarly to the spin-flip reflectivity, the angular dependence of the spin asymmetry is non-linear meaning that equal positive and negative changes in angle will result in different sizes of changes in the spin asymmetry. Whereas the spin-flip reflectivity increases as the magnetisation angle increases, the magnitude of the spin asymmetry decreases with magnetisation angle. This indicates that, when the on state spin asymmetry has a smaller magnitude than the off state, the fitting would result in the magnetisation angle of the on state being larger than that of the off state. The angular dependence of the difference between the on and off states shows that the largest differences in spin asymmetry occur with a starting magnetisation angle of around 60°. The difference between the on and off states, in figure 6.22b, is negative for all angles so the on state spin-asymmetry is smaller in magnitude than the off state. Therefore, these simulation results suggest that the experimentally observed magnetisation angle of the on state should be larger than that of the Off state.

In the cases of both the spin-flip reflectivity and spin asymmetry, the simulation results suggest that, at an initial magnetisation angle of around 35°, the observed magnetisation angle of the on state will be greater than that of the off state. Therefore,

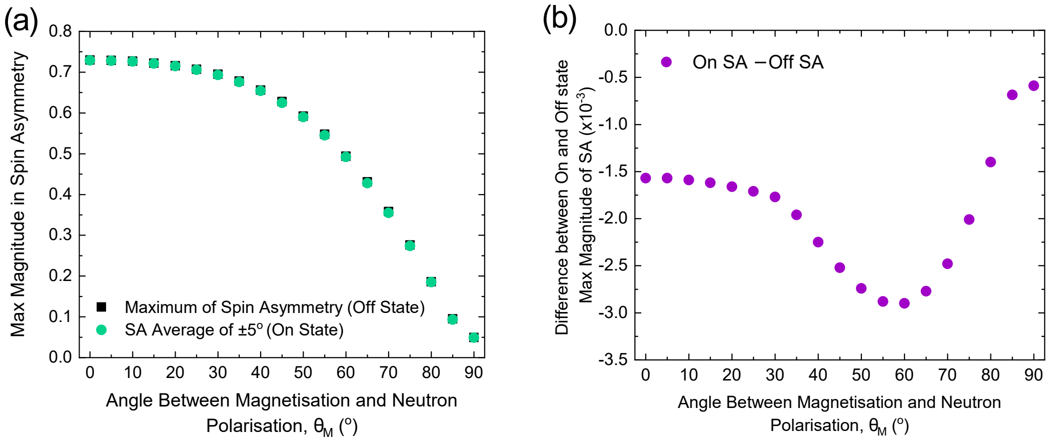

Figure 6.22: (a) Magnetisation angle dependence of the maximum in the spin asymmetry (black squares) and the average of spin asymmetry for $\theta_M \pm 5^o$ (blue circles) e.g for 30° this is the maximum of the average of the spin asymmetry for 25° and 35°. This is the on resonance state in this scenario. (b) Magnetisation angle dependence of the difference in the on and off states (On - Off) as shown in (a).

these results support the experimental PNR results in which the obtained θ_M values for the on and off states were $(34.8 \pm 0.2)°$ and $(34.6 \pm 0.2)°$ respectively. This difference is not large enough to be statistically significant as the difference between the angles is equal to the uncertainty in each. However, the agreement in trend between the simulation and experimental results suggests that we have observed a small but real effect of the FMR precession of the magnetisation using PNR measurements.

The differences between the on and off states can be converted into an estimated shift in magnetisation angle by dividing the difference at each angle by the gradient in the maximum magnitude at the same angle. This calculation uses the small angle assumption that the gradient between each adjacent point in the angular dependence of the spin-flip reflectivity and spin asymmetry is linear. The estimated shift in magnetisation angle can therefore be written as

$$\Delta\theta_M = \frac{\text{(On SA - Off SA)}}{m_{SA}(\theta_M)} \qquad \Delta\theta_M = \frac{\text{(On SF - Off SF)}}{m_{SF}(\theta_M)}$$

where $m_{SA}(\theta_M)$ and $m_{SF}(\theta_M)$ are the gradients of the magnitude of the spin asymmetry and spin-flip reflectivity as a function of magnetisation angle respectively. Figure 6.23

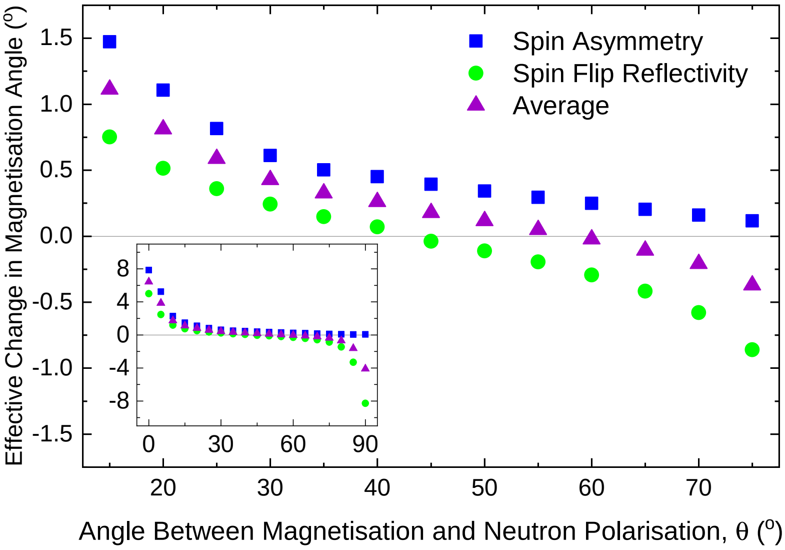

Figure 6.23: The effective change in magnetisation angle calculated from the simulations of the on and off resonance states shown in figures 6.21 and 6.22. The inset shows the full θ_M range of 0-90°. The main plot highlights a smaller region of 15-75° as either the spin asymmetry or spin-flip reflectivity would be too small to measure experimentally outside of this angular range. Note that all of the preceding simulations have assumed a cone angle of 5°.

shows the calculated effective changes in magnetisation between the on and off states for both the spin asymmetry and the spin-flip reflectivity. Also plotted, is the average change in the magnetisation angle as, experimentally, fitting to PNR data will take into account all of the reflectivity channels. Assuming the modelling of the on state to be accurate to the experimental reality, the average here shows the expected observed shift in magnetisation angle between the on and off states with a cone angle of 5°. This figure shows how the observed change in the magnetisation angle changes in magnitude and sign depending on the initial magnetisation angle.

To compare these simulation results to the experimental data shown previously in this chapter, we must look at the results with a starting θ_M angle of 35°. The simulation results presented so far all use a cone angle of 5^o. To understand the relationship between the change in magnetisation angle and the cone angle we can use the simula-

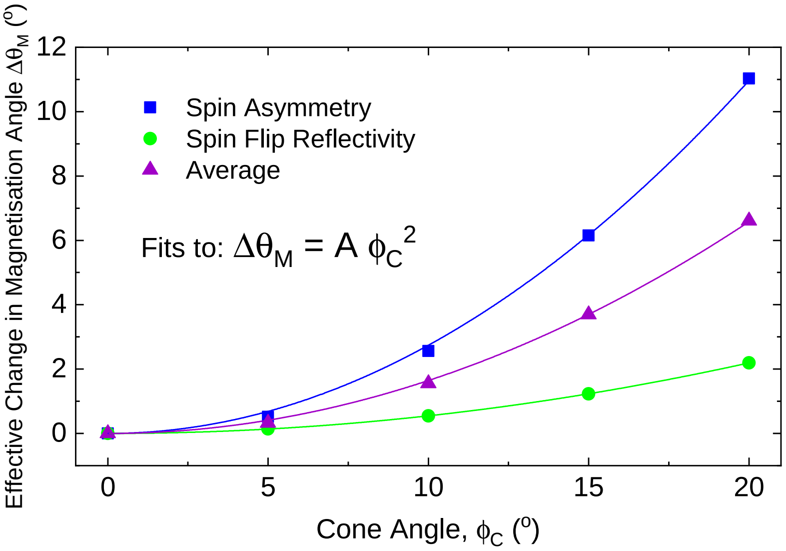

Figure 6.24: The calculated effective change in magnetisation angle between the on and off states for different cone angles using a starting magnetisation angle of $\theta_M = 35°$. The solid lines show fits to the data using a square relationship as described by the equation in the annotation of the figure.

tions to estimate the results for different values of the cone angle. The results of this are shown in figure 6.24. The solid lines in this figure show fits to

$$\Delta\theta_M = A\phi_C^2 \tag{6.5}$$

where A is an arbitrary fitting parameter. Here we see that the relationship between the cone angle and the change in magnetisation angle for the spin asymmetry, spin-flip reflectivity and the average of the two all follow a square relationship. Using the fitting results of the parameter A we obtain an equation that allows for conversion between the measured change in magnetisation angle into an estimated cone angle. In the experimental PNR data, all 4 spin states are measured and therefore we expect the relationship between the observed shift in θ_M and the sample cone angle to follow the relationship shown by the average in figure 6.24. Fitting to this curve resulted in a value of $A = (0.0164 \pm 0.0002)\,\mathrm{deg}^{-1}$. The experimental PNR results previously shown in this chapter resulted in a change in magnetisation angle of $(0.2 \pm 0.3)°$ between the

Difference between On and Off states	ρ_M		θ_M	
	PNR (10^{-6}Å^{-2})	Cone Angle (°)	PNR (°)	Cone Angle (°)
1σ	0.17	16	0.19	3.3
2σ	0.34	23	0.35	4.6
3σ	0.51	28	0.53	5.7
4σ	0.68	33	0.70	6.5

Table 6.8: Comparison of the differences in ρ_M and θ_M required to separate the on and off states by 1,2,3 and 4 σ. The differences between the on and off states have also been converted into an effective cone angle. For ρ_M, this is done using equation 6.3 with the off state ρ_M value of 4.26 $\times 10^{-6}\text{Å}^{-2}$ taken from table 6.6. For θ_M the cone angles are calculated using the equation 6.5 with $A = 0.0164$.

on and off states. Using equation 6.5 we can estimate the cone angle to be $(3 \pm 2)°$.

Using this relationship between the change in θ_M and the cone angle also allows us to approximate the cone angle required to observe a full separation between the on and off resonance states. Performing the same calculation as for ρ_M and using the numerical data in table 6.6, the 2σ range is found to be 0.35° for θ_M. This can be approximated to a required cone angle of 4.6°. This is over 5 times smaller than the required cone angle to achieve a 2σ change in ρ_M, which was 25°. These results clearly show that measurements of the magnetisation angle, and therefore a 4 spin state PNR measurement, are vital when trying to observe the magnetic changes in a sample when under FMR precession. To further demonstrate the difference in resolution between ρ_M and θ_M, table 6.8 shows the changes in the two magnetic parameters needed to separate the on and off states by different σ ranges.

6.3.2 Repeat Measurements

During the beamtime, further PNR measurements were taken, whereby the whole cavity was rotated 180 degrees in the beamline. In this configuration, the sample magnetisation is at an angle of approximately 135° to the neutron polarisation. The same experiment, as previously described, is repeated. First, the microwave frequency that results in a resonance at -50 Oe is found. In this case, that frequency is 6.6 GHz. In the field sweep measurement in this configuration, the resonance peaks are not as clear, so some referencing to other measurements is required. Figure 6.25a shows a comparison between the field sweep measurements at 6.6 GHz and 6.75 GHz. In the field sweep at 6.75 GHz, there are two clear resonance peaks. In a typical ferromagnetic material, these peaks would be at equal positive and negative fields but, due to the exchange bias, the peaks are shifted by approximately 200 Oe. The 6.6 GHz field sweep shows a clear peak at around 280 Oe, a slightly lower field to the peak for the 6.75 GHz field sweep. The other resonance peak, just above 0 Oe, is less clear but there is a small peak at around 50 Oe, shifted slightly from the same peak in the 6.75 GHz field sweep. We can also take frequency slices from the waveguide FMR maps for the sample, as seen in figure 6.11, to help predict where we expect the peaks to be. The frequency slices from maps with the easy axis is parallel and perpendicular to the applied field direction can be seen in figure 6.25b and c, respectively. The dashed lines correspond to the peak positions picked out from the in-situ cavity field sweep at 6.6 GHz. Compared to the two peaks in the 0° data, the dashed lines are clearly at lower fields. However, the comparison between the 0° and 90° data shows that, as the angle between the easy axis and the applied field direction increases, the peak positions shift to lower fields meaning that by 90° there is only one peak seen in the positive field range. Therefore, it follows that with the sample easy axis at 45° to the applied field, as it is in the cavity, the peak positions will shift to lower fields than those seen in the 0° data. The 0° data also shows that as the frequency decreases, the two resonance peaks get closer together and in the in-situ cavity field sweeps the small peaks at 6.6 GHz are slightly closer together than those for 6.75 GHz.

Once the resonance condition was verified and the field and frequency were set to these values, the four spin state PNR measurement can be taken, alternating each hour between the microwave output being switched on or off. The FMR field sweep taken of the sample in the cavity in the beamline, as well as the on and off resonance PNR

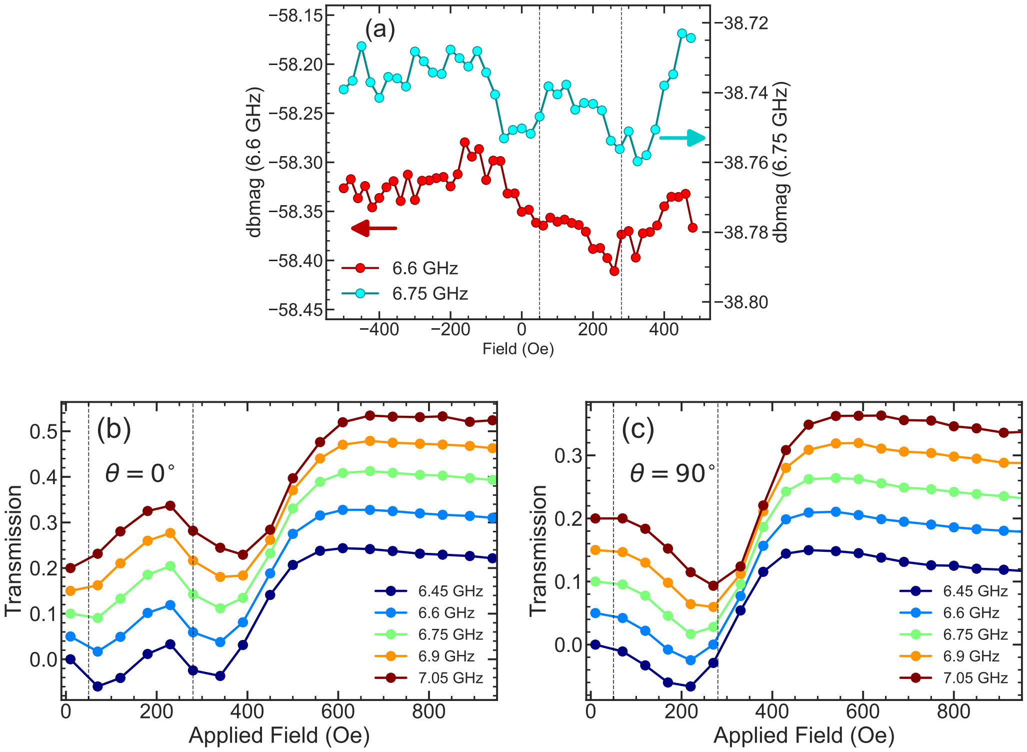

Figure 6.25: (a) Field sweep FMR measurements taken at 6.6 GHz and 6.75 GHz inside the cavity in the beamline with the sample magnetisation at approximately 135° to the applied field. (b) and (c) show waveguide FMR field sweeps measured ex-situ with the magnetisation at 0° and 90° to the applied field respectively. The dashed lines show the field positions of the two resonances when measured in the cavity at 6.6 GHz.

data, can be seen in figure 6.26. The PNR data is extremely similar to the data from the previous section, except now the R^{++} and R^{--} channels have swapped over as the sample magnetisation is pointing in the opposite direction to the neutron polarisation. The uncertainties in the reflectivities in this data set are larger as each state was only counted for 9 hours. By fitting the data using Refl1D we can, once again, extract the magnetic parameters of the on and off states to compare the change that has occurred due to the microwave excitation. The parameter probability histograms and numerical values from the fitting are shown in figure 6.28 and table 6.9 respectively.

When discussing the data and fitting results, the data from section 6.3.1 will be called the 7.3 GHz data and the data displayed here in this section, in figures 6.26

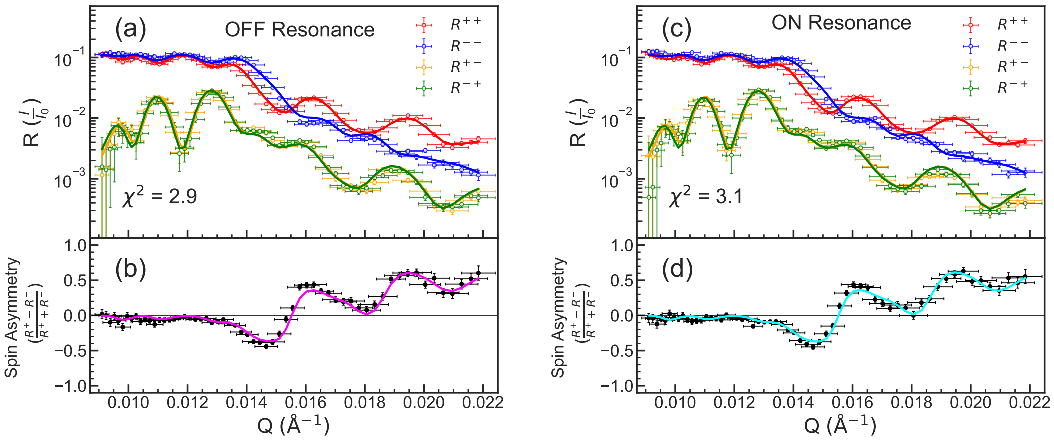

Figure 6.26: PNR measurements at a microwave frequency of 6.6 GHz and a sample angle of approximately 135°. (a) and (b) show the 4 spin state measurement and spin asymmetry for the off resonance state respectively. (c) and (d) show the 4 spin state measurement and spin asymmetry for the on resonance state. Solid lines show fits to the data. Fitting is done for both data sets and a full Q, half polarised PNR data set simultaneously so all structural parameters are shared.

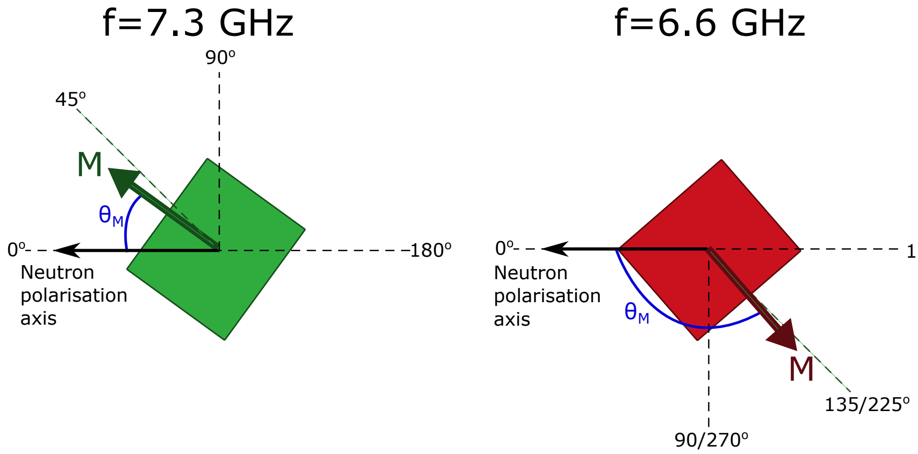

Figure 6.27: Schematic showing the sample magnetisation angle relative to the neutron polarisation. The angle labels show the angle moving clockwise/anticlockwise from the neutron polarisation. These are symmetric in terms of the measured PNR data.

and 6.28, will be called the 6.6 GHz data. In the 6.6 GHz data fitting, the model was additionally constrained by setting the magnetic interfaces and dead layers in the on and off states to be equal. In the fitting of the 7.3 GHz data, there was no change in dead layers and interfaces between the on and off states. The counting time for the 6.6 GHz data is a third of that of the 7.3 GHz data so the uncertainty in the data is greater and therefore the redundant fitting parameters were removed to reduce the degrees of freedom in the model.

The ρ_M histograms for the on and off resonance states completely overlap as was seen for the 7.3 GHz data, showing that there is no change in magnetisation. The uncertainty in ρ_M is large, with $2\sigma = 0.46$ for the off state, which is over 10% of the mean value. This demonstrates that the sensitivity to magnetisation using this measurement geometry and 9 hour counting times is too poor to observe small changes in magnetisation.

Similarly to the 7.3 GHz results, the mean values for the off and on resonance θ_M lie outside of the σ range of the other. The fitting for the 6.6 GHz data set gives a larger change in angle between the off and on states of $(0.5 \pm 0.4)^\circ$ compared to the $(0.2 \pm 0.3)^\circ$ degrees for the 7.3 GHz results. In both data sets the on resonance state is at a greater angle than the off resonance state. However, for the 7.3 GHz data this shift in angle means that the on resonance state is moved towards being perpendicular

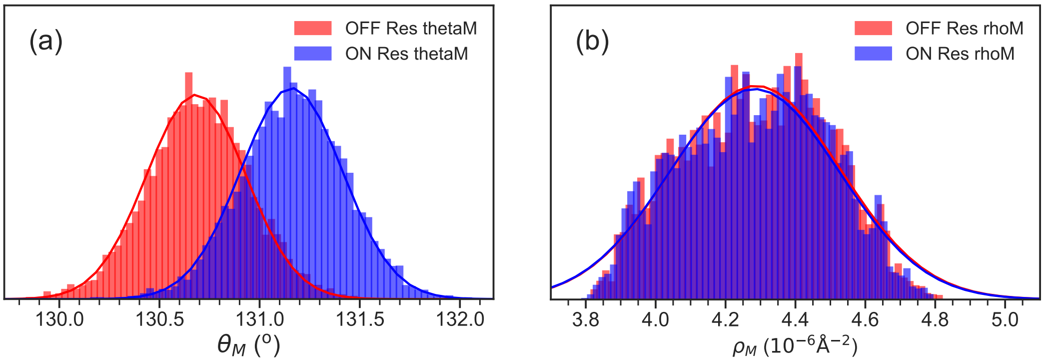

Figure 6.28: Probability histograms for the magnitude of the magnetisation angle (θ_M) (a) and the magnetic moment (ρ_M) (b) for the on and off states obtained from the fits for the 6.6 GHz data shown in figure 6.26. The solid lines show a Gaussian fit to the histogram.

Parameter	Mean Value	σ range	2σ range
Off ρ_M	4.29	(4.05, 4.51)	(3.91, 4.66)
On ρ_M	4.28	(4.05, 4.50)	(3.91, 4.65)
Off θ_M	130.70	(130.45, 130.94)	(130.20, 131.19)
On θ_M	131.17	(130.91, 131.42)	(130.66, 131.67)

Table 6.9: ρ_M and θ_M fitting parameter results for the on and off resonance PNR data sets shown in figure 6.26.

to the neutron polarisation angle whereas for the 6.6 GHz data this change moves the on resonance state towards being anti-parallel to the neutron polarisation. It should be noted that the angle of 131° is physically in the opposite direction than the 34° in the 7.3 GHz data set, however, as the PNR results for positive and negative angles are symmetric, all of the angles are quoted as positive numbers for ease. Figure 6.27 shows a schematic to show the angles in relation to each other. Although the sample is rotated 180° between the two measurements, the neutron guide field acts on the sample in the opposite direction in each case hence why the magnetisation angles are not exactly 180° from each other in the fitting results. The θ_M 2σ range for the 6.6 GHz data is 0.49 which is almost 50% greater than that of the 7.3 GHz data. This is because the counting time for the 6.6 GHz data is much smaller and so the uncertainty in the reflectivity channels is significantly larger. However, we still see that with only 9 hours of counting for each state, the required angle change is still less than 1°, showing that the angular resolution of this measurement technique is very good.

We can extend the simulation analysis as described in section 6.3.1 to the magnetisation angle range of 90° to 180° and compare to the experimental results for this measurement. The simulation results, shown in figure 6.29, show that at 130° the expected change in effective magnetisation angle due to FMR precession is the opposite sign for the spin asymmetry and spin-flip scattering. The interpretation of how these results would manifest in one combined 4 spin state measurement is not clear. The change in magnetisation angle experimentally is positive; that is, the magnetisation angle of the on state is greater than the off state. This is consistent with the simulated changes for the spin-flip component. However, the simulations suggest that the change in spin asymmetry due to FMR precession would appear as a reduction in magnetisation angle, with an initial magnetisation angle of 130°. Another implication of the

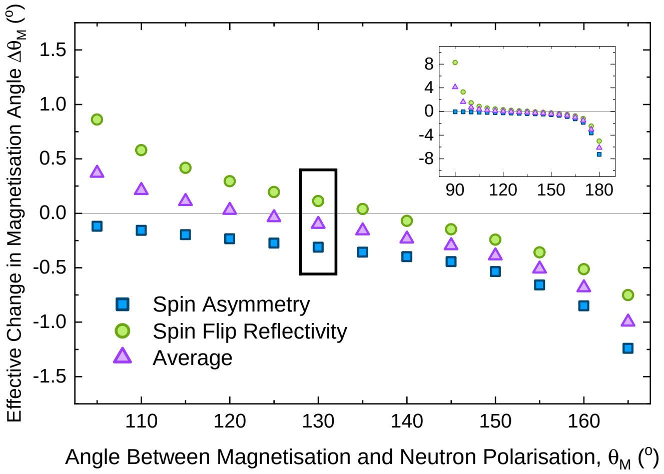

Figure 6.29: The effective change in magnetisation angle calculated from the simulations of the on and off resonance states for an initial magnetisation angle of between 90° and 180°. The inset shows the full range and the main plot is zoomed in to 105° to 165°. The black box highlights the results for 130° which corresponds to the initial sample angle for the 6.6 GHz experimental results. Note that all of the preceding simulations have assumed a cone angle of 5°.

simulations is that the observed change in magnetisation angle should be larger at an initial magnetisation angle of 35° than at 130°. This is not the case in the experimental results as at a starting magnetisation angle of 35° (7.3 GHz data), the change in θ_M was $(0.2 \pm 0.3)°$ whereas at 130° (6.6 GHz data) the change was $(0.5 \pm 0.4)°$. Nonetheless, some factors change between the two measurements which mean that a direct comparison is not completely accurate. First, the count time is substantially different. The 7.3 GHz data had over 3 times the count time of the 6.6 GHz data meaning that the uncertainty in the extracted fitting parameters varies significantly between the two results. Also, the cone angle is inversely proportional to the microwave frequency so the cone angle at 6.6 GHz should be slightly larger than the cone angle at 7.3 GHz. Overall, the experimental results for the 6.6 GHz data presented here are somewhat inconsistent with the simulation results. However, there is insufficient information to either confirm or deny the simulation methodology or conclusions. In future experiments, many different initial magnetisation angles or frequencies could be used to test the conclusions of the simulation results more thoroughly.

6.4 Improving the Measurement Technique

The results presented in this chapter demonstrate the ability to detect the FMR precession of the magnetisation using PNR measurements and furthered our understanding of how a PNR measurement interacts with a dynamic system. The results show that the microwave cavity can be used for FMR measurements without negatively impacting the PNR measurements by blocking or depolarising the beam.

Using a measurement sample geometry whereby the sample magnetisation was at an angle to the neutron polarisation, the magnetisation angle values, θ_M, were different between the on and off states. Qualitatively, this can be seen by the small but clear difference in the parameter probability histograms in figure 6.19. The difference in the mean θ_M of the on and off states was 0.19, just larger than the 1σ range of 0.17. Although the uncertainty ranges of θ_M for the on and off states did overlap, the comparison between the parameter histograms of θ_M and ρ_M for this sample clearly showed the difference between a parameter that is the same in both states and one that had changed. The clear difference in magnetisation angle between the two states is evidence that we have successfully measured the change in magnetisation due to FMR precession using an in-situ PNR measurement.

In terms of improvements to the measurement technique, some conclusions are clear from our measurements and fitting analysis. First, we have seen that being able to measure the magnetisation angle is vital when attempting to measure FMR precession using PNR. The fitting results show that the change in magnetisation needed to see clear differences between on and off resonance outside of uncertainty ranges is equivalent to a cone angle of over 20°. In contrast, we find that an effective cone angle of 4.6° could be resolved when fitting the magnetisation angle. This result also shows that, when producing a sample for this experiment, it is the cone angle, rather than the magnetisation, that is most important.

To be able to calculate the cone angle of a material, we follow the derivations in Gaun et al [273] and Mosendz et al [223]. From this, we obtain a relationship for the cone angle ϕ_c as follows

$$\phi_c \propto \frac{H_{rf}}{\alpha\omega} \tag{6.6}$$

where H_{rf} is the magnitude of the RF magnetic field produced by the microwave source, α is the Gilbert damping parameter and ω is the precession frequency. This relationship shows the three main parameters that can be changed to increase the FMR cone angle.

The Gilbert damping is the only of these three parameters that is dictated by the sample structure used. For our experiments, we decided to use Co instead of a magnetic material such as Py which has a lower α as Co has a larger magnetisation and therefore any changes in effective magnetisation would be greater. If one was to solely focus on observing a change in magnetisation angle then switching to Py could help to improve the experiment. YIG is not factored into this comparison because for the magnetisation angle to be measurable, the sample magnetisation must be at some angle to the neutron polarisation and for this reason, the sample structure requires a relatively strong anisotropy. This would be extremely hard to achieve in a YIG system because for YIG to have its low damping, it must be crystalline and therefore requires specific growth conditions and substrates and/or annealing treatment [277–280]. Therefore, it is very difficult to use YIG in multilayer systems, such as the samples we have used in out measurements, because the high annealing temperatures would destroy the interfaces and cause diffusion within the sample. Recently, it has been found that certain alloy compositions of CoFe have very low Gilbert damping of the order of 10^{-3} [65]. Therefore, this could be a candidate magnetic material that would combine a low Gilbert damping, and therefore larger cone angle, as well as a larger magnetisation.

The precession frequency is limited by the microwave cavity used. All cavities have a range of frequencies that they can operate over, determined by their size. To access lower frequency ranges a larger microwave cavity would be needed. This would bring other benefits as a larger cavity would allow a larger sample to be used which would maximise the flux. If the sample could be increased from the 10 mm × 10 mm size used in our measurements to a 20 mm × 20 mm sample, then the flux would be 4 times larger. Increasing flux means that the uncertainty in the reflectivity is reduced and therefore the resolution in the fitting parameters would improve. However, in the current iteration of the experiment, it is not so simple. As the sample magnetisation is not aligned to the applied neutron guide field, the FMR measurement is effectively a zero-field measurement. Therefore, the minimum FMR frequency is dictated by the sample behaviour. If we look back to the FMR measurements for the Co/FeMn multilayer sample that was used for the previous measurements as seen in figure 6.11, we see that the minimum FMR frequency of the sample is just over 4 GHz and for this an applied field of around 200 Oe is required.

The amplitude of the RF magnetic field is determined by the input microwave power. Any connections between wires, the VNA or the microwave cavity itself cause losses meaning that the microwave power that reaches the cavity to produce the magnetic field is significantly reduced from the power initially supplied by the VNA. When performing the experiment we took measures to reduce this by using 1 cable that was as short as possible which was kept as straight as possible whilst also avoiding the beam path. Still, some losses are unavoidable. Also, as in a cavity FMR setup there is one in/out port so the VNA is both producing the microwave output and measuring the returning signal. Therefore, there is a limit to how much power returns to the VNA so that it is not damaged.

CHAPTER 7

Conclusion

7.1 Controlled Ionic Diffusion in Molecular Thin Films Summary

In Chapter 5, controlled ionic diffusion in molecular thin films of C_{60} was investigated using trilayer samples of C_{60}/CoB/C_{60}. SQUID measurements showed that the room temperature magnetisation increased by approximately 50% after annealing at 300°C. This was evidence of B leaving the CoB layer, leaving Co rich regions that have a larger magnetisation. In a sample containing Co in place of CoB, the magnetisation increased by only around 10%, showing that there is some effect of crystallisation but this cannot explain the large increase in magnetisation in the CoB sample. SQUID measurements of the magnetic moment during annealing showed the moment of the CoB sample increasing throughout the annealing process, whereas the moment of the Co sample stayed constant after the first 4 hours. This was further evidence of annealing causing B to migrate from the CoB, leaving Co rich regions with higher magnetisation.

The investigation was continued using PNR measurements. The sample was measured before, after and during a 300°C anneal by using an in-situ vacuum furnace. The observed changes in the sample due to annealing were:

- The decrease in B% mass of CoB layer from $(13.0 \pm 0.1)\%$ to $(10.3 \pm 0.1)\%$ corresponding to atomic percentages of $(44.9 \pm 0.8)\%$ and $(38 \pm 3)\%$ respectively
- B rich regions in the C_{60} close to the cap and substrate interfaces
- Reduction in the CoB thickness from (142 ± 3)Å to (82 ± 7)Å
- 80% increase of the magnetisation in the CoB layer

Another notable feature in the PNR results was a substantial reduction in the top C_{60} density which was hypothesised to be due to metallic Al from the cap diffusing into the C_{60} layer. Through PNR measurements during annealing, the reduction in the B composition of the CoB layer and C_{60} density changing over time was observed. These results showed the capabilities of PNR with in-situ heating to monitor structural changes during the annealing process.

To investigate the ability to control the movement of ions in the C_{60} layers using a gate voltage a sample holder was developed to allow for electrical contact with the sample in-situ in addition to sample heating. During the study of this sample, two annealing steps were performed at 200°C and 250°C to inject B into the C_{60} for gating afterwards. A summary of the changes seen due to annealing for these measurements compared to the 300°C anneal is shown in table 7.1 This study also confirmed the hypothesis from previous samples that the metallic Al was diffusing into the top C_{60} layer as the Al cap on this sample was thinner meaning that more of it had oxidised and there was no significant decrease in the top C_{60} density.

Change compared to as-grown sample	Anneal Temperature		
	200°	250°	300°
Reduction in B Mass % of CoB	1.1 ± 0.5	1.72 ± 0.4	2.8 ± 0.8
Reduction in B atomic % of CoB	3 ± 2	4 ± 2	7 ± 4
Reduction in CoB thickness (Å)	10 ± 5	20 ± 4	60 ± 8
Increase in magnetic moment (%)	30 ± 50	20 ± 30	80 ± 30

Table 7.1: Comparison of the changes due to annealing at different temperatures observed in the PNR measurements. The sample for the 200°C and 250°C measurements was $Si/SiOx/Nb/C_{60}/CoB/C_{60}/Al$ and for the 300°C measurement the sample was $Si/SiOx/C_{60}/CoB/C_{60}/Al$.

7.1.1 Future Work

The results presented in this thesis provide evidence of the ability to force migration of B from CoB into adjacent layers of C_{60}. Future investigations should focus on optimising the gated control of ions in the C_{60} layers. Including a top electrode in the structure would allow for electric fields to act across the trilayer. This would allow for PNR studies of the voltage control of B migration and bring the research closer to device applications. Magnetic measurements such as Kerr microscopy or VSM could be used either with in-situ gating or after an applied gate voltage to more closely investigate the changes in the magnetisation and anisotropy due to the movement of ions. Another avenue of research is to investigate the impacts of grain size on ionic diffusion in molecular thin films. Using the Royce Deposition System at the University of Leeds, it is possible to grow highly crystalline C_{60} films [281, 282]. Comparing the diffusion between the amorphous C_{60} samples used in this thesis and crystalline films would help to understand how to optimise the sample growth for gated ionic migration.

The ability to control the flow of ions in C_{60} using a gate voltage would make it a potential alternative to ionic liquids for the gated control of magnetism. Current ionic liquid devices utilise O injection from the ionic liquid or solid electrolyte to alter the magnetic state of Co [33, 283]. By instead using C_{60} thin films, devices would be able to be made much smaller and have full functionality at low temperatures.

7.2 FMR-PNR Summary

Chapter 6 presented the development of the in-situ FMR-PNR measurement technique. The results show that the microwave cavity can be used for FMR measurements without negatively impacting the PNR measurements by blocking or depolarising the beam. In the aligned magnetisation and neutron polarisation measurement geometry, the difference between the on and off state ρ_M values was an order of magnitude less than its uncertainty resulting in a change in ρ_M of $(0.0 \pm 0.1) \times 10^{-6} \text{Å}^{-2}$ meaning there is no measurable change in magnetisation. The cone angle needed to observe a 2σ change in ρ_M in this geometry under our measurement conditions (e.g sample, flux, count time) was estimated to be approximately 18°. These results demonstrated that performing the experiment with a half polarised PNR measurement would require either a very large cone angle of the order of 20° or extremely long counting times to fully separate the measured magnetisation in the on and off states.

The experiment was performed again in a different configuration where a 4 spin state measurement was used to allow for the magnetisation angle as well as the magnitude to be extracted from fitting. An exchange bias multilayer was used so that the sample had a strong enough anisotropy so that the magnetisation would remain at the desired angle when the neutron guide field was applied. In these measurements, the off and on resonance mean ρ_M values were equal with values of $4.3 \pm 0.2 \times 10^{-6} \text{Å}^{-2}$ for both states. The difference in the mean θ_M of the on and off states was $(0.2 \pm 0.3)^{\circ}$. The θ_M parameter probability histograms showed a clear separation which suggests that the change in magnetisation angle is significant. This was supported by comparing to the ρ_M histograms which demonstrated that if the parameter did not change between the on and off states, the parameter histograms would completely overlap. The difference in magnetisation angle between the two states is evidence that we have successfully measured the change in magnetisation due to FMR precession using an in-situ PNR measurement.

Difference between on and off states	Aligned Geometry	Angular Sensitivity	
	ρ_M	ρ_M	θ_M
Experimental	$(0.01 \pm 0.1) \times 10^{-6}\text{Å}^{-2}$	0	$(0.2 \pm 0.3)^\circ$
Estimated cone angle	$(4 \pm 30)^\circ$	0	$(3 \pm 2)^\circ$
Required for 2σ separation	$0.19\ \times 10^{-6}\text{Å}^{-2}$	$0.36\ \times 10^{-6}\text{Å}^{-2}$	0.34°
Cone angle for 2σ separation	18°	25°	4.6°

Table 7.2: Comparison of the differences observed between the on and off states during the FMR-PNR measurements using two different measurement geometries. The sample used for the aligned geometry was Si/SiOx/Ru/[Co/Ru]x10, and for the angular sensitivity measurement the sample was Si/SiOx/Ta/[Co/FeMn]x10/Ta.

Simulations have been used to explain the reason why the FMR precession can be observed in a PNR experiment as a change in the PNR angle. The simulations showed that, if we consider the time average of the FMR precession in the on state to act as the average of a positive and negative change in angle by ϕ_C about the initial magnetisation angle, the resulting PNR signal will be different to the off state where there is no deviation about the initial angle. Using these simulation results, it was found that the change in magnetisation angle in PNR was proportional to the square of the FMR cone angle,

$$\Delta\theta_M \propto \phi_C^2$$

This clearly shows that the PNR measurement of the magnetisation angle is much more sensitive than the magnetisation magnitude to the FMR precession and therefore a 4 spin state PNR measurement where the magnetisation angle can be extracted is essential for this experiment.

7.2.1 Future Work FMR-PNR

The results for this experiment presented in this thesis do show changes in the sample magnetisation measured using PNR when it is in an FMR precession. However, the changes observed were small and therefore to move this new measurement technique towards further applications in research uses such as the depth-dependent measurements of the damping and cone angle described in the introduction to this thesis, the measurement resolution needs to be improved. This can be done by either increasing the FMR cone angle or increasing the PNR measurement flux. The cone angle is related to the RF magnetic field, Gilbert damping and resonant frequency by $\phi_c \propto \frac{H_{rf}}{\alpha\omega}$. Therefore, the cone angle can be increased by increasing the RF magnetic field strength or reducing the sample Gilbert damping or the resonant frequency used.

As a microwave cavity is used for FMR, the operational frequency range is governed by the size of the cavity. The operational frequency range of the cavity used in our experiments was 5 - 8.3 GHz. A larger cavity would be required to access smaller frequencies. This would also provide other benefits to the experiment as it would allow for the use of a larger sample. In our work, a 10 mm × 10 mm sample was used, whereas, in a larger cavity where the RF magnetic field is constant over a wider area, a larger 15 mm × 15 mm or 20 mm × 20 mm sample could be used. This would have the benefit of increasing the PNR measurement flux, leading to an improvement in the resolution of the PNR measurement. With less uncertainty in each PNR data point, the extracted values of ρ_M and θ_M from fitting would also have smaller uncertainty therefore meaning that smaller changes between the on and off states can be resolved. Increasing the RF magnetic field strength would be a universal way to increase the cone angle, irrespective of the sample damping or resonance conditions. In a cavity, the magnetic field strength is proportional to the square root of the input power of the microwave signal, so an increase in the input power will increase the RF field strength.

Once optimised, this measurement technique could be used to perform depth dependant measurements of the cone angle and damping as well as to investigate spin pumping effects.

REFERENCES

[1] P. Barla, V. K. Joshi, and S. Bhat, “Spintronic devices: a promising alternative to CMOS devices,” *Journal of Computational Electronics*, vol. 20, no. 2, pp. 805–837, 2021.

[2] Ching Tsang, R. Fontana, Tsann Lin, D. Heim, V. Speriosu, B. Gurney, and M. Williams, “Design, fabrication and testing of spin-valve read heads for high density recording,” *IEEE Transactions on Magnetics*, vol. 30, no. 6, pp. 3801–3806, 1994.

[3] J. S. Moodera, L. R. Kinder, T. M. Wong, and R. Meservey, “Large magnetoresistance at room temperature in ferromagnetic thin film tunnel junctions,” *Physical Review Letters*, vol. 74, no. 16, pp. 3273–3276, 1995.

[4] S. Ikeda, K. Miura, H. Yamamoto, K. Mizunuma, H. D. Gan, M. Endo, S. Kanai, J. Hayakawa, F. Matsukura, and H. Ohno, “A perpendicular-anisotropy CoFeB-MgO magnetic tunnel junction,” *Nature Materials*, vol. 9, no. 9, pp. 721–724, 2010.

[5] J. Åkerman, “Toward a universal memory,” *Science*, vol. 308, no. 5721, pp. 508–510, 2005.

[6] M. Natsui, A. Tamakoshi, H. Honjo, T. Watanabe, T. Nasuno, C. Zhang, T. Tanigawa, H. Inoue, M. Niwa, T. Yoshiduka, Y. Noguchi, M. Yasuhira, Y. Ma, H. Shen, S. Fukami, H. Sato, S. Ikeda, H. Ohno, T. Endoh, and T. Hanyu, “Dual-Port SOT-MRAM Achieving 90-MHz Read and 60-MHz Write Operations under Field-Assistance-Free Condition,” *IEEE Journal of Solid-State Circuits*, vol. 56, no. 4, pp. 1116–1128, 2021.

[7] D. Apalkov, A. Khvalkovskiy, S. Watts, V. Nikitin, X. Tang, D. Lottis, K. Moon, X. Luo, E. Chen, A. Ong, A. Driskill-Smith, and M. Krounbi, "Spin-transfer torque magnetic random access memory (STT-MRAM)," *ACM Journal on Emerging Technologies in Computing Systems*, vol. 9, no. 2, pp. 1–35, 2013.

[8] S. Tehrani, J. M. Slaughter, M. DeHerrera, B. N. Engel, N. D. Rizzo, J. Salter, M. Durlam, R. W. Dave, J. Janesky, B. Butcher, K. Smith, and G. Grynkewich, "Magnetoresistive random access memory using magnetic tunnel junctions," *Proceedings of the IEEE*, vol. 91, no. 5, pp. 703–712, 2003.

[9] K. D. Stenning, X. Xiao, H. H. Holder, J. C. Gartside, A. Vanstone, O. W. Kennedy, R. F. Oulton, and W. R. Branford, "Low-power continuous-wave all-optical magnetic switching in ferromagnetic nanoarrays," *Cell Reports Physical Science*, vol. 4, no. 3, p. 101291, 2023.

[10] Y. L. van Hees, P. van de Meugheuvel, B. Koopmans, and R. Lavrijsen, "Deterministic all-optical magnetization writing facilitated by non-local transfer of spin angular momentum," *Nature Communications*, vol. 11, no. 1, 2020.

[11] A. V. Kimel and M. Li, "Writing magnetic memory with ultrashort light pulses," *Nature Reviews Materials*, vol. 4, no. 3, pp. 189–200, 2019.

[12] C. H. Lambert, S. Mangin, B. S. S. Varaprasad, Y. K. Takahashi, M. Hehn, M. Cinchetti, G. Malinowski, K. Hono, Y. Fainman, M. Aeschlimann, and E. E. Fullerton, "All-optical control of ferromagnetic thin films and nanostructures," *Science*, vol. 345, no. 6202, pp. 1337–1340, 2014.

[13] W. G. Wang, M. Li, S. Hageman, and C. L. Chien, "Electric-field-assisted switching in magnetic tunneljunctions," *Nature Materials*, vol. 11, no. 1, pp. 64–68, 2012.

[14] S. Kanai, M. Yamanouchi, S. Ikeda, Y. Nakatani, F. Matsukura, and H. Ohno, "Electric field-induced magnetization reversal in a perpendicular-anisotropy CoFeB-MgO magnetic tunnel junction," *Applied Physics Letters*, vol. 101, no. 12, 2012.

[15] Y. H. Chu, L. W. Martin, M. B. Holcomb, M. Gajek, S. J. Han, Q. He, N. Balke, C. H. Yang, D. Lee, W. Hu, Q. Zhan, P. L. Yang, A. Fraile-Rodríguez, A. Scholl,

S. X. Wang, and R. Ramesh, “Electric-field control of local ferromagnetism using a magnetoelectric multiferroic,” *Nature Materials*, vol. 7, no. 6, pp. 478–482, 2008.

[16] C. Song, B. Cui, F. Li, X. Zhou, and F. Pan, “Recent progress in voltage control of magnetism: Materials, mechanisms, and performance,” *Progress in Materials Science*, vol. 87, pp. 33–82, 2017.

[17] J. De Rojas, A. Quintana, G. Rius, C. Stefani, N. Domingo, J. L. Costa-Krämer, E. Menéndez, and J. Sort, “Voltage control of magnetism with magneto-ionic approaches: Beyond voltage-driven oxygen ion migration,” *Applied Physics Letters*, vol. 120, no. 7, 2022.

[18] K. Uchida, S. Takahashi, K. Harii, J. Ieda, W. Koshibae, K. Ando, S. Maekawa, and E. Saitoh, “Observation of the spin Seebeck effect,” *Nature*, vol. 455, no. 7214, pp. 778–781, 2008.

[19] S. Liu, M. Chen, C. Fu, and T. Zhu, “The Interplay of Magnetism and Thermoelectricity: A Review,” *Advanced Physics Research*, vol. 2, no. 9, 2023.

[20] A. Meo, J. Chureemart, R. W. Chantrell, and P. Chureemart, “Magnetisation switching dynamics induced by combination of spin transfer torque and spin orbit torque,” *Scientific Reports*, vol. 12, no. 1, pp. 1–14, 2022.

[21] C. O. Avci, A. Quindeau, C. F. Pai, M. Mann, L. Caretta, A. S. Tang, M. C. Onbasli, C. A. Ross, and G. S. Beach, “Current-induced switching in a magnetic insulator,” *Nature Materials*, vol. 16, no. 3, pp. 309–314, 2017.

[22] S. J. Callori, J. Bertinshaw, D. L. Cortie, J. W. Cai, A. P. Le Brun, T. Zhu, and F. Klose, “90° magnetic coupling in a NiFe/FeMn/biased NiFe multilayer spin valve component investigated by polarized neutron reflectometry,” *Journal of Applied Physics*, vol. 116, no. 3, 2014.

[23] M. Pannetier, T. D. Doan, F. Ott, S. Berger, N. Persat, and C. Fermon, “Polarised neutron reflectometry for GMR sensors optimization,” *Europhysics Letters*, vol. 64, no. 4, pp. 524–528, 2003.

[24] H. Zabel, K. Theis-Bröhl, M. Wolff, and B. P. Toperverg, “Polarized neutron reflectometry for the analysis of nanomagnetic systems,” *IEEE Transactions on Magnetics*, vol. 44, no. 7, pp. 1928–1934, 2008.

[25] M. R. Fitzsimmons, P. Yashar, C. Leighton, I. K. Schuller, J. Nogués, C. F. Majkrzak, and J. A. Dura, "Asymmetric magnetization reversal in exchange-biased hysteresis loops," *Physical Review Letters*, vol. 84, no. 17, pp. 3986–3989, 2000.

[26] X. Z. Zhan, G. Li, J. W. Cai, T. Zhu, J. F. Cooper, C. J. Kinane, and S. Langridge, "Probing the Transfer of the Exchange Bias Effect by Polarized Neutron Reflectometry," *Scientific Reports*, vol. 9, no. 1, pp. 1–9, 2019.

[27] T. Moorsom, M. Wheeler, T. Mohd Khan, F. Al Ma'Mari, C. Kinane, S. Langridge, D. Ciudad, A. Bedoya-Pinto, L. Hueso, G. Teobaldi, V. K. Lazarov, D. Gilks, G. Burnell, B. J. Hickey, and O. Cespedes, "Spin-polarized electron transfer in ferromagnet/C_{60} interfaces," *Physical Review B*, vol. 90, no. 12, p. 125311, 2014.

[28] S. Singh and S. Basu, "Investigation of interface magnetism of complex oxide heterostructures using polarized neutron reflectivity," *Current Applied Physics*, vol. 17, no. 5, pp. 615–625, 2017.

[29] T. L. Meyer, A. Herklotz, V. Lauter, J. W. Freeland, J. Nichols, E. J. Guo, S. Lee, T. Z. Ward, N. Balke, S. V. Kalinin, M. R. Fitzsimmons, and H. N. Lee, "Enhancing interfacial magnetization with a ferroelectric," *Physical Review B*, vol. 94, no. 17, 2016.

[30] G. L. Causer, M. Kostylev, D. L. Cortie, C. Lueng, S. J. Callori, X. L. Wang, and F. Klose, "In Operando Study of the Hydrogen-Induced Switching of Magnetic Anisotropy at the Co/Pd Interface for Magnetic Hydrogen Gas Sensing," *ACS Applied Materials and Interfaces*, vol. 11, no. 38, pp. 35420–35428, 2019.

[31] C. Leighton, "Electrolyte-based ionic control of functional oxides," *Nature Materials*, vol. 18, no. 1, pp. 13–18, 2019.

[32] A. Goldman, "Electrostatic Gating of Ultrathin Films," *Annual Review of Materials Research*, vol. 44, no. 1, pp. 45–63, 2014.

[33] J. Yang, X. Wang, X. Jia, Y. Zhang, X. Li, Z. Quan, Z. Zeng, and X. Xu, "Ionic liquid gating control of magnetism of a Co film," *Journal of Magnetism and Magnetic Materials*, vol. 515, no. May, p. 167261, 2020.

[34] Q. Yang, L. Wang, Z. Zhou, L. Wang, Y. Zhang, S. Zhao, G. Dong, Y. Cheng, T. Min, Z. Hu, W. Chen, K. Xia, and M. Liu, "Ionic liquid gating control of RKKY interaction in FeCoB/Ru/FeCoB and (Pt/Co) 2 /Ru/(Co/Pt) 2 multilayers," *Nature Communications*, vol. 9, no. 1, pp. 1–11, 2018.

[35] Y. Guan, H. Han, F. Li, G. Li, and S. S. Parkin, "Ionic Gating for Tuning Electronic and Magnetic Properties," *Annual Review of Materials Research*, vol. 53, pp. 25–51, 2023.

[36] Y. Zhang, G. Dubuis, C. Doyle, T. Butler, and S. Granville, "Nonvolatile and Volatile Skyrmion Generation Engineered by Ionic Liquid Gating in Ultrathin Films," *Physical Review Applied*, vol. 16, no. 1, p. 1, 2021.

[37] T. Hirai, T. Koyama, A. Obinata, Y. Hibino, K. Miwa, S. Ono, M. Kohda, and D. Chiba, "Control of magnetic anisotropy in Pt/Co system using ionic liquid gating," *Applied Physics Express*, vol. 9, no. 6, 2016.

[38] L. Reichel, S. Oswald, S. Fähler, L. Schultz, and K. Leistner, "Electrochemically driven variation of magnetic properties in ultrathin CoPt films," *Journal of Applied Physics*, vol. 113, no. 14, 2013.

[39] N. Lu, P. Zhang, Q. Zhang, R. Qiao, Q. He, H. B. Li, Y. Wang, J. Guo, D. Zhang, Z. Duan, Z. Li, M. Wang, S. Yang, M. Yan, E. Arenholz, S. Zhou, W. Yang, L. Gu, C. W. Nan, J. Wu, Y. Tokura, and P. Yu, "Electric-field control of tristate phase transformation with a selective dual-ion switch," *Nature*, vol. 546, no. 7656, pp. 124–128, 2017.

[40] K. Ueno, S. Nakamura, H. Shimotani, H. T. Yuan, N. Kimura, T. Nojima, H. Aoki, Y. Iwasa, and M. Kawasaki, "Discovery of superconductivity in KTaO 3 by electrostatic carrier doping," *Nature Nanotechnology*, vol. 6, no. 7, pp. 408–412, 2011.

[41] K. Ueno, S. Nakamura, H. Shimotani, A. Ohtomo, N. Kimura, T. Nojima, H. Aoki, Y. Iwasa, and M. Kawasaki, "Electric-field-induced superconductivity in an insulator," *Nature Materials*, vol. 7, no. 11, pp. 855–858, 2008.

[42] Y. Saito, Y. Nakamura, M. S. Bahramy, Y. Kohama, J. Ye, Y. Kasahara, Y. Nakagawa, M. Onga, M. Tokunaga, T. Nojima, Y. Yanase, and Y. Iwasa, "Supercon-

ductivity protected by spin-valley locking in ion-gated MoS2," *Nature Physics*, vol. 12, no. 2, pp. 144–149, 2016.

[43] W. Shi, J. Ye, Y. Zhang, R. Suzuki, M. Yoshida, J. Miyazaki, N. Inoue, Y. Saito, and Y. Iwasa, "Superconductivity Series in Transition Metal Dichalcogenides by Ionic Gating," *Scientific Reports*, vol. 5, pp. 1–10, 2015.

[44] J. Choi, R. Pradheesh, H. Kim, H. Im, Y. Chong, and D. H. Chae, "Electrical modulation of superconducting critical temperature in liquid-gated thin niobium films," *Applied Physics Letters*, vol. 105, no. 1, pp. 1–5, 2014.

[45] T. Moorsom, *Electron transfer and spin injection in C_{60}-ferromagnetic composites.* PhD thesis, University of Leeds, 2016.

[46] J. Abrefah, D. R. Olander, M. Balooch, and W. J. Siekhaus, "Vapor pressure of Buckminsterfullerene," *Applied Physics Letters*, vol. 60, no. 11, pp. 1313–1314, 1992.

[47] S. Sanvito, "The rise of spinterface science," *Nature Physics*, vol. 6, no. 8, pp. 562–564, 2010.

[48] C. Barraud, P. Seneor, R. Mattana, S. Fusil, K. Bouzehouane, C. Deranlot, P. Graziosi, L. Hueso, I. Bergenti, V. Dediu, F. Petroff, and A. Fert, "Unravelling the role of the interface for spin injection into organic semiconductors," *Nature Physics*, vol. 6, no. 8, pp. 615–620, 2010.

[49] M. Cinchetti, V. A. Dediu, and L. E. Hueso, "Activating the molecular spinterface," *Nat Mater*, vol. 16, no. 5, pp. 507–515, 2017.

[50] F. Djeghloul, F. Ibrahim, M. Cantoni, M. Bowen, L. Joly, S. Boukari, P. Ohresser, F. Bertran, P. Le Fèvre, P. Thakur, F. Scheurer, T. Miyamachi, R. Mattana, P. Seneor, A. Jaafar, C. Rinaldi, S. Javaid, J. Arabski, J. P. Kappler, W. Wulfhekel, N. B. Brookes, R. Bertacco, A. Taleb-Ibrahimi, M. Alouani, E. Beaurepaire, and W. Weber, "Direct observation of a highly spin-polarized organic spinterface at room temperature," *Scientific Reports*, vol. 3, no. 1, 2013.

[51] F. A. Ma'Mari, T. Moorsom, G. Teobaldi, W. Deacon, T. Prokscha, H. Luetkens, S. Lee, G. E. Sterbinsky, D. A. Arena, D. A. MacLaren, M. Flokstra, M. Ali,

M. C. Wheeler, G. Burnell, B. J. Hickey, and O. Cespedes, “Beating the Stoner criterion using molecular interfaces,” *Nature*, vol. 524, p. 69, 2015.

[52] F. A. Ma’Mari, M. Rogers, S. Alghamdi, T. Moorsom, S. Lee, T. Prokscha, H. Luetkens, M. Valvidares, G. Teobaldif, M. Flokstra, R. Stewart, P. Gargiani, M. Ali, G. Burnell, B. J. Hickey, and O. Cespedes, “Emergent magnetism at transition-metal-nanocarbon interfaces,” *Proceedings of the National Academy of Sciences of the United States of America*, vol. 114, no. 22, pp. 5583–5588, 2017.

[53] T. Moorsom, S. Alghamdi, S. Stansill, E. Poli, G. Teobaldi, M. Beg, H. Fangohr, M. Rogers, Z. Aslam, M. Ali, B. J. Hickey, and O. Cespedes, “π -anisotropy: A nanocarbon route to hard magnetism,” *Physical Review B*, vol. 101, no. 6, p. 060408, 2020.

[54] S. Alotibi, B. J. Hickey, G. Teobaldi, M. Ali, J. Barker, E. Poli, D. D. O’Regan, Q. Ramasse, G. Burnell, J. Patchett, C. Ciccarelli, M. Alyami, T. Moorsom, and O. Cespedes, “Enhanced Spin-Orbit Coupling in Heavy Metals via Molecular Coupling,” *ACS Applied Materials & Interfaces*, vol. 13, no. 4, pp. 5228–5234, 2021.

[55] A. Goel, J. B. Howard, and J. B. Sande, “Size analysis of single fullerene molecules by electron microscopy,” *Carbon*, vol. 42, no. 10, pp. 1907–1915, 2004.

[56] L. Yin, J. Cho, S. J. Kim, I. Jeon, I. Jeon, M. Park, M. Park, S. Y. Jeong, D. H. Lee, D. H. Seo, and C. R. Cho, “Abnormally High-Lithium Storage in Pure Crystalline C_{60} Nanoparticles,” *Advanced Materials*, vol. 33, no. 43, pp. 1–11, 2021.

[57] M. Okubo, Y. Tanaka, H. Zhou, T. Kudo, and I. Honma, “Determination of activation energy for Li ion diffusion in electrodes,” *Journal of Physical Chemistry B*, vol. 113, no. 9, pp. 2840–2847, 2009.

[58] K. Nakamura, H. Ohno, K. Okamura, Y. Michihiro, T. Moriga, I. Nakabayashi, and T. Kanashiro, “^{7}Li NMR study on Li^+ ionic diffusion and phase transition in Li_xCoO_2,” *Solid State Ionics*, vol. 177, no. 9-10, pp. 821–826, 2006.

[59] M. D. Levi, G. Salitra, B. Markovsky, H. Teller, D. Aurbach, U. Heider, and L. Heider, “Solid-State Electrochemical Kinetics of Li-Ion Intercalation into

$Li_{1-x}CoO_2$: Simultaneous Application of Electroanalytical Techniques SSCV, PITT, and EIS," *Journal of The Electrochemical Society*, vol. 146, pp. 1279–1289, apr 1999.

[60] R. Tärneberg and A. Lunden, "Ion diffusion in the high-temperature phases Li_2SO_4, $LiNaSO_4$, $LiAgSO_4$ and $Li_4Zn(SO_4)_3$," *Solid State Ionics*, vol. 90, pp. 209–220, sep 1996.

[61] E. A. Katz, D. Faiman, S. M. Tuladhar, S. Shtutina, N. Froumin, M. Polak, and Y. Strzhemechny, "Diffusion processes for doping of C_{60} (fullerene) thin films," *Solar Energy Materials and Solar Cells*, vol. 75, no. 3-4, pp. 421–426, 2003.

[62] L. Firlej, A. Zahab, F. Brocard, and N. Kirova, "Contact electrode diffusion into C_{60} thin films," *Synthetic Metals*, vol. 86, no. 1-3, pp. 2331–2332, 1997.

[63] A. Zahab, L. Firlej, F. Brocard, and N. Kirova, "Field-induced metal diffusion into C_{60} thin films," *Synthetic Metals*, vol. 77, pp. 59–61, feb 1996.

[64] J. M. Shaw, H. T. Nembach, T. J. Silva, and C. T. Boone, "Precise determination of the spectroscopic g-factor by use of broadband ferromagnetic resonance spectroscopy," *Journal of Applied Physics*, vol. 114, no. 24, pp. 1–11, 2013.

[65] M. A. Schoen, D. Thonig, M. L. Schneider, T. J. Silva, H. T. Nembach, O. Eriksson, O. Karis, and J. M. Shaw, "Ultra-low magnetic damping of a metallic ferromagnet," *Nature Physics*, vol. 12, no. 9, pp. 839–842, 2016.

[66] G. B. Stenning, L. R. Shelford, S. A. Cavill, F. Hoffmann, M. Haertinger, T. Hesjedal, G. Woltersdorf, G. J. Bowden, S. A. Gregory, C. H. Back, P. A. De Groot, and G. V. Van Der Laan, "Magnetization dynamics in an exchange-coupled NiFe/CoFe bilayer studied by x-ray detected ferromagnetic resonance," *New Journal of Physics*, vol. 17, no. 1, p. 13019, 2015.

[67] D. M. Burn, S. L. Zhang, G. Q. Yu, Y. Guang, H. J. Chen, X. P. Qiu, G. van der Laan, and T. Hesjedal, "Depth-Resolved Magnetization Dynamics Revealed by X-Ray Reflectometry Ferromagnetic Resonance," *Physical Review Letters*, vol. 125, no. 13, p. 137201, 2020.

[68] G. Boero, S. Rusponi, P. Bencok, R. S. Popovic, H. Brune, and P. Gambardella, “X-ray ferromagnetic resonance spectroscopy,” *Applied Physics Letters*, vol. 87, no. 15, pp. 1–3, 2005.

[69] D. M. Burn, S. Zhang, K. Zhai, Y. Chai, Y. Sun, G. Van Der Laan, and T. Hesjedal, “Mode-Resolved Detection of Magnetization Dynamics Using X-ray Diffractive Ferromagnetic Resonance,” *Nano Letters*, vol. 20, no. 1, pp. 345–352, 2020.

[70] M. Kostylev, G. L. Causer, C.-H. H. Lambert, T. Schefer, C. Weiss, S. J. Callori, S. Salahuddin, X. L. Wang, and F. Klose, “In situ ferromagnetic resonance capability on a polarized neutron reflectometry beamline:,” *Journal of Applied Crystallography*, vol. 51, no. 1, pp. 9–16, 2018.

[71] S. Blundell, *Magnetism in Condensed Matter.* Oxford University Press, Incorporated, 2001.

[72] M. Rogers, *Novel spin functionalities of C60 based metallo-molecular interfaces.* PhD thesis, University of Leeds, 2019.

[73] J. M. D. Coey, *Magnetism and Magnetic Materials.* Cambridge University Press, 2009.

[74] J. Stöhr and H. C. Siegmann, *Magnetism : from fundamentals to nanoscale dynamics.* Springer series in solid-state sciences, 152, Berlin: Springer, 2006.

[75] C. E. A. Barker, *Investigating the Static and Dynamic Properties of Skyrmions in a Synthetic Antiferromagnet.* PhD thesis, University of Leeds, 2023.

[76] C. Kittel, *Introduction to Solid State Physics.* Wiley and Sons, Inc, 8th ed., 2005.

[77] K. Spörl and D. Weller, “Interface anisotropy and chemistry of magnetic multilayers: Au/Co, Pt/Co and Pd/Co,” *Journal of Magnetism and Magnetic Materials*, vol. 93, pp. 379–385, feb 1991.

[78] M. T. Johnson, P. J. H. Bloemen, F. J. A. den Broeder, and J. J. de Vries, “Magnetic anisotropy in metallic multilayers,” *Rep. Prog. Phys.*, no. 59, 1996.

[79] I. Benguettat-El Mokhtari, D. Ourdani, Y. Roussigné, R. B. Mos, M. Nasui, F. Kail, L. Chahed, S. M. Chérif, A. Stashkevich, M. Gabor, and M. Belmeguenai, "Perpendicular magnetic anisotropy and interfacial Dzyaloshinskii-Moriya interaction in as grown and annealed X/Co/Y ultrathin systems," *Journal of Physics Condensed Matter*, vol. 32, no. 49, 2020.

[80] R. H. Zhao, Z. Y. Ren, J. P. Cao, Y. S. Yuan, G. L. Zhao, X. G. Xu, K. K. Meng, J. Miao, and Y. Jiang, "Influence of heavy-metal capping layers on perpendicular magnetic anisotropy and spin-orbit torques of Pt/Co/HM stacks structures," *Solid State Communications*, vol. 332, no. October 2020, 2021.

[81] X. Ma, G. Yu, C. Tang, X. Li, C. He, J. Shi, K. L. Wang, and X. Li, "Interfacial Dzyaloshinskii-Moriya Interaction: Effect of 5d Band Filling and Correlation with Spin Mixing Conductance," *Physical Review Letters*, vol. 120, no. 15, 2018.

[82] S. Bandiera, R. R. Sousa, B. B. Rodmacq, and B. Dieny, "Asymmetric Interfacial Perpendicular Magnetic Anisotropy in Pt/Co/Pt Trilayers," *IEEE Magnetics Letters*, vol. 2, pp. 3000504–3000504, 2011.

[83] N. Nakajima, T. Koide, T. Shidara, H. Miyauchi, H. Fukutani, A. Fujimori, K. Iio, T. Katayama, M. Nývlt, and Y. Suzuki, "Perpendicular Magnetic Anisotropy Caused by Interfacial Hybridization via Enhanced Orbital Moment in ¡math display="inline"¿ ¡mi¿Co¡/mi¿ ¡mi¿/¡/mi¿ ¡mi¿Pt¡/mi¿ ¡/math¿ Multilayers: Magnetic Circular X-Ray Dichroism Study," *Physical Review Letters*, vol. 81, pp. 5229–5232, dec 1998.

[84] P. M. Shepley, *Effect of piezoelectric strain on the magnetic properties of Pt/Co thin films.* PhD thesis, University of Leeds, 2015.

[85] Quantum Design, "Introduction to: Broadband FMR Spectroscopy Magnetization dynamics: Landau-Lifshitz-Gilbert Equation Introduction to: Broadband FMR Spectroscopy," *Application Note 1087-201*, vol. Rev. A0, pp. 1087–201, 2017.

[86] G. B. G. Stenning, *X-ray and microwave studies of strongly exchange coupled magnetic multilayers.* PhD thesis, University of Southampton, 2013.

[87] M. A. Ruderman and C. Kittel, “Indirect exchange coupling of nuclear magnetic moments by conduction electrons,” *Physical Review*, vol. 96, no. 1, pp. 99–102, 1954.

[88] T. Kasuya, “A Theory of Metallic Ferro- and Antiferromagnetism on Zener’s Model,” *Progress of Theoretical Physics*, vol. 16, no. 1, pp. 45–57, 1956.

[89] K. Yosida, “Magnetic properties of Cu-Mn alloys,” *Physical Review*, vol. 106, no. 5, pp. 893–898, 1957.

[90] M. Stiles, “Interlayer exchange coupling,” *Journal of Magnetism and Magnetic Materials*, vol. 200, no. 1-3, pp. 322–337, 1999.

[91] S. S. Parkin, N. More, and K. P. Roche, “Oscillations in exchange coupling and magnetoresistance in metallic superlattice structures: Co/Ru, Co/Cr, and Fe/Cr,” *Physical Review Letters*, vol. 64, no. 19, pp. 2304–2307, 1990.

[92] S. S. Parkin and D. Mauri, “Spin engineering: Direct determination of the Ruderman-Kittel-Kasuya-Yosida far-field range function in ruthenium,” *Physical Review B*, vol. 44, no. 13, pp. 7131–7134, 1991.

[93] M. N. Baibich, J. M. Broto, A. Fert, F. N. Van Dau, F. Petroff, P. Eitenne, G. Creuzet, A. Friederich, and J. Chazelas, “Giant magnetoresistance of (001)Fe/(001)Cr magnetic superlattices,” *Physical Review Letters*, vol. 61, no. 21, pp. 2472–2475, 1988.

[94] J. Nogués and I. K. Schuller, “Exchange bias,” *Journal of Magnetism and Magnetic Materials*, vol. 192, no. 2, pp. 203–232, 1999.

[95] M. Ali, P. Adie, C. H. Marrows, D. Greig, B. J. Hickey, and R. L. Stamps, “Exchange bias using a spin glass,” *Nature Materials*, vol. 6, no. 1, pp. 70–75, 2007.

[96] W. H. Meiklejohn and C. P. Bean, “New Magnetic Anisotorpy,” *Physical Review*, vol. 105, no. 3, pp. 904–913, 1957.

[97] M. Kiwi, “Exchange bias theory,” *Journal of Magnetism and Magnetic Materials*, vol. 234, no. 3, pp. 584–595, 2001.

[98] W. Stoecklein, S. S. Parkin, and J. C. Scott, “Ferromagnetic resonance studies of exchange-biased Permalloy thin films,” *Physical Review B*, vol. 38, no. 10, pp. 6847–6854, 1988.

[99] C. H. Marrows, S. Langridge, M. Ali, A. T. Hindmarch, D. T. Dekadjevi, S. Foster, and B. J. Hickey, “Mapping domain disorder in exchange-biased magnetic multilayers,” *Physical Review B*, vol. 66, no. 2, p. 024437, 2002.

[100] C. Leighton, M. R. Fitzsimmons, A. Hoffmann, J. Dura, C. F. Majkrzak, M. S. Lund, and I. K. Schuller, “Thickness-dependent coercive mechanisms in exchange-biased bilayers,” *Physical Review B - Condensed Matter and Materials Physics*, vol. 65, no. 6, pp. 644031–644037, 2002.

[101] A. E. Berkowitz and K. Takano, “Exchange anisotropy - a review,” *Journal of Magnetism and Magnetic Materials*, vol. 200, no. 1-3, pp. 552–570, 1999.

[102] T. C. Schulthess and W. H. Butler, “Coupling mechanisms in exchange biased films (invited),” *Journal of Applied Physics*, vol. 85, no. 8 II B, pp. 5510–5515, 1999.

[103] M. Ali, C. H. Marrows, and B. J. Hickey, “Onset of exchange bias in ultrathin antiferromagnetic layers,” *Physical Review B*, vol. 67, no. 17, p. 172405, 2003.

[104] J. Nogués, J. Sort, V. Langlais, V. Skumryev, S. Suriñach, J. S. Muñoz, and M. D. Baró, “Exchange bias in nanostructures,” *Physics Reports*, vol. 422, no. 3, pp. 65–117, 2005.

[105] H. Ohldag, A. Scholl, F. Nolting, E. Arenholz, S. Maat, A. T. Young, M. Carey, and J. Stöhr, “Correlation between Exchange Bias and Pinned Interfacial Spins,” *Physical Review Letters*, vol. 91, no. 1, pp. 2–5, 2003.

[106] H. Ohldag, T. J. Regan, J. Stöhr, A. Scholl, F. Nolting, J. Lüning, C. Stamm, S. Anders, and R. L. White, “Spectroscopic identification and direct imaging of interfacial magnetic spins,” *Physical Review Letters*, vol. 87, no. 24, pp. 2–5, 2001.

[107] P. Kappenberger, S. Martin, Y. Pellmont, H. J. Hug, J. B. Kortright, O. Hellwig, and E. E. Fullerton, “Direct Imaging and Determination of the Uncompensated Spin Density in Exchange-Biased CoO/(CoPt) Multilayers,” *Physical Review Letters*, vol. 91, no. 26, p. 267202, 2003.

[108] H. Tarazona, M. Tafur, J. Quispe-Marcatoma, C. Landauro, E. Baggio-Saitovitch, and D. Schmool, “Thickness effect on the easy axis distribution in exchange biased Co/IrMn bilayers,” *Physica B: Condensed Matter*, vol. 567, no. April, pp. 11–16, 2019.

[109] Z. Shi, J. Du, and S. M. Zhou, “Exchange bias in ferromagnet/antiferromagnet bilayers,” *Chinese Physics B*, vol. 23, no. 2, 2014.

[110] Y. G. Yoo, S. G. Min, H. J. Ryu, N. S. Park, and S. C. Yu, “Angular and NiFe thickness dependence of exchange bias in IrMn/NiFe/IrMn thin film,” *Journal of Magnetism and Magnetic Materials*, vol. 303, no. 2 SPEC. ISS., pp. 188–191, 2006.

[111] R. Morales, A. C. Basaran, J. E. Villegas, D. Navas, N. Soriano, B. Mora, C. Redondo, X. Batlle, and I. K. Schuller, “Exchange-bias phenomenon: The role of the ferromagnetic spin structure,” *Physical Review Letters*, vol. 114, no. 9, pp. 1–5, 2015.

[112] J. McCord, R. Mattheis, and D. Elefant, “Dynamic magnetic anisotropy at the onset of exchange bias: The NiFe/IrMn ferromagnet/antiferromagnet system,” *Physical Review B - Condensed Matter and Materials Physics*, vol. 70, no. 9, pp. 1–8, 2004.

[113] Y. Xu, Q. Ma, J. W. Cai, and L. Sun, “Evidence of bulk antiferromagnet spin rearrangement during ferromagnetic layer reversal in a double exchange bias sandwich,” *Physical Review B*, vol. 84, p. 054453, aug 2011.

[114] A. Paul and S. Divinski, *Handbook of solid State diffusion : Volume 1.* Oxford, England: Elsevier, 2017.

[115] J. R. Whitman, G. L. Aranovich, and M. D. Donohue, “Thermodynamic driving force for diffusion: Comparison between theory and simulation,” *Journal of Chemical Physics*, vol. 134, no. 9, 2011.

[116] P. G. Shewmon, *Diffusion in solids.* Warrendale, Pa: Minerals, Metals & Materials Society, second ed., 1989.

[117] D. S. Wilkinson, *Mass Transport in Solids and Fluids.* Cambridge: Cambridge University Press, 2000.

[118] A. Fick, “Ueber Diffusion,” *Annalen der Physik*, vol. 170, no. 1, pp. 59–86, 1855.

[119] D. Gupta, “1.2.1 Mathematical Basis,” in *Diffusion Processes in Advanced Technological Materials*, William Andrew Publishing/Noyes, 2005.

[120] L. Maidich, D. Pontiroli, M. Gaboardi, S. Lenti, G. Magnani, G. Riva, P. Carretta, C. Milanese, A. Marini, M. Riccò, and S. Sanna, “Investigation of Li and H dynamics in Li_6C_{60} and $Li_6C_{60}H_y$,” *Carbon*, vol. 96, pp. 276–284, 2016.

[121] R. Gorelik, A. Asaduzzaman, V. R. Manga, A. Thakur, and K. Muralidharan, “A First-Principles Investigation of Lithium and Sodium Ion Diffusion in C_{60} Molecular Solids,” *Journal of Physical Chemistry C*, vol. 126, no. 9, pp. 4259–4266, 2022.

[122] M. F. Luo, Z. Y. Li, and W. Allison, “Study of the kinetics of potassium diffusion in thin C_{60} films,” *Surface Science*, vol. 523, no. 1-2, pp. 168–178, 2003.

[123] M. Riccò, M. Belli, M. Mazzani, D. Pontiroli, D. Quintavalle, A. Jánossy, and G. Csányi, “Superionic conductivity in the Li_4C_{60} fulleride polymer,” *Physical Review Letters*, vol. 102, no. 14, pp. 2–5, 2009.

[124] N. Sarzi Amadè, M. Gaboardi, G. Magnani, M. Riccò, D. Pontiroli, C. Milanese, A. Girella, P. Carretta, and S. Sanna, “H and Li dynamics in $Li_{12}C_{60}$ and $Li_{12}C_{60}$Hy,” *International Journal of Hydrogen Energy*, vol. 42, no. 35, pp. 22544–22550, 2017.

[125] P. Nancarrow, A. Al-Othman, D. K. Mital, and S. Döpking, “Comprehensive analysis and correlation of ionic liquid conductivity data for energy applications,” *Energy*, vol. 220, 2021.

[126] A. S. Cattaneo, V. Dall’asta, D. Pontiroli, M. Riccò, G. Magnani, C. Milanese, C. Tealdi, E. Quartarone, and P. Mustarelli, “Tailoring ionic-electronic transport in PEO-Li_4C_{60}: Towards a new class of all solid-state mixed conductors,” *Carbon*, vol. 100, pp. 196–200, 2016.

[127] B. Sundqvist, O. Andersson, C. Gong, B. Liu, B. Tonpheng, J. Yu, and M. Yao, “Ac impedance of A_4C_{60} fullerides under pressure,” *New Journal of Physics*, vol. 17, 2015.

[128] D. Pontiroli, M. Aramini, M. Gaboardi, M. Mazzani, A. Gorreri, M. Riccò, I. Margiolaki, and D. Sheptyakov, "Ionic conductivity in the Mg intercalated fullerene polymer Mg_2C_{60}," *Carbon*, vol. 51, no. 1, pp. 143–147, 2013.

[129] G. Klupp, P. Matus, D. Quintavalle, L. F. Kiss, É. Kováts, N. M. Nemes, K. Kamarás, S. Pekker, and A. Jánossy, "Phase segregation on the nanoscale in Na_2C_{60}," *Physical Review B - Condensed Matter and Materials Physics*, vol. 74, no. 19, pp. 1–7, 2006.

[130] J. C. Bachman, S. Muy, A. Grimaud, H. H. Chang, N. Pour, S. F. Lux, O. Paschos, F. Maglia, S. Lupart, P. Lamp, L. Giordano, and Y. Shao-Horn, "Inorganic Solid-State Electrolytes for Lithium Batteries: Mechanisms and Properties Governing Ion Conduction," *Chemical Reviews*, vol. 116, no. 1, pp. 140–162, 2016.

[131] H. Tachikawa, "Diffusion Dynamics of the Li Ion on C_{60} : A Direct Molecular Orbital-Molecular Dynamics Study," *The Journal of Physical Chemistry C*, vol. 111, pp. 13087–13091, sep 2007.

[132] H. Tachikawa, "Diffusion of the Li^+ Ion on C_{60} : A DFT and Molecular Dynamics Study," *The Journal of Physical Chemistry C*, vol. 115, pp. 20406–20411, oct 2011.

[133] M. Gobet, S. Greenbaum, G. Sahu, and C. Liang, "Structural Evolution and Li Dynamics in Nanophase Li_3PS_4 by Solid-State and Pulsed-Field Gradient NMR," *Chemistry of Materials*, vol. 26, pp. 3558–3564, jun 2014.

[134] A. A. Arie and J. K. Lee, "A study of Li-ion diffusion kinetics in the fullerene-coated Si anodes of lithium ion batteries," *Physica Scripta*, vol. T139, p. 014013, may 2010.

[135] A. A. Arie and J. K. Lee, "Effect of boron doped fullerene C_{60} film coating on the electrochemical characteristics of silicon thin film anodes for lithium secondary batteries," *Synthetic Metals*, vol. 161, no. 1-2, pp. 158–165, 2011.

[136] A. Hamed, "Effects of oxygen and illumination on the in situ conductivity of C_{60} thin films," *Physical Review B*, vol. 47, no. 16, 1993.

[137] C.-M. Yang, J.-L. Liao, and K.-C. Chiu, “Diffusion of O_2 in C_{60} crystal by measuring the decay of electrical conductivity,” *Journal of Applied Physics*, vol. 96, pp. 1934–1938, aug 2004.

[138] B. Pevzner and A. Hebard, “Role of molecular oxygen and other impurities in the electrical transportand dielectric properties of films,” *Physical Review B - Condensed Matter and Materials Physics*, vol. 55, no. 24, pp. 16439–16449, 1997.

[139] E. A. Katz, A. I. Shames, D. Faiman, S. Shtutina, Y. Cohen, S. Goren, W. Kempinski, and L. Piekara-Sady, “Do structural defects affect semiconducting properties of fullerene thin films?,” *Physica B: Condensed Matter*, vol. 273-274, pp. 934–937, 1999.

[140] E. Halac, E. Burgos, and H. Bonadeo, “Oxygen diffusion in solid C_{60}: A molecular-dynamics calculation,” *Physical Review B*, vol. 52, pp. 4764–4767, aug 1995.

[141] R. Fabiański, L. Firlej, A. Zahab, and B. Kuchta, “Relationships between crystallinity, oxygen diffusion and electrical conductivity of evaporated C_{70} thin films,” *Solid State Sciences*, vol. 4, no. 8, pp. 1009–1015, 2002.

[142] B. Li, A. R. Allnatt, C. S. Zhang, and P. R. Norton, “Model and theory for the determination of diffusion coefficients by Auger electron spectroscopy measurements and an application to oxygen diffusion along the [0001] and $[10\bar{1}0]$ axes in single crystal zirconium,” *Surface Science*, vol. 330, no. 3, pp. 276–288, 1995.

[143] F. Bernardi, M. Behar, A. Ruzzarin, J. H. Dos Santos, and F. Dyment, “Diffusion study of 180 implanted into α-Hf using the nuclear resonance technique,” *Applied Physics A: Materials Science and Processing*, vol. 83, no. 1, pp. 37–40, 2006.

[144] H. H. Wu, P. Wisesa, and D. R. Trinkle, “Oxygen diffusion in hcp metals from first principles,” *Physical Review B*, vol. 94, no. 1, pp. 1–7, 2016.

[145] J. Kummer, “β-Alumina electrolytes,” *Progress in Solid State Chemistry*, vol. 7, pp. 141–175, jan 1972.

[146] S. Ikeda, J. Hayakawa, Y. Ashizawa, Y. M. Lee, K. Miura, H. Hasegawa, M. Tsunoda, F. Matsukura, and H. Ohno, “Tunnel magnetoresistance of 604% at 300 K by

suppression of Ta diffusion in CoFeB/MgO/CoFeB pseudo-spin-valves annealed at high temperature," *Applied Physics Letters*, vol. 93, no. 8, 2008.

[147] X. Kozina, S. Ouardi, B. Balke, G. Stryganyuk, G. H. Fecher, C. Felser, S. Ikeda, H. Ohno, and E. Ikenaga, "A nondestructive analysis of the B diffusion in Ta-CoFeB-MgO-CoFeB-Ta magnetic tunnel junctions by hard x-ray photoemission," *Applied Physics Letters*, vol. 96, no. 7, 2010.

[148] S. Mukherjee, R. Knut, S. M. Mohseni, T. N. Anh Nguyen, S. Chung, Q. Tuan Le, J. Åkerman, J. Persson, A. Sahoo, A. Hazarika, B. Pal, S. Thiess, M. Gorgoi, P. S. Anil Kumar, W. Drube, O. Karis, and D. D. Sarma, "Role of boron diffusion in CoFeB/MgO magnetic tunnel junctions," *Physical Review B*, vol. 91, p. 085311, feb 2015.

[149] H. Bouchikhaoui, P. Stender, Z. Balogh, D. Baither, A. Hütten, K. Hono, and G. Schmitz, "Nano-analysis of Ta/FeCoB/MgO tunnel magneto resistance structures," *Acta Materialia*, vol. 116, pp. 298–307, 2016.

[150] J. F. Ying, S. T. Lim, M. Tran, and R. Ji, "Effects of post-growth annealing in a CoFeB/MgO/CoFeB trilayer structure," *Journal of Physics D: Applied Physics*, vol. 48, no. 45, 2015.

[151] X. D. Xu, K. Mukaiyama, S. Kasai, T. Ohkubo, and K. Hono, "Impact of boron diffusion at MgO grain boundaries on magneto-transport properties of MgO/CoFeB/W magnetic tunnel junctions," *Acta Materialia*, vol. 161, pp. 360–366, 2018.

[152] S. Yuasa, Y. Suzuki, T. Katayama, and K. Ando, "Characterization of growth and crystallization processes in CoFeB/MgO/CoFeB magnetic tunnel junction structure by reflective high-energy electron diffraction," *Applied Physics Letters*, vol. 87, no. 24, pp. 1–3, 2005.

[153] B. Dieny and M. Chshiev, "Perpendicular magnetic anisotropy at transition metal/oxide interfaces and applications," *Reviews of Modern Physics*, vol. 89, no. 2, 2017.

[154] W. H. Butler, X. G. Zhang, T. C. Schulthess, and J. M. MacLaren, "Spin-dependent tunneling conductance of Fe/MgO/Fe sandwiches," *Physical Review*

B - Condensed Matter and Materials Physics, vol. 63, no. 5, pp. 544161–5441612, 2001.

[155] H. X. Yang, M. Chshiev, B. Dieny, J. H. Lee, A. Manchon, and K. H. Shin, “First-principles investigation of the very large perpendicular magnetic anisotropy at Fe—MgO and Co—MgO interfaces,” *Physical Review B - Condensed Matter and Materials Physics*, vol. 84, no. 5, pp. 1–5, 2011.

[156] A. A. Greer, A. X. Gray, S. Kanai, A. M. Kaiser, S. Ueda, Y. Yamashita, C. Bordel, G. Palsson, N. Maejima, S. H. Yang, G. Conti, K. Kobayashi, S. Ikeda, F. Matsukura, H. Ohno, C. M. Schneider, J. B. Kortright, F. Hellman, and C. S. Fadley, “Observation of boron diffusion in an annealed Ta/CoFeB/MgO magnetic tunnel junction with standing-wave hard x-ray photoemission,” *Applied Physics Letters*, vol. 101, no. 20, 2012.

[157] J. J. Cha, J. C. Read, R. A. Buhrman, and D. A. Muller, “Spatially resolved electron energy-loss spectroscopy of electron-beam grown and sputtered CoFeB/MgO/CoFeB magnetic tunnel junctions,” *Applied Physics Letters*, vol. 91, no. 6, 2007.

[158] H. Kurt, K. Rode, K. Oguz, M. Boese, C. C. Faulkner, and J. M. Coey, “Boron diffusion in magnetic tunnel junctions with MgO (001) barriers and CoFeB electrodes,” *Applied Physics Letters*, vol. 96, no. 26, pp. 28–31, 2010.

[159] J. Sinha, M. Gruber, M. Kodzuka, T. Ohkubo, S. Mitani, K. Hono, and M. Hayashi, “Influence of boron diffusion on the perpendicular magnetic anisotropy in Ta—CoFeB—MgO ultrathin films,” *Journal of Applied Physics*, vol. 117, no. 4, 2015.

[160] A. Çalik, M. S. Karakaş, N. Ųcar, and F. ÜnÜvar, “Boriding kinetics of pure cobalt,” *Kovove Materialy*, vol. 52, no. 2, pp. 107–112, 2014.

[161] J. Borowiecka-Jamrozek and J. Lachowski, “Diffusion of Boron in Cobalt Sinters,” *Archives of Metallurgy and Materials*, vol. 58, pp. 1131–1136, dec 2013.

[162] R. Kouba, M. Keddam, and M. Kulka, “Simulation of the Growth Kinetics of CoB and Co_2B Layers on Alloy ASTM F-75,” *Metal Science and Heat Treatment*, vol. 63, no. 1-2, pp. 106–113, 2021.

[163] R. Hasegawa and R. Ray, “Magnetization of glassy Co-B alloys,” *Journal of Applied Physics*, vol. 50, no. B3, pp. 1586–1588, 1979.

[164] K. H. J. Buschow, “Magnetic Properties of Borides,” in *Boron and Refractory Borides* (V. I. Matkovich, ed.), pp. 494–515, Berlin, Heidelberg: Springer Berlin Heidelberg, 1977.

[165] T. Hamaguchi, R. Nakamura, K. Asano, T. Wada, and T. Suzuki, “Diffusion of boron in an amorphous iron-boron alloy,” *Journal of Non-Crystalline Solids*, vol. 601, p. 122070, feb 2023.

[166] I. Campos-Silva, M. Ortiz-Domínguez, H. Cimenoglu, R. Escobar-Galindo, M. Keddam, M. Elías-Espinosa, and N. López-Perrusquia, “Diffusion model for growth of Fe_2B layer in pure iron,” *Surface Engineering*, vol. 27, pp. 189–195, apr 2011.

[167] D. K. Belashchenko, V. V. Hoang, and P. K. Hung, “Computer simulation of local structure and magnetic properties of amorphous Co-B alloys,” *Journal of Non-Crystalline Solids*, vol. 276, no. 1, pp. 169–180, 2000.

[168] A. Gibaud and S. Hazra, “X-ray reflectivity and diffuse scattering,” *Current Science*, vol. 78, no. 12, pp. 1467–1477, 2000.

[169] M. F. Toney and S. Brennan, “Measurements of carbon thin films using x-ray reflectivity,” *Journal of Applied Physics*, vol. 66, no. 4, pp. 1861–1863, 1989.

[170] M. Tolan, *X-ray scattering from soft-matter thin films : materials science and basic research.* Springer tracts in modern physics ; 148, Berlin: Springer, 1999.

[171] L. G. Parratt, “Surface studies of solids by total reflection of x-rays,” *Physical Review*, vol. 95, no. 2, pp. 359–369, 1954.

[172] D. Sivia, *Elementary Scattering Theory.* Oxford University PressOxford, jan 2011.

[173] C. MacDonald, “Coherent Scatter I: Refraction and Reflection,” in *An Introduction to X-Ray Physics, Optics, and Applications*, ch. 11, pp. 174–200, Princeton University Press, 2017.

[174] J. Als-Nielsen and D. McMorrow, *Elements of modern X-ray physics*. Chichester: Wiley, 2001.

[175] C. J. Kinane, *The Interplay of Magnetism and Structure in Patterned Multilayer Thin Films*. PhD thesis, University of Leeds, 2008.

[176] P. Kienzle, "Neutron Activation and Scattering Calculator - NIST," 2024. URL: `https://www.ncnr.nist.gov/resources/activation/`, date accessed: 12/09/24.

[177] P. Kienzle, J. Krycka, N. Patel, and I. Sahin, "Refl1D (Version 0.8.16) [Computer Software]," 2024.

[178] P. Tippmann-Krayer, H. Möhwald, and Y. M. L'vov, "Structural Changes before and during Desorption of Langmuir-Blodgett Films," *Langmuir*, vol. 7, no. 10, pp. 2298–2302, 1991.

[179] A. M. Miller, M. Lemon, M. A. Choffel, S. R. Rich, F. Harvel, and D. C. Johnson, "Extracting information from X-ray diffraction patterns containing Laue oscillations," *Zeitschrift fur Naturforschung - Section B Journal of Chemical Sciences*, vol. 77, no. 4-5, pp. 313–322, 2022.

[180] M. Birkholz, "Thin films and multilayers," in *International Tables for Crystallography, Online MRW*, pp. 581–600, John Wiley and Sons, Ltd, dec 2007.

[181] H. Kiessig, "Untersuchungen zur Totalreflexion von Röntgenstrahlen," *Annalen der Physik*, vol. 402, no. 6, pp. 715–768, 1931.

[182] G. L. G. L. Squires, *Introduction to the theory of thermal neutron scattering* . Cambridge: New York, 1978.

[183] T. Chatterji, "Magnetic Neutron Scattering," in *Neutron Scattering from Magnetic Materials*, pp. 1–24, Amsterdam: Elsevier, 2006.

[184] Psi, "Neutron Physics," 2024. URL: `https://www.psi.ch/en/niag/neutron-physics`, date accessed: 12/09/24.

[185] R. Pynn, "Neutron Scattering - A Non-destructive Microscope for Seeing Inside Matter," in *Neutron Applications in Earth, Energy and Environmental Sciences.*, pp. 15–36, Springer, Boston, MA, 2009.

[186] C. Majkrzak, K. O'Donovan, and N. Berk, "Polarized Neutron Reflectometry," in *Neutron Scattering from Magnetic Materials*, vol. 200, pp. 397–471, Elsevier, 2006.

[187] J. F. Ankner and G. P. Felcher, "Polarized-neutron reflectometry," *Journal of Magnetism and Magnetic Materials*, vol. 200, no. 1-3, pp. 741–754, 1999.

[188] S. K. Sinha, E. B. Sirota, S. Garoff, and H. B. Stanley, "X-ray and neutron scattering from rough surfaces," *Physical Review B*, vol. 38, no. 4, pp. 2297–2311, 1988.

[189] F. Radu, V. Leiner, M. Wolff, V. K. Ignatovich, and H. Zabel, "Quantum states of neutrons in magnetic thin films," *Physical Review B*, vol. 71, p. 214423, jun 2005.

[190] C. Höglund, J. Birch, K. Andersen, T. Bigault, J. C. Buffet, J. Correa, P. Van Esch, B. Guerard, R. Hall-Wilton, J. Jensen, A. Khaplanov, F. Piscitelli, C. Vettier, W. Vollenberg, and L. Hultman, "B 4C thin films for neutron detection," *Journal of Applied Physics*, vol. 111, no. 10, pp. 1–8, 2012.

[191] A. R. Rennie, A. Engberg, O. Eriksson, and R. M. Dalgliesh, "Understanding neutron absorption and scattering in a polymer composite material," *Nuclear Instruments and Methods in Physics Research Section A: Accelerators, Spectrometers, Detectors and Associated Equipment*, vol. 984, p. 164613, 2020.

[192] G. J. Safford, T. I. Taylor, B. M. Rustad, and W. W. Havens, "Precision Determination of the Slow Neutron Absorption Cross Section of B^{10}," *Physical Review*, vol. 119, no. 4, pp. 1291–1294, 1960.

[193] M. B. Stone, L. Crow, V. R. Fanelli, and J. L. Niedziela, "Characterization of shielding materials used in neutron scattering instrumentation," *Nuclear Instruments and Methods in Physics Research, Section A: Accelerators, Spectrometers, Detectors and Associated Equipment*, vol. 946, no. September, p. 162708, 2019.

[194] V. F. Sears, "Neutron scattering lengths and cross sections," *Neutron News*, vol. 3, no. 3, pp. 26–37, 1992.

[195] Y. Ren and X. Zuo, “Synchrotron X-Ray and Neutron Diffraction, Total Scattering, and Small-Angle Scattering Techniques for Rechargeable Battery Research,” *Small Methods*, vol. 2, no. 8, 2018.

[196] M. Tokaç, C. J. Kinane, D. Atkinson, and A. T. Hindmarch, “Temperature dependence of magnetically dead layers in ferromagnetic thin-films,” *AIP Advances*, vol. 7, no. 11, 2017.

[197] S. Singh and S. Basu, “Investigation of interface magnetism of complex oxide heterostructures using polarized neutron reflectivity,” *Current Applied Physics*, vol. 17, no. 5, pp. 615–625, 2017.

[198] G. L. Causer, L. Guasco, O. Paull, and D. Cortie, “Topical Review of Quantum Materials and Heterostructures Studied by Polarized Neutron Reflectometry,” *physica status solidi (RRL) - Rapid Research Letters*, vol. 17, no. 6, 2023.

[199] J. B. Kortright, D. D. Awschalom, J. Stöhr, S. D. Bader, Y. U. Idzerda, S. S. Parkin, I. K. Schuller, and H. C. Siegmann, “Research frontiers in magnetic materials at soft X-ray synchrotron radiation facilities,” *Journal of Magnetism and Magnetic Materials*, vol. 207, no. 1-3, pp. 7–44, 1999.

[200] D. Roe, “Spin Polarised Solar Cells: Investigating the photoabsorption of Co/C60/MnOx photovoltaic devices. MPhys Dissertation, University of Leeds,” 2020.

[201] J. Shuai, *Interaction of surface acoustic waves and magnetic thin films.* PhD thesis, University of Leeds, 2023.

[202] W. Kiyotaka, K. Makoto, and A. Hideaki, *Sputtering Sytems*, ch. 4. William Andrew Publishing/Noyes, 2004.

[203] K. Seshan and D. Schepis, *Handbook of Thin Film Deposition (4th Edition).* Elsevier, 2018.

[204] C. A. Bishop, *DC Planar Magnetron Sputtering Source*, ch. 20.2. Elsevier, 2015.

[205] A. E. Wendt, M. A. Lieberman, and H. Meuth, “Radial current distribution at a planar magnetron cathode,” *Journal of Vacuum Science and Technology*, vol. 6, pp. 1827–1831, 1988.

[206] R. Parsons, “Sputter Deposition Processes,” in *Thin Film Processes II* (W. Kern, ed.), ch. 5, pp. 177–208, Elsevier, 1991.

[207] R. Pankajavalli, C. Mallika, O. M. Sreedharan, M. Premila, and P. Gopalan, “Vapour pressure of C60 by a transpiration method using a horizontal thermobalance,” *Thermochimica Acta*, vol. 316, no. 1, pp. 101–108, 1998.

[208] H. K. Pulker and J. P. Decosterd, “Chapter 3 - Applications of Quartz Crystal Microbalances for Thin Film Deposition Process Control,” in *Applications of Piezoelectric Quartz Crystal Microbalances* (C. LU and A. W. CZANDERNA, eds.), vol. 7 of *Methods and Phenomena*, pp. 63–123, Elsevier, 1984.

[209] T. Thomson, “Magnetic properties of metallic thin films,” in *Metallic Films for Electronic, Optical and Magnetic Applications*, pp. 454–546, Elsevier, 2014.

[210] R. L. Fagaly, “Superconducting quantum interference device instruments and applications,” *Review of Scientific Instruments*, vol. 77, no. 10, 2006.

[211] J. Pekola, “Superconducting Devices,” in *Encyclopedia of Physical Science and Technology*, pp. 219–234, Elsevier, 2003.

[212] J. B. Miller, “Nuclear Quadrupole Resonance Detection of Explosives,” in *Counterterrorist Detection Techniques of Explosives*, pp. 157–198, Elsevier, 2007.

[213] R. C. Jaklevic, J. Lambe, A. H. Silver, and J. E. Mercereau, “Quantum interference effects in Josephson tunneling,” *Physical Review Letters*, vol. 12, no. 7, pp. 159–160, 1964.

[214] M. Buchner, K. Höfler, B. Henne, V. Ney, and A. Ney, “Tutorial: Basic principles, limits of detection, and pitfalls of highly sensitive SQUID magnetometry for nanomagnetism and spintronics,” *Journal of Applied Physics*, vol. 124, no. 16, 2018.

[215] Quantum Design, “MPMS 3 Oven Option Installation Manual, 1505-200, Rev. A2,” 2016.

[216] K. Kago, H. Endo, H. Matsuoka, H. Yamaoka, N. Hamaya, M. Tanaka, and T. Mori, “Characterization of thin polymer films by X-ray reflectometry with

synchrotron radiation," *Journal of Synchrotron Radiation*, vol. 5, no. 5, pp. 1304–1308, 1998.

[217] M. Björck and G. Andersson, "GenX : an extensible X-ray reflectivity refinement program utilizing differential evolution," *Journal of Applied Crystallography*, vol. 40, no. 6, pp. 1174–1178, 2007.

[218] A. Adeyeye and G. Shimon, "Growth and Characterization of Magnetic Thin Film and Nanostructures," in *Handbook of Surface Science*, vol. 5, pp. 1–41, Elsevier B.V., 2015.

[219] R. S. Indeck, M. W. Muller, and L. Avazpour, "Magnetic Recording Measurements," in *Reference Module in Materials Science and Materials Engineering*, Elsevier, 2018.

[220] N. Kuhlmann, A. Vogel, and G. Meier, "Magnetization dynamics and cone angle precession in permalloy rectangles," *Physical Review B - Condensed Matter and Materials Physics*, vol. 85, no. 1, pp. 1–7, 2012.

[221] J. C. Rojas-Sánchez, N. Reyren, P. Laczkowski, W. Savero, J. P. Attané, C. Deranlot, M. Jamet, J. M. George, L. Vila, and H. Jaffrès, "Spin pumping and inverse spin hall effect in platinum: The essential role of spin-memory loss at metallic interfaces," *Physical Review Letters*, vol. 112, no. 10, pp. 1–14, 2014.

[222] F. Yang and P. Chris Hammel, "FMR-driven spin pumping in Y 3 Fe 5 O 12 -based structures," *Journal of Physics D: Applied Physics*, vol. 51, p. 253001, jun 2018.

[223] O. Mosendz, J. E. Pearson, F. Y. Fradin, G. E. W. Bauer, S. D. Bader, and A. Hoffmann, "Quantifying Spin Hall Angles from Spin Pumping: Experiments and Theory," *Physical Review Letters*, vol. 104, no. 4, p. 046601, 2010.

[224] I. S. Maksymov and M. Kostylev, "Broadband stripline ferromagnetic resonance spectroscopy of ferromagnetic films, multilayers and nanostructures," *Physica E: Low-Dimensional Systems and Nanostructures*, vol. 69, pp. 253–293, 2015.

[225] S. Beguhn, Z. Zhou, S. Rand, X. Yang, J. Lou, and N. X. Sun, "A new highly sensitive broadband ferromagnetic resonance measurement system with lock-in detection," *Journal of Applied Physics*, vol. 111, no. 7, 2012.

[226] E. Montoya, T. McKinnon, A. Zamani, E. Girt, and B. Heinrich, “Broadband ferromagnetic resonance system and methods for ultrathin magnetic films,” *Journal of Magnetism and Magnetic Materials*, vol. 356, pp. 12–20, apr 2014.

[227] Y. Zhao, Q. Song, S. H. Yang, T. Su, W. Yuan, S. S. Parkin, J. Shi, and W. Han, “Experimental Investigation of Temperature-Dependent Gilbert Damping in Permalloy Thin Films,” *Scientific Reports*, vol. 6, pp. 4–11, 2016.

[228] T. Gerrits, M. L. Schneider, and T. J. Silva, “Enhanced ferromagnetic damping in Permalloy/Cu bilayers,” *Journal of Applied Physics*, vol. 99, no. 2, 2006.

[229] K. Ounadjela, H. Lefakis, V. S. Speriosu, C. Hwang, and P. S. Alexopoulos, “Thickness Dependence of Magnetization and Magnetstriction of NiFe and NiFeRh films,” *Le Journal de Physique Colloques*, vol. 49, pp. C8–1709–C8–1710, dec 1988.

[230] J. B. Hayter and H. A. Mook, “Discrete thin-film multilayer design for X-ray and neutron supermirrors,” *Journal of Applied Crystallography*, vol. 22, no. 1, pp. 35–41, 1989.

[231] F. Mezei and P. Dagleish, “Corrigendum and first experimental evidence on neutron supermirrors,” *Communications on Physics*, vol. 2, no. 2, pp. 41–43, 1977.

[232] F. Mezei, “Novel polarized neutron devices: supermirror and spin component amplifier,” *Communications on Physics*, vol. 1, no. 3, pp. 81–85, 1976.

[233] M. Rossbach, O. Schärpf, W. Kaiser, W. Graf, A. Schirmer, W. Faber, J. Duppich, and R. Zeisler, “The use of focusing supermirror neutron guides to enhance cold neutron fluence rates,” *Nuclear Inst. and Methods in Physics Research, B*, vol. 35, no. 2, pp. 181–190, 1988.

[234] R. Maruyama, D. Yamazaki, T. Ebisawa, and K. Soyama, “Development of high-reflectivity neutron supermirrors using an ion beam sputtering technique,” *Nuclear Instruments and Methods in Physics Research, Section A: Accelerators, Spectrometers, Detectors and Associated Equipment*, vol. 600, no. 1, pp. 68–70, 2009.

[235] M. Hino, H. Sunohara, Y. Yoshimura, R. Maruyama, S. Tasaki, H. Yoshino, and Y. Kawabata, “Recent development of multilayer neutron mirror at KURRI,”

Nuclear Instruments and Methods in Physics Research, Section A: Accelerators, Spectrometers, Detectors and Associated Equipment, vol. 529, no. 1-3 SPEC. ISS., pp. 54–58, 2004.

[236] Y. Feng, Z. Zhang, R. Qi, Q. Huang, and Z. Wang, “Microstructural evolution of Ni/Ti multilayers doped with nitrogen at different d-spacings for neutron supermirrors,” *Vacuum*, vol. 210, no. June 2022, p. 111881, 2023.

[237] V. G. Syromyatnikov, A. F. Schebetov, and Z. N. Soroko, “FeAl neutron polarizing supermirror on a Si crystal substrate with antireflecting Cd layer,” *Nuclear Inst. and Methods in Physics Research, A*, vol. 324, no. 1-2, pp. 401–403, 1993.

[238] M. Kreuz, V. Nesvizhevsky, A. Petoukhov, and T. Soldner, “The crossed geometry of two super mirror polarisers - A new method for neutron beam polarisation and polarisation analysis,” *Nuclear Instruments and Methods in Physics Research, Section A: Accelerators, Spectrometers, Detectors and Associated Equipment*, vol. 547, no. 2-3, pp. 583–591, 2005.

[239] O. Schaerpf, “Properties of beam bender type neutron polarizers using supermirrors,” *Physica B: Physics of Condensed Matter*, vol. 156-157, no. C, pp. 639–646, 1989.

[240] M. Hino, H. Hayashida, M. Kitaguchi, Y. Kawabata, M. Takeda, R. Maruyama, T. Ebisawa, N. Torikai, T. Kume, and S. Tasaki, “Development of large-m polarizing neutron supermirror fabricated by using ion beam sputtering instrument at KURRI,” *Physica B: Condensed Matter*, vol. 385-386, pp. 1187–1189, nov 2006.

[241] T. Saerbeck, F. Klose, A. P. Le Brun, J. Füzi, A. Brule, A. Nelson, S. A. Holt, and M. James, “Invited Article: Polarization ”down under”: The polarized time-of-flight neutron reflectometer PLATYPUS,” *Review of Scientific Instruments*, vol. 83, no. 8, 2012.

[242] X. Tong, J. Robertson, and R. Pynn, “Non-uniform transmission of supermirror devices for neutron polarization,” *Nuclear Instruments and Methods in Physics Research Section A: Accelerators, Spectrometers, Detectors and Associated Equipment*, vol. 768, pp. 77–83, 2014.

[243] F. Mezei, "Neutron spin echo: A new concept in polarized thermal neutron techniques," *Zeitschrift für Physik*, vol. 255, no. 2, pp. 146–160, 1972.

[244] B. P. Toperverg and H. Zabel, "Chapter 6 - Neutron Scattering in Nanomagnetism," in *Neutron Scattering - Magnetic and Quantum Phenomena* (F. Fernandez-Alonso and D. L. B. T. E. M. i. t. P. S. Price, eds.), vol. 48, pp. 339–434, Academic Press, 2015.

[245] D. Findlay, J. Thomason, S. Fletcher, R. de Laune, and E. Cooper, "A Practical Guide to the ISIS Neutron and Muon Source," 2021.

[246] C. Brundle, C. A. J. Evans, and S. Wilson, *Encyclopedia of Materials Characterization - Surfaces, Interfaces, Thin Films - 11.2 Neutron Reflectivity.* Elsevier, 1992.

[247] P. Kienzle, J. Krycka, N. Patel, and I. Sahin, "Bumps (Version 0.9.1) [Computer Software]," 2011.

[248] J. A. Vrugt, C. ter Braak, C. Diks, B. A. Robinson, J. M. Hyman, and D. Higdon, "Accelerating Markov Chain Monte Carlo Simulation by Differential Evolution with Self-Adaptive Randomized Subspace Sampling," *International Journal of Nonlinear Sciences and Numerical Simulation*, vol. 10, no. 3, pp. 273–290, 2009.

[249] E. Pitthan, M. Moro, S. Corrêa, and D. Primetzhofer, "Assessing boron quantification and depth profiling of different boride materials using ion beams," *Surface and Coatings Technology*, vol. 417, p. 127188, 2021.

[250] K. Yasuda, "Time-of-flight erda for depth profiling of light elements," *Quantum Beam Science*, vol. 4, no. 4, 2020.

[251] M. Nastasi, Y. Wang, and J. W. Mayer, *Ion Beam Analysis : Fundamentals and Applications.* CRC Press, 2014.

[252] J. Jokinen, J. Keinonen, P. Tikkanen, A. Kuronen, T. Ahlgren, and K. Nordlund, "Comparison of TOF-ERDA and nuclear resonance reaction techniques for range profile measurements of keV energy implants," *Nuclear Instruments and Methods in Physics Research, Section B: Beam Interactions with Materials and Atoms*, vol. 119, no. 4, pp. 533–542, 1996.

[253] P. Ström, P. Petersson, M. Rubel, and G. Possnert, “A combined segmented anode gas ionization chamber and time-of-flight detector for heavy ion elastic recoil detection analysis,” *Review of Scientific Instruments*, vol. 87, no. 10, 2016.

[254] S. Giangrandi, K. Arstila, B. Brijs, T. Sajavaara, A. Vantomme, and W. Vandervorst, “Depth resolution optimization for low-energy ERDA,” *Nuclear Instruments and Methods in Physics Research Section B: Beam Interactions with Materials and Atoms*, vol. 261, pp. 512–515, aug 2007.

[255] S. Giangrandi, T. Sajavaara, B. Brijs, K. Arstila, A. Vantomme, and W. Vandervorst, “Low-energy heavy-ion TOF-ERDA setup for quantitative depth profiling of thin films,” *Nuclear Instruments and Methods in Physics Research Section B: Beam Interactions with Materials and Atoms*, vol. 266, pp. 5144–5150, dec 2008.

[256] M. V. Moro, R. HoleÅˆák, L. Zendejas Medina, U. Jansson, and D. Primetzhofer, “Accurate high-resolution depth profiling of magnetron sputtered transition metal alloy films containing light species: A multi-method approach,” *Thin Solid Films*, vol. 686, no. July, 2019.

[257] P. Ström, P. Petersson, and M. Hamberg, “Surface oxide and roughness on test samples for the Ultra High Vacuum section of the Laser Heater for the European XFEL,” *Vacuum*, vol. 149, pp. 83–86, 2018.

[258] S. Corrêa, E. Pitthan, M. Moro, and D. Primetzhofer, “A multipurpose setup using keV ions for nuclear reaction analysis, high-resolution backscattering spectrometry, low-energy PIXE and in-situ irradiation experiments,” *Nuclear Instruments and Methods in Physics Research Section B: Beam Interactions with Materials and Atoms*, vol. 478, pp. 104–110, sep 2020.

[259] E. Ligeon and A. Bontemps, “Nuclear reaction analysis of boron and oxygen in silicon,” *Journal of Radioanalytical Chemistry*, vol. 12, no. 2, pp. 335–351, 1972.

[260] E. Piatti, “Ionic gating in metallic superconductors: A brief review,” *Nano Express*, vol. 2, no. 2, p. 024003, 2021.

[261] S. Finizio, S. Wintz, K. Zeissler, A. V. Sadovnikov, S. Mayr, S. A. Nikitov, C. H. Marrows, and J. Raabe, “Dynamic Imaging of the Delay- and Tilt-Free Motion of

Néel Domain Walls in Perpendicularly Magnetized Superlattices," *Nano Letters*, vol. 19, no. 1, pp. 375–380, 2019.

[262] E. Darwin, R. Tomasello, P. M. Shepley, N. Satchell, M. Carpentieri, G. Finocchio, and B. J. Hickey, "Antiferromagnetic interlayer exchange coupled Co68B32/Ir/Pt multilayers," *Scientific Reports*, vol. 14, no. 1, pp. 1–10, 2024.

[263] C. E. A. Barker, S. Finizio, E. Haltz, S. Mayr, P. M. Shepley, T. A. Moore, G. Burnell, J. Raabe, and C. H. Marrows, "Domain wall motion at low current density in a synthetic antiferromagnet nanowire," *Journal of Physics D: Applied Physics*, vol. 56, no. 42, 2023.

[264] Z. Guo, J. Yin, Y. Bai, D. Zhu, K. Shi, G. Wang, K. Cao, and W. Zhao, "Spintronics for Energy- Efficient Computing: An Overview and Outlook," *Proceedings of the IEEE*, vol. 109, no. 8, pp. 1398–1417, 2021.

[265] I. Barsukov, Y. Fu, A. M. Gonçalves, M. Spasova, M. Farle, L. C. Sampaio, R. E. Arias, and I. N. Krivorotov, "Field-dependent perpendicular magnetic anisotropy in CoFeB thin films," *Applied Physics Letters*, vol. 105, no. 15, 2014.

[266] T. Zhu, Y. Yang, R. C. Yu, H. Ambaye, V. Lauter, and J. Q. Xiao, "The study of perpendicular magnetic anisotropy in CoFeB sandwiched by MgO and tantalum layers using polarized neutron reflectometry," *Applied Physics Letters*, vol. 100, no. 20, 2012.

[267] K. Watanabe, S. Fukami, H. Sato, S. Ikeda, F. Matsukura, and H. Ohno, "Annealing temperature dependence of magnetic properties of CoFeB/MgO stacks on different buffer layers," *Japanese Journal of Applied Physics*, vol. 56, no. 8, 2017.

[268] M. Mao, S. Ke, D. Tang, X. Sang, and D. He, "Structure and Performance Optimization of Co Magnetic Thin Films Deposited by Vacuum Evaporation Coating," *Materials*, vol. 16, no. 9, 2023.

[269] W. Griggs, B. Eggert, M. O. Liedke, M. Butterling, A. Wagner, U. Kentsch, E. Hirschmann, M. Grimes, A. J. Caruana, C. Kinane, H. Wende, R. Bali, and T. Thomson, "Depth selective magnetic phase coexistence in FeRh thin films," *APL Materials*, vol. 8, no. 12, 2020.

[270] P. Mohn, “The calculated electronic and magnetic properties of the tetragonal transition-metal semi-borides,” *Journal of Physics C: Solid State Physics*, vol. 21, pp. 2841–2851, may 1988.

[271] T. Moorsom, M. Rogers, I. Scivetti, S. Bandaru, G. Teobaldi, M. Valvidares, M. Flokstra, S. Lee, R. Stewart, T. Prokscha, P. Gargiani, N. Alosaimi, G. Stefanou, M. Ali, F. Al Ma’Mari, G. Burnell, B. J. Hickey, and O. Cespedes, “Reversible spin storage in metal oxide-fullerene heterojunctions,” *Science Advances*, vol. 6, no. 12, pp. 1–8, 2020.

[272] J. Fassbender, F. Nörtemann, R. Stamps, R. Camley, B. Hillebrands, G. Güntherodt, and S. Parkin, “Oscillatory interlayer exchange coupling of Co/Ru and permalloy / Ru multilayers investigated by Brillouin light scattering,” *Journal of Magnetism and Magnetic Materials*, vol. 121, no. 1-3, pp. 270–274, 1993.

[273] Y. Guan, W. Bailey, E. Vescovo, C.-C. Kao, and D. Arena, “Phase and amplitude of element-specific moment precession in,” *Journal of Magnetism and Magnetic Materials*, vol. 312, no. 2, pp. 374–378, 2007.

[274] M. V. Costache, S. M. Watts, M. Sladkov, C. H. Van Der Wal, and B. J. Van Wees, “Large cone angle magnetization precession of an individual nanopatterned ferromagnet with dc electrical detection,” *Applied Physics Letters*, vol. 89, no. 23, pp. 1–4, 2006.

[275] B. Rana, Y. Fukuma, K. Miura, H. Takahashi, and Y. Otani, “Effect of excitation power on voltage induced local magnetization dynamics in an ultrathin CoFeB film,” *Scientific Reports*, vol. 7, no. 1, pp. 1–9, 2017.

[276] N. Bahlmann, R. Gerhardt, M. Wallenhorst, and H. Dötsch, “Determination of the ferrimagnetic precession cone of in-plane magnetized garnet films using optical modulation technique,” *Journal of Applied Physics*, vol. 80, no. 7, pp. 3977–3981, 1996.

[277] C. Hauser, T. Richter, N. Homonnay, C. Eisenschmidt, M. Qaid, H. Deniz, D. Hesse, M. Sawicki, S. G. Ebbinghaus, and G. Schmidt, “Yttrium Iron Garnet Thin Films with Very Low Damping Obtained by Recrystallization of Amorphous Material,” *Scientific Reports*, vol. 6, p. 20827, feb 2016.

[278] Y. Sun, Y.-Y. Song, H. Chang, M. Kabatek, M. Jantz, W. Schneider, M. Wu, H. Schultheiss, and A. Hoffmann, "Growth and ferromagnetic resonance properties of nanometer-thick yttrium iron garnet films," *Applied Physics Letters*, vol. 101, no. 15, 2012.

[279] H. Chang, P. Li, W. Zhang, T. Liu, A. Hoffmann, L. Deng, and M. Wu, "Nanometer-Thick Yttrium Iron Garnet Films with Extremely Low Damping," *IEEE Magnetics Letters*, vol. 5, pp. 1–4, 2014.

[280] Y. M. Kang, S. H. Wee, S. I. Baik, S. G. Min, S. C. Yu, S. H. Moon, Y. W. Kim, and S. I. Yoo, "Magnetic properties of YIG(Y 3Fe 5O 12) thin films prepared by the post annealing of amorphous films deposited by rf-magnetron sputtering," *Journal of Applied Physics*, vol. 97, no. 10, pp. 3–6, 2005.

[281] C. Knox, M. Rogers, and T. Moorsom, "Van der Waals epitaxy of C60 on the topological insulator Bi2Se3," Tech. Rep. Materials from the Royce Deposition System (2), University of Leeds, 2020.

[282] T. Moorsom, "Growth of crystalline C_{60} by evaporation," Tech. Rep. Materials from the Royce Deposition System, University of Leeds, 2020.

[283] Z. Tan, Z. Ma, L. Fuentes, M. O. Liedke, M. Butterling, A. G. Attallah, E. Hirschmann, A. Wagner, L. Abad, N. Casañ-Pastor, A. F. Lopeandia, E. Menéndez, and J. Sort, "Regulating Oxygen Ion Transport at the Nanoscale to Enable Highly Cyclable Magneto-Ionic Control of Magnetism," *ACS Nano*, vol. 17, no. 7, pp. 6973–6984, 2023.